Comprehensive Study on the Low-energy Atomic Hydrogen Beam: From Production to Velocity Distribution Measurement

SUBMITTED IN PARTIAL FULFILLMENT OF THE REQUIREMENTS
FOR THE DEGREE OF DOCTOR OF ENGINEERING

YUJI SHIMABUKURO

Graduate School of Science and Engineering
Doshisha University

NOVEMBER 2019

Abstract

In this dissertation, the author opened and developed the new approach for fragmentation mass spectrometry in identifying the complex biomolecular structures. Unlike charged particles, electrically neutral atomic hydrogen can induce the fragmentation of massive biomolecules by the high reactivity without destroying fragile yet hydrogen insensitive bonding of functional groups. Two types of microwave driven compact radical beam sources which efficiently produce various kinds of reactive radicals were developed. The versatility of the radical source achieved realization of the peptide and lipid analyses. In order to understand the mechanism responsible for atom induced dissociation reactions, velocity distribution functions characterized by atomic temperature of hydrogen atoms produced in the two different radical sources have been measured by developing a dedicated atom velocity measurement system. The experimental results show a good agreement with calculated results of dissociation reaction for peptide molecules by density functional theory.

This study focused on the development of a new fragmentation technique to analyze the primary structures of unknown fragile biomolecules, especially in the post-translational modification (PTM) that characterizes the peptides. The PTMs have been believed to be the causes of several diseases, however, the structural analyses of the peptide ions including PTMs is considerably complicated due to their uncontrolled dissociation processes leading to different fragments. Although there are conventional ways to analyze a portion of the PTMs based upon the electron induced dissociation processes, the analyzable targets are strictly limited since both incident electrons and analyzable targets have electrical charges. In order to resolve the problem of the existing methods, a new fragmentation technique, HAD (Hydrogen Attachment/Abstraction Dissociation), was proposed in 2016. In HAD method, electrically neutral atomic hydrogen works as a trigger of the peptide fragmentation preserving PTMs. In the original HAD study, a thermal cracking type atomic hydrogen source with a high temperature tungsten capillary injected atomic hydrogen to the reaction chamber. High temperature components of the source do not only cause outgassing, but also shortens the operational lifetime ($\sim$ 100 h) as tungsten becomes reactive against residual oxygen and halogens at an elevated temperature. Although the HAD experiment achieved the cleavage of the peptide ions, several prior researches could not induce the peptide fragmentation by atomic hydrogen injection. Thus, a wide energy range of the atomic hydrogen production is important for elucidation of the HAD mechanism.

A radio frequency (RF) plasma generator neither has high-temperature components

nor has requirements to arrange complicated electrode structures to maintain high electric current necessary to run an ohmic heater in vacuum. The electrode structure of the RF source determines the discharge modes; the RF plasma are distinguished by plasma density into capacitively coupled plasma (CCP) and inductively coupled plasma (ICP). In general, RF plasma source utilize frequency in the MHz order to ignite and sustain a plasma. However, in this study, a 2.45 GHz microwave with a wavelength shorter than a typical MHz RF wave to reduce the operation gas pressure and increase the radical density. Microwave driven CCP and localized inductively coupled plasma (LICP) sources were developed in this study.

The development of the 1st and 2nd generation microwave driven CCP source indicated that the electrode geometry to enhance the local electric field was an important factor in drastically reducing the operating gas pressure. In contrast, the LICP type radical source that couples the input microwave power to the plasma by winding a coil around a small diameter dielectric tube adopted an electron cyclotron resonance (ECR) which significantly enhanced the ignition and stable production of the plasma. The modified 1.5th gen LICP source exhibited a high degree of dissociation of hydrogen compared with the CCP source. Though both microwave CCP and LICP source produced atomic hydrogen within the source plasma, microwave leakage and heat loss from the impedance matching circuit are not negligible because these dissipative factors induce the instability of the source operation.

In order to resolve these problems on the previous generation radical sources, tuner-integrated type microwave driven CCP and LICP sources were developed. Unlike the 2nd gen CCP source, the newly developed 3rd and 4th gen CCP sources were able to emit plasma efficiently as a form of a plasma plume. A copper plunger tunes the impedance of the source system easily without any external matching circuit. The 2nd gen LICP source is similarly tuned by the copper plunger which contacts the surface of the spiral antenna coiled around the dielectric tube. The developed 2nd gen LICP source exhibited three types of plasma excitation mode attributable to the field configuration, which is quite similar with the mode transitions well studied in the MHz-RF plasma sources. A velocity distribution function of produced atomic hydrogen in the developed sources have been measured by developing a dedicated mass separated time of flight (MSTOF) system. The atomic temperature of the 2nd gen hydrogen LICP was determined as 600 K by chi-square test regarding to the theoretical calculation. The atomic temperature of the 3rd gen CCP source was obtained to be ranging from 872 K to 1020 K for 40 W to 70 W power input. In contrast, hydrogen atoms produced in the thermal cracking source exhibited the two representative temperatures that can be attributable to the hot capillary and filament.

Demonstration of the HAD reaction with developed radical sources concluded that the cleavage of the peptide ions by atomic hydrogen injection requires a threshold energy for a hydrogen atom to induce the fragmentation. The 2nd gen hydrogen LICP injection

did not show any fragmentation. However, the 3rd gen CCP and 1.5th gen LICP showed fragment ions similar to the original HAD product ions. Therefore, the atomic temperature generated in the 1.5th gen LICP source can be considered higher than that of the 2nd gen LICP source and lower than that of the thermal cracking cell.

The developed sources of three different energy ranges are applied as a probe of the negative hydrogen ion surface production at the cesiated low work function surface. The hydrogen atoms emitted from the thermal cracking source and the 3rd gen CCP source achieved conversion from an atomic hydrogen to the negative hydrogen ion at the surface. These phenomena also identical with the relationship in the temperatures obtained in the previous chapters.

A series of experiments have identified the characteristic of each radical source behavior for the three types of developed sources. The versatile tuner-integrated microwave driven sources can produce various kinds of reactive radicals without the need for preliminary impedance matching. The difference in temperature or the velocity distribution functions of three types of radical sources may open a new field of study in the fragmentation mass spectrometry utilizing radical induced dissociation.

Contents

List of Tables

List of Figures

Nomenclature

ACN Acetonitrile

β Phase constant

c Speed of the light

C Capacitance

C_{cavity} Capacitance of the copper cavity

$C_{coupler}$ Capacitance of the coupler

C_{gap} Capacitance of the electrode gap

C_{plasma} Capacitance of the plasma

C_{quartz} Capacitance of the quartz tube

CCP Capacitively Coupled Plasma

CHCA α-Cyano-4-hydroxycinnamic acid

CI Chemical Ionization

CID Collision Induced Dissociation

CSF Corebrospinal fluid

DAWI Digital Assymmetric Wave Isolation

DFT Density functional theory

DNA Deoxyribonucleic acid

D Radius of the outer conductor

δ Skin depth

ECR Electron Cyclotron Resonance

$E_{electron}$ Energy of the electron

$\boldsymbol{E}$ Electric field

EI Electron-impact Ionization

E_a Electron affinity

E-mode Electrostatic mode

ϵ Permittivity

ϵ_r Relative permittivity

f Frequency

FT-ICR Fourier Transform Ion Cyclotron Resonance

γ Propagation constant

G Conductance

HAD Hydrogen Attachment/Abstraction Dissociation

H^0 Atomic hydrogen

H• Hydrogen radical

$\boldsymbol{H}$ Magnetic field

H-mode Electromagnetic mode

H^- Negative hydrogen ion

H_2^* Vibrationally excited hydrogen molecule

ICP Inductively Coupled Plasma

I_b Current of the plasma grid

I_{coil} Coil current

I_{dis} Emission current

I_{ext} Electron current

I_{H^-} Negative hydrogen ion current

I_{SEM} Current detected at the secondary electron multiplier

K_{DA} Rate coefficients for dissociative electron attachment reaction

λ Wavelength

LD Laser diode

LE-CID Low-energy collision induced dissociation

LEO Low-Earth Orbit

LICP Localized Inductively Coupled Plasma

$L_{antenna}$ Inductance of the spiral antenna

$L_{coupler}$ Inductance of the coupler

L_{plasma} Inductance of the inductively coupled plasma

L_{tube} Inductance of the copper tube

L Inductance

MALDI Matrix-Assisted Laser Desorption/Ionization

m/z Mass to charge ratio

MBE Molecular Beam Epitaxy

m_e Mass of the electron

m_i Mass of the ion

M Sample molecule

μ Permeability

μ_r Relative permeability

$[M + H]^+$ Protonated ion

NBI Neutral Beam Injection

ν_e Collision frequency among the electron, ion, and neutral particle

n_e Electron density

OAD Oxygen Attachment Dissociation

PD	Penetration depth
PET	Positron Emission Tomography
ϕ	Electric potential
Φ_{H}	Relative atomic hydrogen flux
ϕ_W	Work function
PD	Photo diode
h	Planck constant
P	Power consumption
PTM	Post-Translational Modification
q	Electric charge
QIT	Quadrupole Ion Trap
r_0	Minimum radius of the ring electrode
R	Resistance
R_{tube}	Resistance of the copper tube
RF	Radio Frequency
r	Radius of the inner conductor
r_L	Larmor radius
R_∞	Rydberg constant
SEM	Secondary Electron Multiplier
σ	Conductivity
σ_{1s}	Electron-impact ionization cross section for 1s state of atomic hydrogen
σ_{AD}	Cross section for associative electron detachment
σ_{CD}	Cross section for collisional electron detachment
σ_{col}	Cross section for collisional electron detachment
σ_{det}	Cross section for electron detachment

$\sigma_{excitation}$ Total electron impact excitation cross section

σ_{mn} Cross section for mutual neutralization

TEM Transverse Electro Magnetic

t Time

TMP Turbo molecular pump

TOF Time-Of-Flight

v Voltage

V_{att} Microwave control voltage

V_b Small bias voltage to the plasma grid

V_{bias} Bias voltage to the ionizer

V_{dis} Acceleration voltage of the electron

V_{ext} Voltage of the extraction electrode

$V_{\mathrm{f.c.}}$ Voltage of the Faraday cup

V_{fil} Voltage of the filament

V_{freq} Frequency control voltage

$V_{repeller}$ Voltage of the repeller

V_{tune} Voltage of the Einzel lens

$v_{\perp}$ Component of the velocity perpendicular to the direction of the magnetic field

v_p Velocity of a traveling wave

ω Frequency

ω_{ce} Electron cyclotron frequency

ω_{ci} Ion cyclotron frequency

W-mode Propagating wave mode

ω_{pe} Electron plasma frequency

ω_{pi} Ion plasma frequency

XRD	X-ray diffraction
Y	Admittance
Z_0	Characteristic impedance
Z_{in}	Input impedance
Z_l	Load impedance
z	Length of the circuit
z_0	Minimum distance bewteen the center and the end cap electrode

Chapter 1

Introduction

1.1 Mass spectrometry as a medical diagnosis

The capability of gas-phase mass spectrometry has been rapidly expanding due to the progress in the vacuum and ion beam technologies [1]. Mass spectrometry has been an indispensable generic tool for the research in the field of biology and chemistry after the development of MALDI (Matrix-Assisted Laser Desorption/Ionization) which enabled the ionization of large molecules fragile against disintegration such as a peptide [2]. Other than mass spectrometry, optical spectroscopy, NMR (Nuclear Magnetic Resonance), and XRD (X-ray diffraction) have been widely used to reveal a variety of molecular structures, however, some complex molecular structures are still almost unknown. Among these techniques, mass spectrometry has potential to extract important biological information from a very small amount of sample. Moreover the overall system can be made relatively compact among other instruments. For example, pervasive diagnostic methods for Alzheimer's disease utilize PET (Positron-Emission Tomography) and CSF (Cerebrospinal fluid) analysis. However the thresholds for these diagnostics are too high due to the limited medical institutions possessing PET and the high invasiveness for CSF analysis. In 2018, Nakamura *et al* reported that the mass spectrometric analysis of deposited amyloid-β in the brain from a 0.6 mL of blood plasma sample is an effective way to detect the Alzheimer's disease at a very early stage [3]. This is an example that mass spectrometry has a great potential to be utilized as a medical diagnostic tool in characterizing several kinds of diseases within medical institutions in near future. This study serves as a fundamental research of mass spectrometry in drastically expanding the analyzable targets.

1.2 Fragmentation mass spectrometry

The base sequence of DNA (Deoxyribonucleic acid) is translated to a linear sequence of amino acids of peptide. The structured peptides are modified or integrated to the PTM (Post-Translational Modification) that realizes the specific function of the peptides. It is known that several kinds of PTMs are related to our diseases. However, the peptide structural analysis involving PTMs have not advanced much due to the fragile PTMs. Identification of which functional groups attached to which amino acid requires cleaving techniques of amino acids preserving fragile PTMs in the mass spectrometer system. There are two types of fragmentation methods of the peptides to individual amino acids keeping PTMs: the low energy electron induced dissociation, and the HAD analysis. The low energy electron transfer based analyses can be utilized for unstable PTM analyses, however, these are not applicable to negative ions or singly charged ions, but only applicable to highly charged positive ions [4, 5, 6, 7]. Contrary to the electron based analyses, Takahashi *et al* proposed a new technique utilizing the atomic hydrogen [8]. In the new technique, HAD (Hydrogen Attachment/Abstraction Dissociation), electrically neutral hydrogen attaches to peptide ions or abducts atomic hydrogen from peptide ion to cause fragmentation of peptide ions preserving PTMs. Since the atomic hydrogen is electrically neutral, HAD method does not depend upon the charged state of the target ions unlike the conventional electron based techniques.

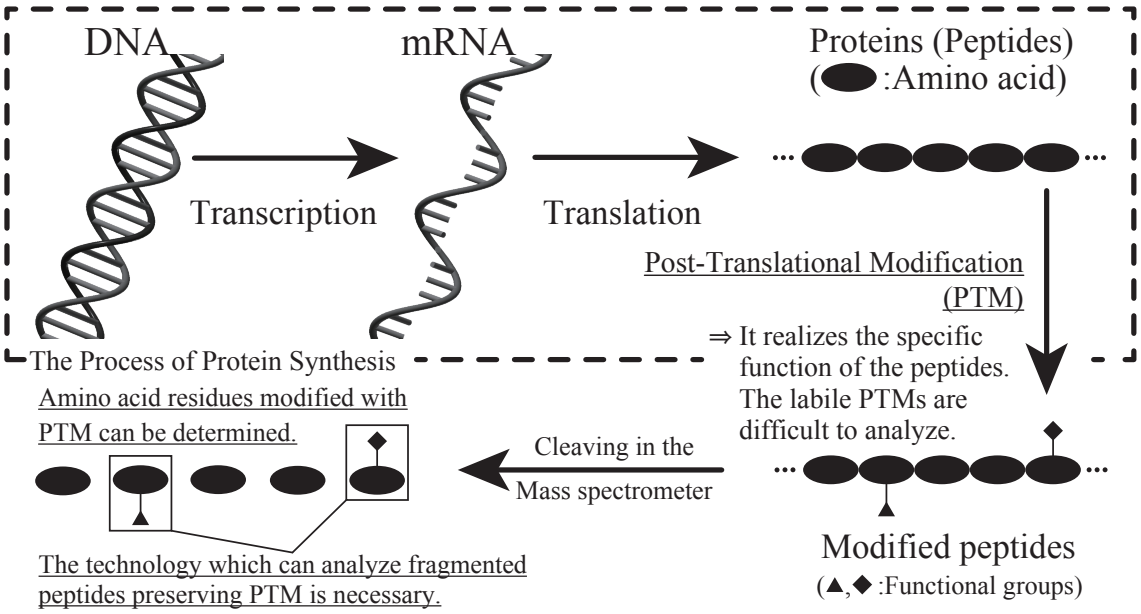

Fig. 1.1. A conceptual diagram of the research background from peptide synthesis to cleaving peptide.

1.3 Scope of this research

Although the HAD method has been developed, the characteristics of the atomic hydrogen used in the original study and the fundamental physical aspect of the HAD have not been clarified. The thermal cracking type atomic hydrogen source developed in the original HAD study has a limited life-time about 100 hours due to its high temperature components and is only capable of producing atomic hydrogen. A miniaturization of the source is difficult because the thermal cracking source requires water cooling and heat shields to avoid damaging the surrounded components. No investigation on the fragmentation study was made by cleaving biomolecules with low-energy reactive radicals other than hydrogen. Thus, in order to expand the analyzable biomolecules by opening the new fragmentation methods using a various kinds of low-energy radicals, versatile radical beam sources has been developed in this study. Thermal dissociation of typical molecules except for hydrogen is impossible due to the high bond-dissociation energies. Thus, chemically reactive radicals should be produced by discharge of gases or liquids. A radio frequency (RF) plasma source can dissociate many kinds of reactive gases, such as oxygen, water vapor, hydrochloric acid, etc., and is suitable as a radical source for operation with chemically reactive species because the RF source can generate plasma in the vacuum vessel with electrode less configuration. Especially in the application of gas-phase mass spectrometry, gas introduction to the reaction chamber of the system with high flow rate induces poor S/N ratio, insufficient mass separation, and damage to the detector. Thus, the radical source must be operated under a low gas pressure condition to realize high sensitivity measurement. In general, microwave excited plasma can ignite and sustain plasma at the lower gas pressure condition than typical RF plasma source. Moreover, the combination with electron cyclotron resonance (ECR) can enhance the density and the degree of dissociation by effective electron acceleration. In order that the reactive radicals realize the biomolecular structural analyses with sufficient reaction rate, microwave driven radical beam sources were developed to satisfy high atomic flux, high degree of dissociation, low operating pressure, and less heat loss.

Chapter 2 illustrates the design and improvement in microwave driven compact radical sources. The design and performance evaluation of tuner-integrated type microwave driven radical beam sources are provided in Chapter 3. Chapter 4 investigates the velocity distribution functions that are characterized by the atomic temperature of produced atomic hydrogen beams in the developed radical sources. Chapter 5 gives the discussion about the HAD fragmentation operated with three types of radical beam sources. In addition to the mass spectrometric studies, the developed atomic hydrogen sources are applied to a negative hydrogen ion production study to utilize the developed sources as an index of negative hydrogen ion surface production in Chapter 6. Chapter 7 discusses the further

applications of the developed sources not only as atomic hydrogen sources but also as versatile radical beam sources. Finally Chapter 8 provides the conclusion of this study.

References

[1] E. Hoffmann and J. V. Stroobant, *Mass Spectrometry Principles and Applications* (John Wiley & Sons, 2007).

[2] K. Tanaka, H. Waki, Y. Ido, S. Akita, Y. Yoshida, T. Yoshida, and T. Matsuo, "Protein and polymer analyses up to *m/z* 100000 by laser ionization time-of-flight mass spectrometry", *Rapid Commun. Mass Spectrom.* **2**, 151 1988.

[3] A. Nakamura, N. Kaneko, V. L. Villemagne, T. Kato, J. Doecke, V. Dore, C. Fowler, Q. Li, R. Martins, C. Rowe, T. Tomita, K. Matsuzaki, K.Ishii, K. Ishii, Y. Arahata, S. Iwamoto, K. Ito, K. Tanaka, C. L. Masters, and K. Yanagisawa, "High performance plasma amyloid-β biomarkers for Alzheimer's disease", *Nature* **554**, 249 2018.

[4] R. A. Zubarev, N. L. Kelleher, and F. W. McLafferty, "Electron Capture Dissociation of Multiply Charged Protein Cations. A Nonergodic Process", *J. Am. Chem. Soc.* **120**, 3265 1998.

[5] R. A. Zubarev, D. M. Horn, E. K. Fridriksson, N. L. Kelleher, N. A. Kruger, M. A. Lewis, B. K. Carpenter, and F. W. McLafferty, "Electron Capture Dissociation for Structural Characterization of Multiply Charged Protein Cations", *Anal. Chem.* **72**, 563 2000.

[6] J. E. P. Syka, J. J. Coon, M. J. Schroeder, J. Shabanowitz, and D. F. Hunt, "Peptide and protein sequence analysis by electron transfer dissociation mass spectrometry", *Proc. Natl. Acad. Sci. U.S.A.* **101(26)**, 9528 2004.

[7] J. J. Coon, J. Shabanowitz, D. F. Hunt, and J. E. P. Syka, "Electron Transfer Dissociation of Peptide Anions", *J. Am. Soc. Mass Spectrom.* **16(6)**, 880 2005.

[8] H. Takahashi, S. Sekiya, T. Nishikaze, K. Kodera, S. Iwamoto, M. Wada, and K. Tanaka, "Hydrogen Attachment/Abstraction Dissociation (HAD) of Gas-Phase Peptide Ions for Tandem Mass Spectrometry", *Anal. Chem.* **88**, 3810 2016.

Chapter 2

Neutral Beam Sources for Low-energy Radical Beam Production

2.1 Importance of electrically neutral particles

Electrically neutral beam has been used in a lot of applications and studies. Atomic hydrogen is applicable to surface cleaning of the substrate through a reduction process for oxide film [1, 2, 3, 4], high speed imaging method of the diffractive scattering [5], NBI (Neutral Beam Injection) system for nuclear fusion research [6] and so on. Surface coating by plasma processes improves the performance of industrial materials. For example, nitriding process of machining tools increases surface hardness and fatigue resistance [7]. During a radical nitriding process, neutral atomic nitrogen plays an important role [8, 9, 10]. In MBE (Molecular Beam Epitaxy) process, vaporized materials are deposits onto substrate surface as a thin film in ultrahigh vacuum condition. It had been reported that an improvement of flatness of the surface and increase in growth rate is achieved in atomic hydrogen-assisted MBE, as atomic hydrogen is doped during growing crystals [11, 12, 13]. Other applications of atomic beam include realization of the simulation of extreme environment. Oxygen atoms present in LEO (Low-Earth Orbit) degrades polymeric materials as they collide with the spacecraft surface. Thus, oxygen radicals are essential to test the durability against aging of spacecraft materials in terrestrial surface environment [14, 15, 16]. There are a variety of ways to realize neutral particle beam sources suitable for these applications. The size of the source should be small as the original aim for the system development was for the analysis of biomolecule that did not allow a substantial volume to produce neutral atoms. In this chapter, the first phase of the development of compact neutral beam sources is described.

2.2 Electrically neutral particle production methods

2.2.1 Thermal cracking

Thermal cracking of the molecular hydrogen (H_2) as a production method of the atomic hydrogen (H^0) is most popular way since Langmuir found that the H_2 easily atomized on the tungsten wire heated to a temperature between 1300 to 2500 K in reduced gas pressure condition [17]. Table 2.1 shows typical bond-dissociation energies for several representative molecules [18]. The high temperature of the metal surface can decompose H_2 into H^0 efficiently with less than 0.22 eV ($\approx$ 2500 K) due to its catalytic effect on the heated metal surface, while the bond-dissociation energy for the H_2 is 4.519 eV ($\approx 5.2 \times 10^4$ K).

Table 2.1. Bond-dissociation energies of molecules [18].

Gas species	Energy [eV]
H-H	4.519
H-O	4.436
H-OH	5.169
N-N	9.798
N≡N	9.805
O=O	5.165

The degree of dissociation of H^0 depends upon the temperature of the metal catalyst and gas pressure [19, 20]. Lockwood *et al* measured the degree of dissociation of thermally cracked H^0 by fast protons and reported it as 87.5% at 2380 K [21]. Abe *et al* investigated the produced atomic hydrogen density and activation energies regarding to several metallic catalyst such as tungsten, platinum, nickel, molybdenum, tantalum, and tungsten 5% rhenium [22]. They concluded that the tantalum effectively dissociates H_2 in the range of the temperature from 1473 to 1673 K.

After the report of Langmuir, several kinds of thermal cracking type H^0 source have been developed [23, 24, 25, 26, 27, 28]. Tschersich and Bonin classified H^0 sources into three categories: (a) hot filament, (b) hot source chamber with wall aperture followed by differentially pumped skimmer, and (c) hot capillary [23]. The hot filament type H^0 source is the simplest thermal cracking source which is composed of a coiled hot filament. Molecular hydrogens in the vicinity of the filament are decomposed by radiant heat. Flux densities produced in this type of source is low. In the hot source chamber, the H^0 dissociated in the thermal chamber is delivered as a homogeneous flux density through differential pumping chambers. The source can produce higher flux H^0, while the entire setup is relatively large due to the differential pumping system. The hot capillary is

intermediate type source among the discussed atomic sources. Apart from the capillary being able to form a collimated beam, operating pressure is also lower than second type H^0 source with no differential pumping. Koschmieder and Raible adopted a configuration that radiant heat from the 0.15 mm thickness 15mm width tungsten ribbon heated the enclosed tungsten capillary [24]. They measured the degree of dissociation with respect to the oven temperature from 1800 to 2600 K by quadrupole mass spectrometer. Bischler and Bertel accelerated the electrons emitted from a tungsten capillary to 560 V positively biased tungsten capillary. Although they restrict the temperature to 1800 K to prevent damaging the sample from the radiant heat, the source exhibited the 45% of degree of dissociation and the experiment demonstrated that the additional electron bombardment heating to the capillary was efficient for reducing the temperature [25]. Zyl and Gealy developed a H^0 and O source utilizing a thoria coated iridium filament coiled around the tungsten capillary. This configuration achieved 80% for the degree of dissociation at 2150 K [26].

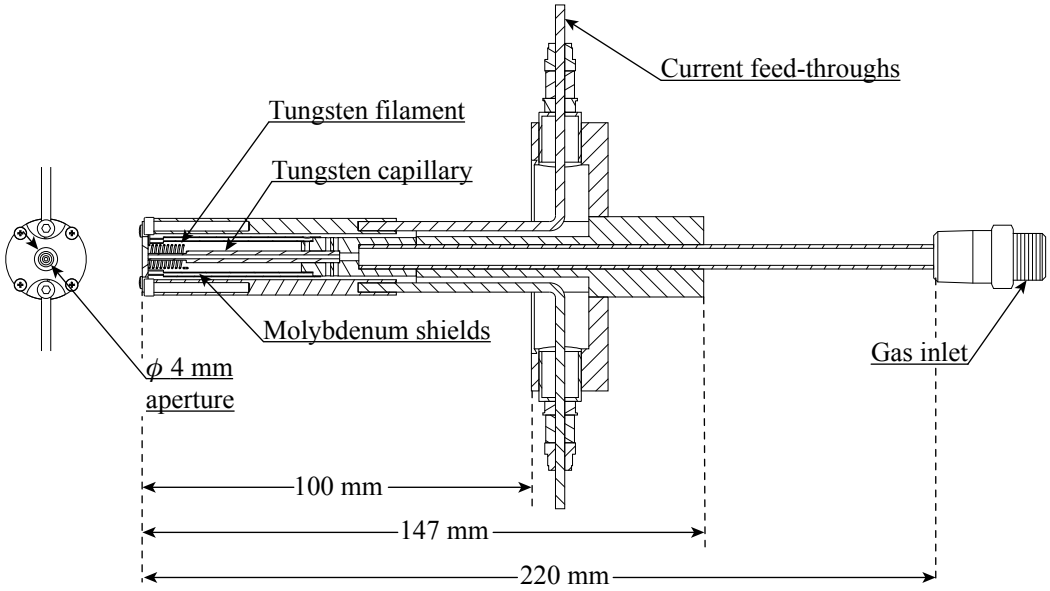

Fig. 2.1. A sectional view of the compact thermal cracking atomic source apparatus. The source diameter is 21 mm and the total length is 220 mm.

Figure 2.1 schematically shows the developed compact thermal cracking atomic hydrogen source apparatus used as a reference source. The compact source based on an ICF 70 standard stainless-steel flange houses a tungsten capillary in a 21mm inner diameter stainless-steel tube. Two current feedthroughs (CeramTec, 3888-10-W) welded sideways of the flange introduce an electric power to a tungsten filament. A tungsten wire of 0.4 mm diameter is wound eight turns around a 1 mm inner diameter 3 mm outer diameter tungsten capillary at the source tip. This tungsten filament is kept electrically floated with the capillary to avoid overheating due to electron emission current of the base flange

and chamber made of stainless steel. Two 0.4 mm thickness molybdenum shields that enclose the filament and capillary keep higher temperature of the capillary about 2000 K. A molybdenum cover electrode that has a 4 mm of collimation aperture arranged at the source tip screens the emitted electron and sputtered tungsten atoms to be released to the reaction chamber. A copper tube with coolant water wound around the stainless steel pipe reduces the heat loading from the high temperature components of the thermal cracker source to the source supporting cylinder.

2.2.2 Effusion from radio frequency (RF) plasmas

Despite the ability of the thermal dissociation technique in the production of atomic hydrogen, the tungsten filament does not realize stable cracking of the gas species reactive to tungsten, such as oxygen. Moreover, high temperature components in the source not only produce contaminants, but this also limit the operational lifetime. Thus, discharge plasma excitation based atom sources are considered promising. Although there are some arc discharge type atomic sources [29, 30, 31], longer lifetime of the source can be realized in RF (Radio Frequency) plasma. There are three ways to produce neutral beams: charge exchange neutralization, surface neutralization, and effusion from the source plasma. The neutralization in the charge exchange cell which is adopted in NBI (Neutral Beam Injection) system is inefficient against to low-flux and low-energy ion beams due to the large space charge effect. Meanwhile, atomic beam sources with surface neutralization have been developed for a long time to apply for a semiconductor process and space development [32, 33, 34, 35, 36, 37]. In surface neutralization plasma source, accelerated ions are neutralized to excited neutrals as these pass through a neutralization grid by an electron tunneling. The neutralized excited species accelerated by an image charge are de-excited as ground state atoms [38]. Because the controllable energy range of the produced neutrals is from 1 to 100 eV, such an energetic atom produced by the surface neutralization is not suitable for biomolecular analyses. In this study, the neutral particles effused from the source plasma which has an energy depends upon their velocity distributions are utilized in order to irradiate low-energy beams (< 0.5 eV). High frequency plasma generally adopts wavebands such as RF (13.56 MHz) and microwave (2.45 GHz). In comparison to RF frequency range, microwave has the plasma cut off at higher electron density and shorter wavelength suitable for miniaturization of the plasma source system. Microwave driven sources are free from high temperature components and dissociate not only nitrogen and hydrogen, but also other reactive gases such as oxygen, water vapor, and chemically active species like hydrochloric acid.

2.3 Development of microwave driven radical beam sources

2.3.1 Microwave propagation

In the high frequency circuit in the range of the microwave, the power source supplies a negative half cycle of the signal before the arrival of a positive half cycle to the load. Thus, the dimension of the electrical circuit cannot be negligible considering the short wavelength of the power propagation. For the distributed-element model, the telegrapher's equations for voltage v and current i are given by

$$-\frac{\partial v}{\partial z} = L\frac{\partial i}{\partial t} + Ri \tag{2.1}$$

$$-\frac{\partial i}{\partial z} = C\frac{\partial v}{\partial t} + Gv \tag{2.2}$$

where z is the length of the circuit, t is the time, R is the resistance, L is the inductance, C is the capacitance, and G is the conductance. When the circuit is considered to be a lossless transmission line, $R = 0, G = 0$, the following wave equations are obtained.

$$\frac{\partial^2 v}{\partial z^2} = LC\frac{\partial^2 v}{\partial t^2} \tag{2.3}$$

$$\frac{\partial^2 i}{\partial z^2} = LC\frac{\partial^2 i}{\partial t^2} \tag{2.4}$$

These second order partial differential equations have two linearly independent d'Alembert's solutions,

$$v = v_1(z - v_p t) + v_2(z + v_p t) \tag{2.5}$$

$$i = \sqrt{\frac{C}{L}}\Big(v_1(z - v_p t) + v_2(z + v_p t)\Big) \tag{2.6}$$

where

$$v_p = \frac{1}{\sqrt{LC}} \tag{2.7}$$

is the phase velocity of a traveling wave. The first and second term of the Eq.2.5 express the forward and backward traveling wave, respectively. Ratio between the Eqs.2.5 and 2.6,

$$Z_0 = \sqrt{\frac{L}{C}} \tag{2.8}$$

is the characteristic impedance of the distributed-element model. Although the characteristic impedance is generally a complex number, the impedance actually can be considered as pure resistance since the imaginary part is negligible.

2.3.2 Coaxial transmission line

Most of commercially available microwave plasma sources utilize a magnetron as a power source and waveguide for power transmission [39]. However, this research adopted a solid-state microwave oscillator (Tokyo-keiki, TME101B00B) and coaxial cable (Fujikura, 12D-SFA-LITE) in order to miniaturize the system. A coaxial cable is composed of inner conductor, insulator, and outer conductor. The cable used in this study employs a copper-clad aluminum wire for inner conductor, expanded polyethylene for insulator, and copper mesh wire for outer conductor. In principle, the coaxial cable propagates microwave as a form of TEM (Transverse Electro Magnetic) wave. The inductance and capacitance values per an unit length for the coaxial cable are given by

$$L = \frac{\mu}{2\pi} ln\left(\frac{D}{r}\right) \quad [\mathrm{H/m}] \tag{2.9}$$

$$C = \frac{2\pi\epsilon}{ln\left(\frac{D}{r}\right)} \quad [\mathrm{F/m}] \tag{2.10}$$

where, μ is the permeability, ϵ is the permittivity, D is the radius of the outer conductor, and r is the radius of the inner conductor. Therefore, phase velocity and characteristic impedance are

$$v_p = \frac{1}{\sqrt{LC}} \tag{2.11}$$

$$= \frac{1}{\mu\epsilon} \tag{2.12}$$

$$= \frac{c}{\mu_r \epsilon_r} \quad [\mathrm{m/s}] \tag{2.13}$$

$$Z_0 = \sqrt{\frac{C}{L}} \tag{2.14}$$

$$= \frac{1}{2\pi}\sqrt{\frac{\mu}{\epsilon}} ln\left(\frac{D}{r}\right) \tag{2.15}$$

$$= 60\sqrt{\frac{\mu_r}{\epsilon_r}} ln\left(\frac{D}{r}\right) \quad [\Omega] \tag{2.16}$$

where, μ_r is the relative permeability, ϵ_r is the relative permittivity, c is the speed of light. Hence, these parameters for the coaxial cable used in this study are calculated as follows. $Z_0 = 50\,\Omega$, $L = 0.19\,\mu\mathrm{H/m}$, $C = 83\,\mathrm{pF/m}$. The characteristic impedance of the coaxial transmission line does not depend upon the scale of the cable, but upon the ratio of the conductor radii (D/r).

2.3.3 Skin effect

When an electromagnetic wave is traveling in the positive z direction, Maxwell's equations for electric field $\boldsymbol{E}$ and magnetic field $\boldsymbol{H}$ are

$$\frac{\partial^2 \boldsymbol{E}}{\partial x^2} + \frac{\partial^2 \boldsymbol{E}}{\partial y^2} + k_0^2 \boldsymbol{E} = 0, \quad \frac{\partial^2 \boldsymbol{H}}{\partial x^2} + \frac{\partial^2 \boldsymbol{H}}{\partial y^2} + k_0^2 \boldsymbol{H} = 0 \tag{2.17}$$

where

$$k_0^2 = \gamma^2 + \omega^2 \epsilon \mu, \tag{2.18}$$

$\gamma = \sqrt{j\omega\mu(\sigma + j\omega\epsilon)}$ is the propagation constant. For the case of plasma and copper antenna, $\sigma \gg \omega\epsilon$, and γ is

$$\gamma = \alpha + j\beta \approx \frac{1+j}{\sqrt{2}} \sqrt{\omega\mu\sigma}. \tag{2.19}$$

where, σ is the conductivity. This means that the microwave is attenuated with the factor $e^{-\alpha z}$ during the propagation in conductor due to large σ. Here, the skin depth δ is defined as the attenuated distance to e^{-1} from the value at the conductor surface ($z = 0$).

$$\delta = \sqrt{\frac{2}{\omega\mu\sigma}} \tag{2.20}$$

Thus, the skin depth for conductor (copper) for 2.45 GHz is about 1.35 μm. Meanwhile, conductivity of plasma is written as follows when the collision frequency for the electron is ν_e, electron density is n_e,

$$\sigma = \frac{e^2 n_e}{m_e \nu_e} = \frac{\epsilon_0 \omega_{pe}^2}{\nu_e}. \tag{2.21}$$

The skin depth for plasma is obtained by insertion the plasma conductivity into Eq.2.20.

$$\delta = c\sqrt{\frac{m_e \epsilon_0}{e^2 n_e}} \sqrt{\frac{2\nu_e}{\omega}} \tag{2.22}$$

$$= \frac{c}{\omega_{pe}} \sqrt{\frac{2\nu_e}{\omega}} \tag{2.23}$$

In the case when the microwave frequency ω is higher than the electron plasma frequency ω_{pe}, plasma can sustain their discharge by propagating the electric field as an electron plasma wave in the plasma. However, in the opposite case, electric field is reflected because the field accelerates electrons and the discharge produced current is concentrated in the vicinity of the injection point diminishing the field.

2.3.4 Microwave power adsorbed by dielectric materials

Power consumption per unit volume in a dielectric material P can be expressed by the relative permittivity and loss tangent as

$$P = E^2(\sigma + \omega \cdot \epsilon_0 \cdot \epsilon_r \cdot \tan\delta). \tag{2.24}$$

The product of the relative permittivity and loss tangent defined as a loss factor $\epsilon_r \cdot tan\delta$ works as an index of power consumption in the dielectric material. The penetration depth PD is used to denote the depth at which the power density has decreased to 50% of its initial value at the surface [40].

$$PD = \frac{\lambda}{2\pi}\left(\frac{2}{\epsilon_r\sqrt{1+\tan^2\delta}-1}\right)^{\frac{1}{2}} \times 0.35 \quad [\mathrm{m}] \tag{2.25}$$

$$= \frac{3.31 \cdot 10^7}{f\sqrt{\epsilon_r} \cdot \tan\delta} \quad [\mathrm{m}] \tag{2.26}$$

This represents that the materials expressing the shallow penetration depth are lossless materials due to the absorption by dielectrics. In the materials used in this study, the penetration depths and loss factors of the quartz glass, Pyrex® glass, alumina are increased.

2.3.5 Impedance conversion

In case that the load Z_l is connected to the end of the transmission line of length l, the input impedance Z_{in} viewed from the other end is expressed as follows.

$$Z_{in} = Z_0\frac{Z_l + jZ_0\tan\beta l}{Z_0 + jZ_l\tan\beta l} \tag{2.27}$$

Equation 2.27 indicates how the input impedance Z_0 is converted by the transmission line. Here, we consider the two special cases. When the length of the line l satisfies the condition

$$l = 2k\left(\frac{n\lambda}{2}\right), \quad k = 1, 2, 3 \cdot \cdot \tag{2.28}$$

where $\frac{n\lambda}{2}$ is the half wavelength, by using the relationship between the phase constant β and wavelength λ,

$$\beta\lambda = \left(\frac{\omega}{v_p}\right)\left(\frac{v_p}{f}\right) = 2\pi \tag{2.29}$$

we obtain

$$Z_{in} = Z_l \tag{2.30}$$

This denotes that the impedance of the circuit takes the same value on each half-wave length. In contrast, when the line l satisfies the condition

$$l = (2k-1)\left(\frac{2n+1}{4}\right)\lambda, \quad k = 1,2,3\cdots \tag{2.31}$$

the input impedance can be expressed by

$$Z_{in} = \frac{Z_0^2}{Z_l} \tag{2.32}$$

The result expresses the inverse relation of the impedance. Thus, a position quarter-wave length away from the grounded point is electrically open due to its inverse relationship of the impedance.

2.3.6 Microwave power supply

Figure 2.2 shows an image of the microwave power source. The length is 380 mm, height is 220 mm, and width is 230 mm. The power source supplies TEM wave from a N-type coaxial connector mounted on the center of the front panel. The solid-state microwave oscillator (Tokyo-keiki, TME101B00B) can supply a microwave at 2.45 GHz center frequency with the power from 0.72 to 100 W by controlling external supply voltage V_{att}. Figure 2.3 shows the output microwave power with respect to the V_{att}. The oscillator is cooled by forced air-cooling and heatsink inside of the case. Four digital panel meters installed on the front panel show the output control voltage V_{att}, frequency control voltage V_{freq}, incident power, and reflected power. While the power source includes the control circuit to supply the optimum voltage to the V_{att} and V_{freq}, the output power can be controlled by external DC power supply which has a computer interface from the external input terminal on the rear panel. The output microwave can be synchronized with the external input modulation signal.

Fig. 2.2. A photograph of the hand-made microwave power supply.

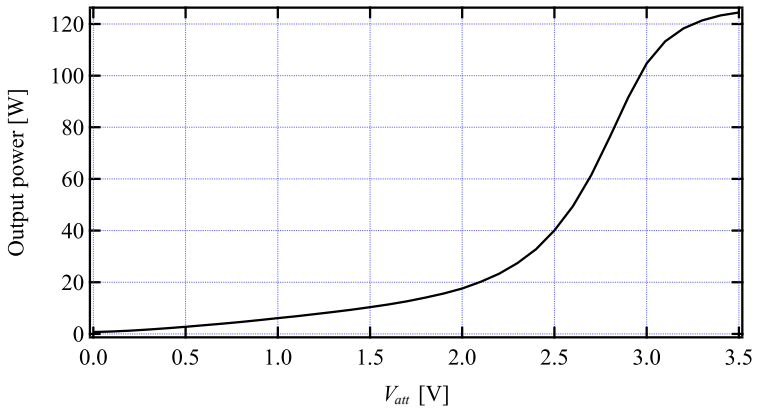

Fig. 2.3. Output microwave power with respect to the control voltage V_{att}.

2.3.7 Impedance matching with triple stub tuner

When the load impedance Z_l is not equal to the characteristic impedance of the line Z_0, the mismatching of the impedances induces reflected power. In order to supply the microwave power to the plasma efficiently, the apparent load impedance should be equal to the transmission impedance Z_0 by using impedance conversion. Figure 2.4 shows a schematic diagram of an aluminum cavity triple stub tuner. The originally designed tuner tunes the impedance of the overall source circuit to resonance. An 8 mm diameter copper rod is extended between two N-type connectors at both sides with the distance of 13/8λ of the tuner mounting three micrometer heads (Mitutoyo, MH2-25T) at locations 1/2λ, 3/4λ, λ away from the input N-type connector, respectively. In order to prevent magnetic components of micrometer heads from absorbing the electric power by induction heating, all surfaces exposed to microwave are covered by copper. Individual manipulation of each micrometer head shifts the point of load impedance on the Smith chart as shown in Fig. 2.5.

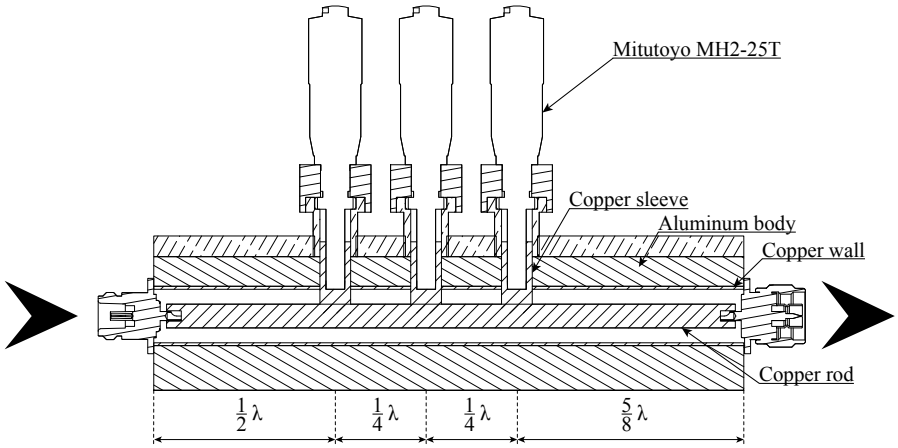

Fig. 2.4. A sectional drawing of the originally developed triple stub tuner, where λ = 12.24 cm at 2.45 GHz.

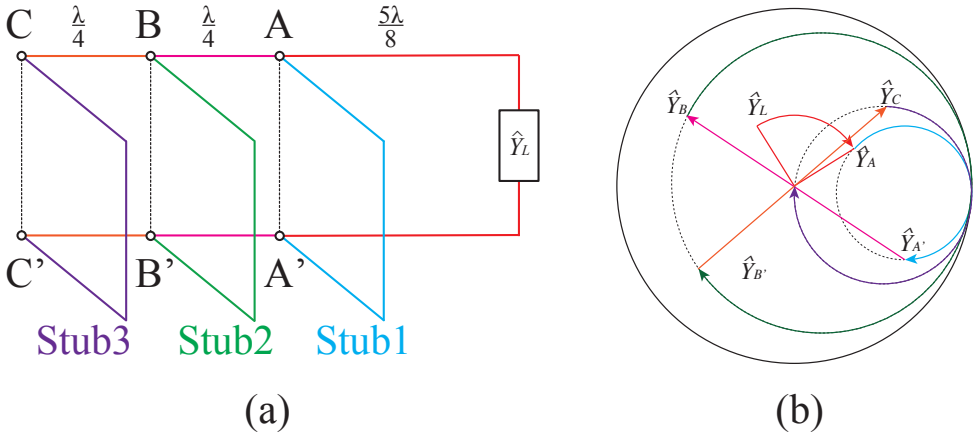

Fig. 2.5. Mechanism of the impedance matching by the triple stub tuner. The phase angle θ on the Smith chart is defined as $\theta = \frac{4\pi}{\lambda}d$, where d is the length of the line.

2.3.8 Capacitively coupled type radical beam source

The structure of the original CCP (Capacitively Coupled Plasma) type atomic source in this work is schematically shown in Fig.2.6 and 2.7 [41]. A 1.5 mm diameter tungsten needle electrode is directly connected to the N-type RF vacuum feedthrough (Cosmotec, C34NR1). The length of the tungsten needle electrode is 12.2 cm corresponding to the wave length of the 2.45 GHz microwave. A Pyrex glass vessel with a 7 mm gas supply hole (inner diameter: 13 mm, outer diameter: 17 mm) encloses a needle shaped tungsten electrode. The end 30mm long part of the glass vessel tapers down to a 3 mm diameter hole. A stainless-steel cylinder surrounds the glass vessel to maintain a discharge at the sharp tungsten electrode tip through intensifying the local electric field.

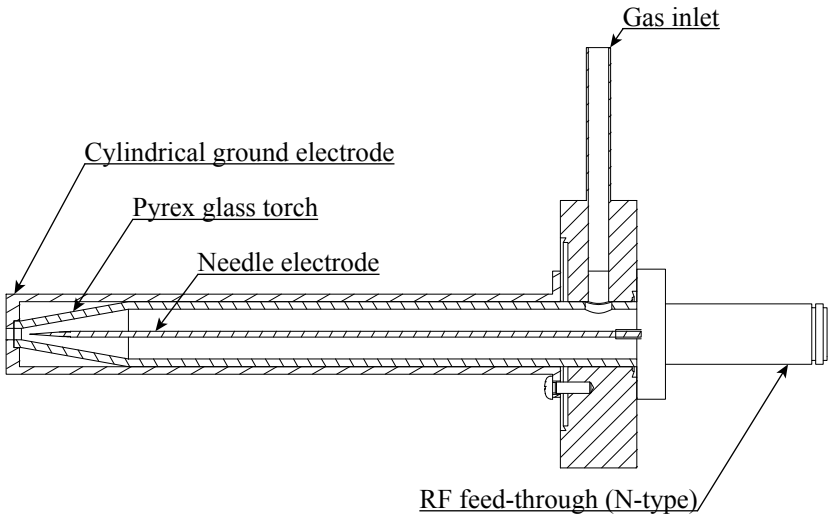

Fig. 2.6. A sectional view of the 1st gen CCP type atomic source.

Fig. 2.7. A photograph of the 1st gen CCP type atomic source apparatus.

2.3.9 Inductively coupled type radical beam sources

An ECR (Electron Cyclotron Resonance) heating is the one of the acceleration techniques of electrons when a frequency of external RF electric field ω is identical to the electron cyclotron frequency $\omega_{ce} = eB/m_e$. Under the ECR condition, electrons are accelerated by the Coulomb force in both positive and negative half cycles of the RF electric field as the RF frequency ω is equal to the frequency of cyclotron motion ω_{ce}. Figure 2.8 schematically shows the structure of a LICP (Localized Inductively Coupled Plasma) type microwave driven ECR radical source [42]. This LICP source can be mounted to a ICF70 standard flange. A water-cooled toroidal Sm-Co magnet ($\phi 22 \times \phi 18 \times 32$) mounted in the source tip forms a magnetic field structure with the region of the intensity greater than 87.5 mT corresponding to ECR at 2.45 GHz along a quartz glass capillary to achieve a higher plasma density. The magnetic field distribution is shown in Fig. 2.9. Although the field structure contains a magnetic mirror to confine the charged particles efficiently, that is not optimized since the ECR points on indicated by the red dots out of the mirror structure. A plasma is ignited in the 119 mm long 6.5 mm inner diameter quartz glass tube through coupling the microwave power by a 15 turns 0.1 mm thick copper ribbon spiral antenna coiled around the glass tube. A 3 mm diameter aperture opened on a stainless-steel source orifice reduces the radius of the radical beam effusing from the plasma.

The discharge power is applied to the copper spiral antenna through a coaxial transmission line via N-type RF feed through. A 3.75 mm copper rod, an alumina insulator, and a 6 mm inner diameter 8 mm outer diameter copper shield tube form a coaxial transmission line from the RF feed through to the spiral antenna. Ceramic coatings are applied to the both ends of the coaxial transmission line to enhance the voltage holding between the center and outer copper electrodes. The coaxial line has 9.7 Ω characteristic impedance while the transmission impedance of the coaxial cable from the microwave power supply is 50 Ω. Thus, the microwave reflection back to the power supply is reduced by inserting the triple stub tuner between the coaxial cable and the N-type feed through.

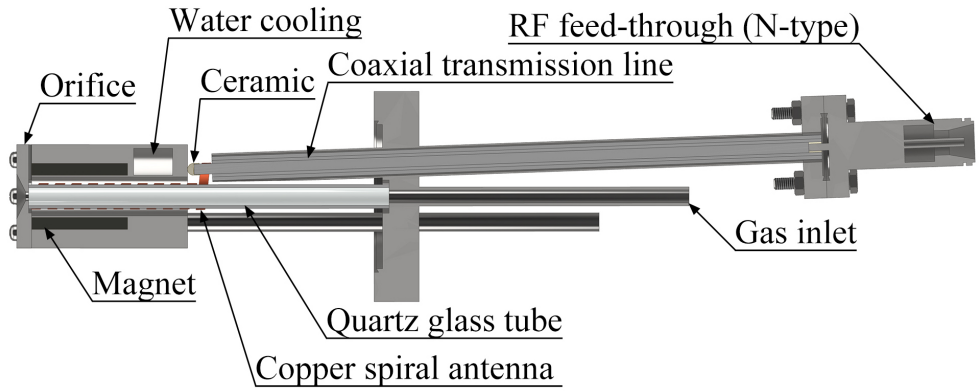

Fig. 2.8. A photograph of the 1st gen LICP type atomic source apparatus.

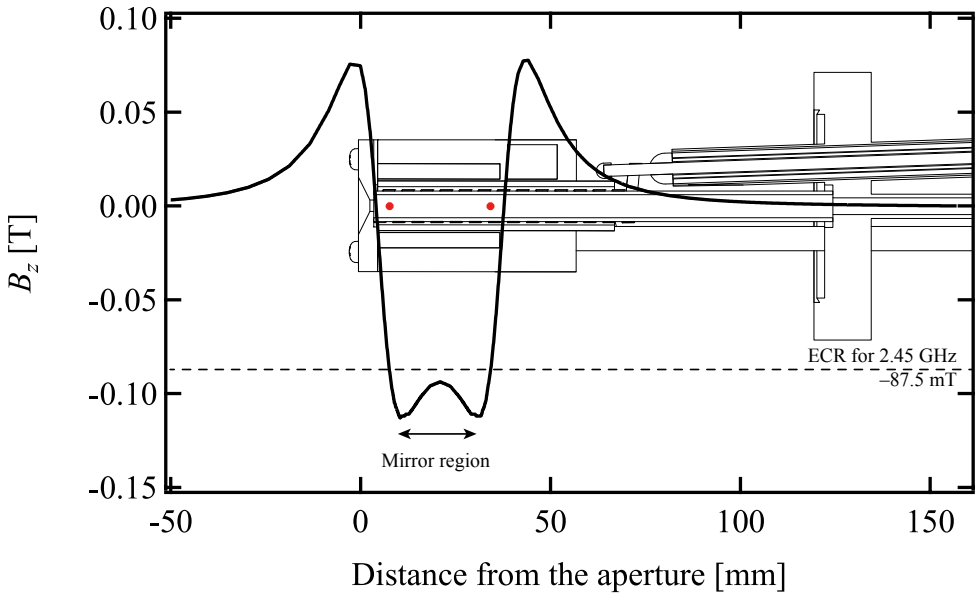

Fig. 2.9. A magnetic field distribution for 1st gen LICP source. Two red dots are corresponding to the ECR points.

2.4 Performance of developed radical sources

2.4.1 Vacuum systems

The cube-shaped vacuum chamber shown in Fig. 2.10 connects the atomic source, glass view ports, a Pirani gauge (ULVAC WP-01), a vacuum ionization gauge (ULVAC, WIT-G1). The chamber is evacuated by a 210 L/s turbomolecular pump (Pfeiffer vacuum, TMH262) to 1.0×10^{-5} Pa. This chamber is made of stainless steel with the size of 70 mm on each side. Two glass viewports are attached in front and the side of the source tip to confirm the plasma glow and take the OES (Optical Emission Spectrum).

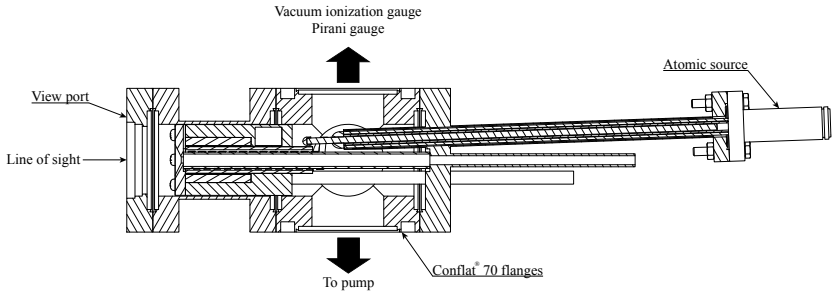

Fig. 2.10. A schematic diagram of the vacuum system to examine the developed atomic sources.

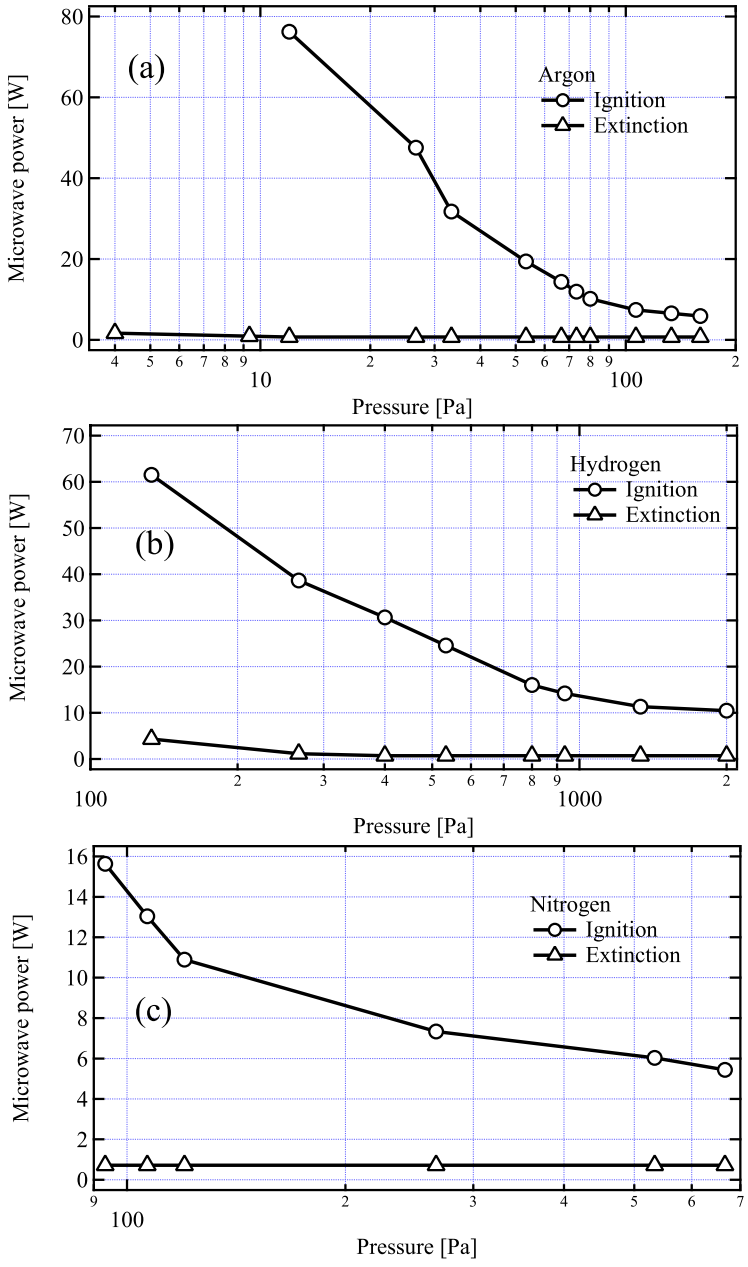

Fig. 2.11. The gas pressure dependence of the 1st gen CCP ignition and extinction with respect to the microwave input power. (a) Argon, (b) Hydrogen, (c) Nitrogen.

2.4.2 Performance of the CCP type radical source

The fine tuning for the microwave power is necessary by the triple stub tuner due to the large reflection power caused by high impedance of the tungsten electrode to excite a capacitive discharge. The local electric field at the tungsten electrode tip commenced the capacitively coupled discharge by electron avalanche. Figure 2.11 indicates the input power required to maintain the discharge. The smallest power output from the microwave source is as low as 0.72 W and this power held the stable discharge once the discharge was ignited. The figure indicates that the input power to start the discharge is higher at low pressure similar to the discharge ignition characteristic for low pressure side of the Paschen's law.

To enable capacitive discharge under low pressure, a structure of the cylindrical grounded electrode was modified by filling up the cavity between the electrode and the region outside of the glass vessel as shown in Fig. 2.12. The 2nd gen CCP source of this structure adopted the insertion of a copper sleeve between the feed through and needle electrode in order to prevent the needle electrode touching the glass vessel as shown in Fig. 2.13. These modifications make the source capacitance larger than the former configuration. Electric field is stronger than the previous structure and the number of accelerated electrons increases in the electric field. These factors made the discharge using the modified 2nd gen CCP source more easily.

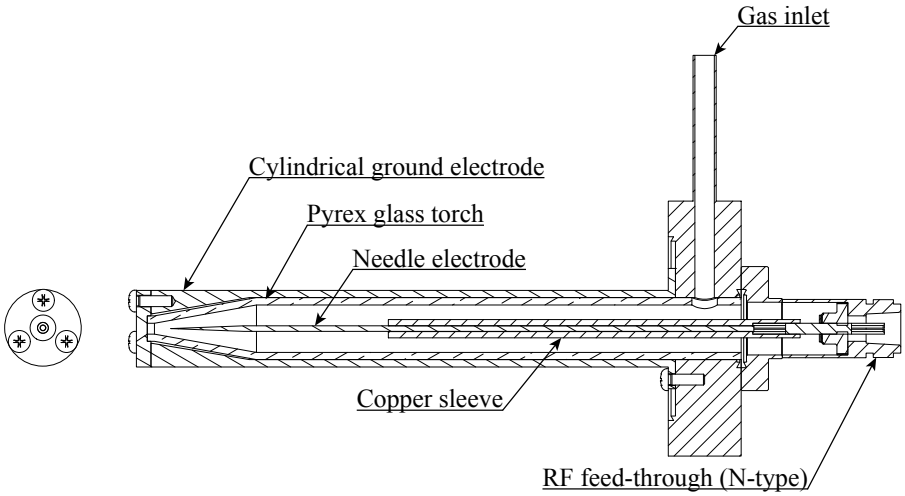

Fig. 2.12. A schematic diagram of the 2nd gen CCP radical source.

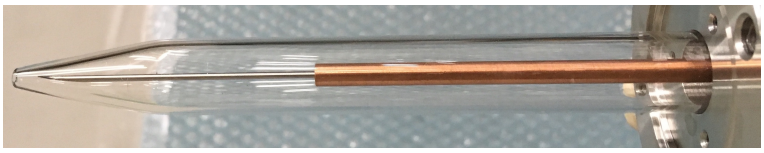

Fig. 2.13. A photograph of the needle elecrode supported by the copper sleeve in the 2nd gen CCP radical source.

Figure 2.14 shows input power to commence the discharge by using the improved 2nd gen CCP source for hydrogen and nitrogen. The graph shows characteristics similar to those of the original source. However, the pressure to ignite plasma is reduced drastically. Since these plasmas required fine tuning for microwave power matching, the measurement of minimum power to sustain discharge was not made.

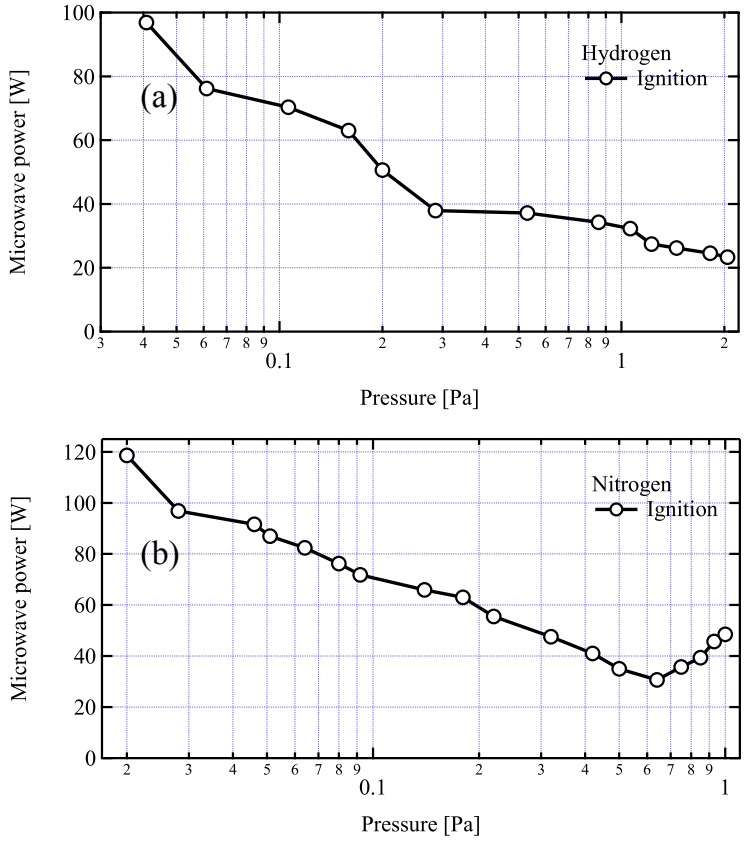

Fig. 2.14. Discharge characteristics of 2nd gen CCP radical source. (a) Hydrogen, (b) Nitrogen.

2.4.3 Performance of the LICP type radical source

The original configuration of the 1st gen LICP source shown in Fig. 2.8 requires high gas pressure ($\sim 10^2$ Pa) and high power input ($\sim$ 100 W) to ignite a plasma. Figure 2.15 are the photographs of the plasmas sustained in these conditions. These discharges are not produced in the quartz tube but the outside of the tube as shown in Fig. 2.16. Essentially, inductively coupled plasma (ICP) is sustained by an eddy current induced by the induction magnetic field, however, these discharges commenced as capacitively coupled plasma due to its unintentional electric field concentration at the magnet holder.

(a) (b) (c)

Fig. 2.15. Photographs of the unexpected capacitive discharges of 1st gen LICP source. (a) Argon (3 Pa, 100 W), (b) Hydrogen (218 Pa, 100 W), (c) Nitrogen (267 Pa, 100 W).

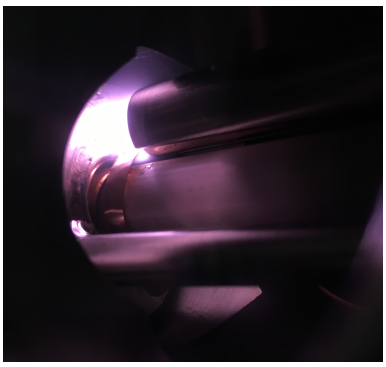

Fig. 2.16. A photograph of the capacitive discharge between the magnet holder and microwave transmission line in the 1st gen LICP source.

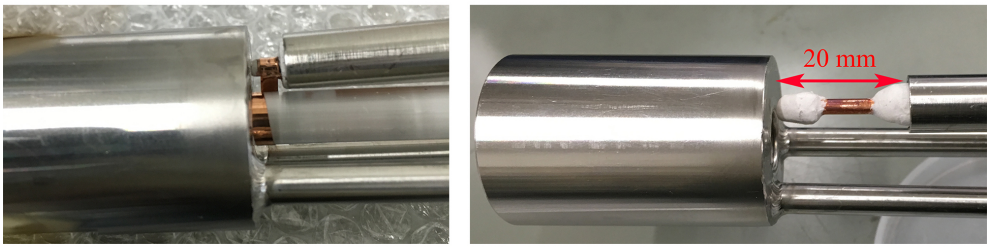

(a) (b)

Fig. 2.17. Photographs of changing the electrode structure for 1st gen LICP source. (a) original configuraion. (b) After cutting the grounded electrode.

In order to avoid these unintended discharges, the ground electrode made of stainless-steel to support the coaxial line was shortened as shown in Fig. 2.17. This modification to the electrode structure contributes to the reduction of the capacitance of the source, as well as that of operating gas pressure. The inductive type discharge is ignited around 20 W power input for all gas species as shown in Fig. 2.18. The reflection power for the LICP source is smaller than the CCP source because the antenna of the LICP is electrically grounded.

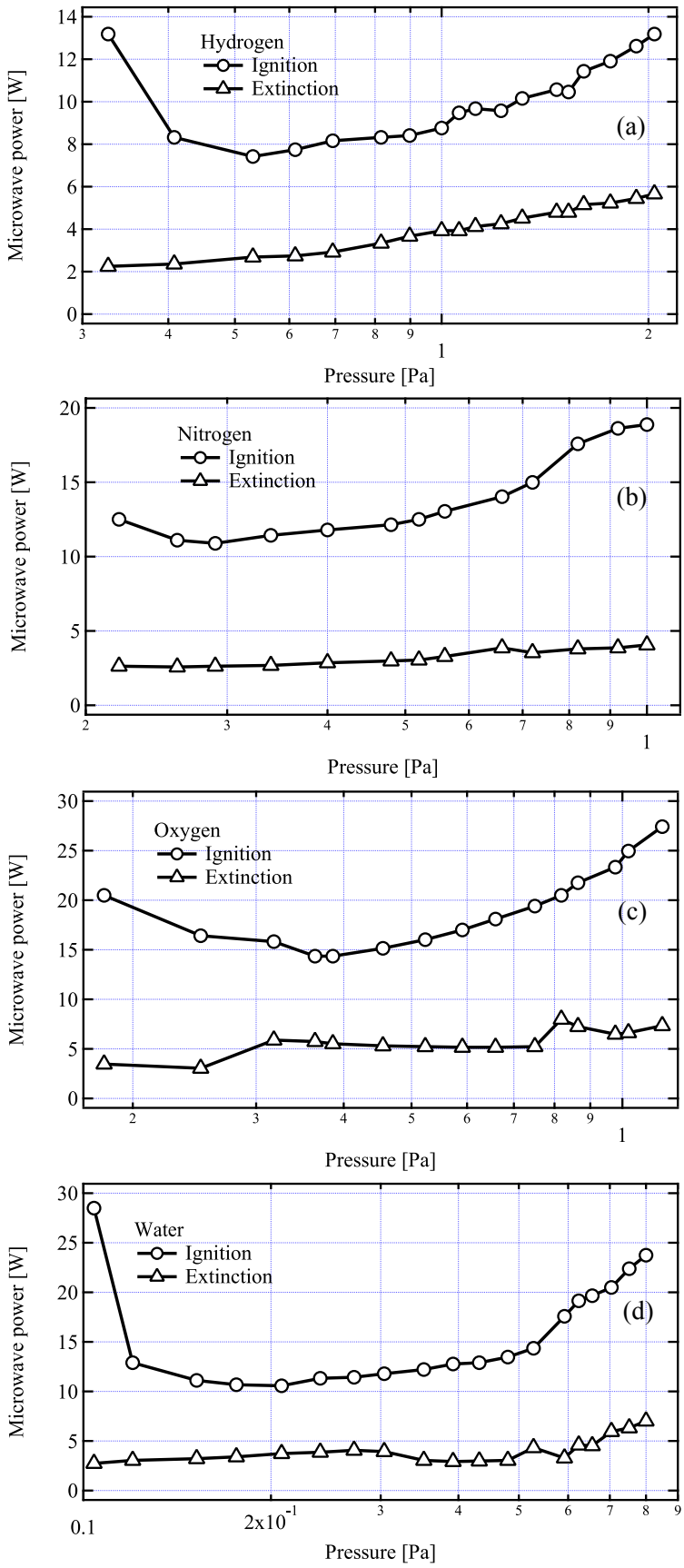

Fig. 2.18. The discharge characteristics of the 1st gen LICP source. (a) Hydrogen, (b) Nitrogen, (c) Oxygen, (d) Water vapor.

In general, ICP originates its discharge capacitively due to the electric field between both ends of an antenna: E-mode (electrostatic) discharge. Then, ICP starts ignition of the plasma inductively induced by eddy current as the input power is increased: H-mode (electromagnetic). This mode transition from E-mode to H-mode can be observed by the jump of brightness and electron density for MHz driven RF plasma [43, 44]. Although the discharge characteristic is improved by modification of the electrode structure, the mode transition for the LICP had not been observed. Moreover, plasma was frequently ignited between the magnet holder and quartz glass as shown in Fig. 2.19 (b). This implies that the power coupling to the plasma is inappropriate due to some parasitic capacitances. Though a quartz glass tube is inserted between the spiral antenna and magnet holder to insulate as shown in Fig. 2.20, the input microwave tends to induce capacitive discharge around the coaxial transmission line as shown in Fig. 2.19 (c). The coaxial structure was heated up by absorbing the microwave power when the plasma is sustained as a form of Fig. 2.19 (c).

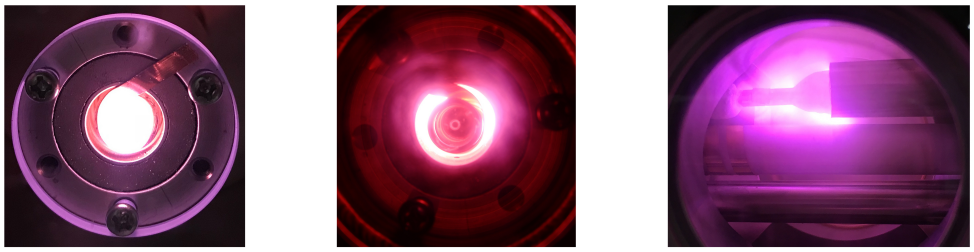

Fig. 2.19. Photographs of three types of plasmas in the LICP source. (a) Inductive discharge, (b) capacitive discharge between the antenna and magnet holder, (c) capacitive discharge at the coaxial transmission line.

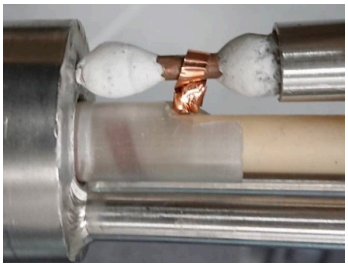

Fig. 2.20. A photograph of the spiral antenna insulated by a quartz tube.

In order to eliminate the lossy line components, the microwave power was fed by the RF feed-through mounted on another vacuum port in addition to adopting the coaxial quartz configuration as shown in Fig. 2.21. As a result of a series of improvements, the microwave power does not induce the capacitive discharge but induces the inductive discharge as shown in Figs. 2.22 (a) and (b).

Fig. 2.21. A photograph of the spiral antenna insulated by a quartz tube after the transmission conaxial line removal.

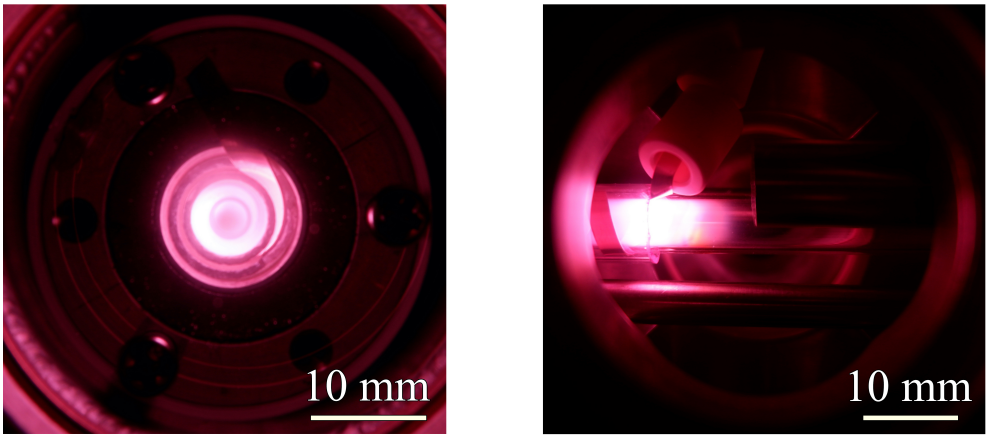

Fig. 2.22. Photographs of the hydrogen LICP after improvement in the 1st gen LICP source. (a) axial view. (b) radial view.

2.5 Optical emission study for developed sources

Motion of electrons in an atom and molecule is determined by the potential field due to the electrostatic force between the electrons and atomic nucleus. The energy eigenvalue for atomic hydrogen resulting from the use of the Bohr model is given as

$$E_n = -\frac{m_e e^4}{8n^2h^2\epsilon_0^2}, \quad n = 1, 2, 3, \cdots \tag{2.33}$$

where, n is the principal quantum number, h is the Planck constant, ϵ_0 is the permittivity of free space, m_e is the electron rest mass, and e is the electric charge of electron. Equation 2.33 gives a discrete set of energy depending upon the n to each energy level. An electron transition from an upper energy level n_2 to a lower energy level n_1 induces the photon

emission of the exact energy ΔE_{12}.

$$\Delta E_{12} = -\frac{m_e e^4}{8h^2\epsilon_0^2}\left(\frac{1}{n_2^2} - \frac{1}{n_1^2}\right) \tag{2.34}$$

$$= \frac{m_e e^4}{8h^2\epsilon_0^2}\left(\frac{1}{n_1^2} - \frac{1}{n_2^2}\right) \tag{2.35}$$

Because the emitted photon energy ΔE_{12} is equal to $h\nu = \frac{hc}{\lambda}$,

$$\Delta E_{12} = h\nu = \frac{hc}{\lambda} \tag{2.36}$$

$$\frac{1}{\lambda} = \frac{m_e e^4}{8h^3\epsilon_0^2 c}\left(\frac{1}{n_1^2} - \frac{1}{n_2^2}\right) \tag{2.37}$$

$$= R_\infty\left(\frac{1}{n_1^2} - \frac{1}{n_2^2}\right) \tag{2.38}$$

where λ is the wavelength of the light, c is the speed of light in vacuum, and R_∞ is the Rydberg constant. Thus, the emission wavelength from the atomic hydrogen is given by Eq. 2.38.

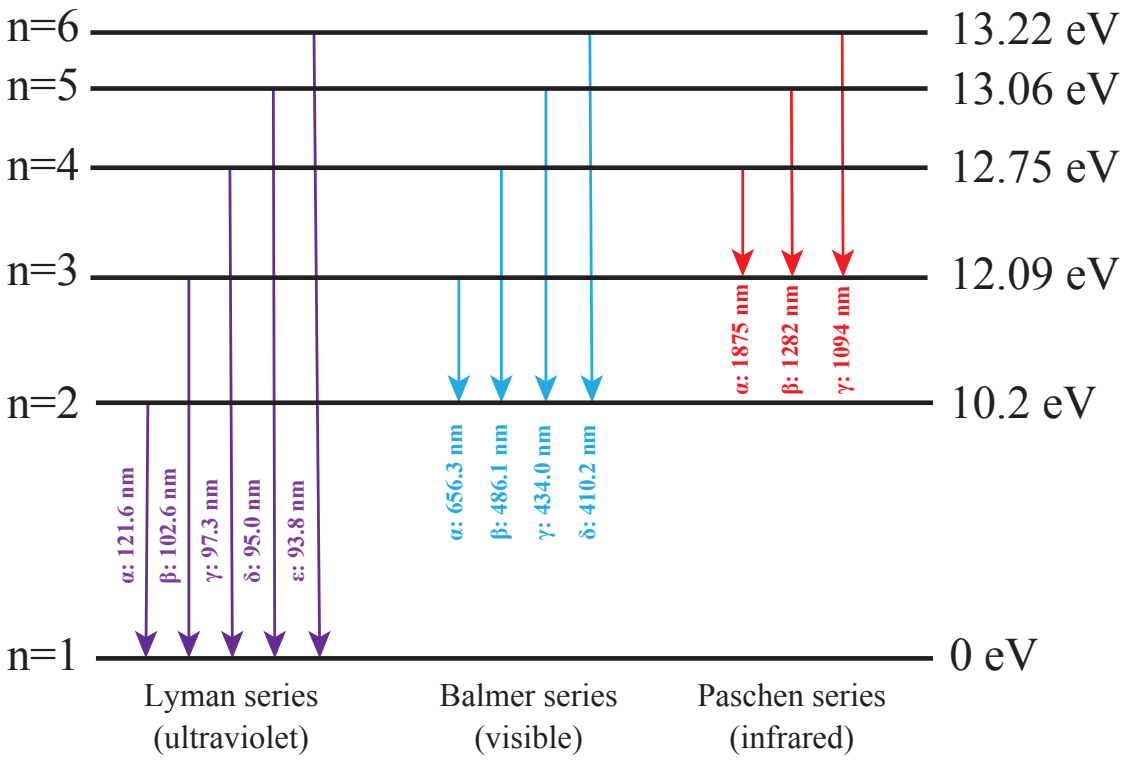

Fig. 2.23. Schematic diagram of the energy levels of atomic hydrogen.

Figure 2.23 schematically shows the calculation results of Eq. 2.38 for $n = 1, 2, 3$. Unlike the Lyman and Paschen series, this study adopts the observation of Balmer-series due to ease of measurement by using a optical fiber coupled to a visible range grating spectrometer. In contrast, excited molecules emit band spectra when the electrons of molecules return from excited states to the ground state. Figure 2.24 shows the potential energy curves for representative excited states of molecular hydrogen [45]. The transition for excited molecular hydrogen that can be measured with a visible range system is the Fulcher series from $d^3\Pi_u$ state to $a^3\Sigma_g^+$ state.

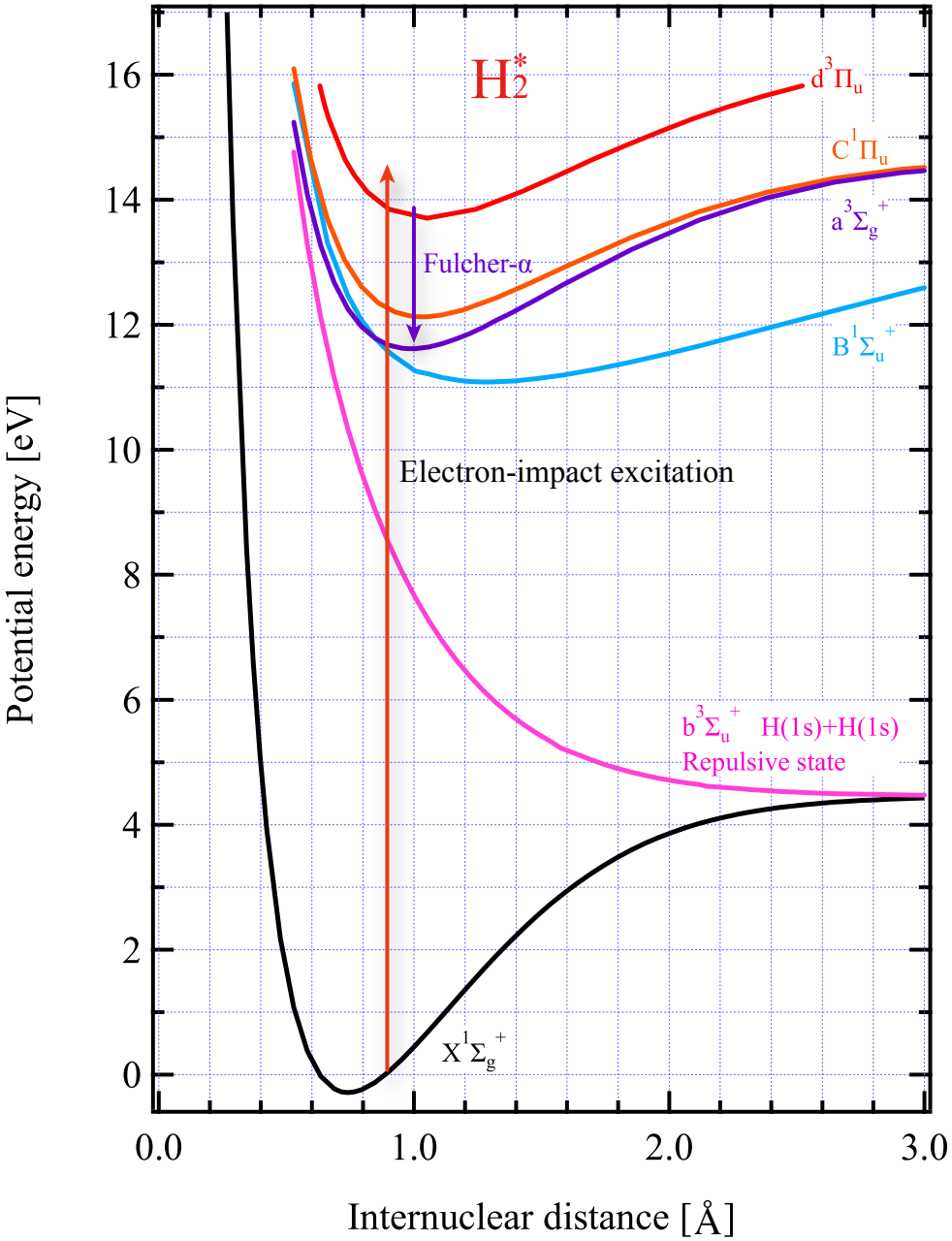

Fig. 2.24. Potential energy curves for H_2 [45].

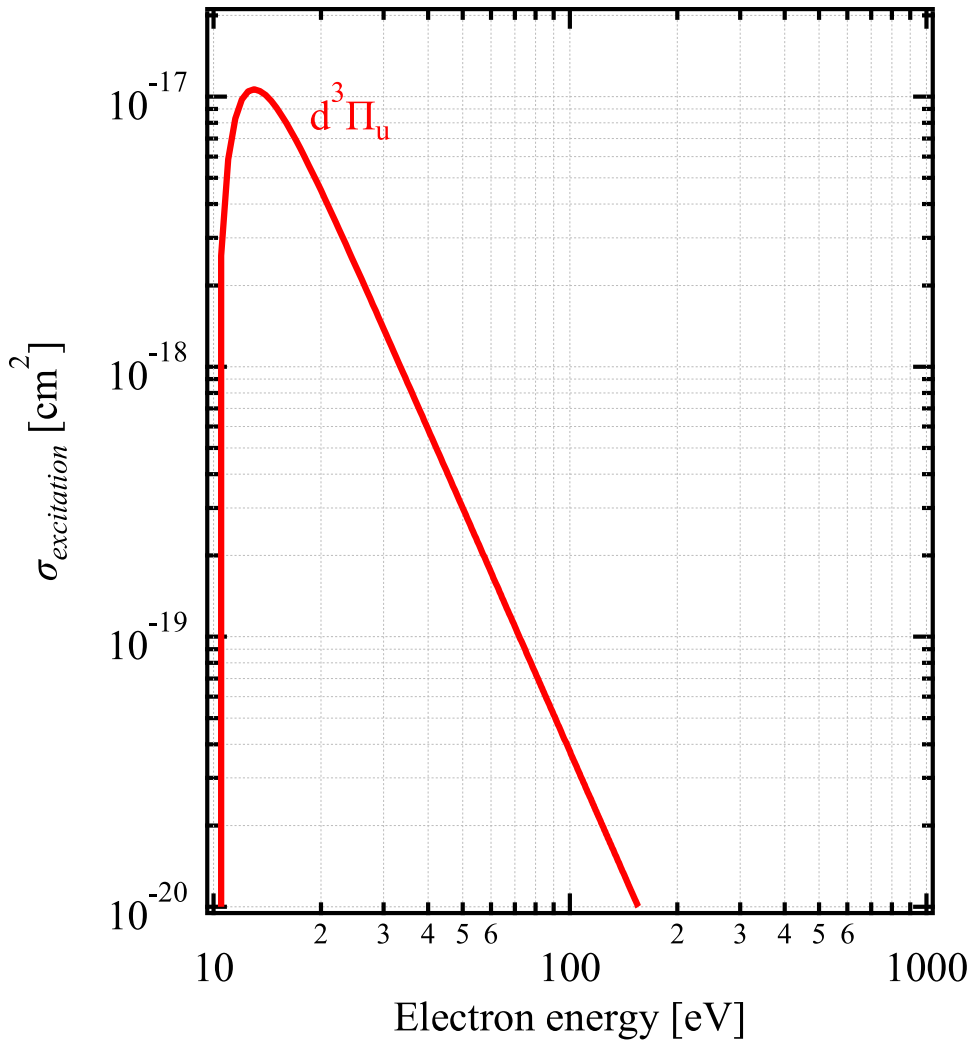

Fig. 2.25. Total electron impact excitation cross section of $d^3\Pi_u$ triplet state of H_2 from its $X^1\Sigma_g^+$ ground state [46]. The maximum cross section for $d^3\Pi_u$ is 13.6 eV.

Typical OES (Optical Emission Spectra) for hydrogen plasmas produced in the 1st and 2nd gen CCP sources are shown in Fig. 2.26. A brightest peak was observed for a hydrogen discharge at 656.3 nm wavelength corresponding to Balmer-alpha (H_α) line spectrum in both CCP atomic sources. Balmer-beta lines were found in the spectra, while hydrogen molecular band spectra were prominent in both sources; the higher operation pressure of the original source structure caused more molecular band spectrum emission. In order to consider the influence of the gas pressure on the produced atom and molecular ratio, OES for different gas pressures were taken and H atom/band spectrum intensity ratio was calculated with 2nd gen CCP source. Figure 2.27 shows proportion of hydrogen atoms vs gas pressure. The lower was the gas pressure, the higher was the ratio of atomic hydrogen line intensity. Because the 1st gen CCP source was operated in several Torr (several hundred Pa) pressure range, the intensity ratio was lower than 6.3% in 160 Pa, while the improved 2nd gen CCP source exhibits above 12% under 1.5×10^{-1} Pa.

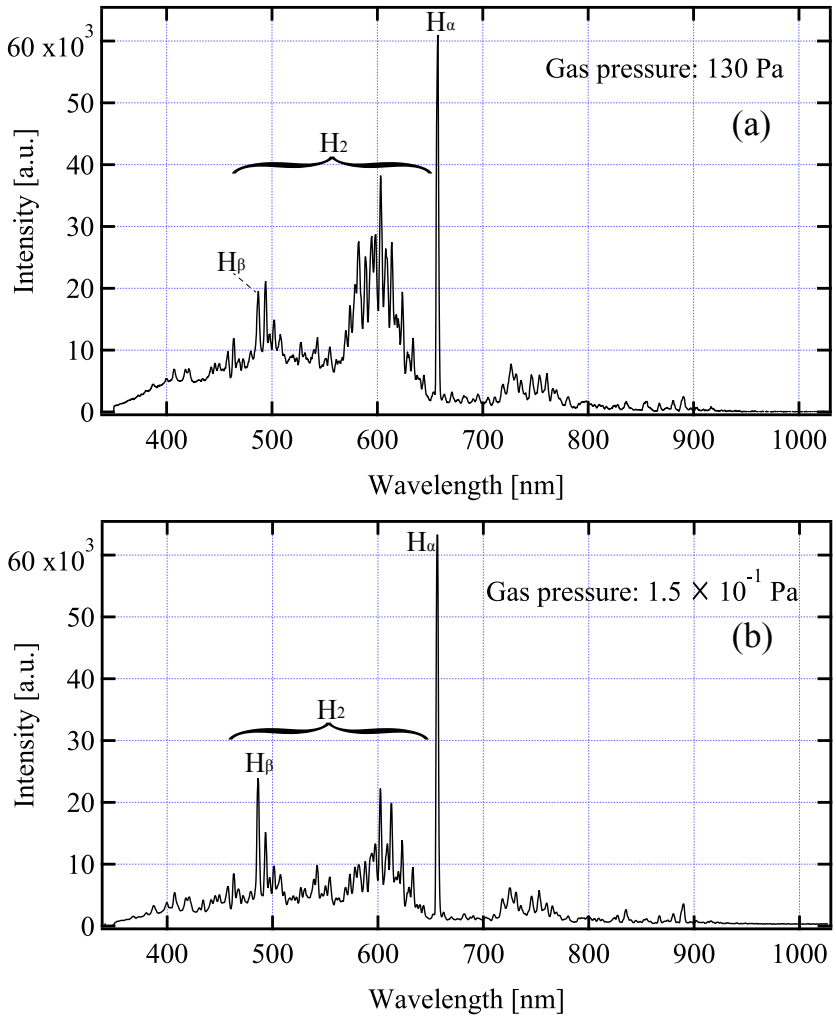

Fig. 2.26. Typical optical emission spectra of the 55 W hydrogen plasmas produced in the (a) 1st gen CCP and (b) 2nd gen CCP source.

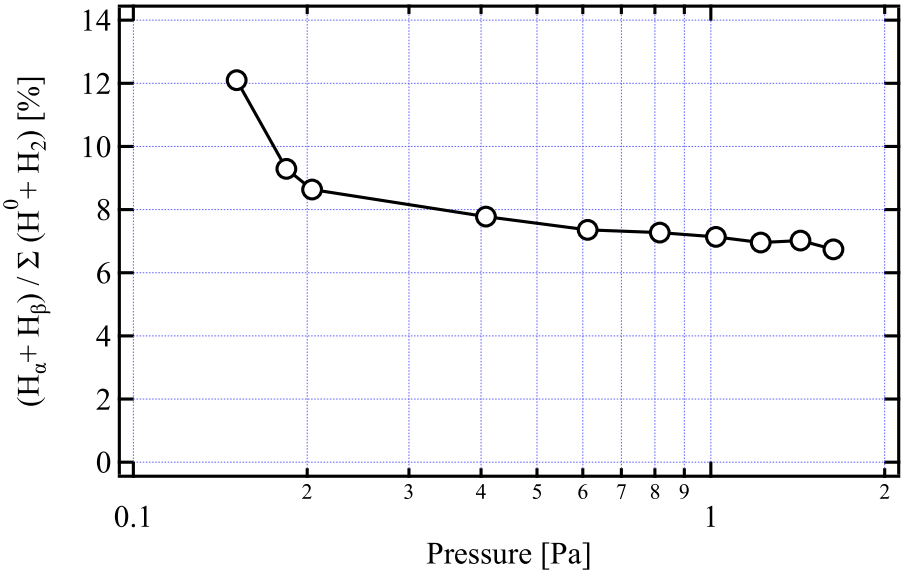

Fig. 2.27. Rate of hydrogen atoms vs different gas pressure calculated from the OES.

The 1st gen LICP source had underwent several modifications to realize stable plasma generation. Here, the 1st gen is defined as the state after cutting the grounded electrode 20 mm from the original configuration. The 1st gen LICP source has the stainless-steel orifice and does not have the insulator between the antenna and magnet holder. Meanwhile, a 1.5th gen LICP source is defined as the source having the structure excluding the coaxial transmission rod and RF vacuum feedthrough in the source. Thus, the 1.5th gen source has the quartz orifice and insulator between the spiral antenna and magnet holder.

Figure 2.28 shows the typical hydrogen OES with the condition of 1.5×10^{-1} Pa, 55 W for 1st and 1.5th gen LICP sources. Both 1st and 1.5th source produced the bright plasmas into the quartz tube. Nevertheless, the 1.5th gen LICP drastically decreased emission from the hydrogen molecular band spectra. The result strongly implies that the difference in plasma production mechanisms. In the 1st gen LICP source, the power coupling to the plasma is inappropriate because the coaxial transmission rod was heated up during the radical source operation. Meanwhile, the 1.5th gen source resolved the power coupling problem by avoiding the large power loss from microwave propagation.

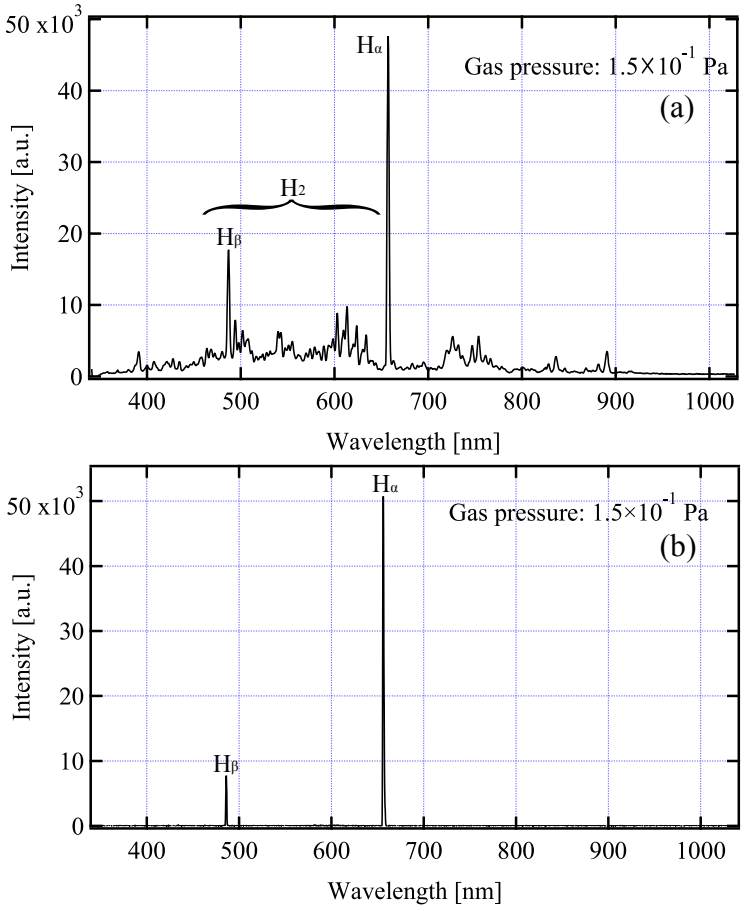

Fig. 2.28. Typical optical emission spectra of the 55 W hydrogen plasmas produced in the (a) 1st gen LICP and (b) 1.5th gen LICP source.

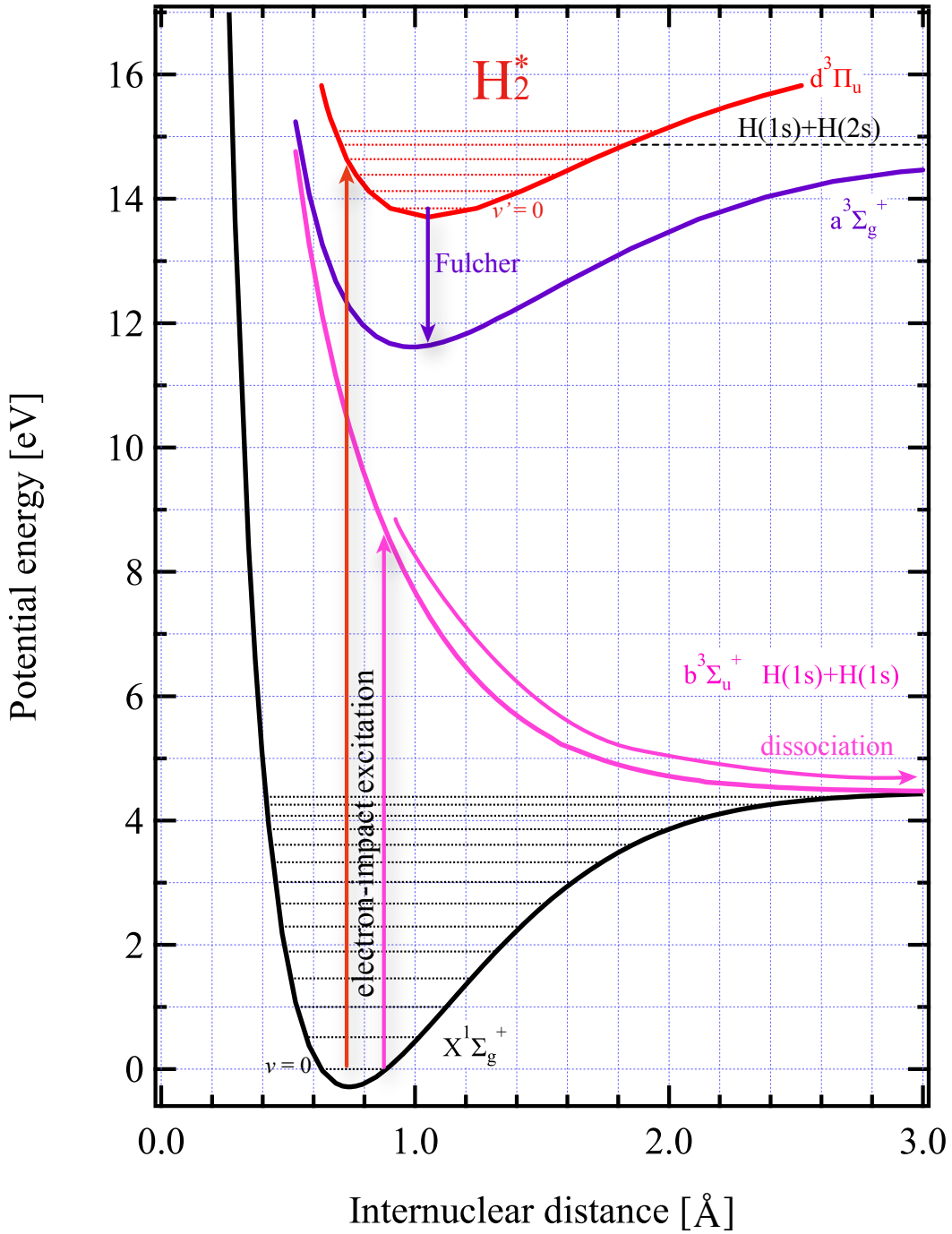

Fig. 2.29. Potential energy curves for H_2 [45, 47].

The spectrum of the 1.5th gen LICP source showed a faint excited molecular spectrum, while the others showed substantial amount of Fulcher molecular band spectra. The photon emissions of Fulcher-alpha band spectra correspond to an electron transition from $d^3\Pi_u$ to $a^3\Sigma_g^+$ triplet state as shown in Fig. 2.29. The Fulcher band emission is originated from the higher electron energy level pushed up by an electron-impact excitation with the energy as large as 13.6 eV from ground $X^1\Sigma_g^+$ state to $d^3\Pi_u$ state. Thus, the absence of the Fulcher-band emission from the 1.5th gen LICP expresses that the electron temperature of

the 1.5th gen LICP is lower than that of the others. The electron-impact excitation with the energy less than the excitation to the H_2^* preferentially dissociate their molecular structures through a repulsive $b^3\Sigma_u^+$ state. Therefore, the electron excitation to the repulsive state may contribute to the realization of a high degree of dissociation for 1.5th gen LICP source. This relationship agrees with the general understanding that CCP has a higher electron temperature than the ICP in the region of MHz-order RF discharges [48]. In other words, the discharge scheme of the 1.5th gen LICP source is electromagnetic discharge, and the 1st gen LICP and CCP sources is electrostatic discharge. The existence of the ICP-like discharge in the range of the microwave has not been studied well with spiral antenna. In order to confirm the presence of the E to H mode transition for microwave LICP, a trace of the Balmer-alpha intensity with respect to the input power was examined as shown in Fig. 2.30. Although the diagram does not show a hysteresis regarding to the intensity jump, the result suggests the existence of the mode transition for GHz range plasma. The detail is discussed in Chapter 3.

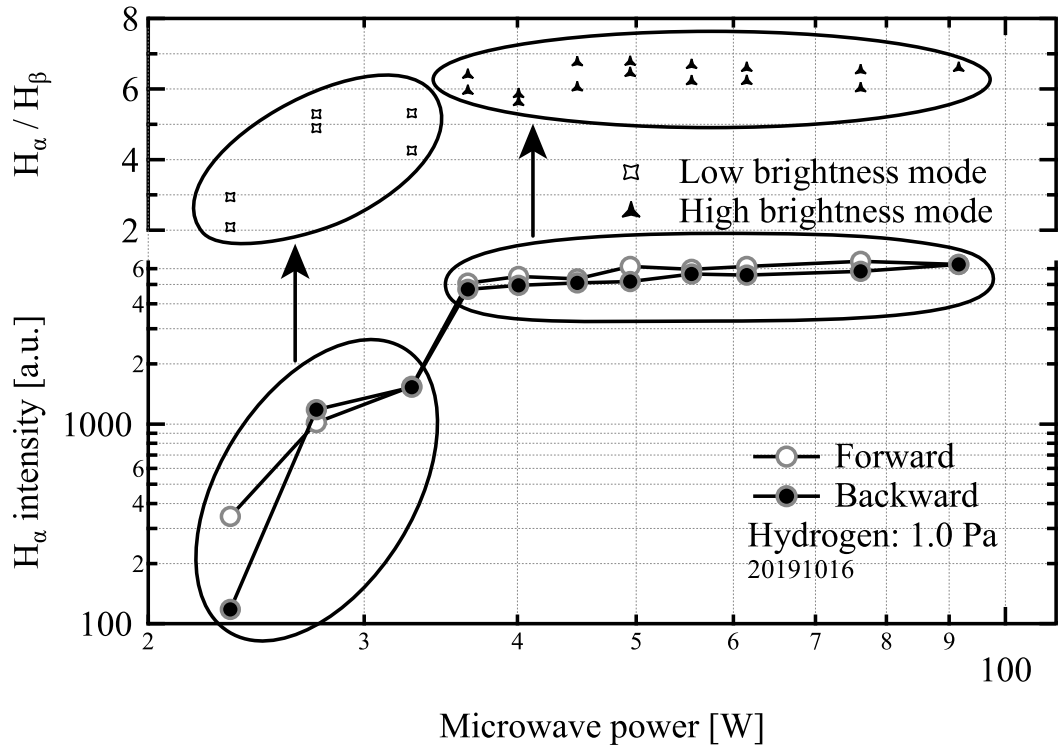

Fig. 2.30. Balmer-alpha intensities and alpha to beta ratio with respect to the input microwave power at 1.0 Pa hydrogen pressure by the 1.5th gen LICP source.

References

[1] A. Takamori, S. Sugata, K. Asakawa, E. Miyauchi, and H. Hashimoto, "Cleaning of MBE GaAs Substrates by Hydrogen Radical Beam Irradiation", *Jpn. J. Appl. Phys.* **26**, L142 1987.

[2] N. Kondo and Y. Nanishi, "Low-Temperature Surface Cleaning of GaAs by Electron Cyclotron Resonance (ECR) Plasma", *Jpn. J. Appl. Phys.* **28**, L7 1989.

[3] I. Suemae, Y. Kunitsugu, Y. Kan, and M. Yamanishi, "Incidence angle effect of a hydrogen plasma beam for the cleaning of semiconductor surfaces", *Appl. Phys. Lett.* **55(8)**, 760 1989.

[4] Z. Lu, M. T. Schmidt, D. Chen, R. M. Osgood Jr., W. M. Holber, D. V. Podlenik, and J. Forster, "GaAs-oxide removal using an electron cyclotron resonance hydrogen plasma", *Appl. Phys. Lett.* **58(11)**, 1143 1991.

[5] T. Kinugawa and T. Arikawa, "Diffractive Scattering Experiment of H Atoms Using Laser and Ion Imaging Techniques", *Jpn. J. Appl. Phys.* **32**, L550 1993.

[6] Y. Ohara, *J. Plasma Fus. Res.* **72**, 393 1996.

[7] H. E. Rebenne and D. G. Bhat, "Review of CVD TiN coatings for wear-resistant applications: deposition processes, properties and performance", *Surf. Coatings Technol.* **63**, 1 1994.

[8] Y. Sakamoto, M. Takuya, T. Ishii, and S. Igarashi, "Surface modified tool fabricated by radical nitriding", *Surf. Coatings Technol.* **142**, 152 2001.

[9] N. V. Gavrilov and A. S. Mamaev, "Low-temperature nitriding of titanium in low-energy electron beam excited plasma", *Tech. Phys. Lett.* **35(8)**, 713 2009.

[10] N. V. Gavrilov, A. S. Mamaev, and A. V. Chukin, "Nitriding of stainless steel in plasma of a pulse electron beam", *Tech. Phys. Lett.* **42**, 491 2016.

[11] Z. Yu, S. L. Buczkowski, N. C. Giles, T. H. Myers, and M. R. Richards-Babb, "The effect of atomic hydrogen on the growth of gallium nitride by molecular beam epitaxy", *Appl. Phys. Lett.* **69**, 2731 1996.

[12] T. H. Myers, L. S. Hirsch, L. T. Romano, and M. R. Richards-Babb, "Influence of growth conditions, inversion domains, and atomic hydrogen on growth of (0001)GaN by molecular beam epitaxy", *J. Vac. Sci. Technol. B* **16(4)**, 2261 1998.

[13] Y. Okamoto, S. Hashiguchi, Y. Okada, and M. Kawabe, "Effects of Atomic Hydrogen on the Growth of GaN by RF-Molecular Beam Epitaxy", *Jpn. J. Appl. Phys.* **38**, L230 1999.

[14] E. M. Silverman, *Space Environmental Effects on Spacecraft: LEO Materials Selection Guide* (National Aeronautics and Space Administration, Virginia, 1995).

[15] L. J. Leger and J. T. Visentine, "A consideration of atomic oxygen interactions with the Space Station", *J. Spacecr. Rockets* **23(5)**, 505 1986.

[16] M. Matsui, S. Yoneda, K. Komurasaki, Y. Yamagiwa, and Y. Arakawa, "Atomic-Oxygen-Flow Generation by Laser-Driven Plasma Wind Tunnel as Low-Earth-Orbit-Environment Simulator", *AIAA J.* **52(8)**, 1806 2014.

[17] I. Langmuir, "A CHEMICALLY ACTIVE MODIFICATION OF HYDROGEN", *J. Am. Chen. Soc.* **34**, 1310 1912.

[18] A. D. McNaught and A. Wilkinson, *Compedium of Chemical Terminology (IUPAC Chemical Data)* (John Wiley & Sons, 1997).

[19] J. N. Smith and W. L. Fite, "Reflection and Dissociation of H_2 on Tungsten", *J. Chem. Phys.* **37(4)**, 898 1962.

[20] M. M. Eisenstadt, "Beam Source for Molecular and Atomic Hydrogen", *Rev. Sci. Instrum.* **36**, 1878 1965.

[21] G. J. Lockwood, H. F. Helbig, and E. Everhart, "Measurements of Thermal Dissociation of Hydrogen, Using Fast Protons", *J. Chem. Phys.* **41(20)**, 3820 1964.

[22] K. Abe, M. Ida, A. Izumi, S. Terashima, T. Sudo, Y. Watanabe, and Y. Fukuda, "Estimation of hydrogen radical density generated from vacious kinds of catalysts", *Thin Solid Films* **517**, 3449 2009.

[23] K. G. Tschersich and V. von Bonin, "Formation of an atomic hydrogen beam by a hot capillary", *J. Appl. Phys.* **84(8)**, 4065 1998.

[24] H. Koschmieder and V. Raible, "Intense atomic-hydrogen bam source", *Rev. Sci. Instrum.* **46(5)**, 536 1975.

[25] U. Bischler and E. Bertel, "Simple source of atomic hydrogen for ultrahigh vacuum applications", *J. Vac. Sci. Technol. A* **11(2)**, 458 1993.

[26] B. Van Zyl and M. W. Gealy, "New molecular-dissociation furnace for H and O atom sources", *Rev. Sci. Instrum.* **57(3)**, 359 1986.

[27] K. G. Tschersich, "Intensity of a source of atomic hydrogen based on a hot capillary", *J. Appl. Phys.* **87(5)**, 2565 1999.

[28] T. Schwarz-Selinger, A. von Keudell, and W. Jacob, "Novel method for absolute quantification of the flux and angular distribution of a radical source for atomic hydrogen", *J. Vac. Sci. Technol. A* **18(3)**, 995 2000.

[29] K. N. Leung, K. W. Ehlers, C. A. Hauck, W. B. Kunkei, and A. F. Lietzke, "Small multicusp H^- source", *Rev. Sci. Instrum.* **59(3)**, 453 1988.

[30] M. Seidl, S. T. Melnychuk, S. W. Lee, and W. E. Carr, "Surface production of negative hydrogen ions by reflection of hydrogen atoms from cesium oxide surfaces", *AIP Conf. Proc.* **210**, 30 1990.

[31] E. C. Samano, W. E. Carr, M. Seidl, and Braian S. Lee, "An arc discharge hydrogen atom source", *Rev. Sci. Instrum.* **64(10)**, 2746 1993.

[32] J. W. Cuthbertson, R. W. Motley, and W. D. Langer, "High-flux source of a low-energy neutral beams using reflection of ions from metals", *Rev. Sci. Instrum.* **63(11)**, 5279 1992.

[33] M. J. Goeckner, T, K. Bennett, and S. A. Cohen, "A source of hyperthermal neutrals for materials processing", *Appl. Phys. Lett.* **71(7)**, 980 1997.

[34] D. Voulot,R. W. McCullough, W. R. Thompson, D. Burns, J. Geddes, G. J. Cosimini, E. Nelson, P. P. Chow, and J. Klaassen, "Determination of the atomic nitrogen flux from a radio frequency plasma nitride source for molecular beam epitaxy systems", *J. Vac. Sci. Technol. A* **16(6)**, 3434 1998.

[35] D. M. Kearns, D. R. Gillen, D. Voulot, R. W. McCullough, W. R. Thompson, G. J. Cosimini, E. Nelson, P. P. Chow, and J. Klaassen, "Study of the emission characteristics of a rf plasma source for atomic oxygen: Measurements of atom, ion, and electron fluxes", *J. Vac. Sci. Technol. A* **19(3)**, 993 2001.

[36] S. Panda, D. J. Economou, and L. Chen, "Anisotropic etching of polymer films by high energy ($\sim$ 100s of eV) oxygen atom neutral beams", *Appl. Phys. Lett.* **71(7)**, 980 1997.

[37] S. Samukawa, K. Sakamoto, and K. Ichiki, "Generating high-efficiency neutral beams by using negative ions in an inductively coupled plasma source", *J. Vac. Sci. Technol. A* **20(5)**, 1566 2002.

[38] J. W. Cuthbertson, W. D. Langer, and R. W. Motley, "Reflection of low energy plasma ions from metal surfaces", *J. Nucl. Mater.* **196-198**, 113 1992.

[39] R. Anton, Th. Wiegner, W. Naumann, M. Liebmann, Chr. Klein, and Chr. Bradley, "Desgin and performance of a versatile, cost-effective microwave electron cyclotron resonance plasma source for surface and thin film processing", *Rev. Sci. Instrum.* **71(2)**, 1177 2000.

[40] A. R. von Hippel, *Dielectric Materials and Applications* (John Wiley & Sons, New York, 1954).

[41] Y. Shimabukuro, H. Takahashi, and M. Wada, "Electrode structure of a compact microwave driven capacitively coupled atomic beam source", *Jpn. J. Appl. Phys.* **57(1S)**, 01AA02 2018.

[42] Y. Shimabukuro, H. Takahashi, S. Iwamoto, K. Tanaka, and M. Wada, "Tandem Mass Spectrometry of Peptide Ions by Microwave Excited Hydrogen and Water Plasmas", *Anal. Chem.* **90**, 7239 2018.

[43] M. M. Turner and M. A. Liebermann, "Hysteresis and the E-to-H transition in radiofrequency inductive discharges", *Plasma Sources Sci. Technol.* **8(2)**, 313 1999.

[44] P. Chabert and N. Braithwaite, *Physics of Radio-Frequency Plasmas* (Cambridge university press, Cambridge, 2011).

[45] T. E. Sharp, "Potential-energy curves for molecular hydrogen and its ions", *ATOMIC DATA* **2**, 119 1971.

[46] R. K. Janev, D. Reiter, and U. Samm, *Collision Processes in Low-Temperature Hydrogen Plasmas* (Forschungszentrum Zentralbibliothek, Julich, 2003).

[47] W. Kolos and L. Wolniewicz, "Vibrational and Rotational Energies for the $B^1\Sigma_u^+$, $C^1\Pi_u$, and $a^3\Sigma_g^+$ States of the Hydrogen Molecule", *J. Chem. Phys.* **48(8)**, 3672 1968.

[48] Y. Sakamoto, S. Maeno, N. Tsumouchi, T. Kasuya, and M. Wada, "Comparison of Plasma Parameters in CCP and ICP Processes Appropriate for Carbon Nanotube Growth.", *J. Plasma Fusion Res.* **8**, 587 2009.

Chapter 3

Tuner Integrated Radical Beam Sources for Low-energy Radical Beam Production

3.1 Issues of previous sources

Chapter 2 illustrated the developed 2.45 GHz microwave driven CCP (Capacitively Coupled Plasma) and LICP (Localized Inductively Coupled Plasma) type radical sources [1, 2]. These radical sources require external impedance matching network to deliver optimum microwave power to the load as with general microwave plasma generators. Problems of radical source operation are listed below:

- Increase in size due to the impedance matching unit
- Power absorption by the RF feed through made of kovar
- Preliminary triple stubs operation
- Microwave leakage and heat loss from the stub tuner

In order to overcome these problems, a tuner-integrated type radical source has been developed. In this chapter, new design of built-in matching type radical sources and performance evaluation of the sources are described.

3.2 Basic concept of built-in matching system

A surface wave that propagates on the boundary surface between the plasma and dielectric material is widely utilized in plasma processes because of the ease of enlarging the device

size with a large diameter for the gas pressure range from 1 Pa to 10^3 Pa [3, 4, 5, 6, 7, 8]. The surface wave plasma generators well-known as surfatron often adopt the axially movable coupler antenna to adjust the capacitance. Figure 3.1 schematically illustrates geometry of the surfatron [4]. The surfatron has two matching components such as a plunger and coupler. The inductance component of the source is varied by changing the cavity space with the plunger. Meanwhile the capacitance component corresponds to the gap between the coupler and the center tube. In this study, two types of tuner-integrated radical sources were developed on the concept of the surfatron. The developed sources adopted the inductance varying system to avoid sparking at the coupler and microwave adsorption by additional magnetic materials such as a micrometer head.

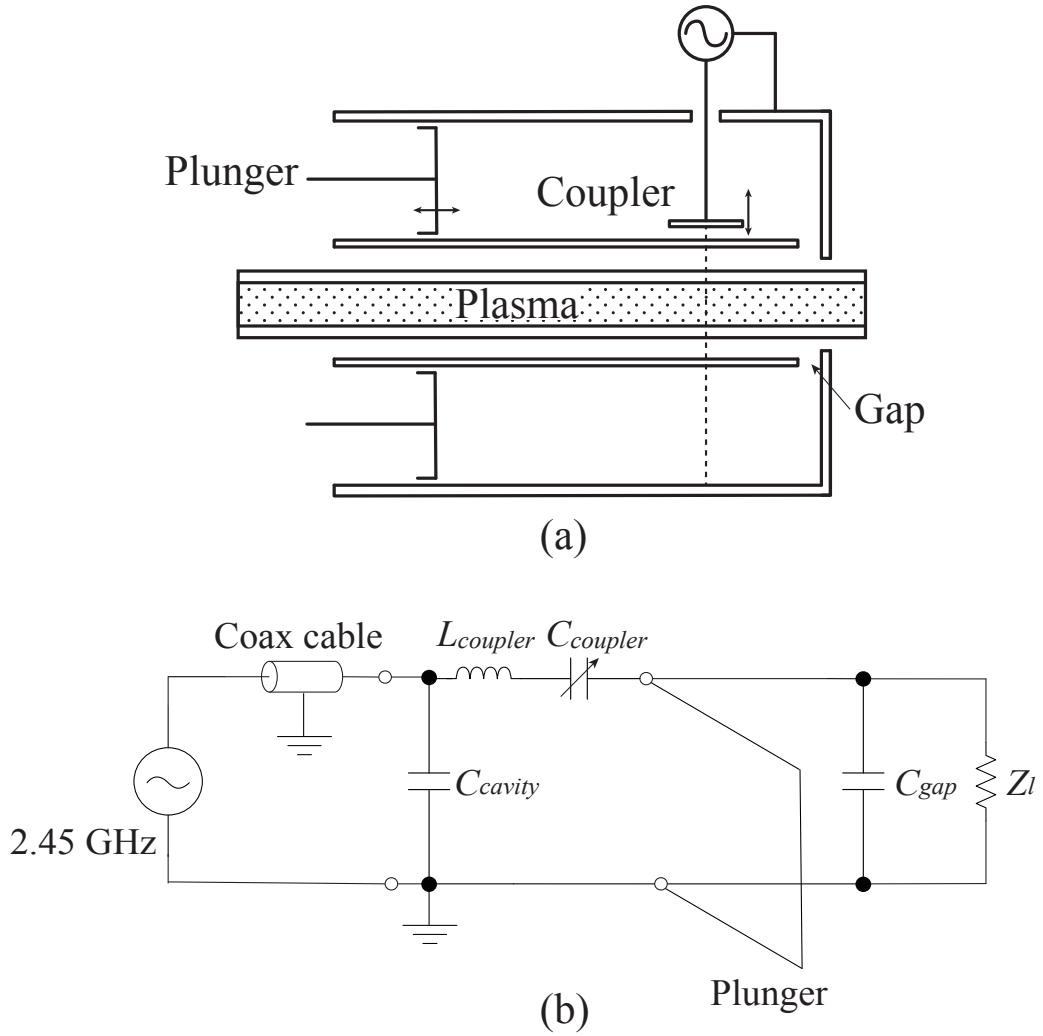

Fig. 3.1. (a) A conceptual diagram of a surfatron. (b) Equivalent circuit of a surfatron.

3.3 Tuner integrated capacitively coupled type radical source

3.3.1 Design of 3rd gen capacitively coupled type radical source

Figure 3.2 schematically shows the compact tuner-integrated 3rd gen CCP source based on previous CCP source design [1]. The 2.45 GHz microwave enables the drastic miniaturization of the plasma generator compared with a typical RF plasma source. The total length of the source corresponds to 2.5 wavelengths of 2.45 GHz microwave. A copper capillary maintained along the source axis is enclosed by an aluminum cylindrical grounded electrode with the 1 mm beam collimation aperture and quartz glass vessel with the 15 mm end part tapered off. A microwave power input into the copper capillary drives the source below 100 W. Figure 3.3 shows the equivalent electric circuit model for the 3rd gen CCP source and its matching network. A coaxial structure composed of the copper tube and grounded copper cylinder gives the certain capacitance C_{cavity}. The input microwave via N-type connector propagates the surface of the copper tube that have resistance R_{tube} and inductance L_{tube} components. A copper plunger attached to the copper tube tunes the impedance of the microwave circuit constituting the atomic source system to a resonance as a single tuning circuit. There are two capacitances at the source tip C_{plasma} and C_{quartz}.

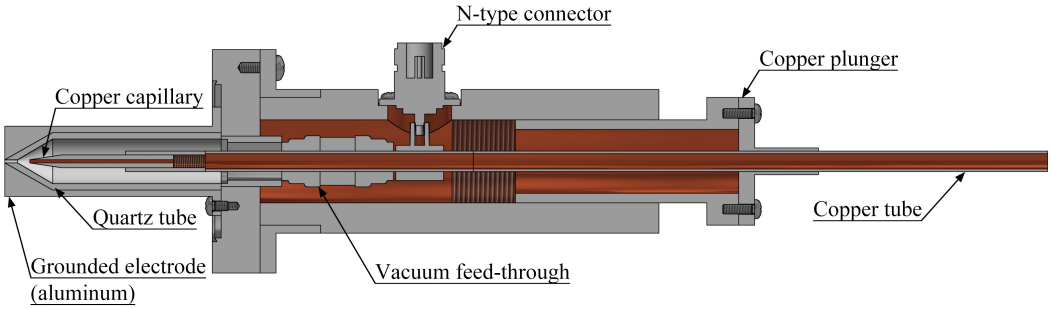

Fig. 3.2. A cross-sectional view of the 3rd gen CCP source.

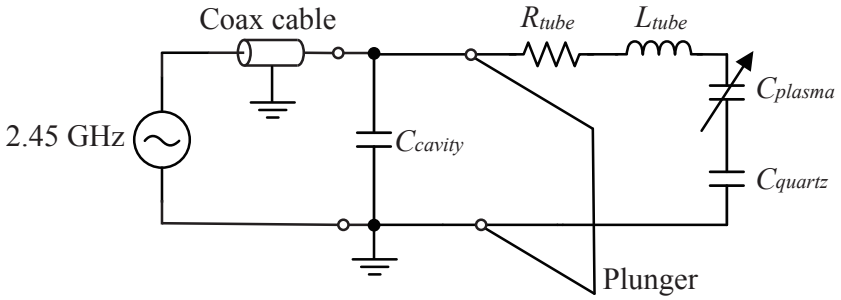

Fig. 3.3. Electric circuit model for the 3rd gen capacitively coupled plasma source, including matching plunger.

3.3.2 Formation of plasma plume by changing a capillary

Figure 3.4 shows the photograph of the quartz tube after the first time operation. The inner wall of the tube showed deposition of substantial amount of the sputtered copper from the copper tube. This suggests that the plasma is mainly sustained around the root part of the copper capillary due to the insufficient electric field concentration at the capillary tip. The improved configuration of 3rd gen CCP source is shown in Fig. 3.5. The new structure changed the size of apertures of the grounded electrode and quartz tube from 1 mm to 4 mm. The aperture size is equal to the inner diameter of the quartz glass vessel and outer diameter of the copper capillary. The minimum distance between the electrodes is 1.7 mm which is 4.6 times closer than the previous configuration. The structure modification of the electrodes intensifies the local electric field at the source tip. As a result, a plasma plume – plasma leaking of the exit aperture due to the high density – is formed under the high input power high pressure condition. Figure 3.6 shows a photograph of the plasma plumes for several kinds of gases. In the CCP radical source, electron overcurrent induces a positive self bias voltage to the plasma due to the difference of the mobility between the electrons and ions [10]. Thus, the grounded electrode extracts ions from positively biased plasma as a form of the plasma plume. A small electrode insertion to the plume measured the floating potential as −40 to −50 V.

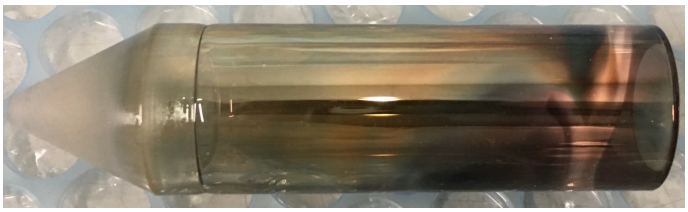

Fig. 3.4. A photograph of the quartz tube which has a 1 mm diameter orifice after the first operation.

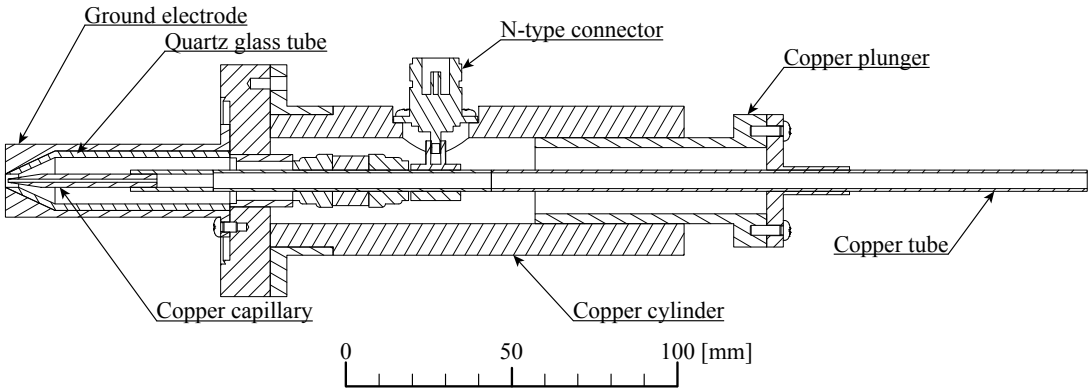

Fig. 3.5. The improved configuration of the 3rd gen CCP source which has a 4 mm aperture.

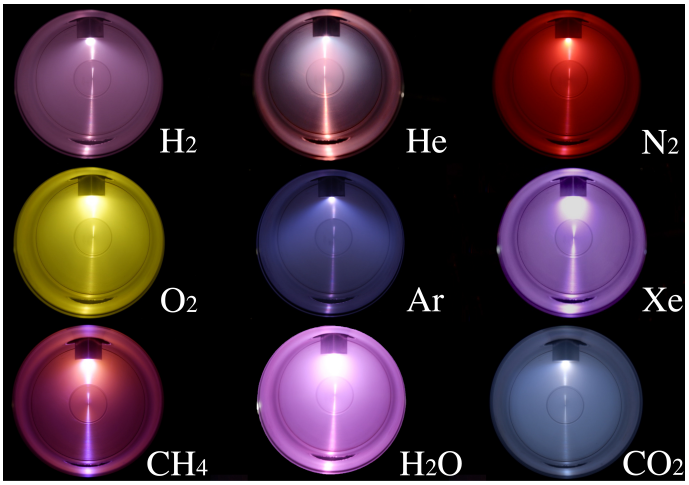

Fig. 3.6. A photograph of the plasma plumes for several kinds of gases.

Figure 3.7 indicates the input power necessary to start a discharge at the corresponding pressure for (a) hydrogen and (b) nitrogen. These figures show similar characteristics of the discharge ignition for low pressure side of the Paschen's law. In order to sustain the stable plasma plume mode, the gas pressure has to be kept above 1.3 Pa for hydrogen and 0.5 Pa for Nitrogen with a power input above 33 W. Otherwise, the plasma is sustained only inside the grounded electrode as the case of 1 mm aperture.

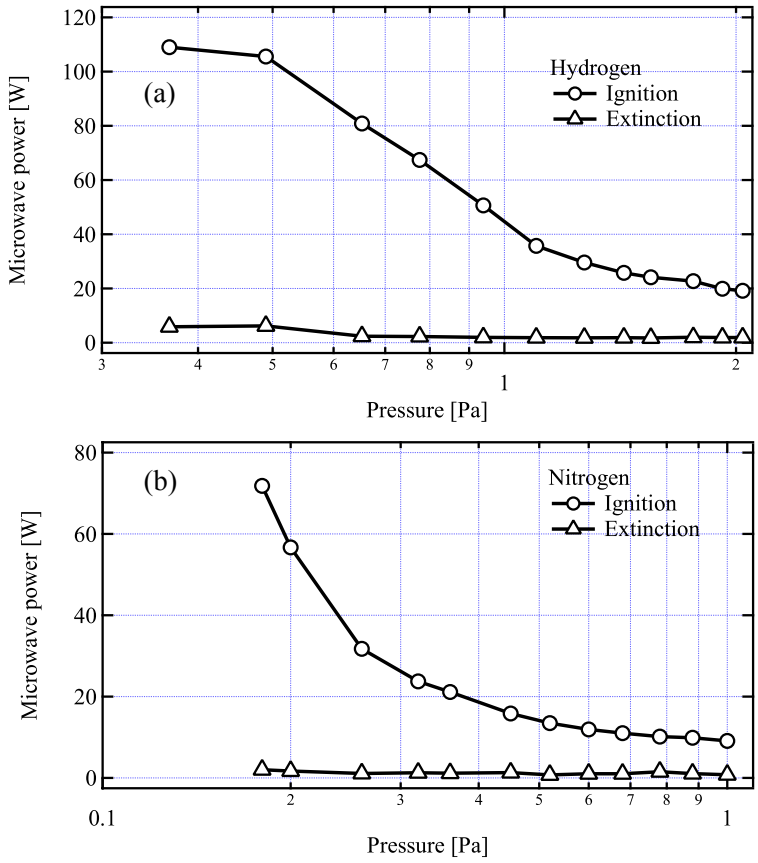

Fig. 3.7. The discharge characteristics of the 3rd gen CCP source. (a) Hydrogen, (b) Nitrogen.

3.3.3 4th gen capacitively coupled type radical source

The 3rd gen CCP source achieved the formation of the plasma plume under the condition of impedance matched, high gas pressure, and high input power. Sakamoto *et al* reported that the combination of ECR (Electron Cyclotron Resonance) and microwave CCP realized low minimum operating pressure at 7×10^{-3} for nitrogen atmosphere [9]. In order to reduce the gas pressure, the effectiveness of the ECR on the plasma plume mode was investigated. Figure 3.8 show the sectional drawing of the 4th gen CCP radical source. The copper cylinder and ICF 70 standard flange is cooled by water circulation to avoid demagnetization of the magnets. Four Nd-Fe magnets ($20 \times 12 \times 5$ mm) installed in the flange forms the magnetic field intensity corresponding to ECR on the beam axis. The magnetic field distribution and ECR points are shown in Fig. 3.9.

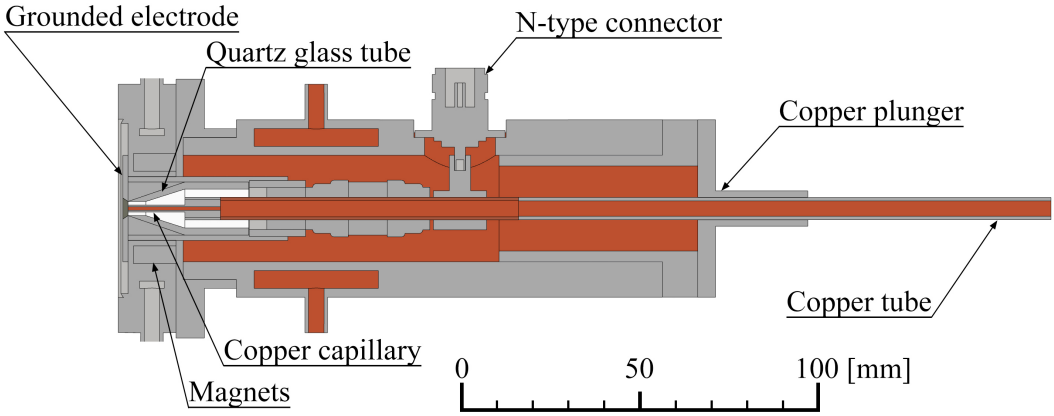

Fig. 3.8. A sectional drawing of the 4th gen CCP radical source.

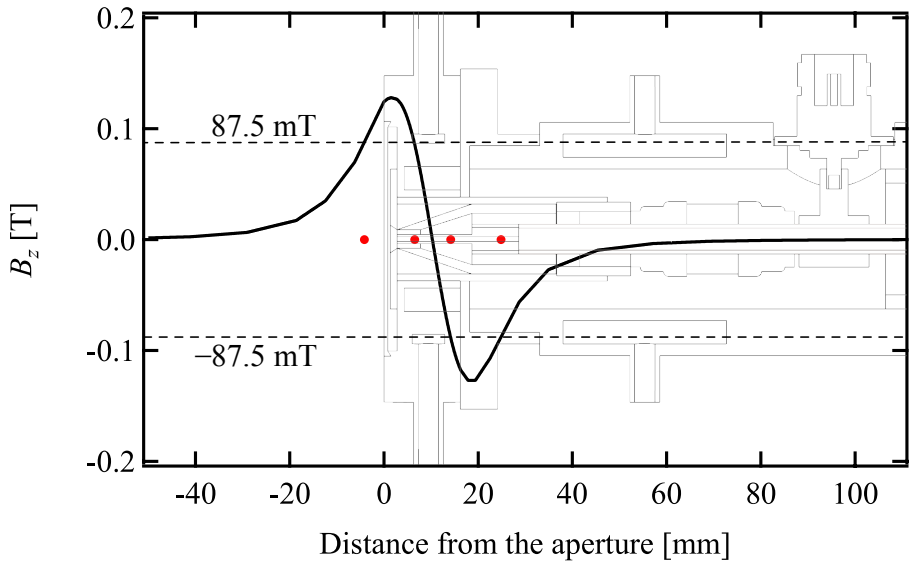

Fig. 3.9. A magnetic field distribution of the 4th gen CCP source. Four red dots on the beam axis indicate the ECR points.

Figure 3.10 shows the microwave power to ignite and sustain plume mode plasmas against the hydrogen gas pressure. The 4th gen CCP source requires higher gas pressure and input power to ignite the plasma than 3rd gen CCP source. Figure 3.11 shows the photographs of the plasma. According to these figures, the plasma is emitted from the inside the capillary on the plume mode. On the other hand, the plasma is sustained inside the vacuum flange when the microwave coupling is inappropriate with higher reflection power. Plasma plume like picture of the Fig. 3.11 (b) indicates the charged particle flow created by the ECR magnet from the plasma inside is transported out of the capillary.

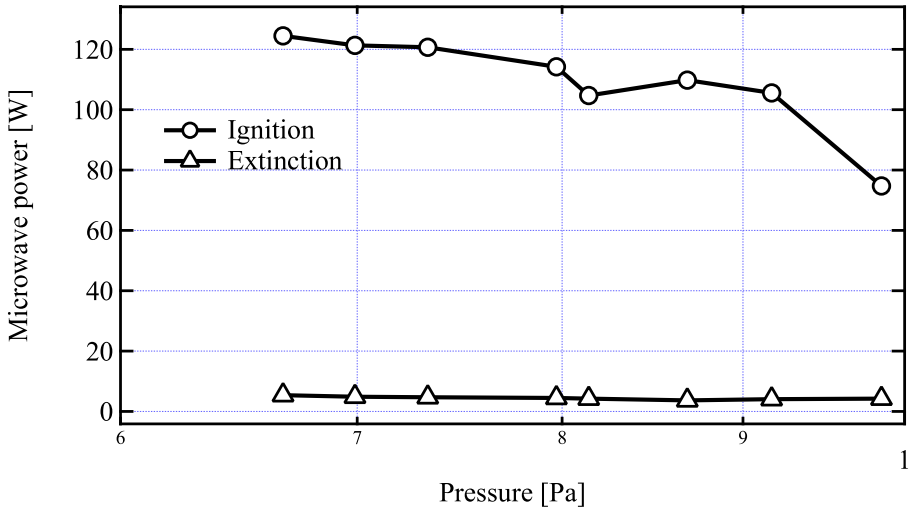

Fig. 3.10. A plasma discharge characteristic of the 4th gen CCP radical source.

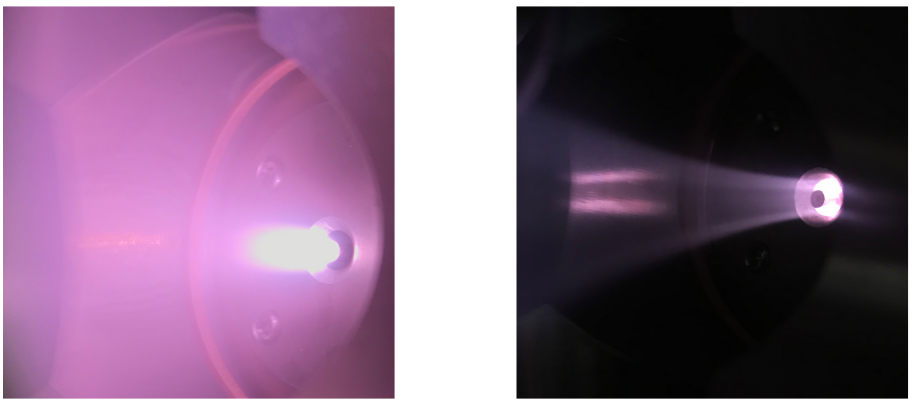

Fig. 3.11. Photographs of the plasma produced in the 4th gen CCP source. (a) Plume mode (b) Out of the plume mode.

Although the alteration of the capillary length corresponding to the rotation on the Smith chart and capacitance components at the source tip by changing the thickness and shape of the quartz tube were tested, the ignition pressure and power consumption

did not improved enough. The overall system is mainly composed of three capacitance components which are attributable to the source cavity C_{cavity} and the source tip structure C_{plasma}, C_{quartz} and the copper plunger as shown in Fig. 3.12. Most of the circuit elements are same as the 3rd gen CCP source except for unpredictable capacitance C_{cavity}. The offset of the vacuum feed-through to the atmospheric pressure side increased in the cavity volume 1.6 times larger than the 3rd gen CCP source. A single plunger/stub circuit can tune the limited tunable load, while the tunable coverage of the triple stub extends the entire region of the Smith chart as illustrated in Chapter 2. The total admittance of the system $\hat{Y}_L$ might have been impossible to approach toward the center of the Smith chart by the single plunger circuit. Thus, in order to realize more stable operation with tuner-integrated ECR-CCP source, further improvement is necessary including some change of the electrical circuit to satisfy the wider coverage of the Smith chart.

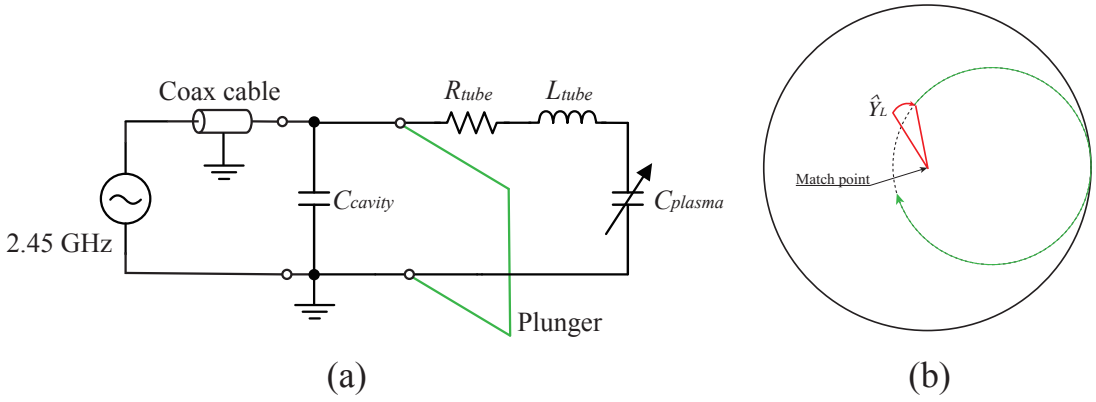

Fig. 3.12. (a) An equivalent circuit of the radical source system. (b) Smith chart for the single stub circuit.

3.4 Tuner integrated inductively coupled type radical source

3.4.1 Design of 2nd gen inductively coupled type radical source

A tuner integration for the LICP source was attempted in parallel to development of 3rd and 4th gen CCP sources. As shown in the improvement in the power consumption from 1st gen to 1.5th gen LICP source, the factor of most concern was the microwave power loss at the coaxial transmission line and RF feed-through. Thus, the elimination and/or the length reduction of the microwave transmission line promise a good power efficiency. The 2nd gen LICP source shown in Fig. 3.13. resolved these problems by adopting a built-in matching system. The source is composed of an ICF 70 standard flange made of stainless-steel and copper cylinder that has two groups of Nd-Fe magnets and copper plunger. The 2.45 GHz power source supplies the microwave to a 0.3 mm thickness copper spiral antenna tightly wound around a 6 mm outer diameter 4 mm inner diameter alumina tube via N-type connector without any external impedance matching unit. The system does not expose any metallic parts from the gas inlet to the atom exit, which leads to the reduction of contaminants in plasma and recombination of atomic hydrogen at the metallic wall. These Nd-Fe magnets form the magnetic field which satisfies the ECR condition in the axial direction. Unlike the poor axial magnetic field distribution of the 1st gen LICP source, the 2nd gen LICP source contains two groups of Nd-Fe magnets(N40). The stronger magnets form the double-bump magnetic structure along the source axis as shown in Fig. 3.14. The field assists the better plasma confinement in the magnetic mirror between ECR resonance regions and guiding the leaking electrons toward the alumina tube wall.

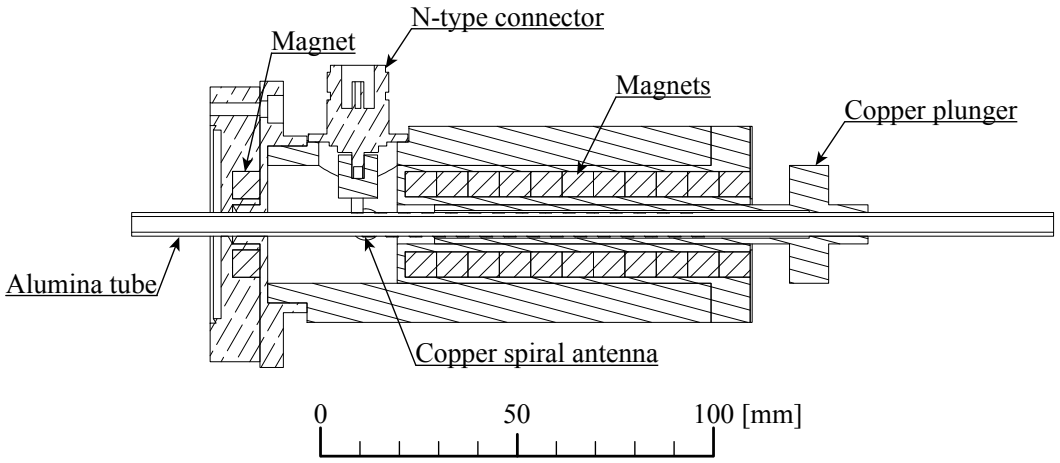

Fig. 3.13. A sectional view of the 2nd gen LICP source.

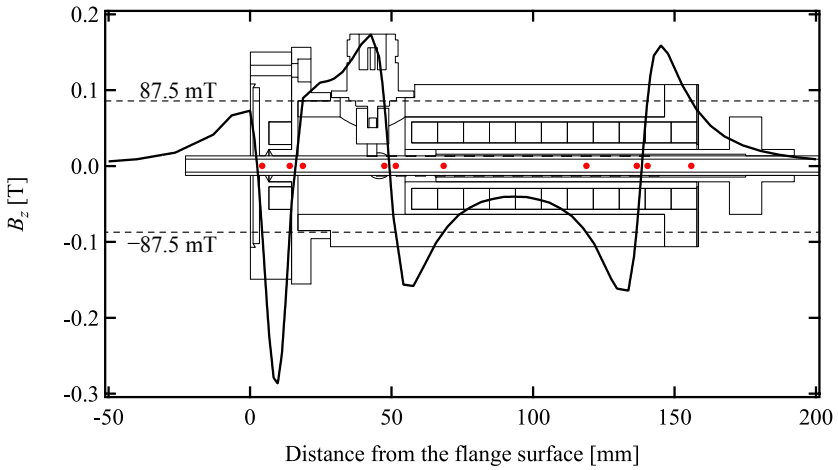

Fig. 3.14. A magnetic field distribution of the 2nd gen LICP source on the beam axis.

3.4.2 Impedance matching system for the 2nd gen LICP source

Previous LICP source requires external impedance matching circuit, while 2nd gen LICP source includes a novel impedance matching system in itself. Figure 3.15 (a) and (b) schematically illustrates the new impedance matching system; (a) and (b) show a photograph of the matching plunger, and an equivalent circuit of entire system, respectively. Axial displacement of the end of a 90 mm long threaded annular copper plunger changes the surface area in contact with the spiral antenna to realize the corresponding variation of the impedance. In Fig. 3.15 (b), $L_{antenna}$ is the effective impedance for the spiral antenna, $R_{surface}$ is correlated to heat loss at the antenna surface, and C_{cavity} is a capacitance between the antenna and the source cavity.

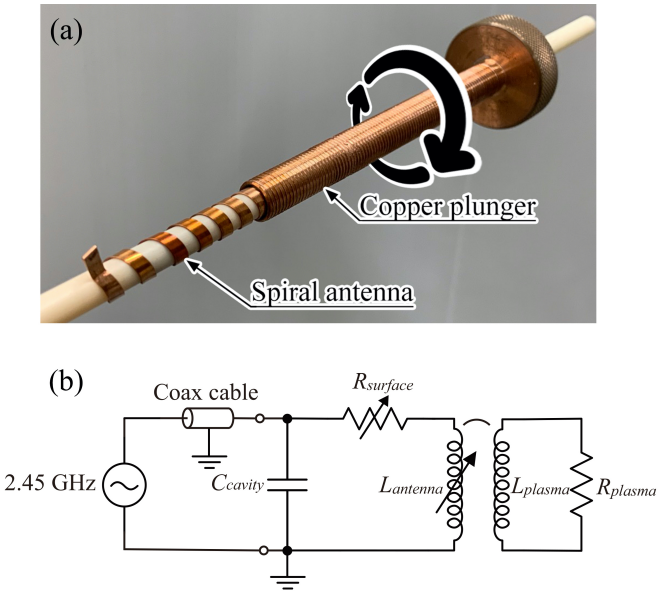

Fig. 3.15. (a) A photograph of the built-in impedance matching system. (b) An equivalent circuit of the tuner-integrated LICP source.

3.4.3 Plasma ignition power

Figures 3.16 (a) and (b) show the input microwave powers to ignite and maintain a discharge with respect to the hydrogen and nitrogen gas pressure for 2nd gen LICP source, respectively. The 1st gen LICP source frequently ignited unfavorable capacitive discharges due to the parasitic capacitance among the adjacent winding of the antenna, chamber wall, and magnet holder below the 0.2 Pa and above the 3.0 Pa. These irregular discharges consume high microwave power at the coaxial feedline requiring about 60 to 100 W input power for discharge with large reflection power. Meanwhile, the 2nd gen LICP source has a wide operational pressure range from 1×10^{-3} Pa to 10 Pa. A power input larger than 70 W ignited sparks in the copper cavity at the atmospheric pressure side.

A major improvement in the LICP radical source modification is the reduction in the loss at the power transmission line. For the 1st gen LICP source, the input microwave power is mainly lost as heat at the triple stub tuner, the N-type vacuum feedthrough made of magnetic material, and the coaxial transmission line. In contrast, the 2nd gen source has drastically improved its performance by adopting the tuner-integrated configuration to remove all of these loss components.

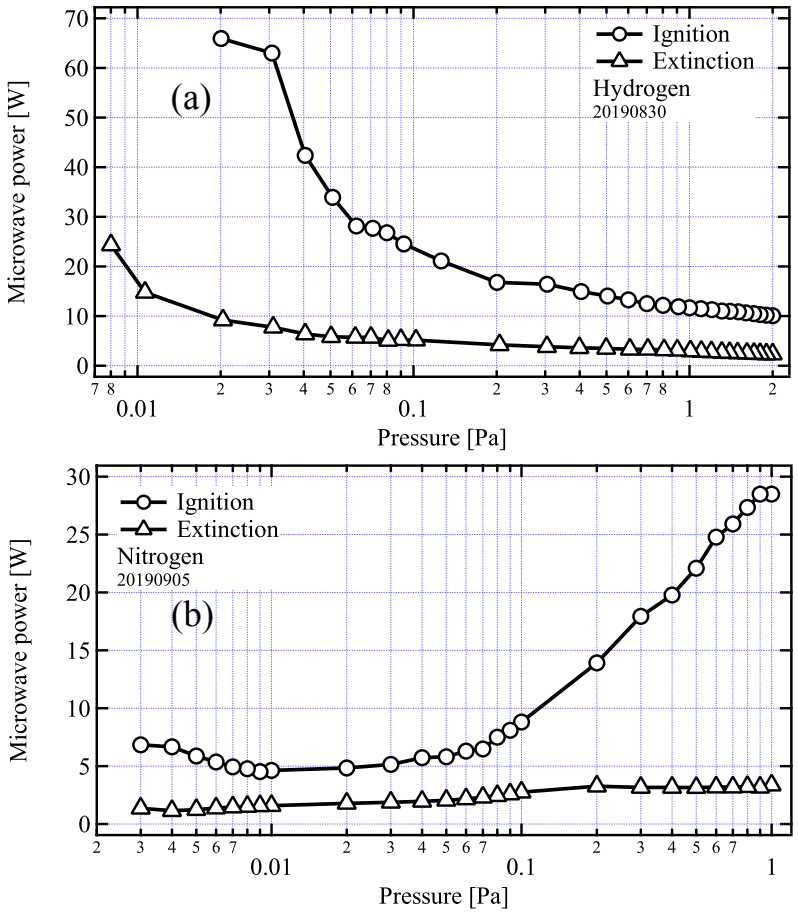

Fig. 3.16. Plasma discharge characteristics of tuner-integrated 2nd gen LICP source. (a) Hydrogen, (b) Nitrogen.

3.5 Optical emission study of built-in matching radical sources

3.5.1 Excitation of Franck-Condon atoms

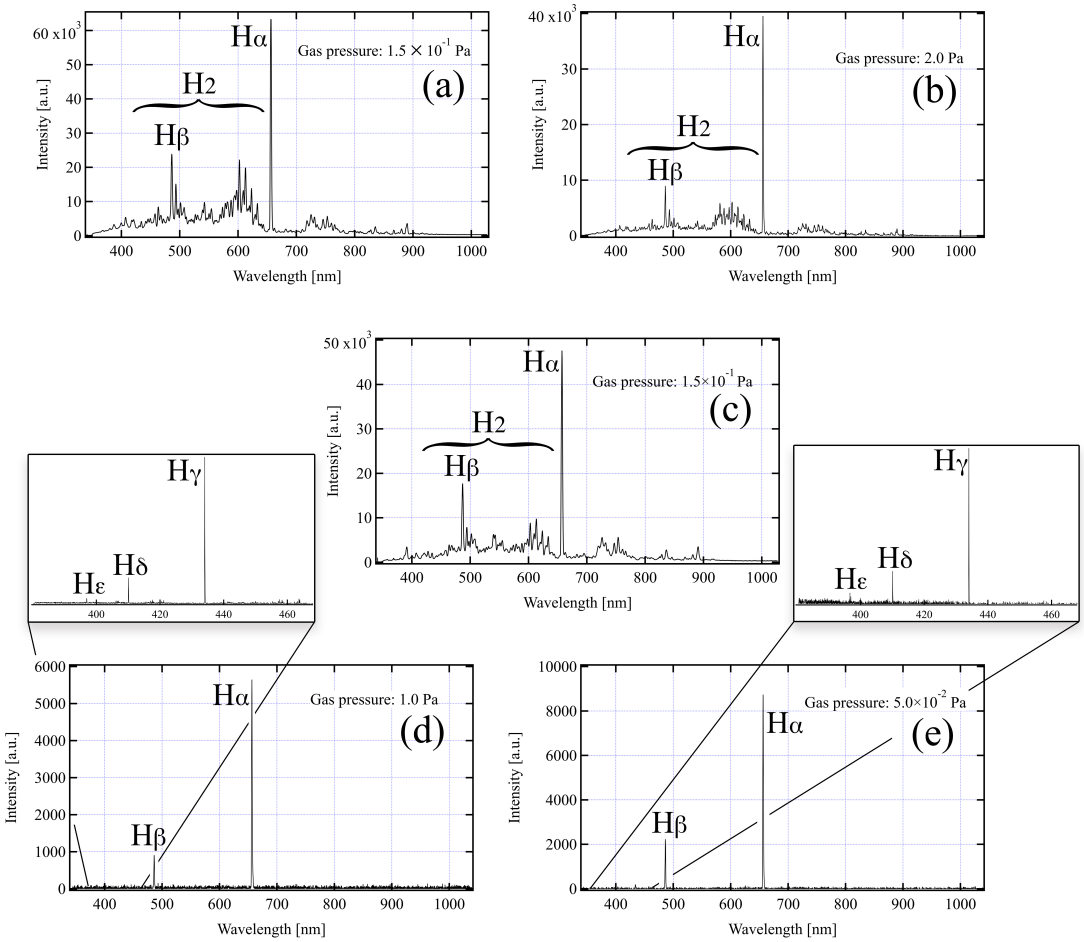

Fig. 3.17. Optical emission spectra taken from 55 W hydrogen plasmas. (a) 2nd gen CCP source in 1.5×10^{-1} Pa, (b) 3rd gen CCP source with plasma plume in 2.0 Pa, (c) 1st gen LICP source in 1.5×10^{-1} Pa, (d) 1.5th gen LICP source in 1.0 Pa, (e) 2nd gen LICP source in 5.0×10^{-2} Pa.

A plasma parameter measurement by inserting a Langmuir probe affected the plasma production of these sources, as the probe electrode affected the microwave tuning condition. Thus, in this study, brightness of the atomic line emission is utilized as an index. Figure 3.17 are typical OES (optical emission spectra) taken from 55 W hydrogen plasmas produced in each radical source. The OES results of the 2nd and 3rd gen CCP sources and 1st gen LICP source emit Balmer-series (H_α: 656 nm and H_β: 486 nm) atomic hydrogen line spectra and Fulcher band excited molecular hydrogen spectra. In contrast, the OES of

1.5th gen and 2nd gen LICP sources show only atomic line spectra (H_α, H_β, H_γ: 434 nm, H_δ: 410 nm, and H_ϵ: 397 nm) without any observable intensity of molecular spectra.

Table 3.1. A table of probable reactions for atomic hydrogen production coinciding optical emission where p is the lower state and q is the upper state.

Reactions	Formulas
H^0 deexcitation	$H^0(p) + e^- \rightarrow H^0(q) + e^-$
	$H^0(q) \rightarrow H^0(2) + h\nu$
H^+ radiative recombination	$H^+ + e^- \rightarrow H^0(2) + h\nu$

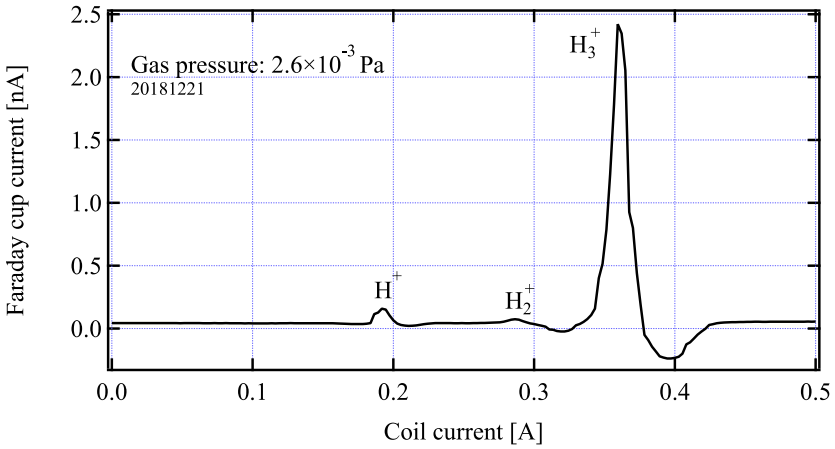

Fig. 3.18. An example mass spectrum of the extracted ion beam from the 2nd gen LICP source with 30 W input power.

Table 3.1 shows the probable reactions for atomic hydrogen production corresponding to optical emission. The ion source under the high gas pressure and low input power actively produce molecular hydrogen ion H_3^+. According to an example of extracted ion beam from the 2nd gen LICP source as shown in Fig. 3.18, the spectrum showed merely 6% proton ratio of the ion beam. The optical emission through a radiative recombination of the proton may be negligible in the H_3^+ abundant ion source because the usual operating pressure and the population of the H_3^+ of these radical sources are higher than that pressure. Figure 3.19 shows the potential curves for molecular hydrogen. The absence of the excited molecular species spectrum in the 1.5th gen and 2nd gen LICP sources suggests a high degree of dissociation and a high concentration of atomic hydrogen, because the Fulcher-band emission requires 13.6 eV of higher energy of electron-impact excitation than excitation to the $b^3\Sigma_u^+$ repulsive state which is attributable to dissociation of molecules as shown in Fig. 3.19. Moreover, the presence of the Balmer-alpha to epsilon lines suggests that the most of atomic hydrogen produced in the radical source is excited by electron-impact excitation of the atomic hydrogen produced in the Franck-Condon process with specific energy as shown in Table 3.2.

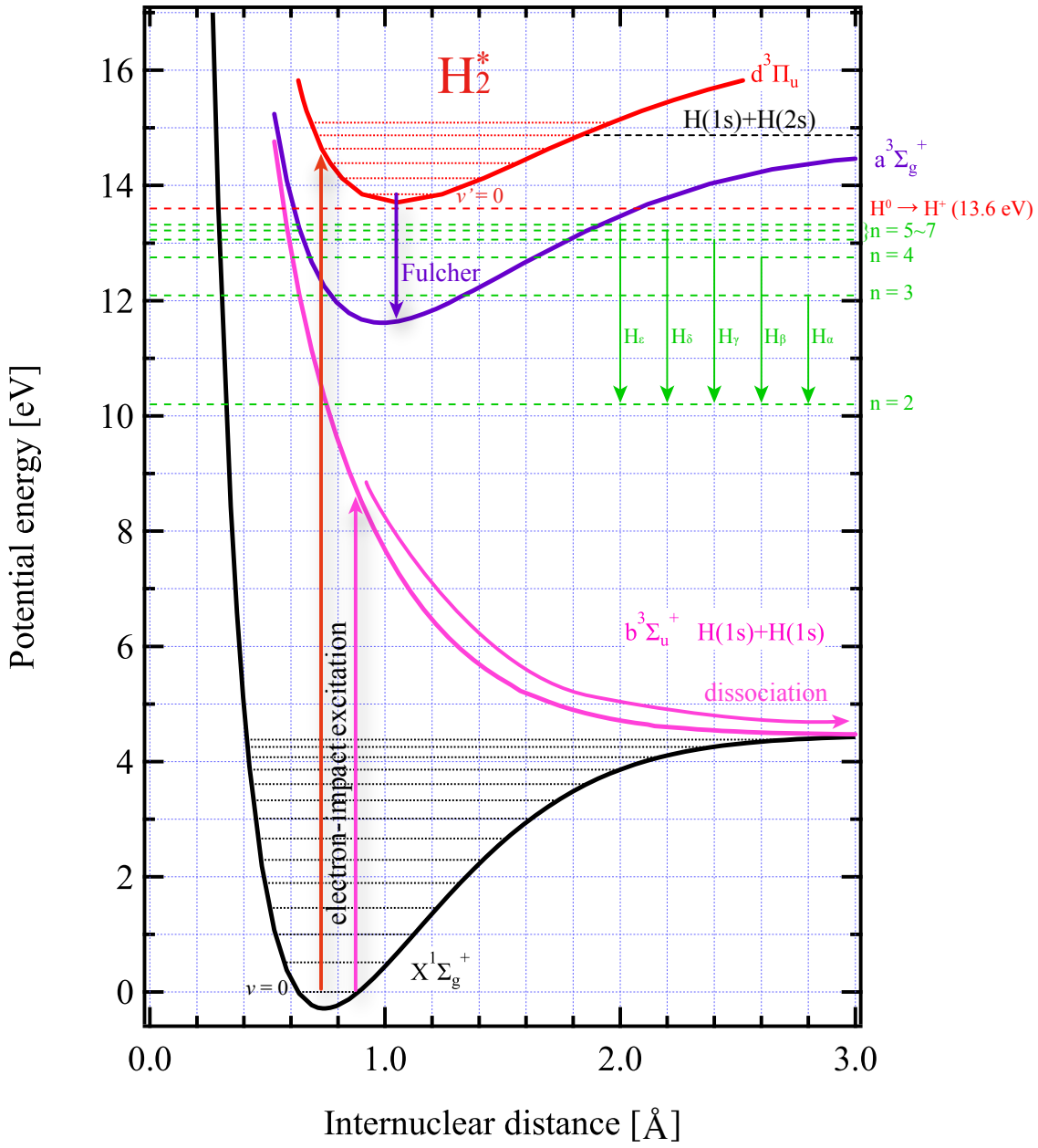

Fig. 3.19. Potential energy curves for molecular hydrogen.

Table 3.2. Atomic transition probabilities (A_{pq}) and upper state energy of each Balmer series transition [11].

Balmer series (q → p)	A_{pq} [10^{-8}s^{-1}]	Energy of the upper state [eV]
$H_\alpha(3 \rightarrow 2)$	4.4101e-1	12.09
$H_\beta(4 \rightarrow 2)$	8.4193e-2	12.75
$H_\gamma(5 \rightarrow 2)$	2.5304e-2	13.06
$H_\delta(6 \rightarrow 2)$	9.7320e-3	13.22
$H_\epsilon(7 \rightarrow 2)$	4.3889e-3	13.32

3.5.2 Source operation modes of microwave excited plasma

In order to further explore the appropriate operating conditions as atomic source, a power characteristic of the sources was investigated. In general, ICP (inductively coupled plasma) starts the discharge capacitively as E (electrostatic)-mode due to the electric field between both ends of an antenna. Then, ICP changes the discharge mode from E-mode to H (electromagnetic)-mode as increasing the input power. This mode transition from E-mode to H-mode has been investigated on the MHz driven RF plasma [12, 13]. Moreover, a magnetized RF plasma can realize mode transition from H-mode to W (propagating wave)-mode [10]. While the basic mechanism is still under study, the highly dense W-mode plasma production is actively employed in the development of electric propulsion system [14]. In a typical MHz-RF driven ICP, the wavelength of RF is much longer than the total circumference length of an antenna to induce an eddy current to a single same direction. Whereas, the LICP can locally excite the eddy current in both directions of the spiral antenna, since the wavelength of microwave (12.24 cm for 2.45 GHz) is almost equal to or smaller than a circumference length of the antenna. A couple of prior researches about the single-loop atmospheric microwave ICP excited by a microwave resonator realize the E-H transition [15, 16]. However, the existence of multi-turns microwave ICP have not been observed.

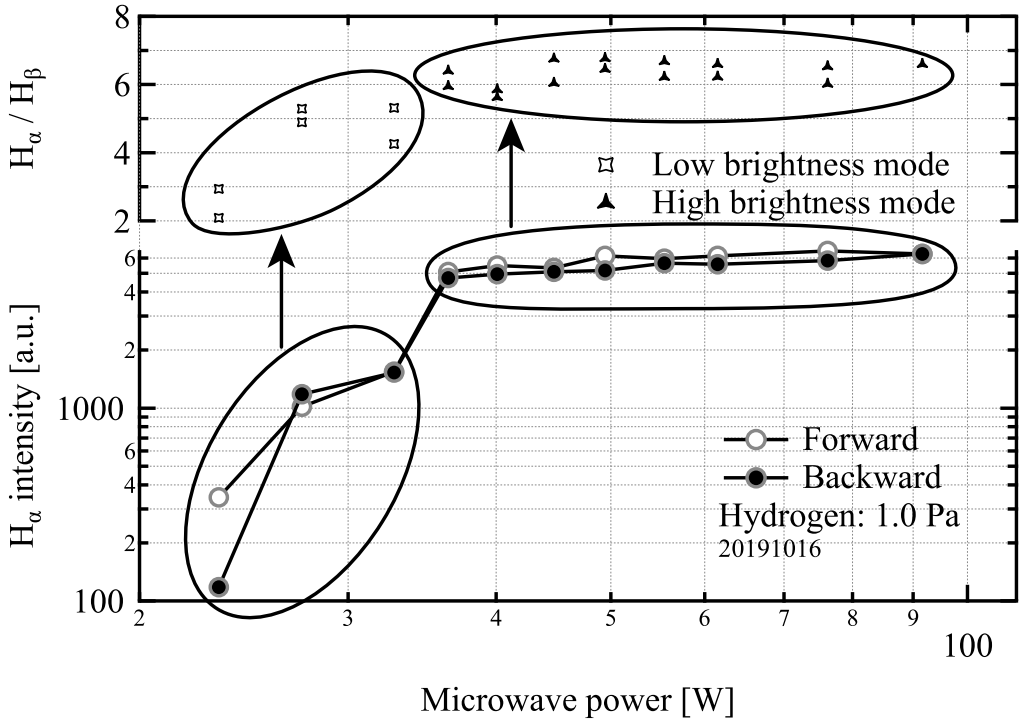

Fig. 3.20. Balmer-alpha intensities and alpha to beta ratio with respect to the input microwave power at 1.0 Pa hydrogen pressure by the 1.5th gen LICP source.

Figure 3.20 shows the trace of the Balmer-alpha line intensities and Balmer-alpha to beta ratios with respect to the input microwave power for 1.5th gen LICP source. The characteristic was taken at the 1.0 Pa hydrogen pressure since the emission from the 1.5th gen LICP became unstable at a condition below 1.0 Pa and 30 W power input. There is an obvious jump in the Balmer-alpha intensity at 36 W input from a faint glow (low brightness mode) to a strong emission (high brightness mode). Although the characteristic may be an indication of a mode jump, no apparent hysteresis loop is observed in the vicinity of the mode transition. Once a MHz range RF plasma attains the H-mode discharge, the plasma sustains the H-mode with the power input lower than the power necessary to commence the H-mode. More precise data for higher excited states are unavailable due to the unstable operation of the 1.5th gen LICP source.

To investigate if the presence of the magnetic field was the cause of the mode jump, the same experiment was performed by designing a tuner integrated electric field driven microwave discharge (CCP) source. Figure 3.21 shows the result of the data taken with the same experimental procedure as that of Fig. 3.20 for the 3rd gen CCP source. The source pressure was controlled at 2.0 Pa hydrogen, which was the minimum stable operating pressure. The result shows no such mode transition for microwave CCP as the Balmer-alpha to beta ratio does not change for input power increase.

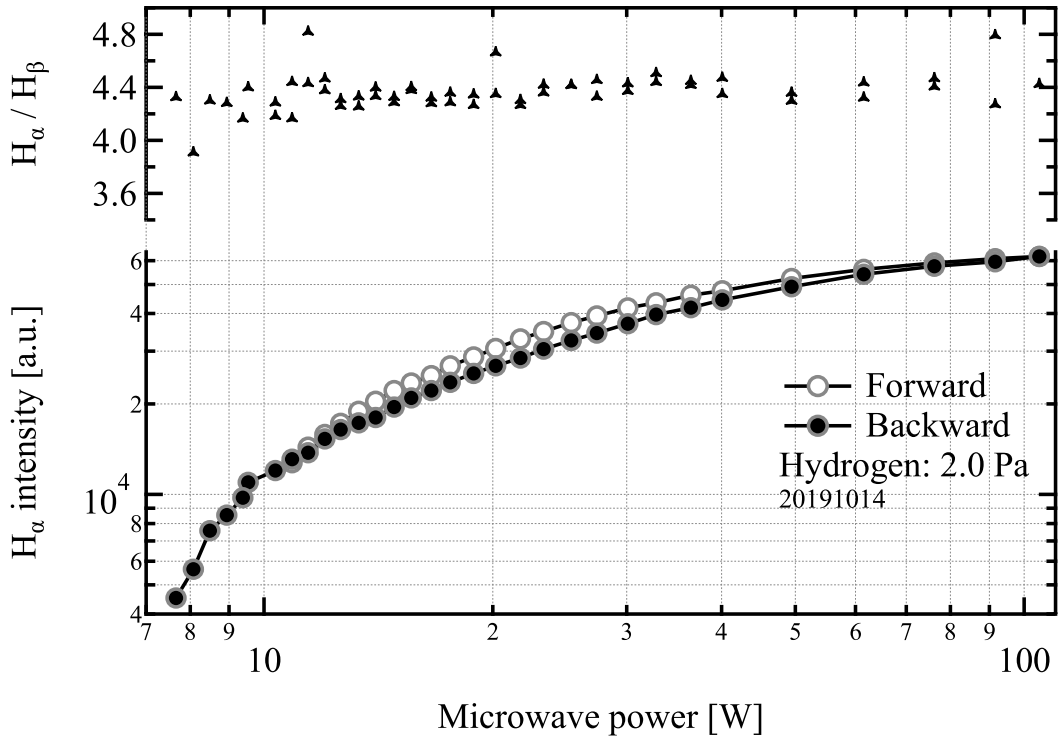

Fig. 3.21. Balmer-alpha intensities and alpha to beta ratio with respect to the input microwave power at 2.0 Pa hydrogen pressure by 3rd gen CCP source.

In order to eliminate the effect of ECR magnets on the produced plasma, the same experiment was conducted under the magnet-free configuration. Because the 1.5th gen source never ignited the plasma with the magnet free condition, magnets of the 2nd gen LICP source was detached. This magnet free source was operated at 1.4 Pa pressure, since the magnet free configuration did not sustain a stable plasma at lower hydrogen pressure. The obtained result is shown in Fig. 3.22. Unlike the result of the CCP source, the magnet-free inductive configuration exhibits change in slope of the intensity curve. Although this tendency is completely different from an E-H transition of an RF discharge, this implies that the difference of the electrode structure affects the plasma production mechanism. An OES result shown in Fig. 3.23 indicates a trace amount of molecular hydrogen band even though the degree of dissociation is still high. This is due to the poor cracking efficiency compared with the ECR condition.

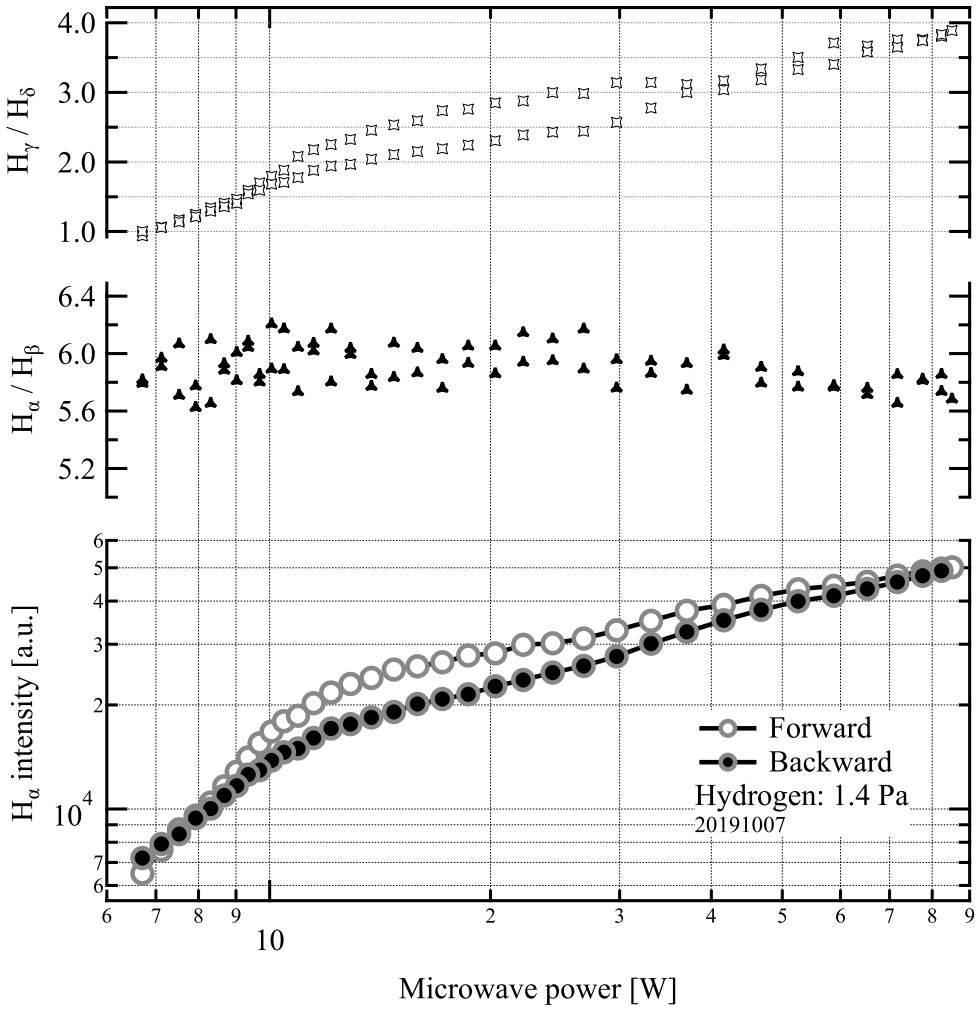

Fig. 3.22. Balmer-alpha intensities and alpha to beta ratio with respect to the input microwave power at 1.4 Pa hydrogen pressure by magnet-less 2nd gen LICP source.

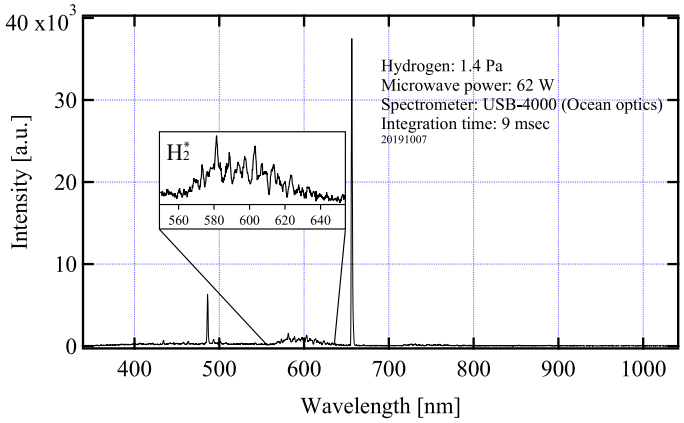

Fig. 3.23. An optical emission spectrum taken by magnet-less 2nd gen LICP source plasma sustained in 1.4 Pa hydrogen.

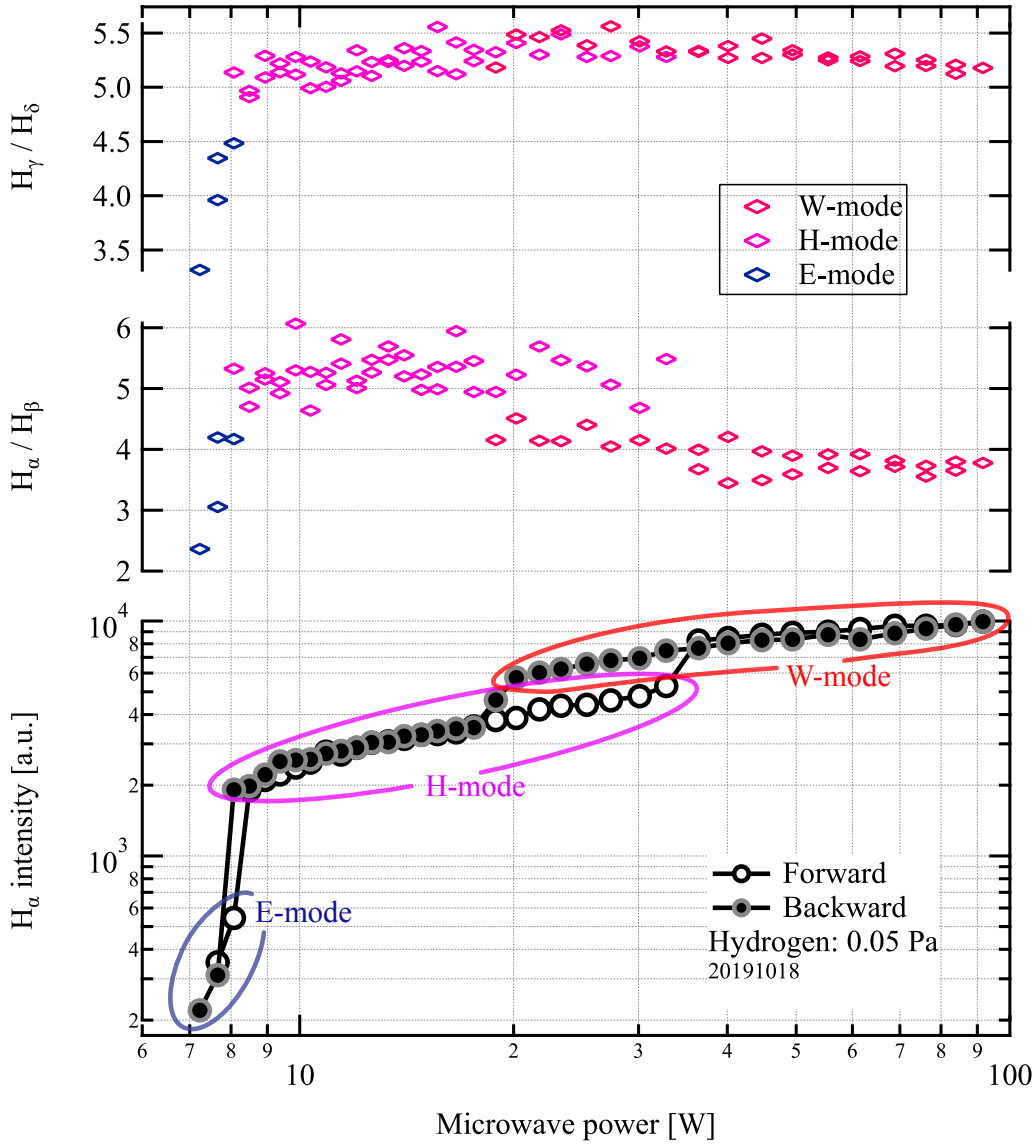

Fig. 3.24. A mode transition diagram plotted by Balmer-gamma and delta intensities with 0.05 Pa hydrogen atmosphere by 2nd gen LICP source.

Finally, the same measurement was made with the 2nd gen LICP source with magnets. Figure 3.24 shows the plots of the Balmer-alpha intensity, the ratio of Balmer-alpha to beta, and the ratio of gamma to delta with respect to the input microwave power. Unlike all sources discussed above, the results obviously show the behavior of mode transition with two steps and correlated with hysteresis. These sets of experiments suggest the existence of at least two transitions. Assuming the lowest level power plasma is excited in E-mode, the plasma excitation modes are indicated in the figure for convenience.

According to prior researches on the W-mode of RF plasma, the principal mechanism that drives the mode transition is considered to be the conversion from Whistler wave to electrostatic Trivelpiece-Gould wave [17, 18, 19]. The experimental results of the mode transition of the ECR-based LICP source imply that the mode conversion from the electron cyclotron wave to other electrostatic wave, because the behavior resembles that of the helicon wave plasma in the range of MHz RF plasma.

The E-H-W mode assignment in Fig. 3.24 can be H-W1-W2 as several jumps can be present in W mode transition in the present magnetic field configuration of a microwave excited plasma. Because of the restriction in putting in diagnostics devices in a densely arranged microwave environment, it is not possible to prove the initial plasma is excited in E-mode. Further increase in input power to the LICP source and change in diameter of the plasma may deepen the understanding of the mode transition in the range of microwave W-mode by observing the successive jumps in the plasma density, which has been observed in typical RF plasma W-mode [18].

3.6 Conclusion

In this chapter, two types of tuner-integrated radical beam sources are discussed. A plunger structure realized an operation without the power loss at the triple stub tuner and easier tuning procedure by tuner integration for the CCP radical source. The 3rd gen CCP source can produce the plasma plume which is the extracted ions by positive self bias voltage under the high gas pressure, high power input, and efficient impedance matching condition. Meanwhile, the ECR assisted 4th gen CCP source required more difficult matching operation than the 3rd gen CCP radical source due to unpredictable capacitance component in the source cavity. The built-in type CCP source can be further improved by expanding the tunable region on the Smith chart because the single plunger/stub circuit is highly restricted in the matching condition.

Whereas, the LICP source had achieved low operating pressure ($\sim 10^{-3}$ Pa), high degree of dissociation, and simple matching system by the tuner-integration. When the antenna and the permanent magnets were properly arranged, the assembled source has exhibited the possible mode jumps. This characteristic plasma coupling to microwave power of the newly developed multi-loop locally excited microwave ICP is considered to

realize the high efficiency in atom production. The LICP source can produce a wide variety of electrically neutral species from selections of gas/liquid samples without exposing any metal surface facing to the produced plasmas.

References

[1] Y. Shimabukuro, H. Takahashi, and M. Wada, "Electrode structure of a compact microwave driven capacitively coupled atomic beam source", *Jpn. J. Appl. Phys.* **57(1S)**, 01AA02 2018.

[2] Y. Shimabukuro, H. Takahashi, S. Iwamoto, K. Tanaka, and M. Wada, "Tandem Mass Spectrometry of Peptide Ions by Microwave Excited Hydrogen and Water Plasmas", *Anal. Chem.* **90**, 7239 2018.

[3] M. Moisan, C. Beaudry, and P. Leprince, "A NEW HF DEVICE FOR THE PRODUCTION OF LONG PLASMA COLUMNS AT A HIGH ELECTRON DENSITY", *Phys. Lett.* **50A(2)**, 125 1974.

[4] M. Moisan, Z. Zakrzewski, and R. Pantel, "The theory and characteristics of an efficient surface wave launcher (surfatron) producing long plasma columns", *J. Phys. D* **12**, 219 1979.

[5] M. Selby and G. M. Hieftje, "Taming the surfatron", *Spectrochimica Acta.* **42B**, 285 1987.

[6] M. Moisan, C. Bar beau, R. Claude, C. M. Ferreira, J. Margot, J. Paraszczak, A. B. Sa, G. Sauve, and M. R. Werthimer, "Radio frequency or microwave plasma reactors? Factors determining the optimum frequency of operation", *J. Vac. Sci. Technol. B* **9(1)**, 8 1991.

[7] E. Carbone, N. Sadeghi, E. Vos, S. Hubner, E. van Veldhuizen, J. van Dijk, S. Nijdam, and G. Kroesen, "Spatio-temporal dynamics of a pulsed microwave argon plasma: ignition and afterglow", *Plasma Sources Sci. Technol.* **24**, 015015 2015.

[8] C. M. Ogun, C. Kaiser, R. Kling, and W. Heering, "Diagnostics of surface wave driven low pressure plasmas based on indium monoiodide-argon system", *J. Phys. D* **48**, 255201 2015.

[9] Y. Sakamoto, T, Kasuya, M. Wada, and S. Maeno, "Compact 2.45 GHz microwave ion/atom source", *Rev. Sci. Instrum.* **79(2)**, 02A318 2008.

[10] P. Chabert and N. Braithwaite, *Physics of Radio-Frequency Plasmas* (Cambridge university press, Cambridge, 2011).

[11] W. L. Wiese and J. R. Fuhr, "Accurate Atomic Transition Probabilities for Hydrogen, Helium, and Lithium", *J. Phys. Chem. Ref. Data* **38(3)**, 565 2009.

[12] H. Conrads and M. Schmidt, "Plasma generation and plasma sources", *Plasma Sources Sci. Technol.* **9**, 441 2000.

[13] M. M. Turner and M. A. Lieberman, "Hysteresis and the E-to-H transition in radiofrequency inductive discharges", *Plasma Sources Sci. Technol.* **8**, 313 1999.

[14] F. R. ChangDiaz, J. P. Squire, A. V. Ilin, G. E. Mccaskill, T. Nguyen, D. S. Winter, A. J. Petro, G. W. Goebel, L. D. Cassady, K. A. Stokke, C. E. Dexter, T. P. Graves, L. Amador JR., J. A. George, R. Bengtson, B. N. Breizman, V. T. Jacobson, A. Arefiev, A. A. Chan, and T. W. Glover, "The physics and Engineering of the VASIMR Engine", *Proc. of 36th JPC*, Huntsville 2000.

[15] J. Giersz, K. Jankowski, A. Ramsza, and E. Reszke, "Microwave-driven inductively coupled plasmas for analytical spectroscopy", *Spectrochim. Acta Part B* **147**, 51 2018.

[16] H. Porteanu, I. Stefanovic, N. Bibinov, M. Klute, P. Awakowicz, R. P. Brinkmann, and W. Heinrich, "Correlated mode analysis of a microwave driven ICP source", *Plasma Sources Sci. Technol.* **28**, 035013 2019.

[17] K. P. Shamrai, V. P. Pavlenko, and V. B. Taranov, "Excitation, conversion and damping of waves in a helicon plasma source driven by an $m = 0$ antenna", *Plasma Phys. Control. Fusion* **39**, 505 1997.

[18] F. F. Chen, "Helicon discharges and sources: a review", *Plasma Sources Sci. Technol.* **24**, 014001 2015.

[19] J. F. Caneses, B. D. Blackwell, and P. Piotrowicz, "Helicon antenna radiation patterns in a high-density hydrogen linear plasma device", *Phys. Plasma* **24(11)**, 113513 2017.

Chapter 4

Measurement of Velocity Distribution of Hydrogen Atoms Produced from the Radical Sources

4.1 Methodology of velocity distribution measurement

4.1.1 Velocity distribution of neutral particles

A variety of electrically neutral species existing in the microwave excited source plasma has been revealed by OES (Optical Emission Spectroscopy) in Chapter 2 and 3. Regarding use of the radical beam, the parameter measurement on the radical beams emitted from the exit of the radical source determines the rate of reactions such as attachments. Chemically active atomic hydrogen can be used for a variety of applications. However, its characteristics such as temperature, velocity, and flux are often unknown since electrically neutral particles do not produce signals to electron based detectors. Especially in the study about collisions between radicals and biomolecules, radical temperature which determines the proportion of radicals with the kinetic energy above the activation energy of the chemical reaction must be measured to clarify the mechanisms of several applications. The difference in velocity distribution of atomic hydrogen effusing out from the two types of compact microwave driven plasma sources can never be characterized by ordinary diagnostics techniques including probe and optical spectrometry. In this chapter, determination of the temperature of radical beam generated by the developed sources are discussed.

4.1.2 Mass separated time of flight

In the field of the surface science, interaction between the supersonic molecular beam and solid surface has been studied. Although Kitatani *et al* measured the velocity distributions of supersonic helium atom, argon atom, and deuterium molecular beams produced in the arc-discharge type ion source, signal originated from the atomic hydrogen could not be acquired due to its poor S/N [1]. Velocity distribution measurement of supersonic molecular beam by MSTOF (mass separated time of flight) method have been studied for a long time [1, 2, 3, 4]. Time of flight (TOF) mass spectrometry invented by Stepens *et al* utilizes a difference of arrival time depending upon their mass to charge ratio m/z; if various weights of neutrals are released to the field free space at the same time, light particles arrive at a detector earlier than heavy particles. Arrival times of ions are depending on their m/z because a general TOF mass spectrometer designed for ion detection in the field of chemistry extracts ions together by an extraction voltage. In contrast, arrival times of neutral particles in MSTOF system are dependent upon their velocity distribution and masses as they leave the emission source.

4.2 Original experimental system

4.2.1 Vacuum system

Figure 4.1 shows the original configuration of designed experimental system to measure the velocity distribution function of low-energy atomic hydrogen. The developed radical sources are attached to the bottom flange of a first chamber. The first chamber pumped down by a 520 L/s turbo molecular pump (TMP)1 (Pfeiffer vacuum, TMU521) has a beam chopper, laser diode, and photo diode. In the first chamber, the atomic beams are pulsed by the beam chopper. The pulsed atomic beam goes through a 285 mm long second chamber and across a magnetic filter to eliminate the charged particles. The second chamber pumped down by a 280 L/s TMP2 (Shimadzu corporation, TMP 280-G) has an electron-impact type ionizer at the end of the flight tube. The ionized signal is detected by a secondary electron multiplier after selection by a sector magnet. The third chamber pumped down by a 67 L/s TMP3 (Pfeiffer vacuum, Hi-Pace 80) contains the electron multiplier tube for ionized atom current detection.

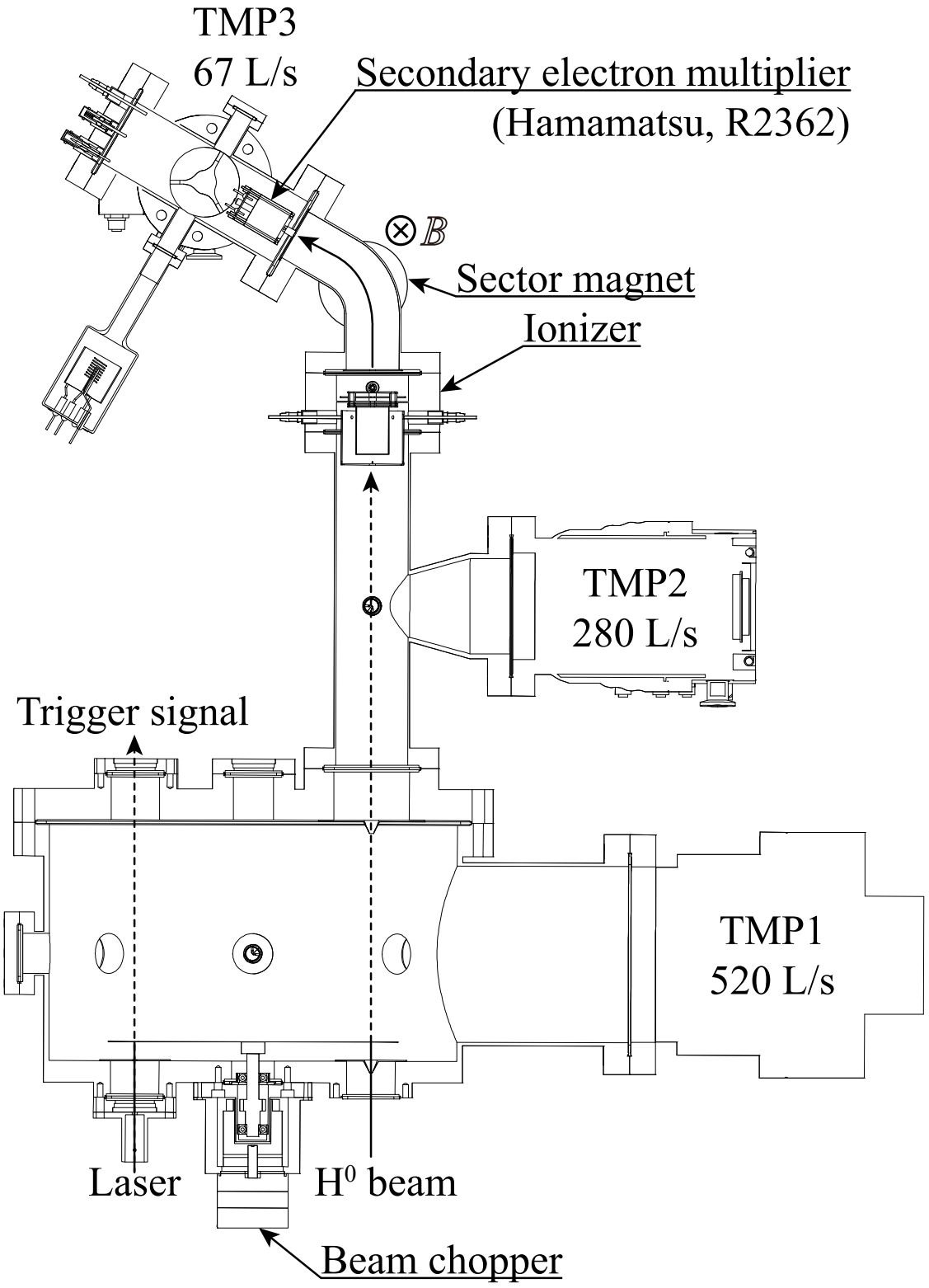

Fig. 4.1. A schematic diagram of the original experimental setup to measure the velocity distribution function.

4.2.2 Pulse beam production

Emitted neutral beams from the radical source are required to be a pulse signal as a criterion of the MSTOF. Installing the mechanical motor into the vacuum chamber pollutes the vacuum atmosphere due to the lubricant oil evaporation. A rotating mechanism that drives the rotor indirectly outside from the vacuum system is necessary. Figure 4.2 shows the sectional drawing of the 1st gen beam chopper. The blue line in the figure indicates the boundary between the vacuum and the atmospheric pressure side. A DC motor (Oriental motor, BLM260-A2) fixed to an aluminum cylinder having a quadrupole cusp magnets and disk cylinder sets the rotation axis. An aluminum helmet levitated by repulsion magnetic field has also the quadrupole driving magnets on the side way. A rotation of the aluminum cylinder gives the torque to the aluminum helmet indirectly by coupling the driving magnets. An 0.2 mm thickness aluminum blade which has 10 sector-shaped holes in each 18° is fixed on the aluminum blade by an o-ring.

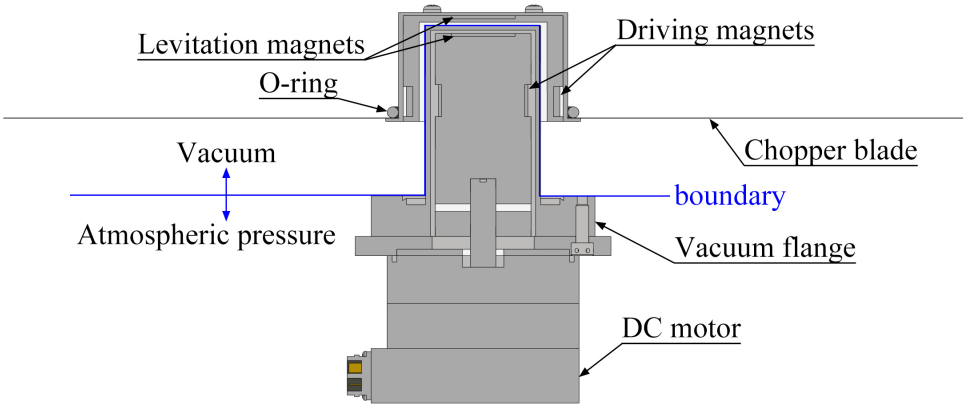

Fig. 4.2. A sectional drawing of the 1st gen beam chopper.

4.2.3 Electron-imapact ionizer

In order to detect the hydrogen atoms with a SEM (Secondary Electron Multiplier), the atomic flux signal has to be converted into an ion flux signal. An EI (Electron-impact Ionization) reaction is one of the most commonly used ionization methods as expressed in the following equations.

$$M + e^- \rightarrow M^+ + 2e^- \tag{4.1}$$

$$H^0 + e^- \rightarrow H^+ + 2e^- \tag{4.2}$$

Figure 4.3 shows the electron impact ionization cross section for 1s state of atomic hydrogen (H^0) [6, 7, 8]. Although the ionization energy for atomic hydrogen as expressed in the Eq. 4.2 is 13.6 eV, the electron energy was set to 55 eV in this experiment to maximize the

ionization efficiency of atomic hydrogen.

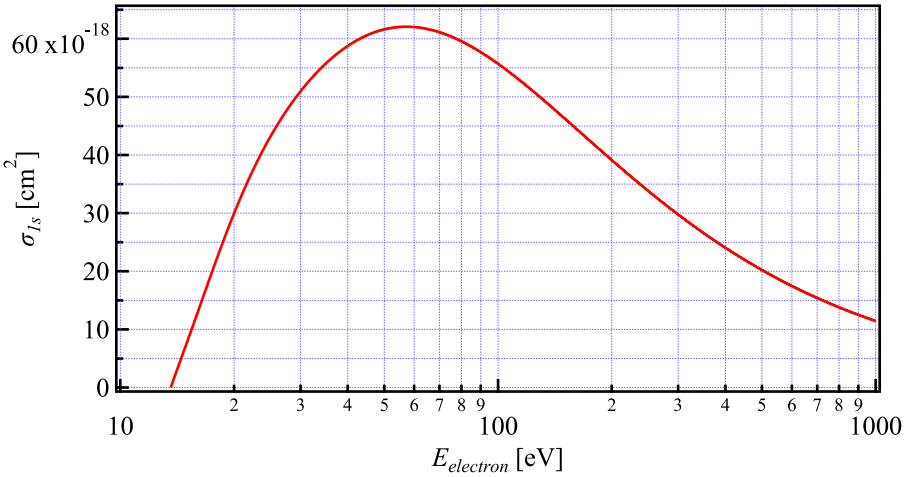

Fig. 4.3. Electron impact ionization cross section for 1s state of atomic hydrogen [6, 7, 8].

Figure 4.4 schematically shows the developed 1st gen EI type ionizer. The ionizer is mounted on the 50 mm thickness ICF 114 standard double side edge flange made of stainless-steel. A 0.3 mm diameter tungsten wire filament sustained by the copper vacuum feed-throughs emit the 55 eV electron toward a mesh electrode. The emitted electrons confined in a repeller electrode ionizes the residual gases such as water vapor and H_2 besides incident H^0 within the 28 mm diameter 40 mm long mesh electrode. The produced ions are extracted by the potential gap between the mesh electrode and grounded electrode and go through a 3 mm diameter holes of an Einzel lens.

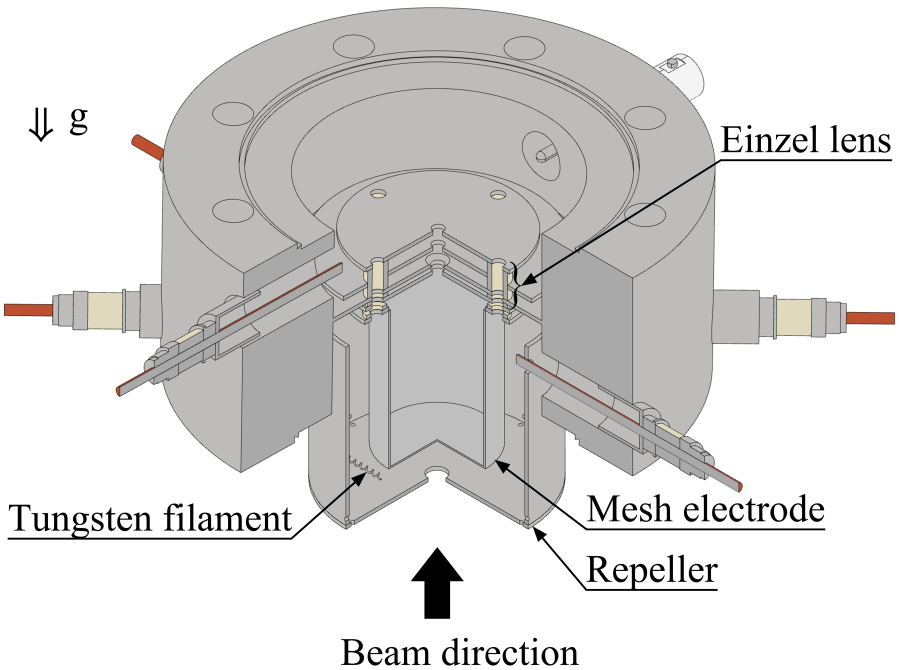

Fig. 4.4. A schematic diagram of the 1st gen ionizer.

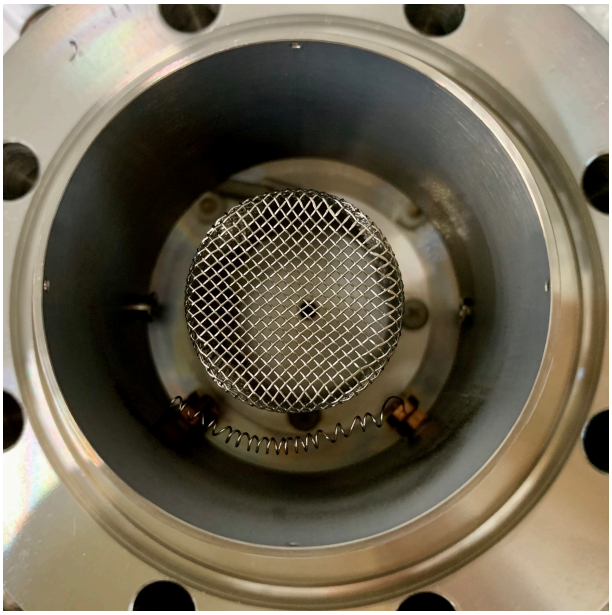

Fig. 4.5. A photograph of inside the 1st gen ionizer.

4.2.4 Sector magnet for selecting the particle species

Charged particles in a magnetic field move along a radius r_L as the cyclotron motion. The Larmor radius r_L in the uniform static magnetic field is given by

$$r_L = \frac{m_i v_\perp}{|q|B} \tag{4.3}$$

where m_i is the mass of the ion, $v_\perp$ is the component of the velocity perpendicular to the direction of the magnetic field, q is the electric charge, and B is the strength of the magnetic field. The velocity v_i of an ion which has an electric charge ze accelerated by the extraction voltage V is

$$v_i = \sqrt{\frac{2zeV}{m_i}}. \tag{4.4}$$

The Larmor radius for hydrogen which is given by the following equation is dependent upon the $\sqrt{m_i}$, since all hydrogen ions, H^+, H_2^+, H_3^+, are singly charged ($z = 1$).

$$r_L = \frac{1}{B}\sqrt{\frac{2V}{e}}\sqrt{m_i} \tag{4.5}$$

Thus, the mixed signal of several ions can be selected into each H^+, H_2^+, H_3^+ signal by using orthogonal magnetic field in the same Larmor radius.

Figure 4.6 shows the cross sectional drawing of the sector magnet. Two groups of magnets are fixed to the iron yokes with 13 mm gap distance. In order to cover the wide range of magnetic field, the sector magnet system adopted a combination of electromagnetic coils and permanent magnets. Each electromagnetic coil has 1000-turns

copper wire wound around a 50 mm diameter iron core. In addition to the electromagnets, the center cavity includes an iron core and ferrite magnet (Y30BH). A measured magnetic flux density with respect to the coil current is shown in Fig. 4.7. That magnetic field strength is sufficient to control hydrogen ions up to 1 keV for 50 mm Larmor radius. The magnetic system has an applicability to higher mass and energy particles by changing the permanent magnets as shown in Table 4.1. Figure 4.8 shows a photograph of the sector magnet and a 60 degree bending flange.

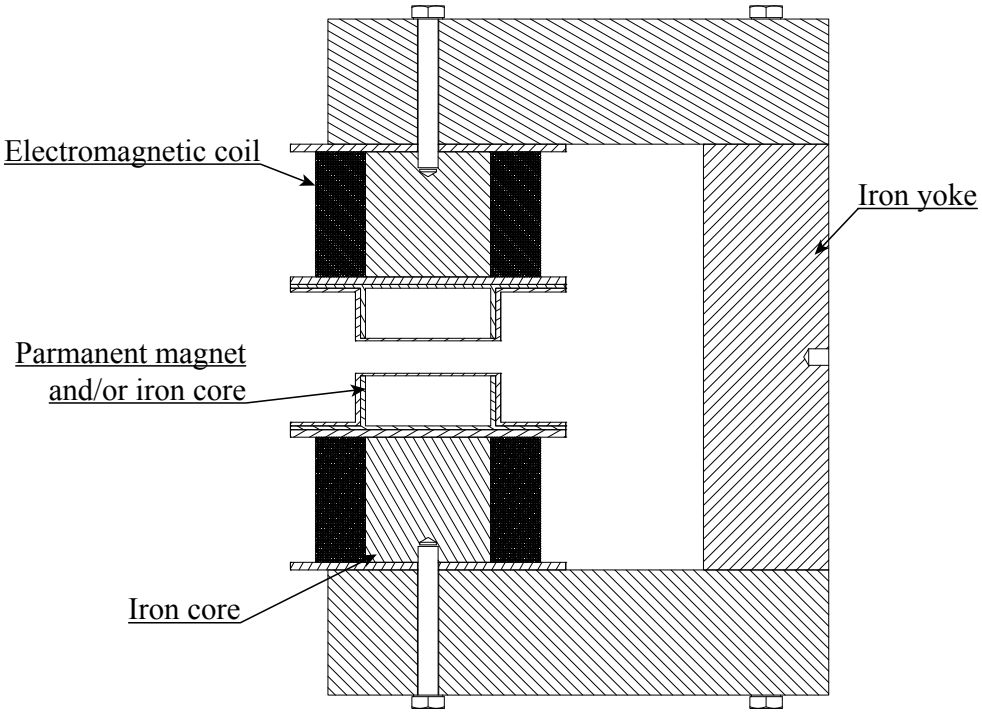

Fig. 4.6. A sectional drawing of the sector magnet.

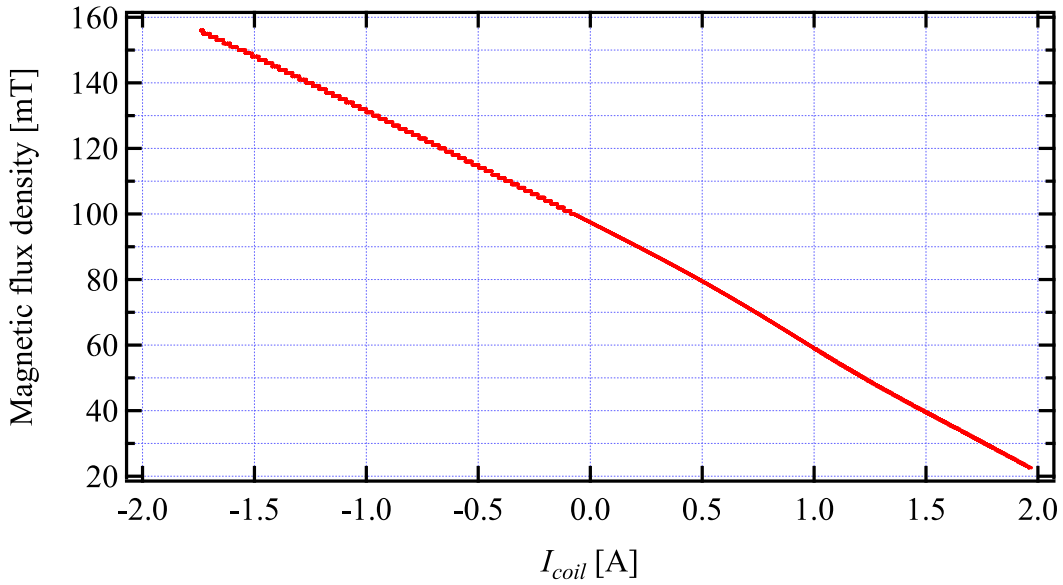

Fig. 4.7. Magnetic flux density of the sector magnet with respect to a coil current in case of the one ferrite magnet condition measured by LakeShore 421 Gaussmeter.

Table 4.1. Magnetic field strengths regarding to the variety of insertion magnet and iron core.

Permanent magnet and/or iron core	$\|B\|$ [mT]
Ferrite magnet + iron core	20-150
Two ferrite magnets	150-260
Neodymium magnet + iron core	250-360

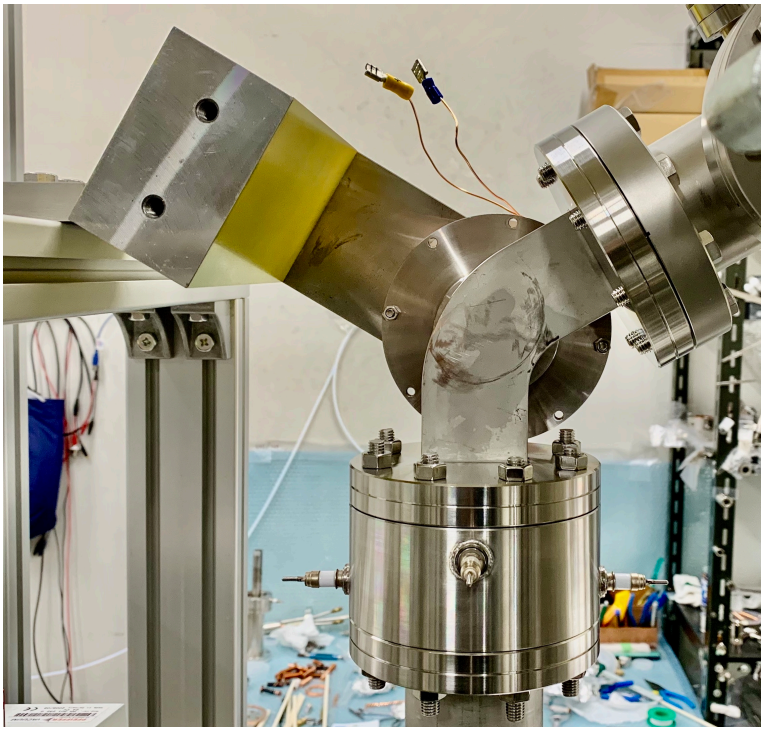

Fig. 4.8. A photograph of the 60 degree ion bending system.

4.2.5 Detector for ionized neutral signal

In order to record the small pulsed ion signal, this experiment utilized SEM (Secondary Electron Multiplier) tube for ion detection. Figure 4.9 illustrates the principal mechanism of the SEM tube. The SEM tube is composed of dynodes, anode, and divider circuit. A high voltage power source supplies negative high voltage from the last dynode to the first dynode. The divider circuit equally distribute the divided voltage to each dynode. If positive ion strikes the first dynode, the first dynode emits the secondary electrons from the surface. Then, emitted electrons are amplified by the succeeding dynodes and reach the anode as an electron bunch [9]. In this experiment, R2362 (Hamamatsu photonics) was installed in the third chamber as shown in Fig. 4.10.

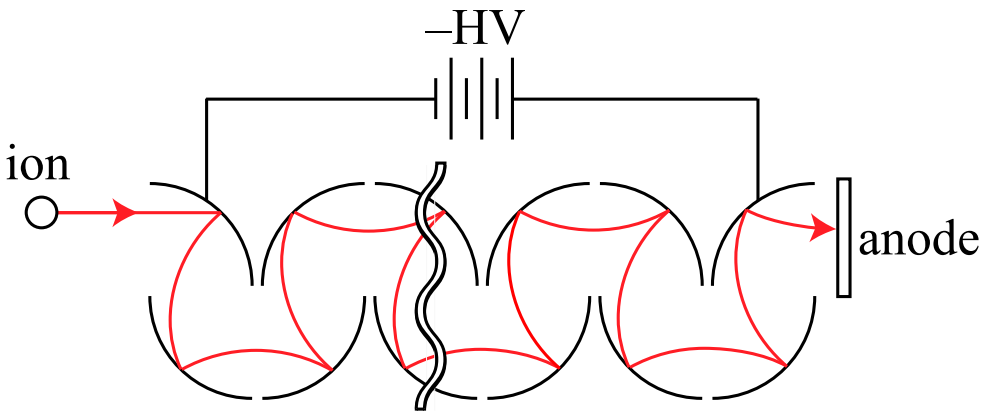

Fig. 4.9. A principal mechanism of the secondary electron multiplier tube.

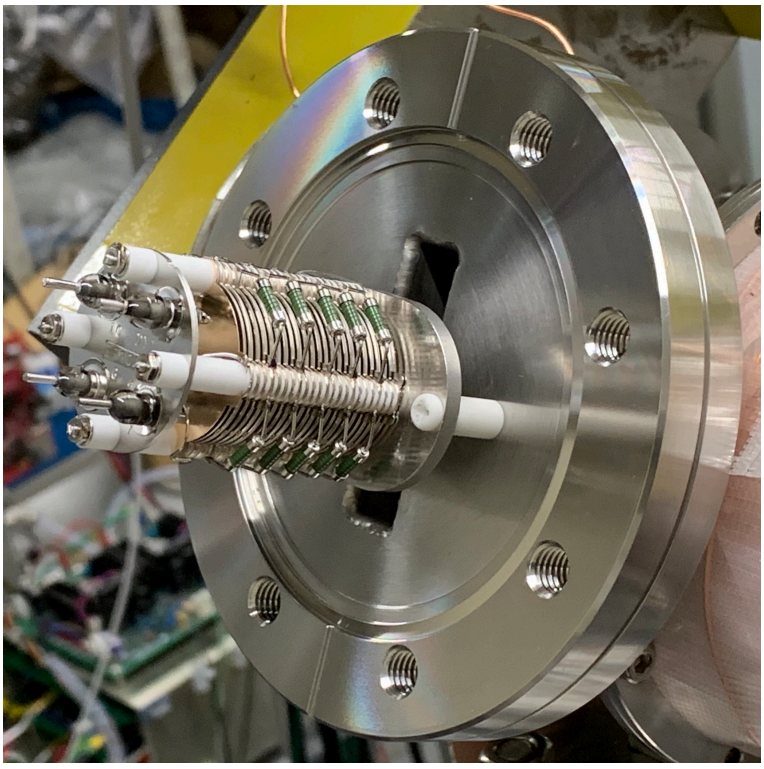

Fig. 4.10. A photograph of the SEM tube, R2362.

4.3 System improvements

The original experimental setup shown in the section 4.2 was not able to obtain sufficient signals originated from the atomic hydrogen. Several instrumental improvements were carried out as described in the following subsections. Figure 4.11 shows the final form of the experimental setup after the modifications.

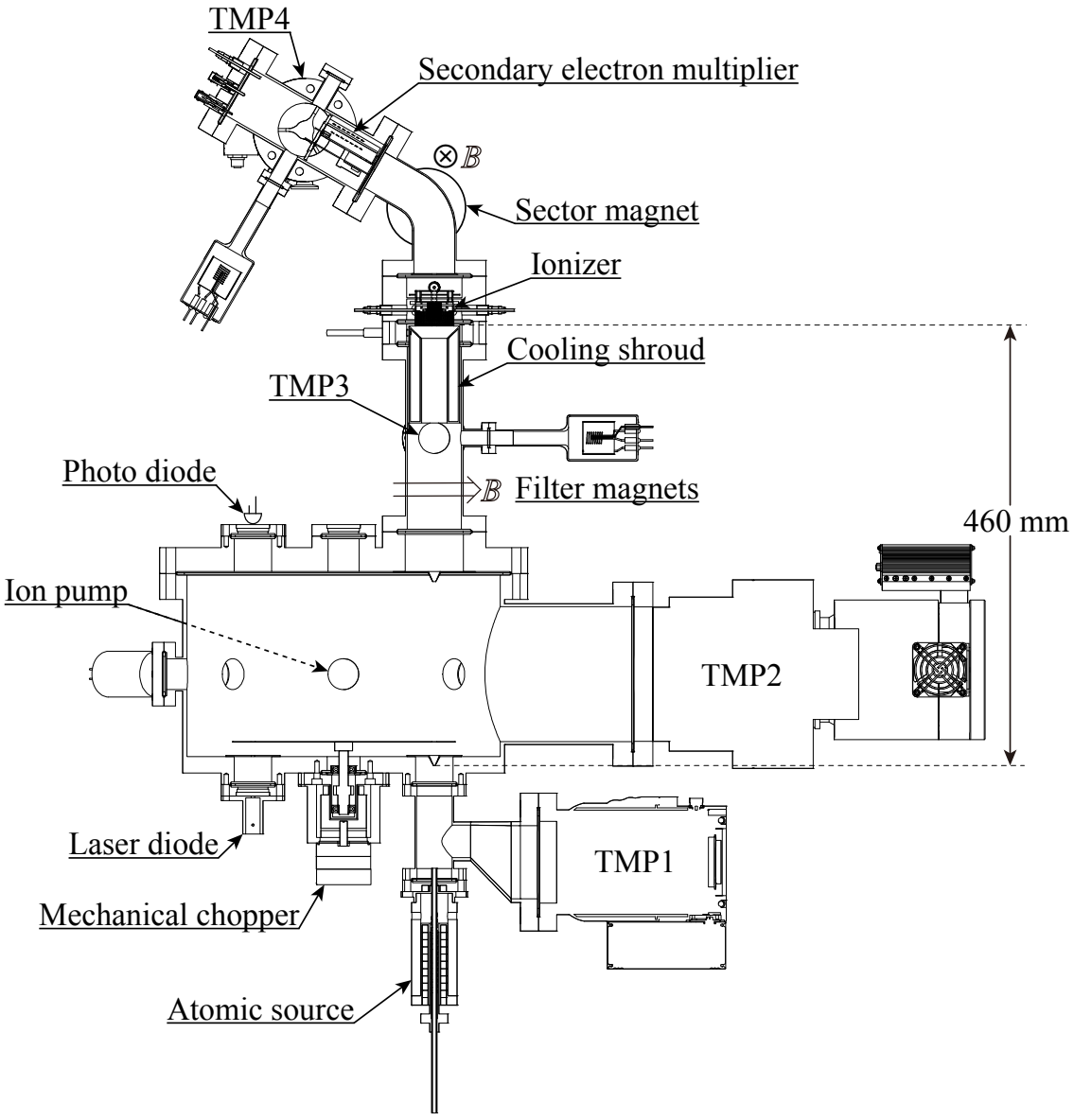

Fig. 4.11. Overall schematic of the apparatus of velocity distribution function measurement system.

4.3.1 Improvement in beam chopper

The 1st gen beam chopper illustrated in the section 4.2.2 can increase rotation speed up to 120 rpm under the vacuum condition. The slow beam chopping is impractical for velocity distribution measurement since the positive pulse width of the chopped beam for 120 rpm is 25 ms. Moreover, the instability of the rotation axis due to the magnetic levitation without any compensation magnets frequently induce the precessional motion, which causes fluctuation of beam modulation frequency.

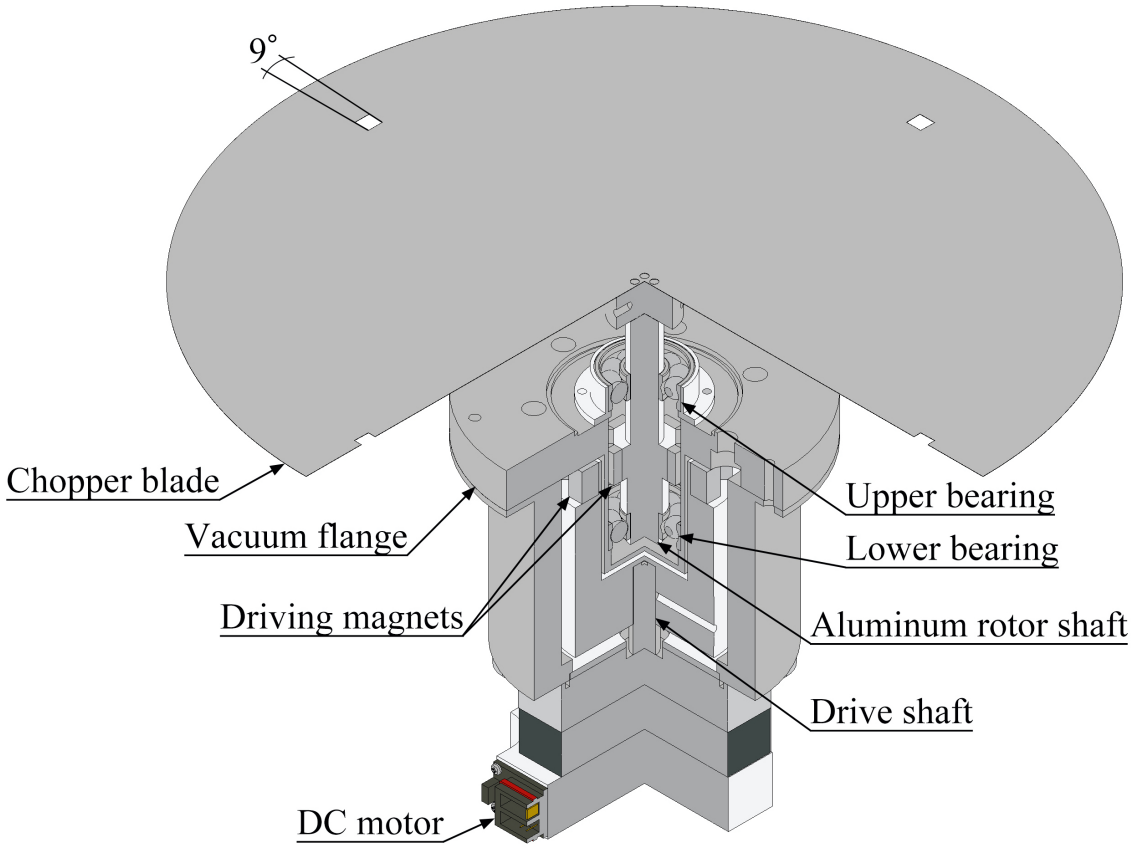

Fig. 4.12. A schematic diagram of the 2nd gen beam chopper.

In order to resolve these problems, the 2nd gen beam chopper shown in Fig. 4.12 was developed. The main change in the structure is adoption of double ball bearings (Koyo, SV6000ZZSTC3 YS) to realize stable rotation of an aluminum rotor shaft. The shaft with a 1.0 mm thickness aluminum blade can speed up the rotary motion up to 3,000 rpm by surrounding octupole driving magnets. Because the chopper blade has four 9° open windows, the positive pulse width is 500 μs, which is 50 times shorter than previous configuration.

4.3.2 Improvement in electron-impact ionizer

Figure 4.13 shows the sectional view of the 2nd gen EI type ionizer. The suspended tungsten filament frequently contacted to surrounding electrodes by deformation of the filament during the operation due to the electromagnetic force. The new ionizer fixed a 25 μm thickness 1.5 mm width circular tantalum ribbon tightly set around the ionization cage to avoid unintentional electrical short by contacting with the surrounding electrodes. A mesh wire made side wall of the electron repeller promotes evacuation of residual gases within the ionizer. Miniaturization of the ionization region involved shortening the total length from 80 mm to 55 mm. Figure 4.14 shows a circuit diagram of the 2nd gen ionizer. Thermionic electrons emitted from the heated tantalum ribbon with 55 eV energy ionizes atomic hydrogen during the orbital movement in the ionizer cavity. The ionization system is biased 600 V positively to give a potential to an ionized hydrogen ion. In this experiment, an emission current flowing into the ionization cage is limited to 1 mA to avoid production of arc plasma inside the cage. The ionized hydrogens are extracted with 600 V and go through an electrostatic lens. The collimated ion beams will enter the sector magnet region through a 3 mm beam collimation aperture. Power supplies used in the ionizer operation were Max-elec RHV-15K16P for V_{bias}, TEXIO PA600-0.1B for V_{dis}, KIKUSUI PAS60-6 for $V_{repeller}$, KIKUSUI PAK60-18A for V_{fil}, and Matsusada precision HWR-5N(A) for V_{tune}.

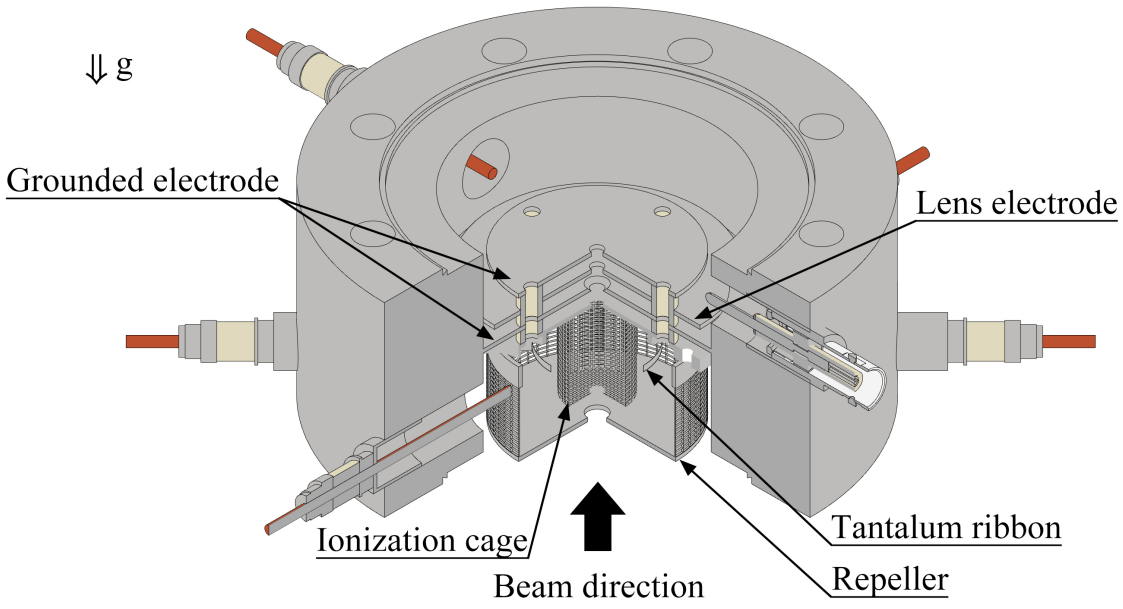

Fig. 4.13. A schematic diagram of the 2nd gen ionizer.

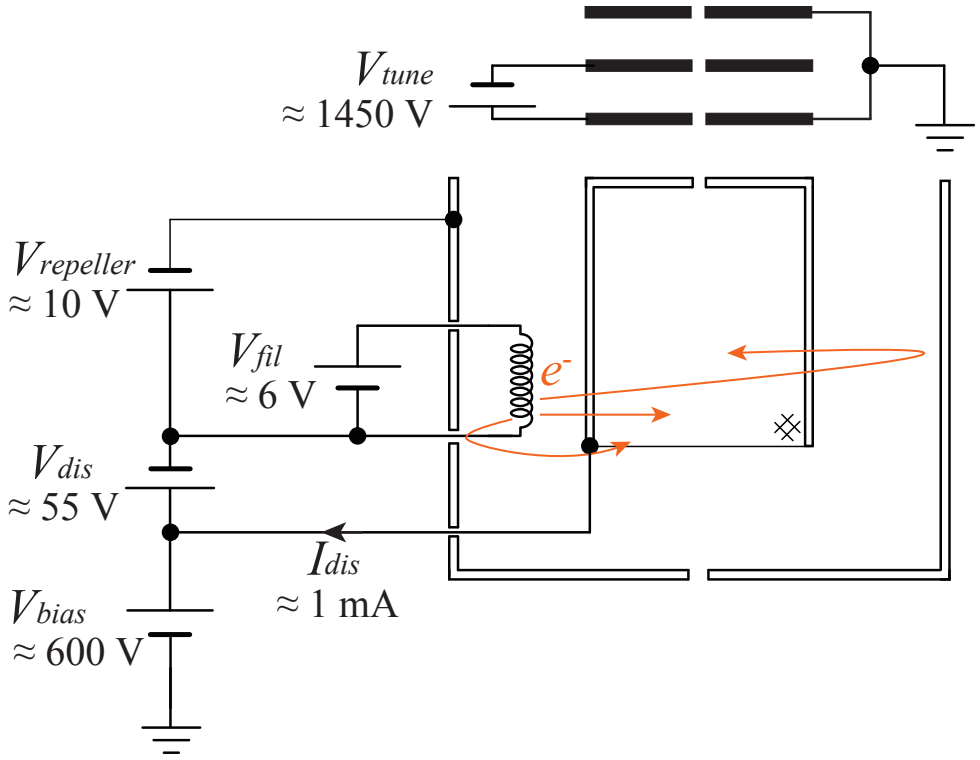

Fig. 4.14. A circuit diagram for the 2nd gen ionizer.

4.3.3 Vacuum system

Although the vacuum requirement for SEM operation is under the 1×10^{-4} Pa, the original vacuum system did not satisfy that requirement during the radical source operation. Thus, the vacuum system was amended in following ways.

The first chamber mounted on the stainless-steel ICF406 standard flange with the dimension of 345.5 mm inner diameter and 201.8 mm depth has three ICF70 standard flange ports on the bottom and two ICF203 and six ICF70 ports on the side of the chamber. In order to promote the evacuation speed against hydrogen, the first chamber has a 75 L/s diode ion pump (Varian, VacIon Plus 75) apart from the 520 L/s TMP2 (Pfeiffer vacuum, TMU521). An additional 210 L/s TMP2 (Pfeiffer vacuum, TMH261) was installed as a differential pumping system between the first chamber and atomic source to reduce the effusing hydrogen gas to the latter stage of the vacuum system.

In this experiment, the overall system is baked out at 260°C for 60 hours by outgassing the adsorbed water on the chamber wall as shown in Fig. 4.15. Even if the vacuum atmosphere is under 1×10^{-5} Pa, water and hydrogen are still present as dominant residual gases on the chamber and on filament surfaces. The difficulty of atomic hydrogen measurement comes from a large number of background H^0 noises due to thermally cracked residual water and hydrogen by a filament of the ionizer. Thus, a cooling shroud was installed in the experiment as shown in Fig. 4.16. The cooling shroud has a hollow structure and the

cavity is thermally isolated from the chamber wall. When the cavity is fully filled with liquid nitrogen, the cryogenic surface of the shroud works as a simple cryo pump to adsorb residual water molecules.

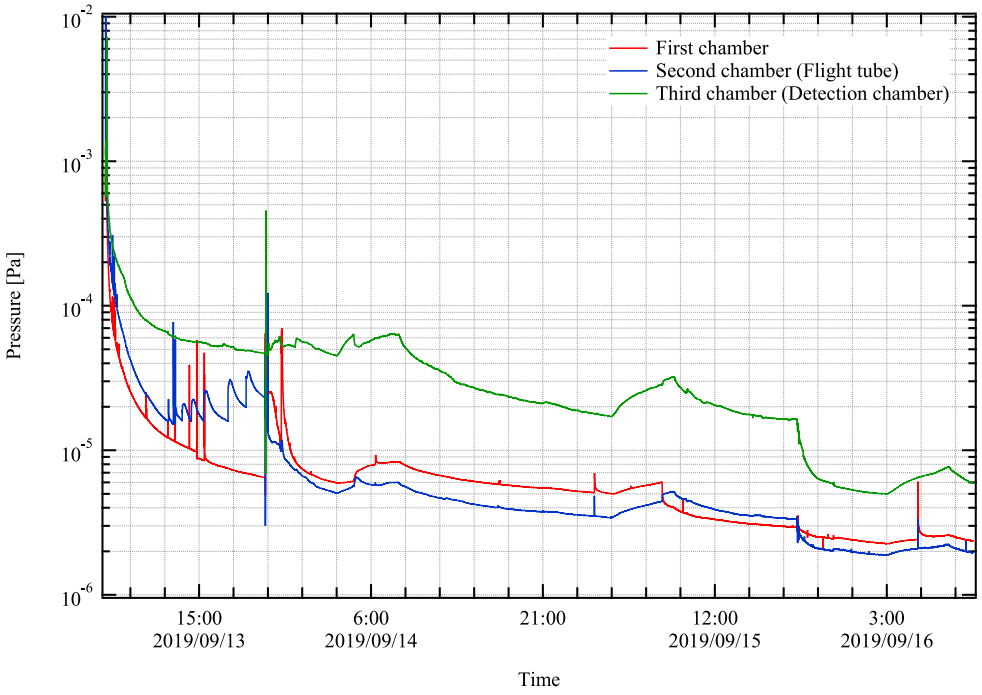

Fig. 4.15. A typical pumpdown curve for 78 hours evacuation.

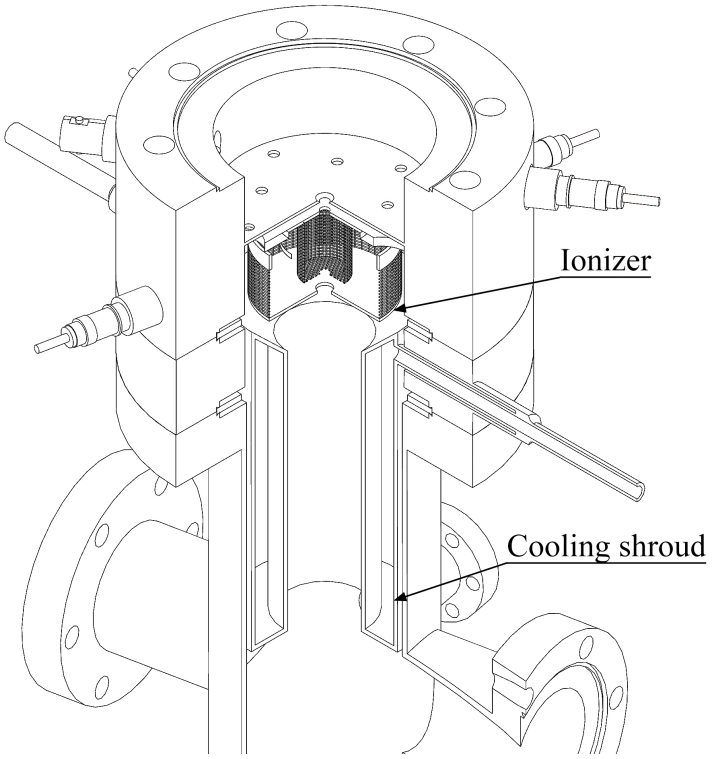

Fig. 4.16. A sectional drawing of the cooling shroud.

The second chamber of flight tube was pumped down by a 280 L/s TMP3 (Shimadzu corporation, TMP280-G) and the cooling shroud. In order to reduce the background signals due to the scattered molecules, two beam skimmers which have 2 mm and 3.5 mm apertures are installed at entrance of the first chamber and flight tube as shown in Fig. 4.11, respectively. The third chamber including SEM tube was pumped down by the 67 L/s TMP4 (Pfeiffer vacuum, Hi-Pace 80) as the original setup.

4.3.4 Change in secondary electron multiplier

The R2362 SEM (Hamamatsu photonics) has a gain of 1×10^6 at 2700 kV dynode voltage. However, the output pulse height from the R2362 is insufficient to measure the small H^0 signal. An off-axis type SEM as shown in Fig. 4.17 has much larger gain due to the high secondary electron emission ability on the conversion dynode and can eliminate noise signals such as neutral particle, X-ray, and UV light unlike the ordinary SEM tube. Figure 4.18 shows the off-axis type SEM tube (ETP, AF627) installed on the third chamber with 5 mm entrance aperture. Figure 4.19 shows the typical current measured by both SEM R2362 and AF627. According to the figure, the off-axis type SEM has a gain of 5 orders of magnitude higher than ordinary SEM tube.

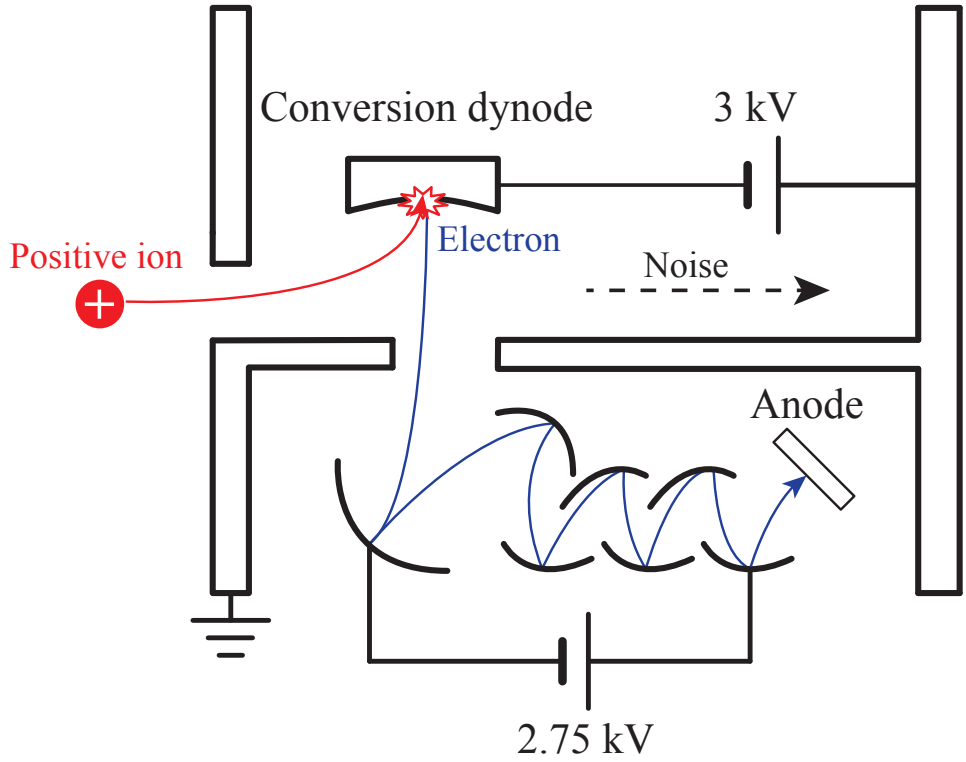

Fig. 4.17. A principal mechanism of the off-axis type secondary electron multiplier tube.

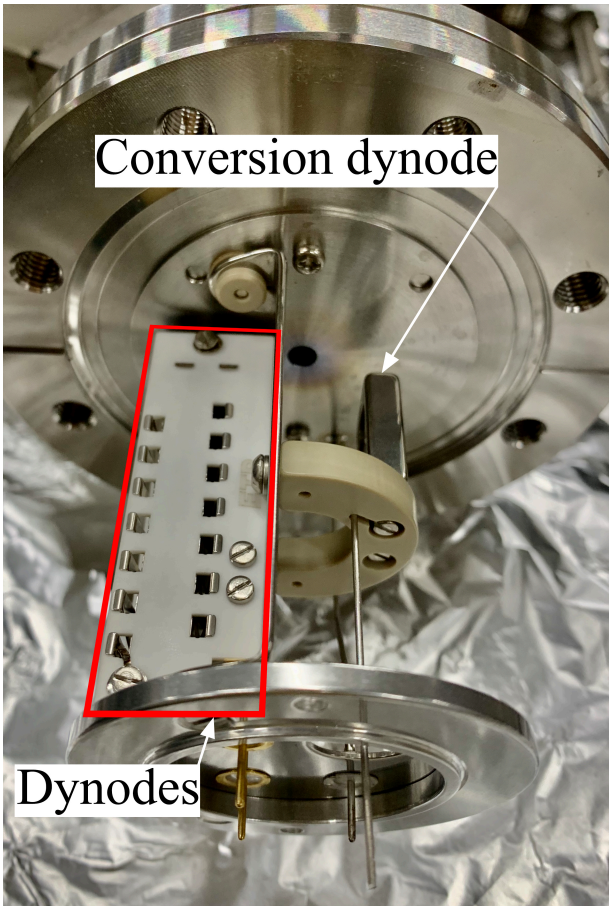

Fig. 4.18. A photograph of the SEM tube installed on the flange. The diameter of the entrance aperture is 5 mm.

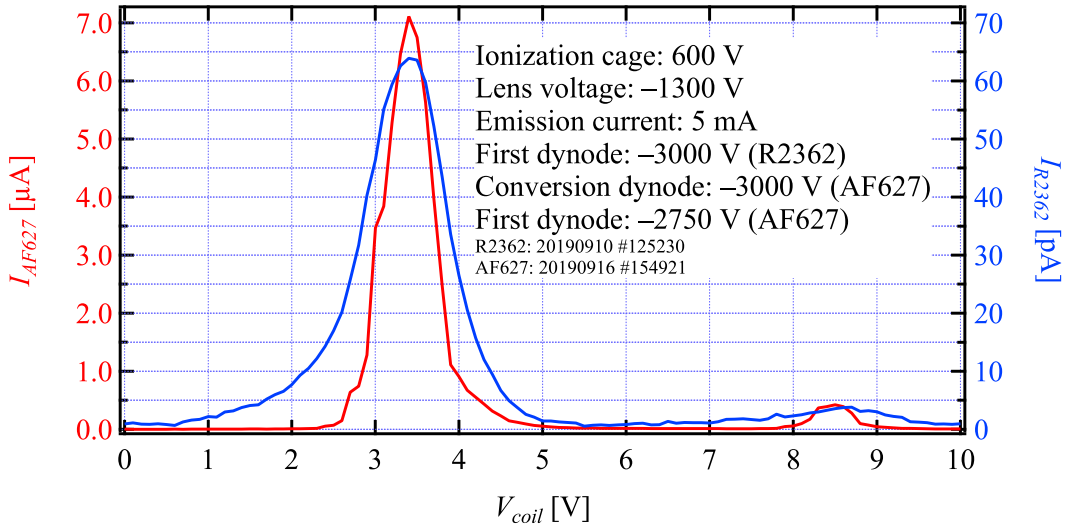

Fig. 4.19. Typical SEM current curves for both R2362 and AF627 multiplier tubes.

4.4 Experimental

The developed experimental system can be operated in two ways: current (DC) mode and pulse mode. Figure 4.20 schematically shows the electric circuit for two measurement modes. Firstly, the current mode system selects the detected ion species and optimize the beam optics for the specific ion. Then, the pulse mode system measures the velocity distribution function of the neutral particles.

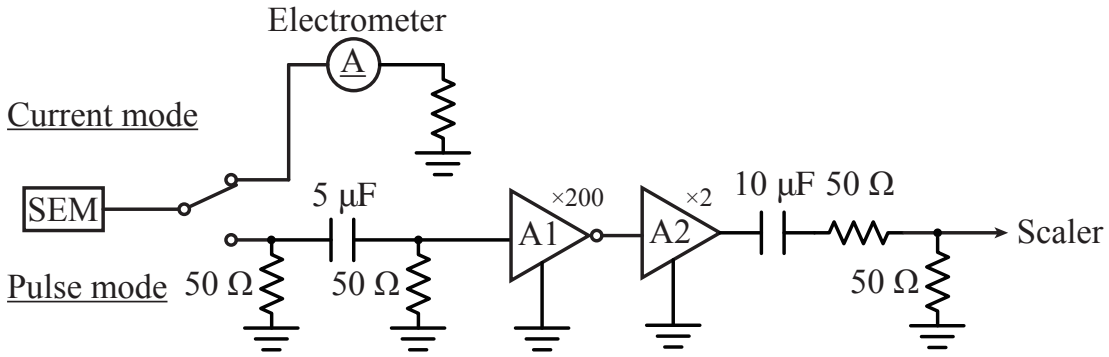

Fig. 4.20. Electric circuit for atomic current meausrement in two modes.

4.4.1 Current mode measurement

In order to select only the proton signal originated from the injected atomic hydrogen, the current mode scan was carried out before each measurement. The output signal from the SEM tube during the DC atom injection to the ionizer flows into the system electrometer (Keithley, 6514) as a current signal. A negative high voltage power source (Kyoto Denkiki, DC5000 V 5 mA) supplies −5 kV to the conversion dynode and a negative high voltage module (Matsusada, HWR-5N) driven by regulated DC power source (YOKOGAWA, GS200) supplies −2.75 kV to the first dynode. A bipolar DC power source (YOKOGAWA, GS610) sweeps the voltage from −15 to 15 V to scan the ion species passing through the sector magnet. The integration time at each voltage was set to 16.67 ms (1 Number of Power Line Cycles). Figure 4.21 shows the typical mass spectrum for 600 eV ion species in the DC mode operation with 1sccm hydrogen injection. Even if the base pressure of the detection chamber is under the 1.2×10^{-6} Pa with cooling shroud, there are substantial amount of residual hydrogens in the vacuum system. The DC mode measurement could not detect the small amount of change in H^+ signal by pulsed atomic beam injection. Therefore, the following pulse mode measurement was carried out to detect a small change in the proton signal.

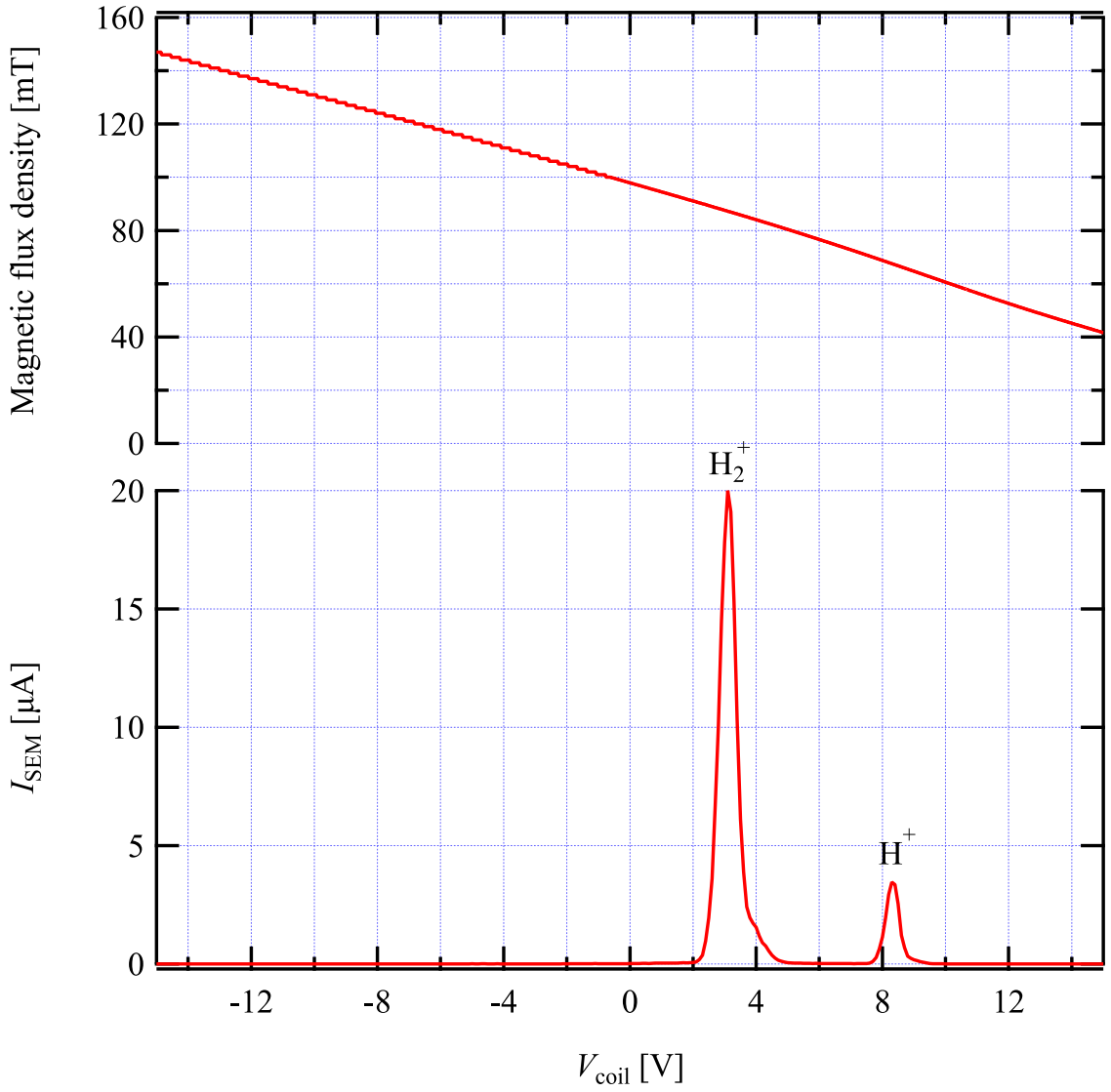

Fig. 4.21. Typical mass spectrum of SEM current for 600 eV H^+ and H_2^+ signals of 1 mA emission current.

4.4.2 Pulse mode measurement

Figure 4.22 schematically illustrates the circuit diagram of the pulse counting system. The pulsed secondary electron signal is amplified by inverting pre-amplifier (NF Corporation, SA-230F5) with the gain of 46 dB as shown in Fig. 4.20. A multi-channel scaler (Stanford Research Systems, SR430) counts the number of events of the input signal synchronized with the trigger signal. In order to supply the trigger signal for pulse counting method, the aluminum blade chops the neutral beam every 5.0 ms in a 10% duty cycle. The number of atoms passing through the chopper window is not a constant as time evolution. That variation scales proportionally with the overlap sections between the chopper window and beam aperture. Here, following the Alcalay's method, a shutter function, $S(t)$, is

represented as trapezoid function as shown in Fig. 4.23 [10].

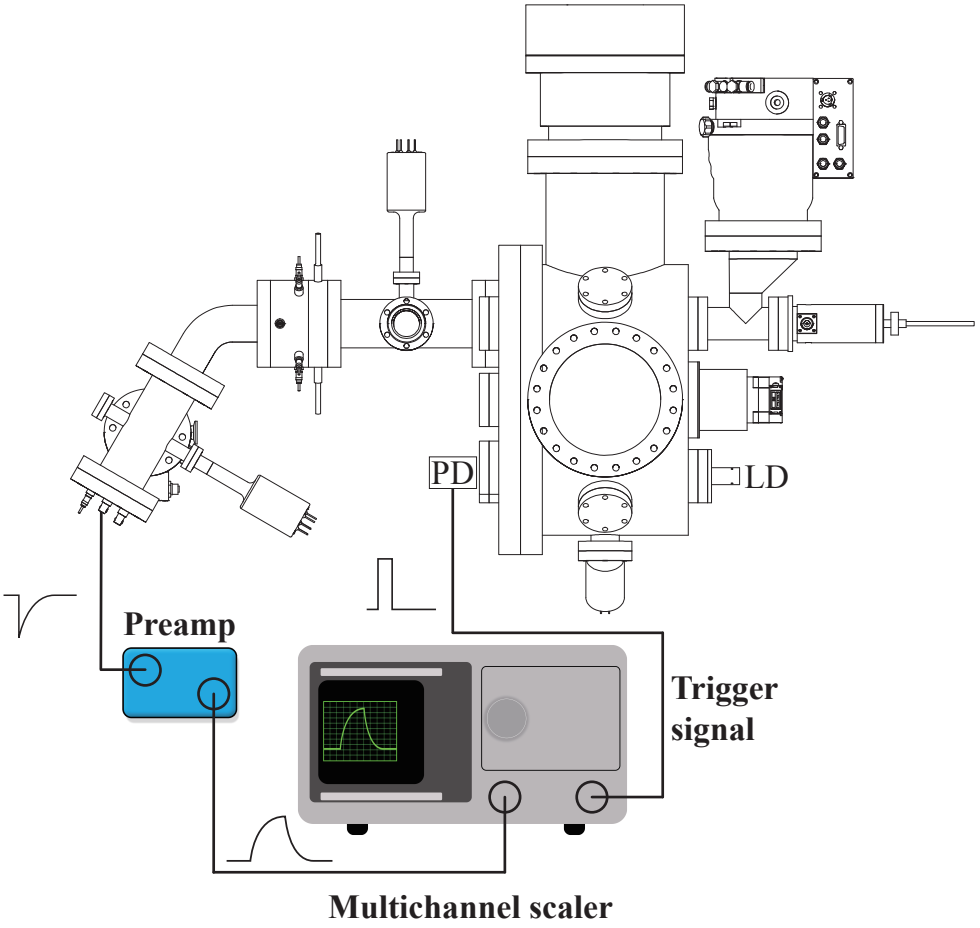

Fig. 4.22. A circuit diagram of the velocity function measurement system.

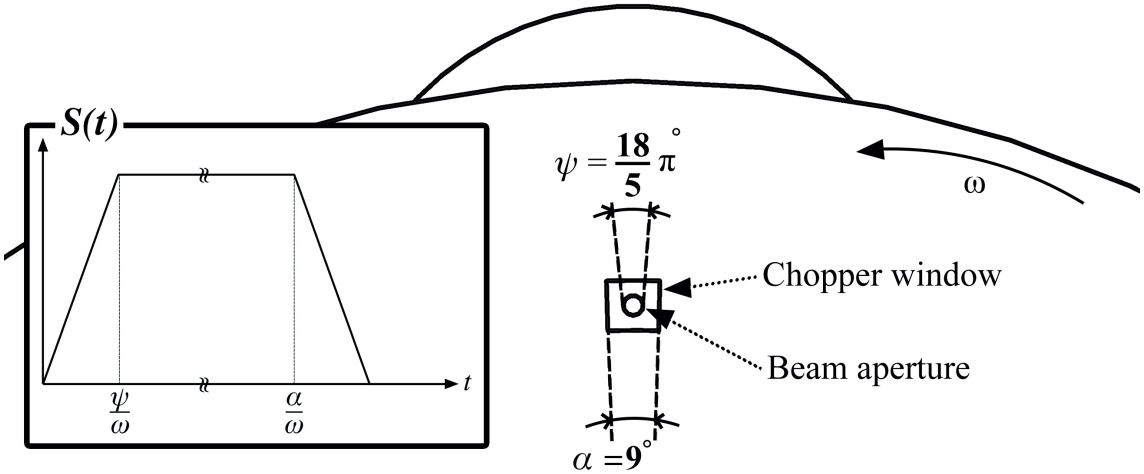

Fig. 4.23. A schematic of the shutter function, $S(t)$, and the geometry for the chopper blade and beam aperture.

The measured signal by the multi-channel scaler, $I(t,T)$, is given by

$$I(t,T) = \int \eta(v) f(v,T) S\left(t - \frac{L}{v}\right) dv \tag{4.6}$$

where $\eta(v)$ is the ionization efficiency that is proportional to the time to pass through the ionizer $d_{ionizer}/v$, $f(v,T)$ is the velocity distribution function assumed to be a Maxwellian, and L is the distance from the chopper to the ionizer. Here χ^2 are defined as

$$\chi^2 = \sum_i \left\{ I_{calc}(t,T) - I_i(t) \right\}^2 \tag{4.7}$$

where $I_{calc}(t,T)$ are the calculated values, $I_i(t)$ are the experimental data sets. The atomic temperature T is found by minimizing the χ^2 value of the $I_{calc}(t,T)$. Data acquisition and control of the scaler were operated on the real-time control software developed for windows® PC as shown in Fig. 4.24. Calculation of velocity distribution function was also calculated on the developed software as shown in Fig. 4.25.

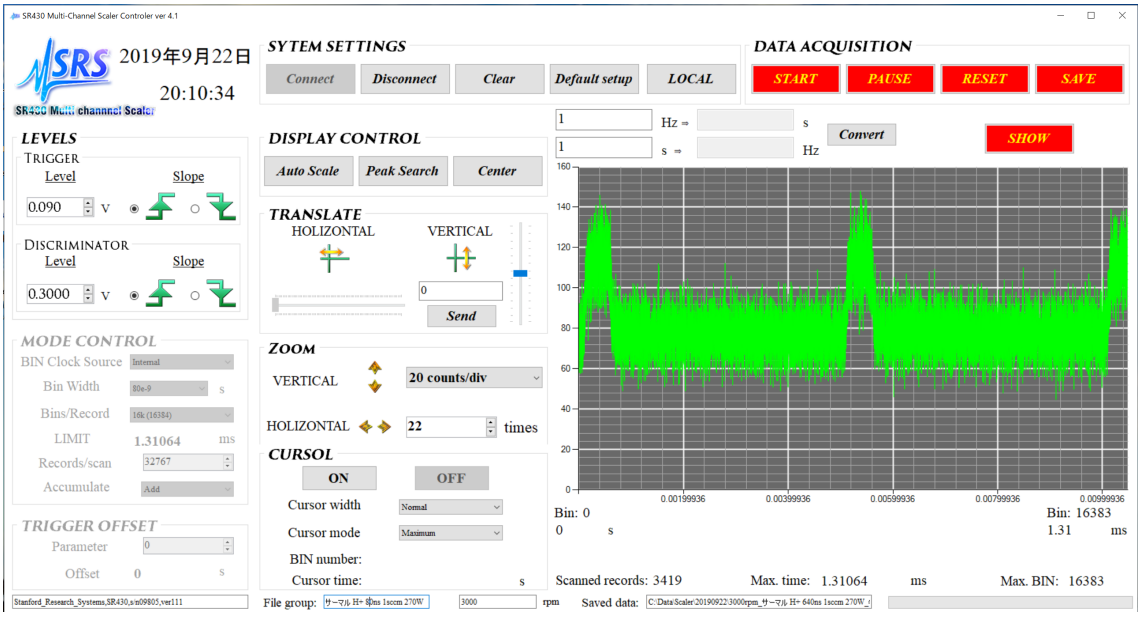

Fig. 4.24. An example of data acquisition by multi-channel scaler.

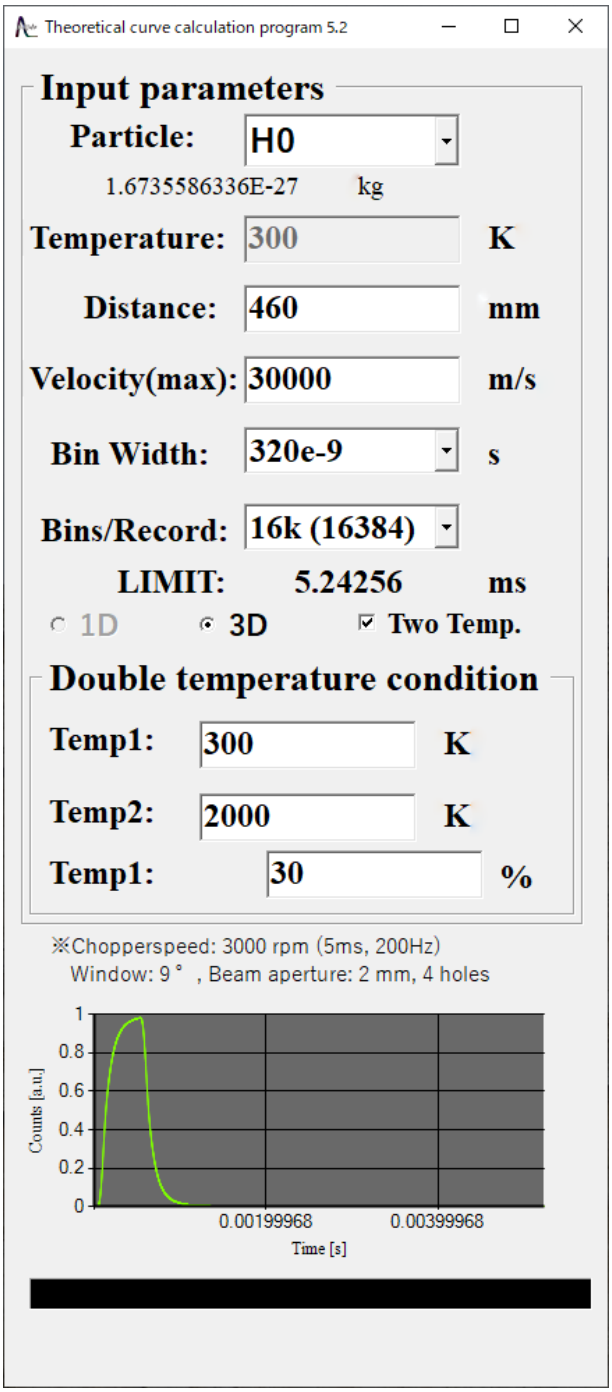

Fig. 4.25. An example of calculation of velocity distribution function assumed to be a Maxwellian.

4.5 Results and Discussion

Experiments were done under the 3 sccm gas injection to keep sufficient S/N ratio for analyzing signals; only the 2nd gen LICP and thermal cracking sources had shown clear velocity distributions.

Figure 4.26 shows the raw data of the experimental result of the velocity distribution function measurement for atomic hydrogen. The spectrum was taken by the 32767 events accumulation of atomic hydrogen signals produced by the 2nd gen hydrogen LICP operated with 23 W and 1sccm hydrogen gas flow.

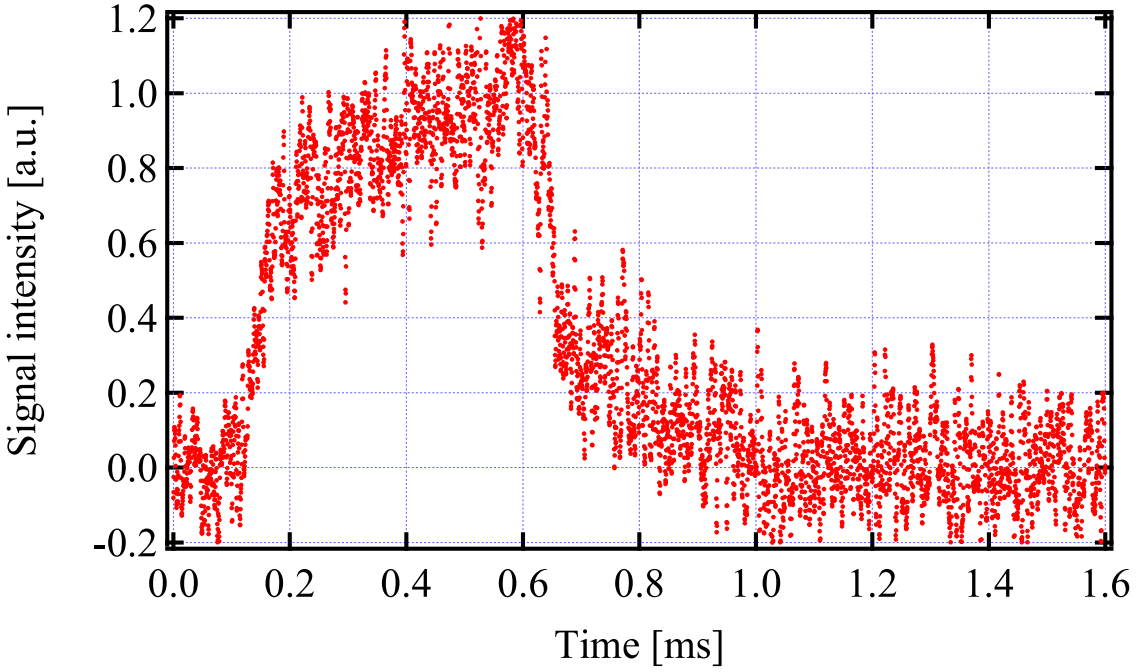

Fig. 4.26. An experimental result of velocity distribution meausrement of atomic hydrogen produced in the 23 W 2nd gen LICP with 1 sccm hydrogen injection.

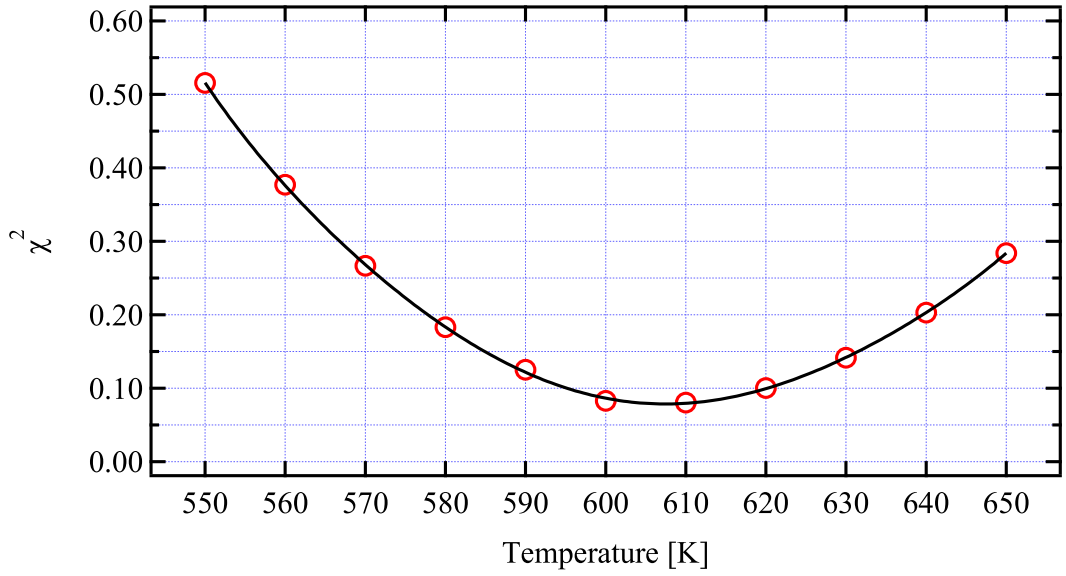

Fig. 4.27. An example of χ^2 test result for 23 W 2nd gen hydrogen LICP.

In order to determine the temperature of atomic hydrogen detected at the SEM tube, calculated curves for atomic hydrogen were calculated from 300 K to 2000 K with the 10 K steps. Then, experimental curves after removing fluctuation component by a binomial smoothing filter are compared with the data sets of theoretical curves by the χ^2 test. According to the result of χ^2 test as shown in Fig. 4.27, the atomic hydrogen temperature of 2nd gen hydrogen LICP at 23 W power was determined to be 607 K. Figure 4.28 shows the measured and calculated curves of velocity distribution functions for atomic hydrogen produced in the 2nd gen hydrogen LICP of 23 W power input. The results of the experiment gave good agreement with calculated curves of 607 K. Table 4.2 shows the summary of calculated atomic hydrogen temperature following the procedure discussed above. The temperatures of atomic hydrogen produced in the 3 sccm plasma were lower than that of 1 sccm plasma, since the higher gas flow rate induced the collisional cooling to neutrals due to the higher particle densities. In contrast, the temperature of atomic hydrogen produced in the W-mode 2nd gen hydrogen LICP did not have significant dependence upon the input microwave power. Thus, the atomic temperature in the LICP type plasma source appears independent upon the input power, but may depend upon the discharge mechanism.

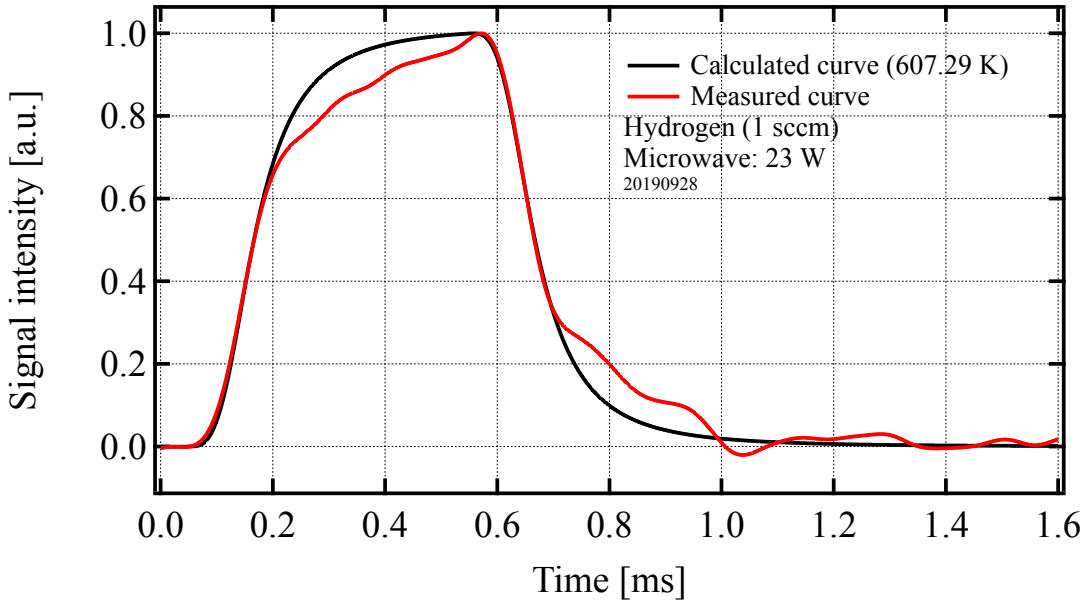

Fig. 4.28. The measured and calculated curves of velocity distribution functions for atomic hydrogen produced in the 2nd gen hydrogen LICP at 23 W power input.

Table 4.2. Temperatures of atomic hydrogen produced in the 2nd gen hydrogen LICP for 1 sccm and 3 sccm hydrogen flow rate.

Power [W]	1 sccm [K]	3 sccm [K]
23	607.29	610.30
30	624.87	609.33
40	614.82	611.31
50	626.38	604.77

The velocity distribution of atomic hydrogen produced in the 2nd gen LICP source obeyed the Maxwellian characterized by a temperature, whereas that of thermal cracking source did not agree with the Maxwellian curve. The 1 mm inner diameter and 1.8 mm outer diameter tungsten capillary are heated by a tungsten filament wound around it with 2.5 mm inner diameter in the thermal cracking source. As discussed in the section 2.2.1, thermally cracked atomic hydrogen can be produced inside the tungsten capillary as well as the surface of high temperature filament. The hydrogen atoms produced at both capillary and filament may have passed through the 2 mm inner diameter beam skimmer. Thus, calculated curves which are calculated from sums of two different temperature velocity distributions are calculated from 300 K to 2000 K with the 50 K step temperature and 10% partial step temperature on the assumption that the produced atomic hydrogen had two representative temperatures. Figure 4.29 shows the measured and calculated curves of velocity distribution functions for atomic hydrogen produced in the 220 W thermal cracking cell. The calculated value which is the sum of 600 K and 1650 K at a ratio three to seven yielded the good agreement to the experimental value. Table 4.3 shows the result of atomic hydrogen temperatures produced in the thermal cracking source.

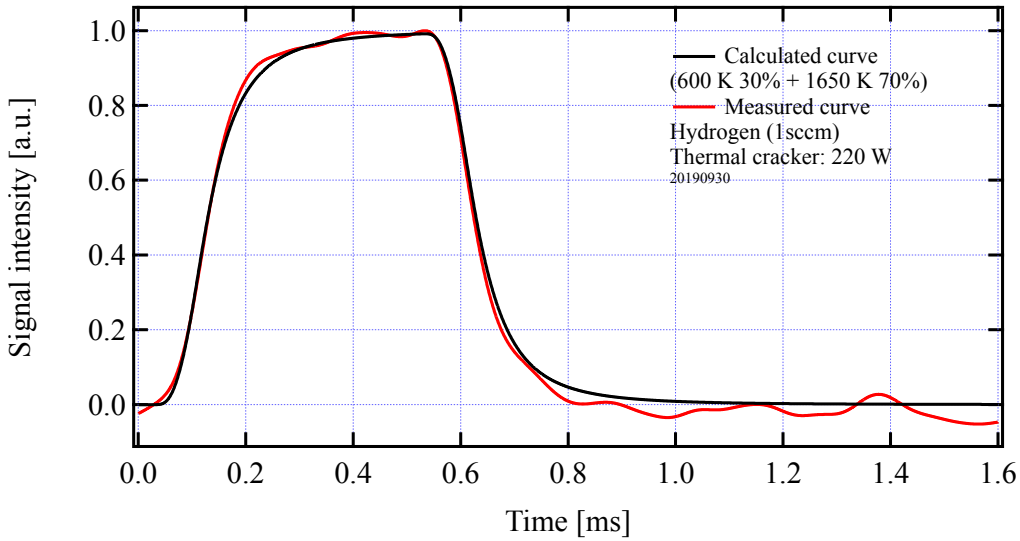

Fig. 4.29. The measured and calculated curves of velocity distribution functions for atomic hydrogen produced in the 220 W thermal cracking cell.

Table 4.3. Temperatures of atomic hydrogen produced in the thermal cracking source for 1 sccm hydrogen flow rate.

Power [W]	Temperature 1 [K]	Temperature 2 [K]	Ratio
140	400	500	1:9
160	400	600	1:9
180	500	1200	3:7
200	500	1550	2:8
220	600	1650	3:7
240	600	1700	3:7
260	600	1750	2:8

The 3rd gen CCP source requires higher gas pressure to ignite and sustain plasma plume compared with the LICP source. In order to enhance the hydrogen pumping speed at the flight tube, the ion pump was installed at not the first chamber but the flight tube. The acquired pulse signals originated from the 3rd gen CCP source were accumulated for 65536 events by the multi-channel scaler due to its poor S/N ratio. Figure 4.30 shows the measured and calculated curves of velocity distribution functions for atomic hydrogen produced in the 3rd gen CCP source. The experimental conditions to sustain a stable operation limited the hydrogen gas flow rate and power input to 60 sccm and 40 W, respectively. For 40 W microwave power, the atomic temperature was fitted to 872 K of Maxwellian. Table 4.4 shows the calculated results of χ^2 test for 3rd gen hydrogen CCP.

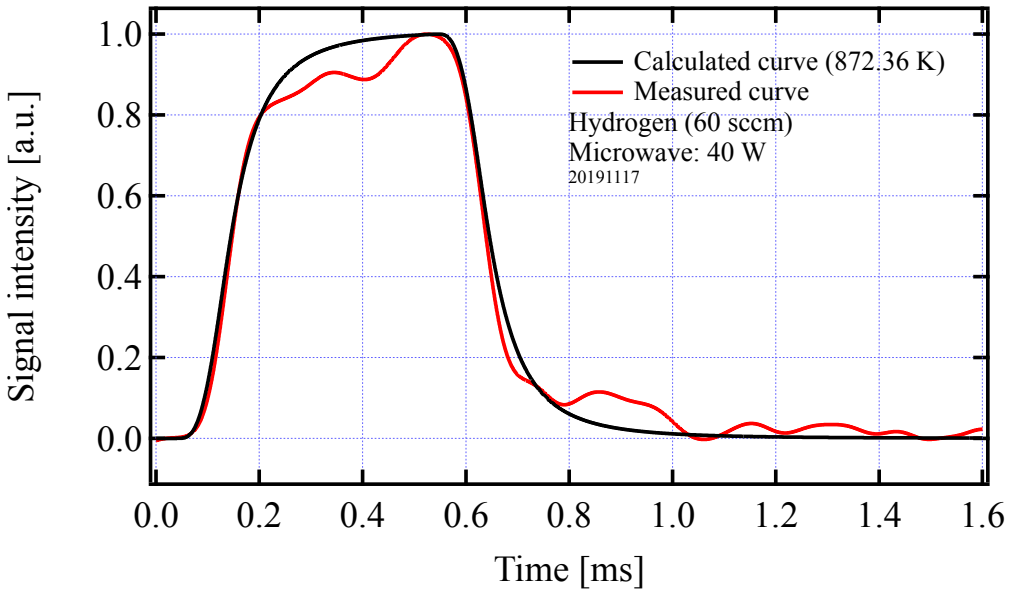

Fig. 4.30. The measured and calculated curves of velocity distribution functions for atomic hydrogen produced in the 40 W 3rd gen hydrogen CCP.

Table 4.4. Temperatures of atomic hydrogen produced in the 3rd gen hydrogen CCP for 60 sccm hydrogen flow rate.

Power [W]	Temperature [K]
40	872.36
50	930.40
60	1027.1
70	1020.1

4.6 Conclusion

In this chapter, temperatures of atomic hydrogen produced in three types of radical beam sources are investigated with the dedicatedly developed MSTOF-type velocity distribution function measurement system. The pulse counting methods clarified the velocity distribution function depending upon the atomic temperature for 2nd gen LICP source, 3rd gen CCP source, and thermal cracking source developed in the previous chapters. Microwave excited LICP and CCP exhibited single temperatures. In contrast, hydrogen atoms formed in the thermal cracking source have two representative temperatures attributable to the tungsten filament and capillary temperatures. In order to measure the poor atomic hydrogen signal, the vacuum pressure inside the first chamber must be kept below 6×10^{-5} Pa during the operation because the developed velocity measurement system is sensitive to the background particle noises due to the residual gases including hydrogen component. Although the 3rd gen CCP source developed in Chapter 3 required very high gas pressure at the source tip to ignite and sustain the plasma plume, the measured atomic temperatures were higher than those of the LICP source.

References

[1] K. Kitatani, "Measurement of velocity distributions of neutral particles in ion source plasmas", Master's thesis, February 2002.

[2] G. Comsa, R. David, and B. J. Schumacher, "Magnetically suspended crosscorrelation chopper in molecular beam surface experiments", *Rev. Sci. Instrum.* **52(6)**, 789 1981.

[3] K. Kitatani, T. Kasuya, T. Nakayama, K. Yamamoto, and M. Wada, "Measurement of velocity distribution functions of neutral particles in ion source plasma", *Rev. Sci. Instrum.* **73(2)**, 958 2002.

[4] W. Christen, "Ultra-precise particle velocities in pulsed supersonic beams", *J. Chem. Phys.* **139(2)**, 024202 2013.

[5] M. M. Wolff and W. E. Stephens, "A Pulsed Mass Spectrometer with Time Dispersion", *Rev. Sci. Instrum.* **24(8)**, 616 1953.

[6] W. Hu, D. Fang, Y. Wang, and F. Yang, "Electron-impact-ionization cross section for the hydrogen atom", *Phys. Rev. A* **49(2)**, 989 1993.

[7] Yong-Ki Kim and M. E. Rudd, "Binary-encounter-dipole model for electron-impact ionization", *Phys. Rev. A* **50(5)**, 3954 1994.

[8] R. K. Janev, D. Reiter, and U. Samm, *Collision Processes in Low-Temperature Hydrogen Plasmas* (Forschungszentrum Zentralbibliothek, Julich, 2003).

[9] T. Hakamata, H. Kume, K. Okano, K. Tomiyama, A. Kamiya, Y. Yoshizawa, H. Matsui, I. Otsu, T. Tagushi, Y. Kawai, H. Yamaguchi, K. Suzuki, S. Suzuki, T. Morita, and D. Uchizono, *PHOTOMULTIPLIER TUBES -Basics and Applications-* (Hamamatsu Photonics K. K., Shizuoka, 2007).

[10] J. A. Alcalay and E. L. Knuth, "Molecular-Beam Time-of-Flight Spectroscopy", *Rev. Sci. Instrum.* **40(3)**, 438 1969.

Chapter 5

Enhancing Mass Spectrometric Analyses Versatility with Radical Induced Dissociation

5.1 Mass spectrometer

5.1.1 Matrix assisted laser desorption/ionization

Mass spectrometric research under vacuum condition now plays an important role to detect diseases for our healthcare in accordance with the progress of life science. During the 1960's, the further improvements in mass spectrometric instruments and ionization techniques were required to expand the application in the field of the synthetic chemistry to modern sciences which utilize more complex molecules such as biochemical, molecular biology, and life science. Conventional ionization techniques such as EI (Electron-impact Ionization) and CI (Chemical Ionization) often thermally resolve and desorb a measurement sample. In order to ionize a low-volatile organic compounds including peptide, soft ionization methods are being developed.

A MALDI (Matrix Assisted Laser Desorption/Ionization) method is one of the most popular soft ionization techniques to ionize large biomolecules under the vacuum condition [1]. Figure 5.1 schematically illustrates the principle of the MALDI. A pulsed nitrogen laser (wavelength = 337 nm, 3.72 eV) immediately ionizes a mixture of sample and matrix into the gas phase with a large amount of energy absorption. The chemical

formula of the reaction process from a sample M to protonated ion $[M + H]^+$ is given as

$$m + m + nh\nu \rightarrow [m + H]^+ + [m - H]^- \tag{5.1}$$

$$M + [m + H]^+ \rightarrow [M + H]^+ + m \tag{5.2}$$

$$M + m + nh\nu \rightarrow [M + H]^+ + [m - H]^- \tag{5.3}$$

where m is a matrix.

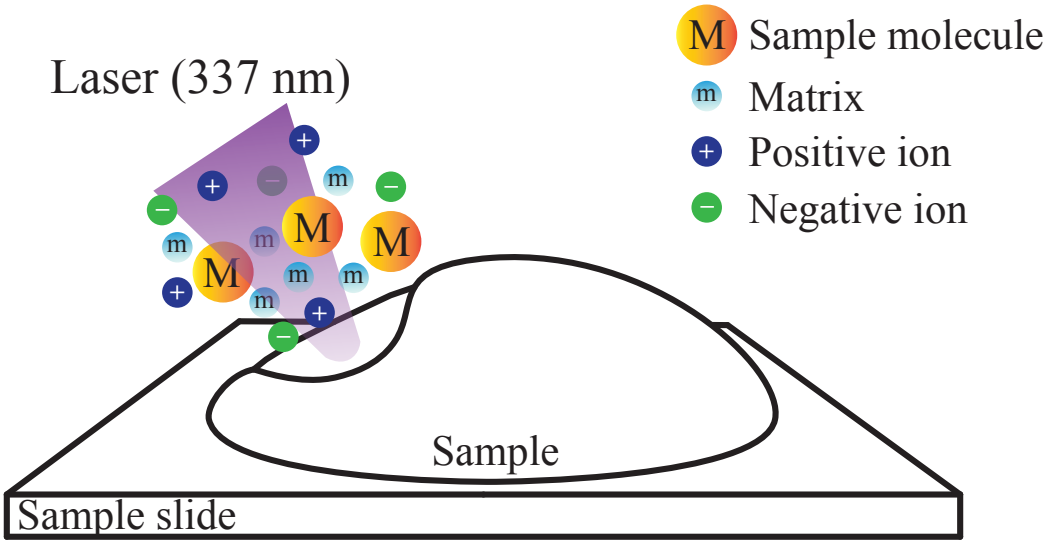

Fig. 5.1. The mechanism of the MALDI (Matrix-Assisted Laser Desorption/Ionization).

5.1.2 Quadrupole ion trap

An ion trap mass spectrometer is classified into two groups: high frequency electric field driven Paul trap and high frequency magnetic field driven Penning trap [2, 3]. In general, QIT (Quadrupole Ion Trap) stands for the Paul trap. The QIT is composed of a toroidal shaped ring electrode and two end cap electrodes at the entrance and exit of the ion trap. These electrodes are rotationally symmetric with respect to the z axis forming a hyperboloid in the cross section expanded by a following equation.

$$\pm \frac{r^2}{r_0^2} \mp \frac{z^2}{z_0^2} = 1 \tag{5.4}$$

where r_0 is the minimum radius of the ring electrode and z_0 is the minimum distance between the center and the end cap electrode. The following shown the relationship between the r_0 and z_0.

$$2z_0^2 = r_0^2 \tag{5.5}$$

If a high voltage RF (Radio Frequency) represented by a superposition of DC high voltage U and RF voltage $V\cos\omega t$ is applied to the end cap and ring electrodes, the electric

potential ϕ in the ion trap is given by

$$\phi = \frac{(U + V\cos\omega t)}{r_0^2}(r^2 - 2z^2) \tag{5.6}$$

Thus, the ion equations of motion on the r and z axes are obtained by using mass m and electric charge $q = Z \times e$.

$$\frac{d^2z}{dt^2} - \frac{2q}{mr_0^2}(U + V\cos\omega t)z = 0 \tag{5.7}$$

$$\frac{d^2r}{dt^2} - \frac{q}{mr_0^2}(U + V\cos\omega t)r = 0 \tag{5.8}$$

Here, variables a, q, and ζ are defined.

$$a_z = -2a_r = -\frac{8qU}{mr_0^2\omega^2} \tag{5.9}$$

$$q_z = -2q_r = \frac{4qV}{mr_0^2\omega^2} \tag{5.10}$$

$$\zeta = \frac{\omega t}{2} \tag{5.11}$$

Equations 5.7 and 5.8 are converted using a, q, and ζ as

$$\frac{d^2r}{d\zeta^2} + (a_r + 2q_r\cos 2\zeta)r = 0 \tag{5.12}$$

$$\frac{d^2z}{d\zeta^2} + (a_z + 2q_z\cos 2\zeta)z = 0 \tag{5.13}$$

The set of equations expressing the vibratory motion is called Mathieu's equation [4, 5]. The solution of the Mathieu's equation has been well studied as shown in Fig. 5.3. The equation has stable solution when the parameters a and q are in the shaded area.

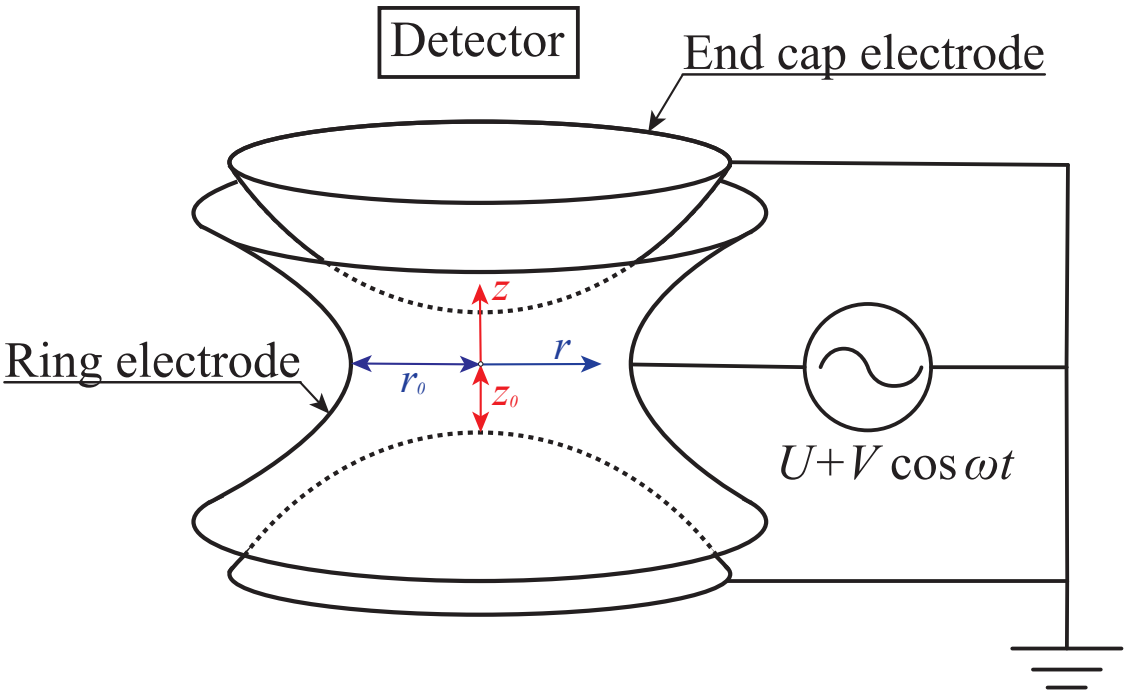

Fig. 5.2. A schematic drawing of the quadrupole ion trap mass spectrometer.

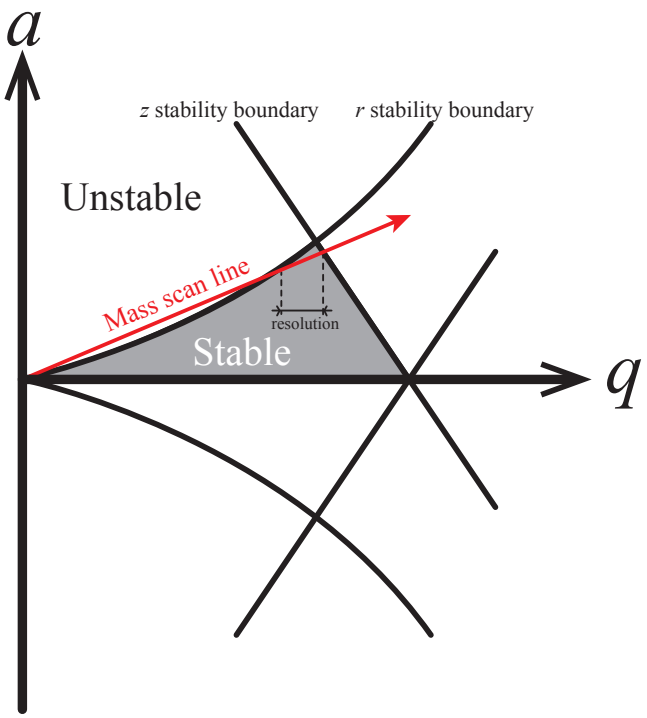

Fig. 5.3. The a-q stability diagram. The shaded area represents those areas in a-q space which correspond to stable solutions of Mathieu's differential equation [4].

5.2 Fragmentation study in mass spectrometry

5.2.1 Electron based fragmentation techniques

The electron based fragmentation techniques, ECD (Electron Capture Dissociation) and ETD (Electron Transfer Dissociation), have been widely utilized to clarify the peptide sequence including PTMs (Post-Translational Modification) in tandem mass spectrometers [6, 7, 8]. These reaction formulas are shown in Table 5.1. However, the use of electrons limit the analyzable targets of multiply positively charged ions for both ECD and ETD.

Table 5.1. A table of reactions utilized in PTM analyses (n $\geqq$ 2).

Reactions	Formulas
ECD [6, 7]	$[M + H]^{n+} + e^{-}(\approx 0.2\,eV) \rightarrow [M + H]^{(n-1)+\bullet}$
ETD [8]	$[M + H]^{n+} + A^{-\bullet} \rightarrow [M + H]^{(n-1)+\bullet} + A$
NETD (Negative ETD) [9]	$[M - H]^{n-} + C^{+\bullet} \rightarrow [M + H]^{(n-1)-\bullet} + C$

5.2.2 Hydrogen attachment/abstraction dissociation (HAD)

Conventional electron based techniques are difficult in clarifying the biomolecular structure of singly charged ions and negative ions. In order to expand the types of analyzable targets, HAD (Hydrogen Attachment/Abstraction Dissociation) method was proposed [10]. Although several prior studies concluded that the atomic hydrogen does not work as a trigger of the peptide fragmentation [11, 12, 13, 14], HAD experiment showed distinct fragmentations. Unlike the ECD and ETD, HAD utilizes electrically neutral atomic hydrogen (H•) to induce chemical fragmentations of biomolecules because neutral particles do not change the charge state of the analyte ions. The HAD method has two reaction channels as shown in Table 5.2.

Table 5.2. A table of HAD reaction channels.

Reactions	Formulas
H attachment	$[M + H]^{+} + H\bullet \rightarrow [M + 2H]^{+\bullet}$
H abstraction	$[M + H]^{+} + H\bullet \rightarrow [M]^{+\bullet} + H_2$

Figure 5.4 shows the schematic diagram of the original HAD experimental setup. All mass analyses in this study were performed on the prototype MALDI-QIT-TOF tandem mass spectrometer based upon the design of the AXIMA Resonance (Shimadzu/Kratos). A thermal cracking type hydrogen radical source is directly mounted outside of the ring electrode of the QIT chamber. The ring electrode of the QIT chamber has two 1.5 mm

diameter holes for injecting radicals from the source. A nitrogen laser (wavelength = 337 nm) ionizes a target material by MALDI system [1, 15, 16]. The ionized target passes through the end cap electrode and is trapped in the QIT chamber. Helium gas cools the trapped ions, while argon gas induces conventional CID (Collision Induced Dissociation). The reaction time between injected radical and target ions is set from 0.5 to 30 s. The pressure inside the QIT chamber is maintained below 5×10^{-4} Pa before the radical injection. Digital asymmetric wave isolation (DAWI) confines the precursor ions in the QIT, and a time-of-flight (TOF) mass spectrum of the detected fragment ions is recorded with 10 kV accelerating voltage in the reflectron mode [17]. Mass spectra were acquired by averaging 50-100 single shots.

Sample solution was dissolved in 30% acetonitrile (ACN) / 0.1% aqueous trifluoroacetic acid (TFA) (v/v). α-Cyano-4-hydroxycinnamic acid (CHCA) matrix was dissolved at a concentration of 10 mg/mL in 50% ACN/0.1% aqueous TFA (v/v). Peptide standards, fullerene C_{60} powder and MALDI matrix were purchased from Sigma-Aldrich (St. Louis, MO), Ana Spec Inc. (San Jose, CA, USA) and Peptide Institute (Osaka, Japan). Sample solution (0.5 μL) and matrix solution (0.5 μL) were mixed on a MALDI sample target well. Powdery C_{60} was dissolved in 100% toluene, and the solution (1 μL) was spotted on the MALDI sample target well.

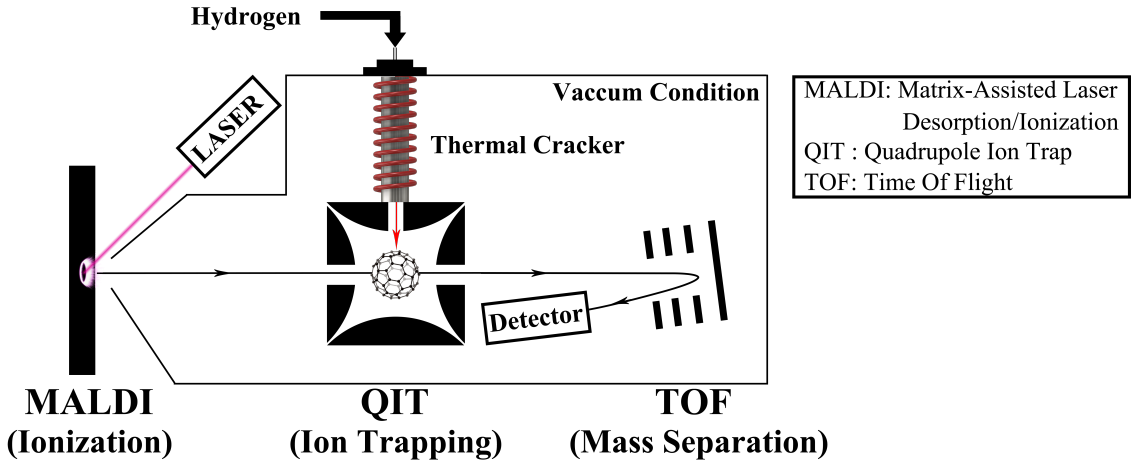

Fig. 5.4. A schematic diagram of the original HAD experimental setup. The MALDI-QIT-TOF tandem mass spectrometer has 1.5 mm diameter hole in the ring electrode to introduce atomic hydrogen to QIT chamber. The original setup utilize the thermal cracker cell as an atomic hydrogen source.

5.2.3 Radical attachment reaction to C_{60} ion

Following Demirev's experiment of hydrogen radical production in Fourier transform ion cyclotron resonance (FT-ICR) [11], relative H radical density inside the ion trap was

estimated by observing H radical attachment to fullerene ions. Figure 5.5 shows the experimental setup of the HAD experiment with the microwave driven radical source. The developed radical sources are mounted on the QIT chamber via ISO100-ICF70 adaptor.

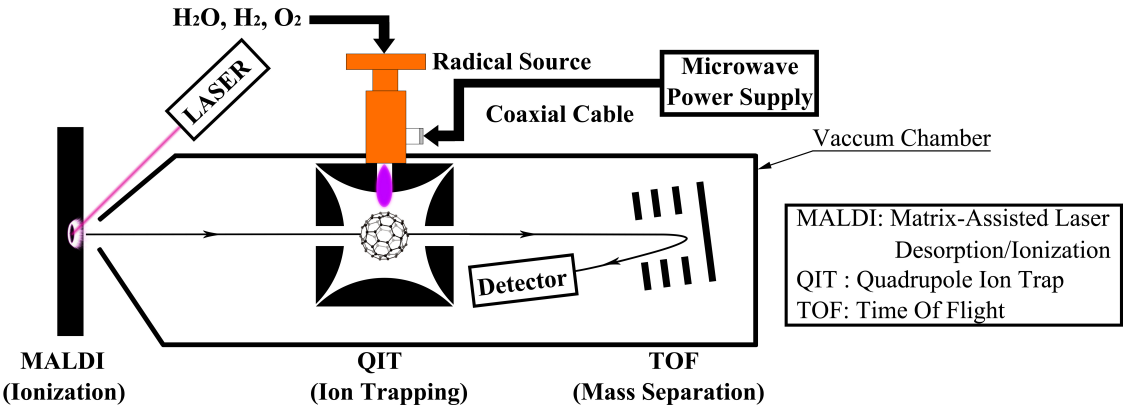

Fig. 5.5. A schematic diagram of the HAD experimental setup using microwave driven radical source. The developed radical sources are mounted to QIT chamber via ISO100-ICF70 adaptor as the case of thermal cracking source.

Figure 5.6 shows the experimental result of the mass spectra after 50 s plasma irradiation of 2nd gen CCP to fullerene ion ($C_{60}^{+\bullet}$). The observable spectra from 720 to 723 Da correspond to the original isotopic distribution of the fullerene ion. Though the input microwave power and reaction time were increased, any attachment reactions to fullerene ion were not observed at all. The result suggested the absence of arrived atomic hydrogen to the center of the QIT chamber due to the low transport efficiency of the 2nd gen CCP source, while the OES result clearly showed the existence of atomic hydrogen.

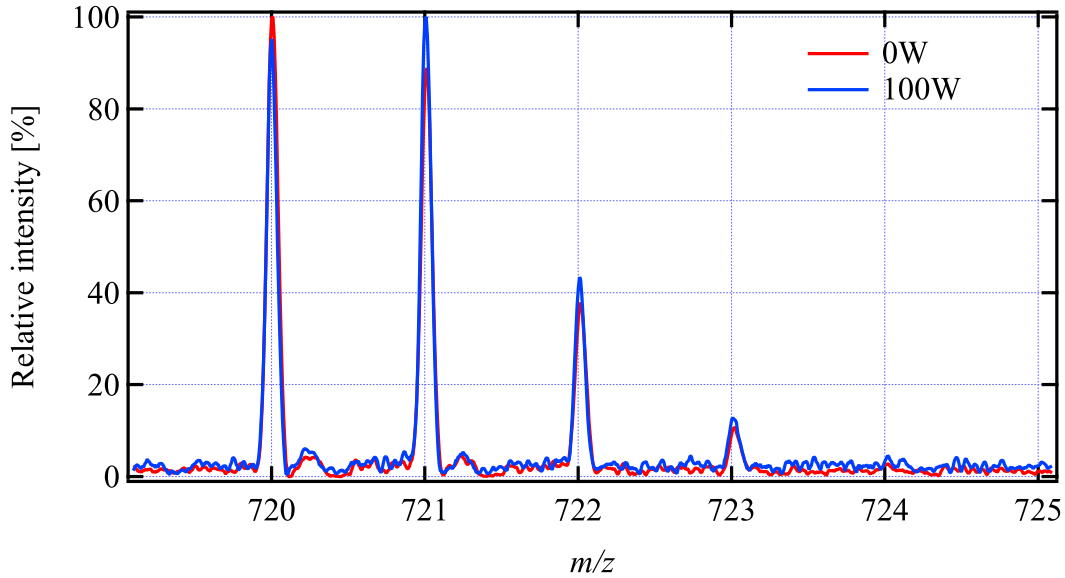

Fig. 5.6. Mass spectra after 50 s hydrogen plasma irradiation of 2nd gen CCP (100 W) to fullerene ion.

Figure 5.7 shows the experimental result of atomic hydrogen irradiation from the 1st gen LICP source to the trapped fullerene ions in the QIT chamber with several reaction times. Unlike the case of the 2nd gen CCP source, the mass spectrum peak distribution shifted to higher mass corresponding to hydrogen radical attachment with increasing reaction time of HAD system. Asakawa calculated the production energy of $C_{60}H^+$ from the trapped $C_{60}^{+\bullet}$ by injecting atomic hydrogen as shown in Fig. 5.8 [18, 19]. The calculation result of negative values for production energy indicates that the H attachment reaction to fullerene ion occurs without the dependence upon the kinetic energy of the incident atomic hydrogen. Therefore, the number of attached hydrogen can be an index to compare the relative atomic flux. Here, in order to compare the atomic flux among developed radical sources, relative atomic flux Φ_H [atoms/mm^2·s] is estimated from the peak height showing the maximum abundance in m/z. In this case, the 1st gen hydrogen LICP exhibited 0.34 atoms/mm^2·s.

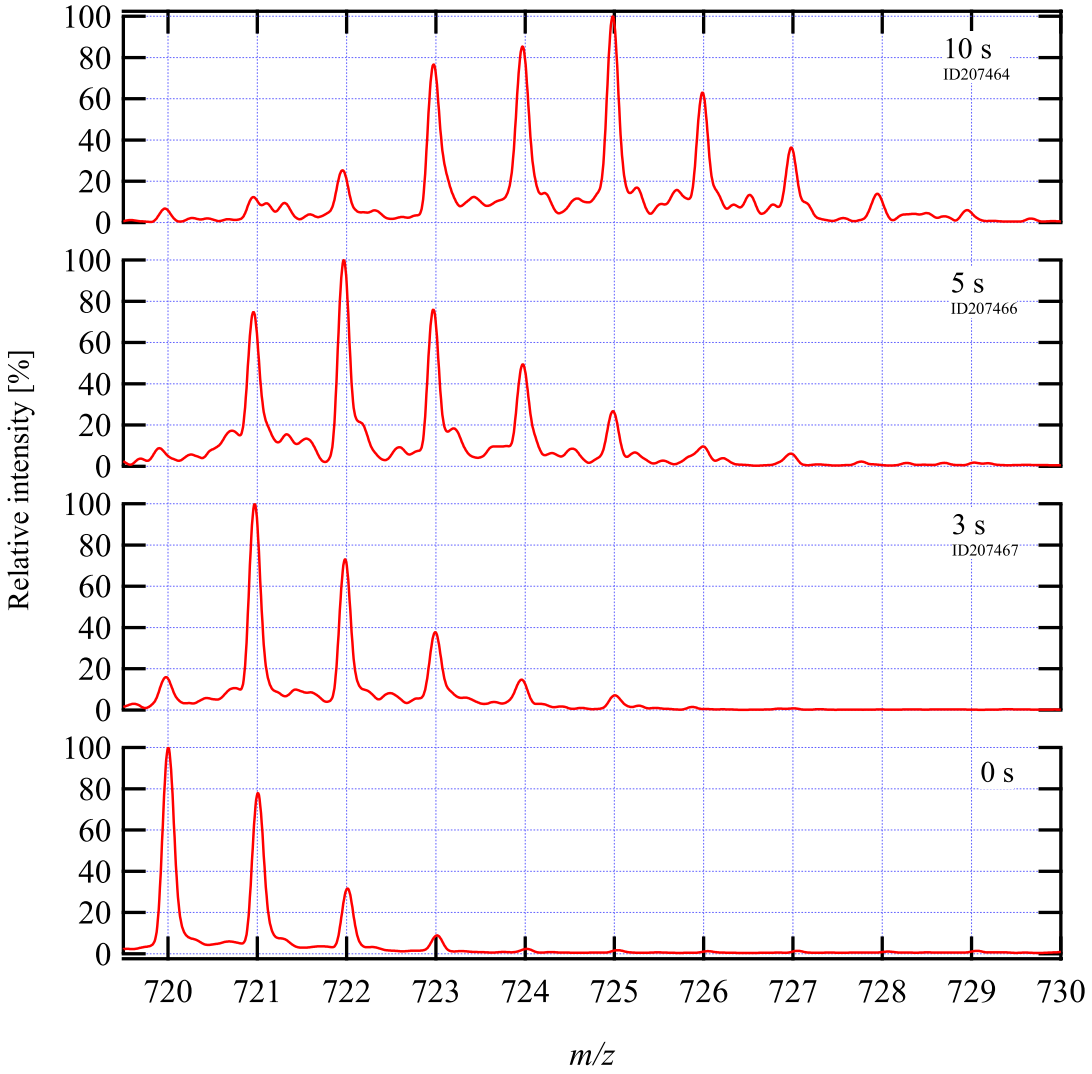

Fig. 5.7. Stepping up spectra of fullerene ions by 1st gen hydrogen LICP (50 W) irradiation for 3, 5, and 10 s reaction times.

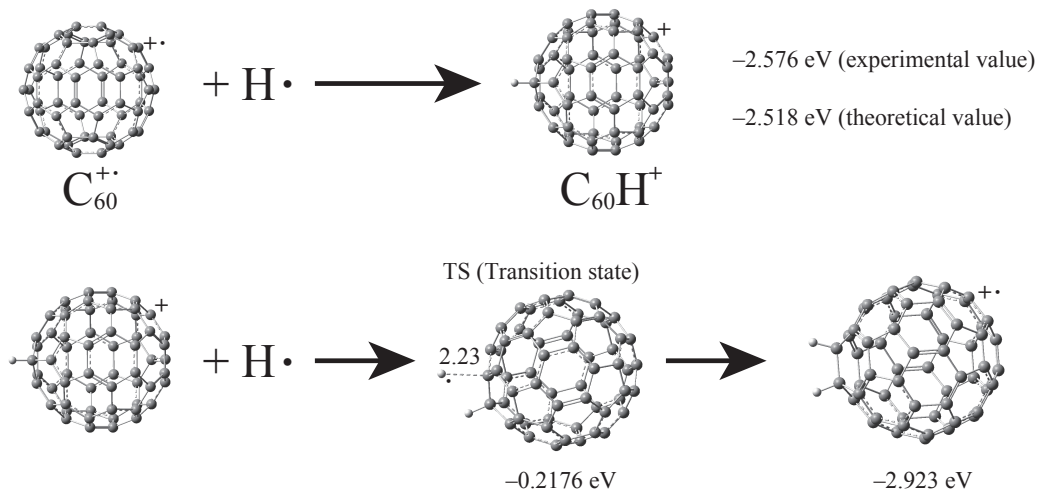

Fig. 5.8. A scheme of the hydrogen radical attachment to fullerene ion radical $C_{60}^{+\bullet}$ [18, 19].

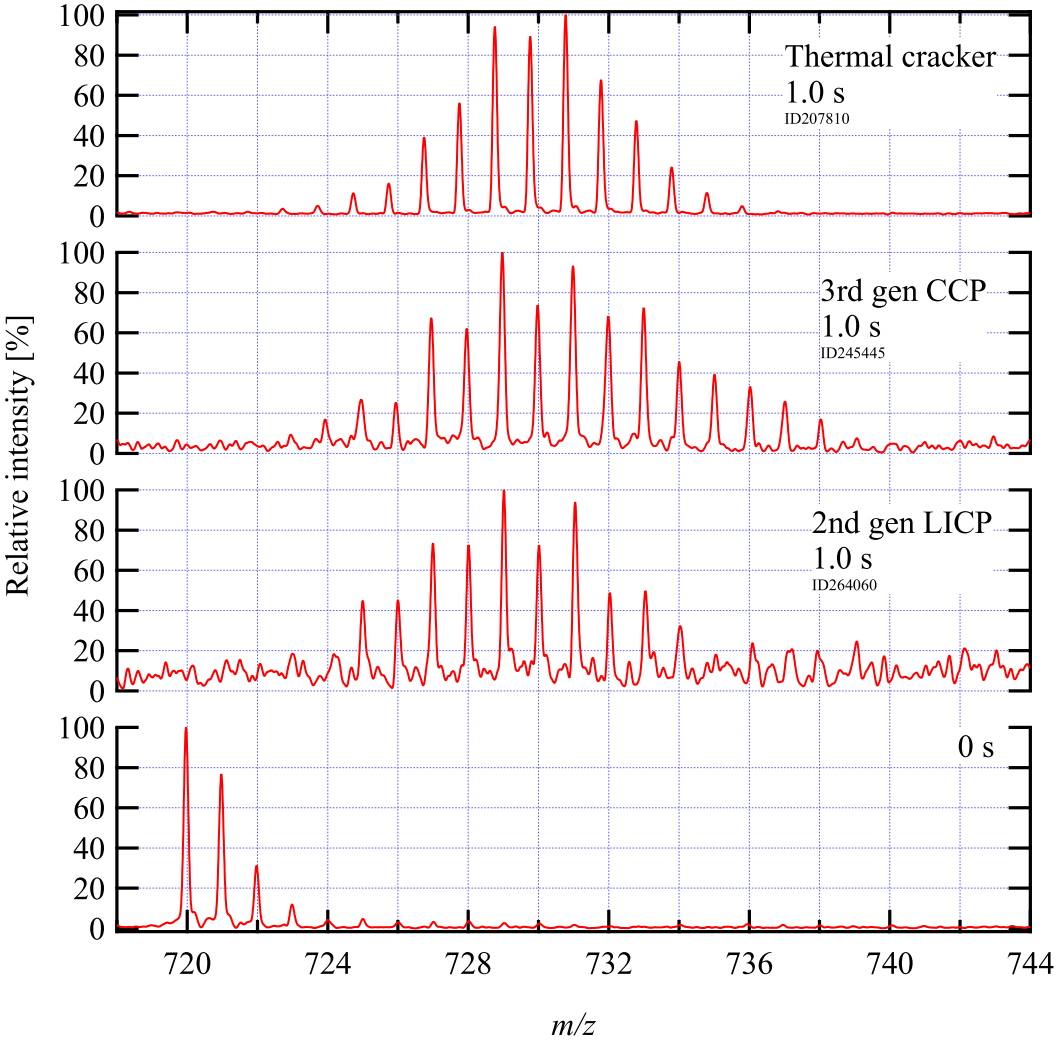

Fig. 5.9. Product ion spectra of H• attachments to fullerene ion radical $C_{60}^{+\bullet}$ for 1.0 s reaction time using thermal cracking source 210 W, 3rd gen hydrogen CCP 50 W, and 2nd gen hydrogen LICP 20 W.

Figure 5.9 shows the isotopic distribution of $C_{60}^{+\bullet}$ observed at 1.0 s of reaction time

using thermal cracking source, 3rd gen CCP source, and 2nd gen LICP source operated with pure H_2 gas. The flow rates of input H_2 gas are set to 4 sccm in thermal cracking source and 2nd gen LICP source, and 100 sccm in the 3rd gen CCP source. From 10 to 20 H• were attached to C_{60} for all H radical sources shown here, indicating that the H• were efficiently transported into the ion trap compared with the 2nd gen CCP and 1st gen LICP sources. The degree of dissociation of thermal cracking source can be estimated below 50% [10, 20]. As discussed in Chapter 3, the degree of dissociation of the 2nd gen LICP source is quite high. Meanwhile, the cracking efficiency of the 3rd gen CCP source appears lower than the thermal cracking source and 2nd gen LICP source as the source requires higher H_2 flow rates. However, the 3rd gen CCP source achieves the highest number of H• attachment to fullerenes among the three sources in the same reaction time as shown in Table 5.3. Although the attachment efficiency cannot be directly compared at different source operation pressure, the efficiency for H• radical transport from the 2nd gen LICP and 3rd gen CCP sources to fullerene ions in QIT can be estimated in comparison to the thermal cracker source which demonstrated the original HAD reaction.

Table 5.3. A table of the relative atomic hydrogen fluxes for all of developed radical sources.

Radical sources	Input power [W]	Flow rates [sccm]	Φ_H [atoms/mm^2·s]
Thermal cracker	210	$1 \sim 10$	7.36
2nd gen CCP	100	$\geqq 100$	0
3rd gen CCP	50	$\geqq 60$	8.49
1st gen LICP	50	$30 \sim 100$	0.34
2nd gen LICP	20	$1 \sim 3$	6.22

5.2.4 Dissociation of peptide ions by hydrogen plasma

To demonstrate the dissociation of peptide ions using microwave driven radical sources, 1+ substance P (RPKPQQFFGLM – NH_2, 1347 Da) in QIT was exposed to H radical irradiation generated by 2nd gen LICP and 3rd gen CCP of H_2 gas as shown in Fig. 5.10. The fragmentation due to H attachment, H abstraction, or any other process by 1st and 2nd gen LICP sources was unobserved even if the reaction time was increased up to 30 s(data not shown), while the 2+ precursor ions corresponding to 674 of m/z were observed. On the other hand, in the hydrogen CCP, the abundant c-/z- and a-/x-type ions attributable to radical-induced dissociation of the peptide backbone were clearly observed. The peak of 2+ ions were also observed with 20% of relative intensity. These results can suggest that the kinetic energy, or "the effective temperature" of H radicals generated by LICP sources is not high enough to react with peptide ions. Turecek and co-workers reported that the rate constant of direct H attachment to amide carbonyl groups is on the order of 10^{-12} cm^{-3}s^{-1} for hot H radicals with their energy exceeding 1 eV, and the rate constant is

decreased by 6 orders of magnitude at room temperature [13]. Density functional theory (DFT) calculation done by Asakawa *et al* shows that cleavage of the N-C_α bond by H radical attachment requires the radical to possess enough kinetic energy, which imply that there is a threshold in the reaction [21]. As shown in Chapter 4, the H radical temperature produced in the 2nd gen LICP source is lower than that of thermal cracking source. It should be this difference in temperature that makes the reaction for 2nd gen LICP less efficient.

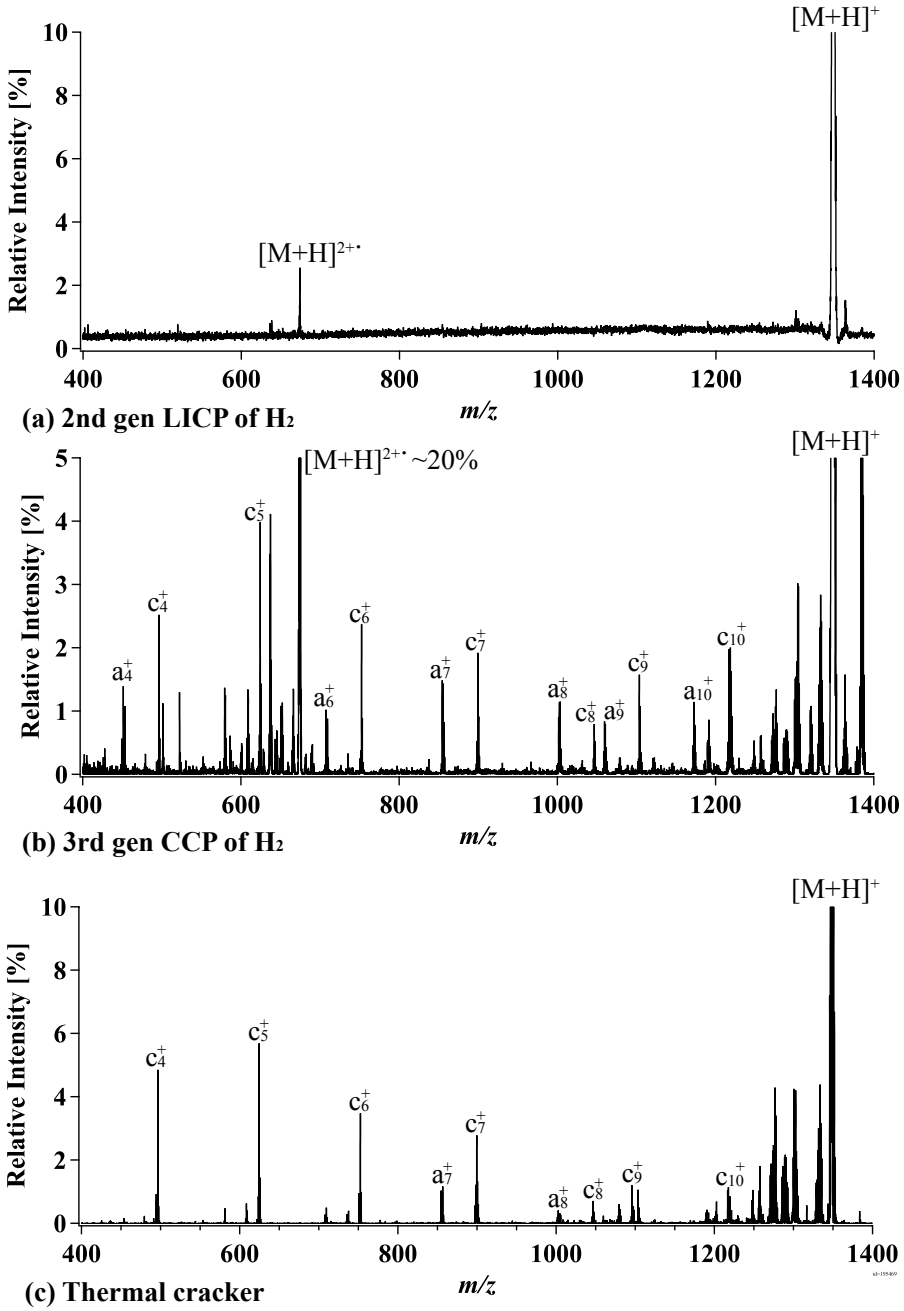

Fig. 5.10. Fragmentation spectra of singly protonated substance P obtained by (a) 2nd gen LICP operated with H_2 gas, 5 s, (b) 3rd gen CCP operated with H_2 gas, 1s, and (c) thermal cracking of H_2 gas, 0.5 s.

In the pure hydrogen CCP, a lot of a- type product ions attributable to cleavage of C_α-C bond are generated in addition to one of the original HAD by the thermal cracking source. According to the OES result shown in Figs. 5.11 (a) and (b), 3rd gen hydrogen CCP contains vibrationally excited hydrogen molecules, hydrogen ions, and probably high energy electrons other than H radicals, while the thermal cracking source mainly produces the hydrogen atoms due to its catalytic effect on the heated tungsten capillary. Since the present microwave driven radical source is not equipped with electron deflection magnets at the source due to space restriction, substantial number of high energy electrons attributable to the plasma plume can penetrate the ion trap compared to the thermal cracking source that has electron deflection magnets.

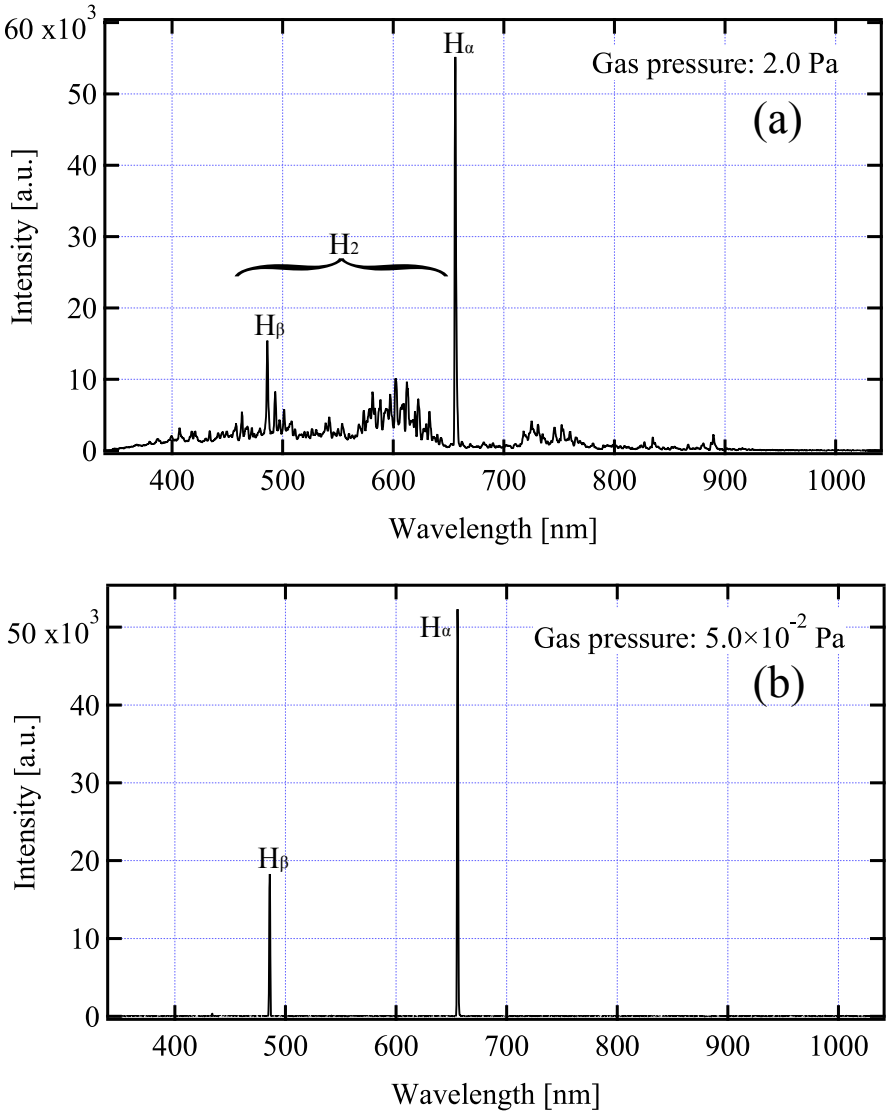

Fig. 5.11. Optical emission spectra of two types of microwave hydrogen plasmas measured by USB-4000. (a) plume mode of the 3rd gen hydrogen CCP, 2.0 Pa, 55 W, (b) 2nd gen hydrogen LICP, 5.0×10^{-2} Pa, 55 W.

5.2.5 Water-HAD with developed radical sources

Water plasmas containing H•, hydroxyl radical (OH•), or O were produced by LICP and CCP source to see the effect of the produced particle flux onto dissociation of 1+ substance P in the QIT. Figures 5.12 (a) and (b) shows the product ion spectra of 1+ substance P using 1st gen LICP source and 3rd gen CCP source of H_2O, respectively. The H_2O plasma irradiation from the 2nd gen LICP did not show any fragmentation ions as the case for hydrogen LICP. The reaction time were set from 0.5 to 1.0 s. The spectra also showed abundant c-/z- and a-/x-type ions, as well as attachments of O(+16) and water molecules (+32). As a comparison, Fig. 5.10 (c) shows the product ion spectrum of substance P using thermal cracking source. While the relative intensity of product ions by the thermal cracking hydrogen source is higher than water plasmas by an order of magnitude, the types of product ions are similar to those of water vapor plasmas. This result indicates that H•, OH•, O or excited molecules mixture generated by water vapor plasmas causes the radical induced dissociation similar to HAD by a thermal cracker source.

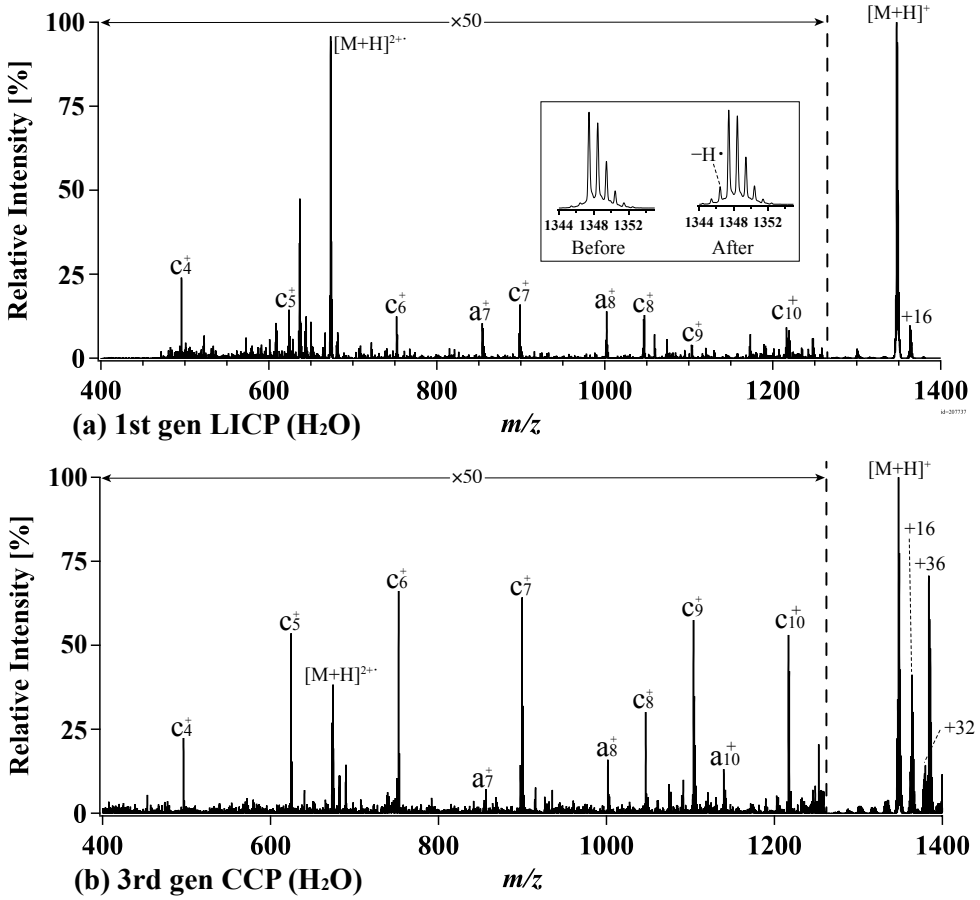

Fig. 5.12. Fragmentation spectra of singly protonated substance P obtained by (a) 1st gen LICP operated with H_2O gas, 120 W and (b) 3rd gen CCP operated with H_2O gas, 50 W.

The charge enhanced 2+ precursor ions of m/z 674 are observed in all spectra obtained by microwave plasma sources. This is possibly due to the electron ionization of the 1+ precursor ions as discussed in the subsection of hydrogen operation. To identify the cause of these 2+ precursor ions, electron beam injection without any discharge was carried out. Figure 5.13 shows the spectrum obtained by injecting an electron beam generated by thermal electron emission from a hot tungsten filament installed at 50 mm away from the inlet hole opened on the ring electrode of the QIT. The 1+/2+ product ions and a lot of charge enhanced 2+ precursor ions are observed like the case of electron ionization dissociation [22]. From this observation, the main factor of 2+ precursor ion production mechanism is speculated as electron injection to the ion trap from the microwave plasma source. There still remains, however, the possibility for other charged and/or excited species entering the system to produce 2+ precursor ions.

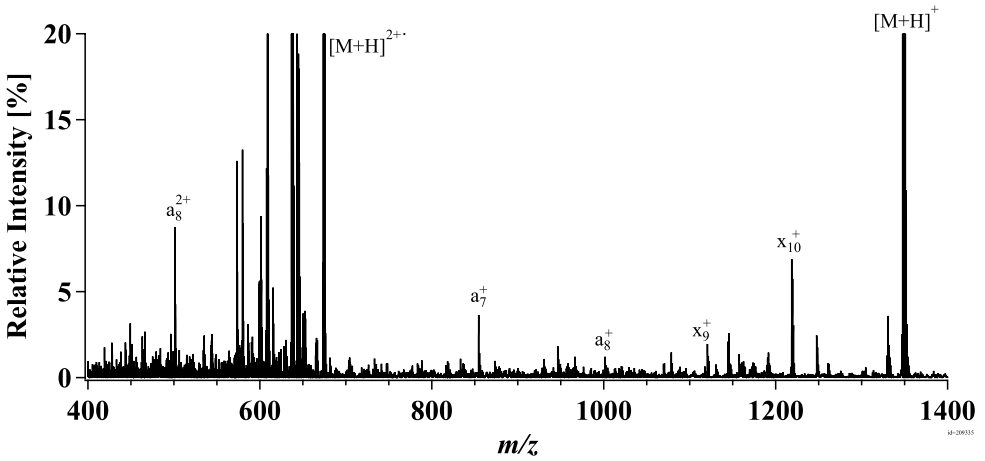

Fig. 5.13. Fragmentation spectra of singly protonated substance P obtained by electron beam injection.

Figure 5.14 shows the optical emission spectra of the water plasma produced by 1st gen LICP and that by 3rd gen CCP source, respectively. Water plasmas contain H•, O, and OH•. The emission signal from OH• radical is observed in ultraviolet region at 309 nm ($A^2\Sigma^+ \rightarrow X^2\Pi$) [23]. In addition, the water plasma shows atomic hydrogen spectra up to Balmer gamma and delta lines (434 and 410 nm) which are the higher excited levels of hydrogen atoms.

The Balmer alpha to Balmer beta intensity ratio (H_α/H_β) can give excited species are preferentially excited in a high temperature plasma. The values for a pure hydrogen and water vapor plasmas are shown in Table 5.4. Fantz and Wunderlich gave the relationship between line ratio (H_α/H_β) and electron temperature in the case of pure hydrogen discharge [24]. According to their data, the line ratio from 2.2 to 3.6 corresponds to about 2-4 eV of electron temperature with the larger intensity ratio corresponding to lower electron temperature. Meanwhile the measured values shown in Table 5.4 indicate that the water plasma contains more highly excited species compared to a pure hydrogen plasma. The

active species formed in a water vapor plasma may also have higher electron temperature compared to a pure hydrogen plasma. This postulation also agrees with the general understanding that CCP plasma has a higher electron temperature than ICP plasma [25].

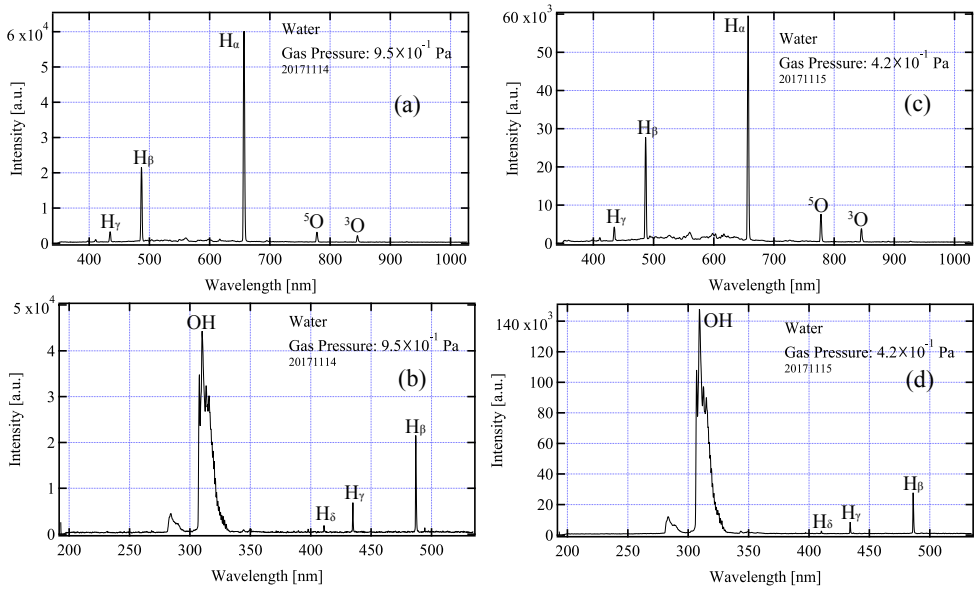

Fig. 5.14. Optical emission spectra of microwave excited water plasma measured by USB 2000+ and Flame-S. (a) 1st gen LICP at 9.5×10^{-1} Pa, 65.0 W of visible light region (b) the same condition of the ultraviolet region, (c) 3rd gen CCP at 4.2×10^{-1} Pa, 26.6 W of visible light region, (d) the same condition of the ultra violet region.

Table 5.4. A table of the (H_α/H_β) ratios for hydrogen and water plasmas at the condition same with the HAD experiments.

Radical Sources	Hydrogen plasma	Water plasma
1st gen LICP	3.6	2.9
3rd gen CCP	3.1	2.2

The product ion spectra by reactive species injection from microwave plasma sources are observed different from those obtained with thermal cracking source. The kinds of product ions generated by water plasma injection are almost identical with the original HAD spectrum shown in Fig. 5.10 (c). Thus, these product ion spectra are probably caused by H attachment or abstraction to or from precursor ions like the case of HAD. A water plasma mainly contains H•, OH•, and O according to the OES results shown in Fig. 5.14. A pure oxygen discharge was run by confirming the effect of oxygen atoms. Oxygen plasma was produced with 1st gen LICP source as CCP source has a copper electrode in contact with plasma, which should contaminate the mass data. An OES obtained for oxygen discharge is shown in Fig. 5.15 with three prominent atomic oxygen line spectra at 777.4 ($3p^5P \rightarrow 3s^5S^0$), 844.6 ($3p^3P \rightarrow 3s^3S^0$), 926.6 nm and the first negative system

($b^4\Sigma_g^- \rightarrow a^4\Pi_u$) of O_2^+ ions [26]. Figure 5.16 shows the product ion spectrum obtained by pure oxygen plasma produced in the 1st gen LICP source for singly protonated substance P. While oxidized precursor ions were clearly observed in the spectrum, the product ions were predominantly oxidized a- type ions ($a^\bullet$ + 16 Da), which were not observed for a water vapor plasma. This result, as compared with Fig. 5.12, suggests that the atomic oxygen does not play an important role in dissociation by water plasma based radical injection. Thus, the fragmentation caused by OH• may exist, while it can be affected due to the presence of H•.

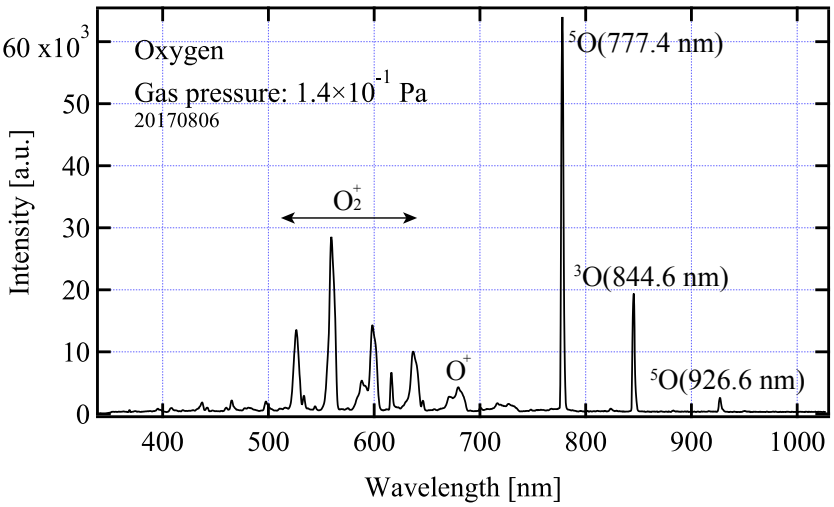

Fig. 5.15. Optical emission spectrum of oxygen plasma produced in the 1st gen LICP source measured by USB-2000+ at 1.4×10^{-1} Pa, 85.0 W.

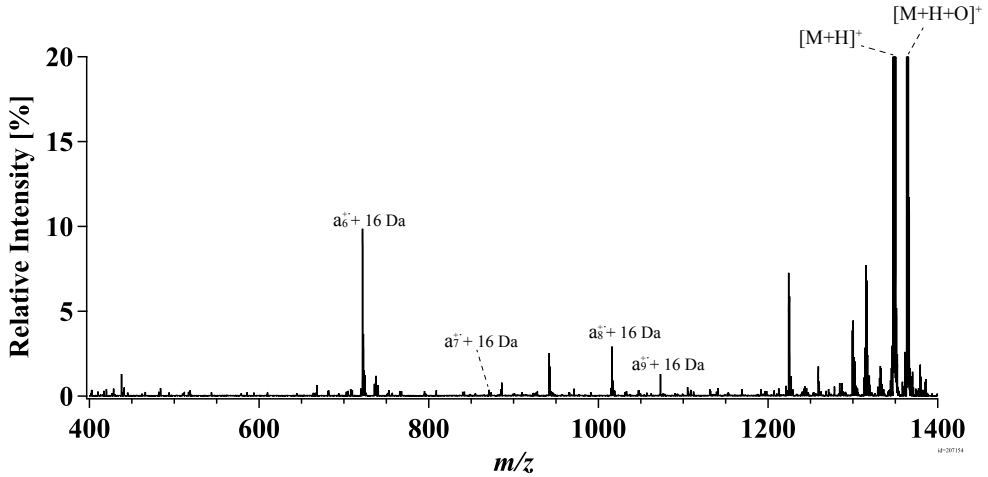

Fig. 5.16. Fragmentation spectrum of singly protonated substance P obtained by pure oxygen plasma produced in the 1st gen LICP source.

5.2.6 Comparison between H_2O and H_2 plasmas

Water vapor can replace gaseous hydrogen injection into the system to realize HAD. Figure 5.12 show the H abducted precursor ions $M^{+\bullet}$ in the fragmentation spectra. To evaluate

the effectiveness of water injection against hydrogen, the relative intensity of abducted precursor ions ($M^{+\bullet} = [M + H - H]^{+\bullet}$) against original precursor ions ($[M + H]^{+}$) was measured as the water gas pressure was changed with respect to hydrogen gas pressure. Note that the observation of H attached precursor ions ($[M + H + H]^{+}$) was difficult because of the isotopic distributions. Figure 5.17 shows the relative intensity increases with decreasing water gas pressure; the efficiency for H abduction from precursor ions by H• is more efficient for a hydrogen plasma operation than a water plasma operation. The water plasma seems to have 50% efficiency against hydrogen plasma, according to the figure.

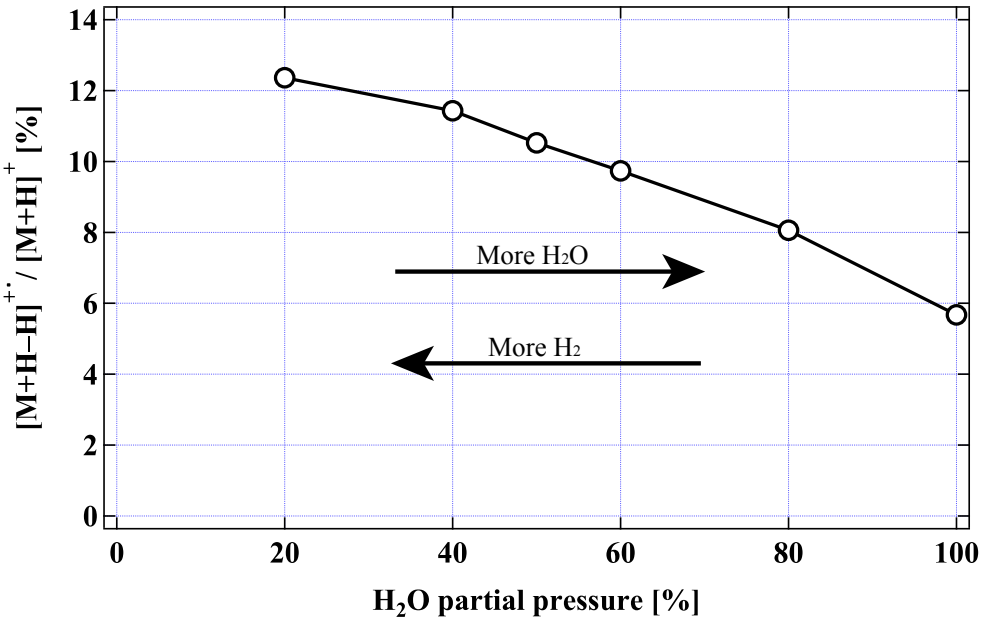

Fig. 5.17. $[M + H - H]^{+\bullet}$ ratio with respect to original precursor $[M + H]^{+}$ intensity when changing the H_2O partial pressure with H_2 pressure.

5.3 Conclusion for peptide analysis

Table 5.5. A table of the HAD experimental results utilizing developed radical sources for H_2 and H_2O plasmas.

Radical Sources	H_2	H_2O	Defects
1st gen LICP (may be identical with 1.5th LICP)	×	○	difficult matching, high power input, high operating pressure, large size
2nd gen LICP	×	×	low H temperature
2nd gen CCP(data not shown)	×	×	no radical transport ability
3rd gen CCP	○	○	2+ precursor ions, high operating pressure

Table 5.5 summarizes the empirical results of peptide analysis through the HAD process for all developed radical sources. Firstly, the 2nd gen CCP source is inappropriate for HAD system, because no H attachment to fullerene ion suggests the absence of H radical in QIT chamber. Though the principal mechanism of 1st and 2nd gen LICP sources are essentially identical from the view point of the hardware design, only H radicals produced in the 1st gen water LICP achieved cleavage of peptide ions. The produced H radical temperature depending upon the plasma production mechanism of the 2nd gen LICP source is about 600 K as shown in Chapter 4. Therefore, the high energy tail of the velocity distribution of 600 K (0.05 eV) is insufficient to cleave the peptide with certain threshold energy. A series of experiments indicated that the H radical temperature produced in the 1st gen LICP source with 120 W power input had exceeded 600 K, since the plasma fortunately may had been sustained as the high brightness mode or the W-mode which is the same plasma condition with 1.5th gen LICP source. The HAD results of the 1st gen LICP source also implies that the temperature of H radicals produced in the water plasma is higher than that of the pure hydrogen plasma.

Although the observed intensity of product ions obtained by water plasma produced in the 3rd gen CCP source are lower than those of thermal cracking source, the fragmentation pattern by water CCP shown in Fig. 5.12 (b) is straightforward to interpret compared with thermal cracking source for c^{8+}, c^{9+}, and c^{10+} ions. There were observed a small difference in their fragmentation patterns in two kinds of microwave plasma excitation. The 3rd gen CCP source realized HAD like fragmentation of substance P with both hydrogen and water plasmas. The results suggest the H radical temperature produced in the 3rd gen CCP source is higher than that of the 2nd gen LICP source, The atomic temperature of 3rd gen hydrogen CCP exhibited 930 K as discussed in Chapter 4. Thus, a qualitative relationship among the atomic temperatures produced in each source suggested from a sets of experimental results showed a good agreement with the measured temperature obtained in Chapter 4. These results concluded that the effective temperature of radicals affect the dissociation process of peptide ions. The 2+ precursor ions in the HAD spectrum obtained

by water CCP was found to be lower as compared to other a-type product ions. From the viewpoint of hardware operation, the 3rd gen CCP source does not need complicated matching procedure like the 1st gen LICP source. Therefore, the 3rd gen CCP source has to be optimized for HAD analyses by resolving problems like the electron drain into QIT causing part of 2+ precursor ions.

References

[1] K. Tanaka, H. Waki, Y. Ido, S. Akita, Y. Yoshida, T. Yoshida, and T. Matsuo, "Protein and polymer analyses up to *m/z* 100000 by laser ionization time-of-flight mass spectrometry", *Rapid Commun. Mass Spectrom.* **2**, 151 1988.

[2] V. W. Paul and H. Steinwedel, "Ein neus Massenspektrometer ohne Magnetfeld (in German)", *Z. Naturforschg.* **8a**, 448 1953.

[3] R. E. March and J. F. J. Todd, *QUADRUPOLE ION TRAP MASS SPECTROMETRY* (John Wiley & Sons, 2005).

[4] P. Miller and M. Denton, "The Quadrupole Mass Filter: Basic Operating Concepts", *J. Chem. Educ.* **63(7)**, 617 1986.

[5] L. Ruby, "Applications of the Mathieu equation", *Am. J. Phys.* **64(1)**, 39 1996.

[6] R. A. Zubarev, N. L. Kelleher, and F. W. McLafferty, "Electron Capture Dissociation of Multiply Charged Protein Cations. A Nonergodic Process", *J. Am. Chem. Soc.* **120**, 3265 1998.

[7] R. A. Zubarev, D. M. Horn, E. K. Fridriksson, N. L. Kelleher, N. A. Kruger, M. A. Lewis, B. K. Carpenter, and F. W. McLafferty, "Electron Capture Dissociation for Structural Characterization of Multiply Charged Protein Cations", *Anal. Chem.* **72**, 563 2000.

[8] J. E. Syka, J. J. Coon, M. J. Schroeder, J. Shabanowitz, and D. F. Hunt, "Peptide and protein sequence analysis by electron transfer dissociation mass spectrometry", *Proc. Natl. Acad. Sci. U.S.A.* **101(26)**, 9528 2004.

[9] J. J. Coon, J. Shabanowitz, D. F. Hunt, and J. E. P. Syka, "Electron Transfer Dissociation of Peptide Anions", *J. Am. Soc. Mass Spectrom.* **16(6)**, 880 2005.

[10] H. Takahashi, S. Sekiya, T. Nishikaze, K. Kodera, S. Iwamoto, M. Wada, and K. Tanaka, "Hydrogen Attachment/Abstraction Dissociation (HAD) of Gas-Phase Peptide Ions for Tandem Mass Spectrometry", *Anal. Chem.* **88**, 3810 2016.

[11] P. A. Demirev, "Generation of hydrogen radicals for reactivity studies in Fourier transform ion cyclotron resonance mass spectrometry", *Rapid Commun. Mass Spectrom.* **14(9)**, 777 2000.

[12] R. A. Zubarev, J. F. Haselmann, B. Budnik, F. Kjeldsen, and F. Jensen, "Towards an understanding of the mechanism of electron-capture dissociation: a historical perspective and modern ideas", *Eur. J. Mass Spectrom.* **8**, 337 2002.

[13] F. Turecek and E. A. Syrstad, "Mechanism and energetics of intramolecular hydrogen transfer in amide and peptide radicals and cation-radicals", *J. Am. Chem. Soc.* **125(11)**, 3353 2003.

[14] F. Turecek and R. R. Julian, "Peptide Radicals and Cation Radicals in the Gas Phase", *Chem. Rev.* **113(8)**, 6691 2013.

[15] M. Karas and F. Hillenkamp, "Laser desorption ionization of proteins with molecular masses exceeding 10,000 daltons", *Anal. Chem.* **60(20)**, 2299 1988.

[16] F. Hillenkamp, M. Karas, R. C. Beavis, and B. T. Chait, "Matrix-Assisted Laser Desorption/Ionization Mass Spectrometry of Biopolymers", *Anal. Chem.* **63(24)**, 1193A 1991.

[17] F. L. Brancia, B. McCullough, A. Entwistle, J. G. Grossmann, and L. J. Ding, "Digital assymmetric waveform isolation (DAWI) in a digital linear ion trap", *J. Am. Soc. Mass Spectrom.* **21**, 1530 2010.

[18] D. Asakawa (private communication).

[19] M. J. Frisch, G. W. Trucks, H. B. Schlegel, G. E. Scuseria, M. A. Robb, J. R. Cheeseman, G. Scalmani, V. Barone, G. A. Petersson, H. Nakatsuji, X. Li, M. Caricato, A. V. Marenich, J. Bloino, B. G. Janesko, R. Gomperts, B. Mennucci, H. P. Hratchina, J. V. Oritz, A. F. Izmaylov, J. L. Sonnenberg, D. Williams-Young, F. Ding, F. Lipparini, F. Egidi, J. Goings, B. Peng, A. Petrone, T. Henderson, D. Ranasinghe, V. G. Zakrzewski, J. Gao, N. Rega, G. Zheng, W. Liang, M. Hada, M. Ehara, K. Toyota, R. Fukuda, J. Hasegawa, M. Ishida, T. Nakajima, Y. honda, O. Kitao, H. Nakai, T. Vreven, K. Throssell, J. J. A. Montgomery, J. E. Peralta, F. Ogliaro, M. J. Bearpark, J. J. Heyd, E. N. Brothers, K. N. Kudin, V. N. Staroverov, T. A. Keith, R. Kobayashi, J. Normand, K. Raghavachari, A. P. Rendell, J. C. Burant, S. S. Iyengar, J. Tomasi, M. Cossi, J. M. Millam, C. Adamo, R. Cammi, J. W. Ochterski, R. L. Martin, K. Morokuma, O. Farkas, J. B. Foresman, and D. J. Fox, *Gaussian 16*, revision A.03; Gaussian, Inc., Wallingford, CT, 2016.

[20] T. Schwarz-Selinger, A. von Keudell, and W. J. Jacob, "Digital assymmetric waveform isolation (DAWI) in a digital linear ion trap", *J. Vac. Sci. Technol. A* **18(3)**, 995 2000.

[21] D. Asakawa, H. Takahashi, S. Yamauchi, S. Sekiya, S. Iwamoto, and K. Tanaka, "Fundamental Aspect of Hydrogen Attachment/Abstraction Dissociation (HAD) Tamdem Mass Spectrometry", *ASMS Conference on Mass Spectrometry and Allied Topics*, **WP210**, Indianapolis, IN June 4-8, 2017.

[22] Y. M. E. Fung, C. M. Adams, and R. A. Zubarev, "Electron Ionization Dissociation of Singly and Multiply Charged Peptides", *J. Am. Chem. Soc.* **131**, 9977 2009.

[23] G. H. Dieke and H. M. Crosswhite, "The ultraviolet bands of OH Fundamental data", *J. Quant. Spectrosc. Radiat. Transfer* **2**, 97 1962.

[24] U. Fantz and D. Wunderlich, "A novel diagnostic technique for $H^-(D^-)$ densities in negative hydrogen ion sources", *New J. Phys.* **8**, 301 2006.

[25] Y. Sakamoto, S. Maeno, N. Tsumouchi, T. Kasuya, and M. Wada, "Comparison of Plasma Parameters in CCP and ICP Processes Appropriate for Carbon Nanotube Growth.", *J. Plasma Fusion Res.* **8**, 587 2009.

[26] E. H. Lock, R. F. Fernsler, S. Slinker, and S. G. Walton, *Experimental and Theoretical Estimation of Excited Species Generation in Pulsed Electron Beam-Generated Plasmas Produced in Pure Argon, Nitrogen, Oxygen, and Their Mixtures*, Naval Research Laboratory, Washington, DC, 2011.

Chapter 6

Injection of Atomic Hydrogen to Study Negative Hydrogen Ion Formation Mechanism

6.1 Neutral beam injection for fusion research

One main application area of negative hydrogen (H^-) ion sources is the field of the thermo nuclear fusion research. According to the Lawson's criterion, the ion temperature in the fusion plasma to optimize the D(deuterium)-T(tritium) reaction has to be higher than several tens of keV [1]. Heating of plasma is a necessary process to meet this criterion by injection energy from the outside of the reactor.

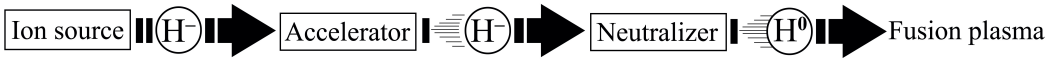

Fig. 6.1. A schematic flow of the negative ion based NBI (N-NBI) system.

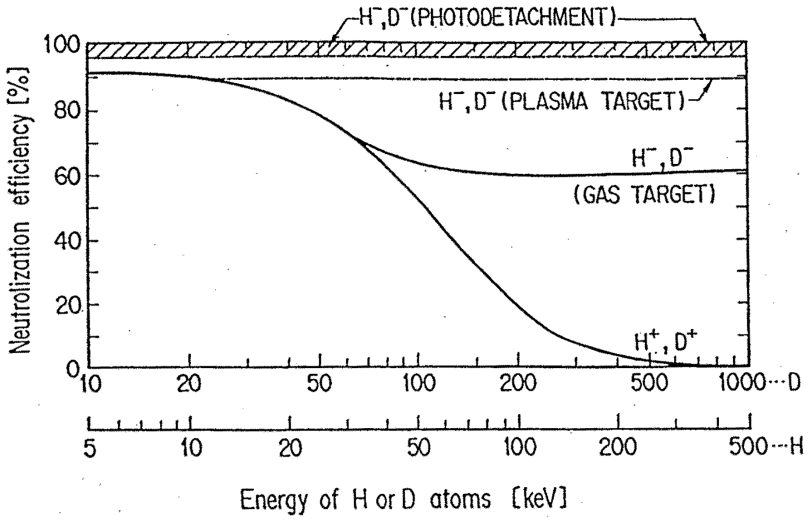

Fig. 6.2. Energy dependence of neutralization efficiency for atomic hydrogen injection. The figure was originally compiled by K. W. Ehlers [2] .

Figure 6.1 shows a schematic diagram for one of the heating techniques: NBI (Neutral Beam Injection). The NBI is composed of an ion source, an accelerator, and a neutralizer. A neuralization efficiency for positive ions (H^+, D^+) decreases drastically decrease above 60 keV/nucleon [2]. Whereas H^- ion beam can be neutralized with more than 60% neutralization efficiency up to 1 MeV. Thus, understanding of the H^- ion production mechanism is an important factor for realization of the nuclear fusion. One of the H^- ion production mechanism is believed due to the low-energy (1 eV) atomic hydrogen injection to the plasma grid surface. However, the phenomenon has yet to be observed in the actual ion source operating condition. In this chapter, developed three types of atomic hydrogen sources are utilized for low-energy H^0 production to see the conversion effect of atomic hydrogen to negative ion as a part of the radical source performance evaluation.

6.2 Production and destruction processes of negative hydrogen ions

6.2.1 H^- ion production

A volume production type H^- ion source is separated into two regions spatially by the difference in electron temperatures: the high electron temperature (driver) region and the low electron temperature (extraction) region [3]. There are two types of H^- ion production processes: volume production and surface production. The volume production mechanism is given by Eqs. 6.1 and 6.2.

$$H_2 + e^-_{\text{fast}}(> 20\,\text{eV}) \rightarrow H_2^* + e^-_{\text{fast}} : \text{vibrationally excitation} \tag{6.1}$$

$$H_2^* + e^-_{\text{slow}}(\approx 1\,\text{eV}) \rightarrow H^- + H^0 : \text{dissociative attachment} \tag{6.2}$$

In the first phase, a collision between accelerated high temperature electrons (> 20 eV) and molecular hydrogens collide to make transitions from the ground level of H_2 to vibrationally excited molecules (H_2^*). A dissociative attachment reaction given in Eq. 6.2 strongly depends upon the quantum number of vibrational states of H_2^* and the energy of electrons [4]. Figure 6.3 shows the rate coefficients for dissociative electron attachment reaction for various vibrational states of H_2 as a function of electron energy [5]. According to the theoretical curve, the electron energy for dissociative attachment must be about 1 eV [6]. Meanwhile, for surface production type H^- ion source, hydrogen atoms and molecules in the source plasma are converted to H^- ions on a low work function metal surface as given by Eq. 6.3.

$$H^0 + \text{surface} \rightarrow H^- : \text{surface production} \tag{6.3}$$

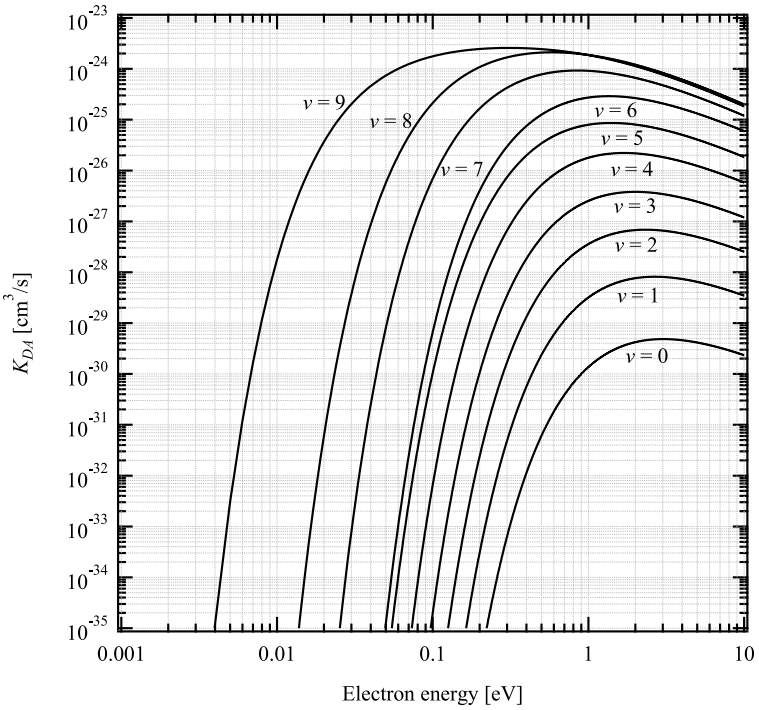

Fig. 6.3. Rate coefficients for dissociative electron attachment reaction $H_2(X^1\Sigma_g^+) + e^- \rightarrow H_2^-(^2\Sigma_u^+) \rightarrow H^- + H^0$ for various vibrational states of H_2 [5].

6.2.2 H^- ion destruction

Not only an H^0 can be converted to a H^- ion by surface production, but also an H^0 contributes to H^- ion destruction processes in the source operation condition through electron detachment as shown below [7, 8].

$$H^- + H^0 \rightarrow H_2 + e^- : \text{associative detachment} \tag{6.4}$$

$$H^- + H^0 \rightarrow 2H^0 + e^- : \text{collisional detachment} \tag{6.5}$$

The process that the atomic hydrogen destroys H^- ions can be written as Eqs. 6.4 and 6.5. The former H^- destruction process or the associative detachment predominates with the cross section three orders of magnitude higher the latter collisional detachment process less than 0.1 eV of atomic hydrogen energy as shown in Fig. 6.4 [5, 7, 9]. The other plausible H^- destruction processes are below [7, 8]. Theoretical curves for all destruction processes are shown in Figs. 6.4 - 6.7.

$$H^- + H^+ \rightarrow H^0 + H^0 : \text{mutual neutralization} \tag{6.6}$$

$$H^- + e^- \rightarrow H^0 + 2e^- : \text{electron detachment} \tag{6.7}$$

$$H^- + H_2 \rightarrow H^0 + e^- + H_2 : \text{collisional detachment} \tag{6.8}$$

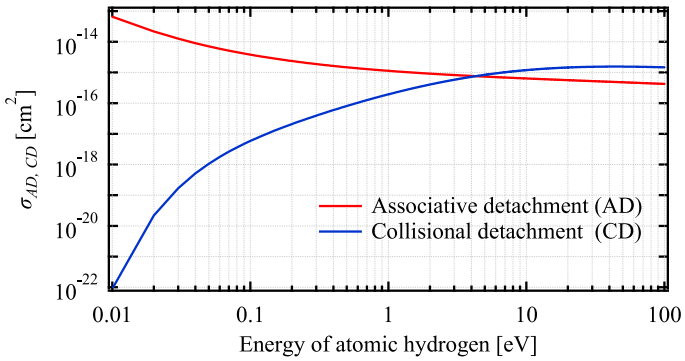

Fig. 6.4. Cross sections for associative and collisional electron detachment processes [5].

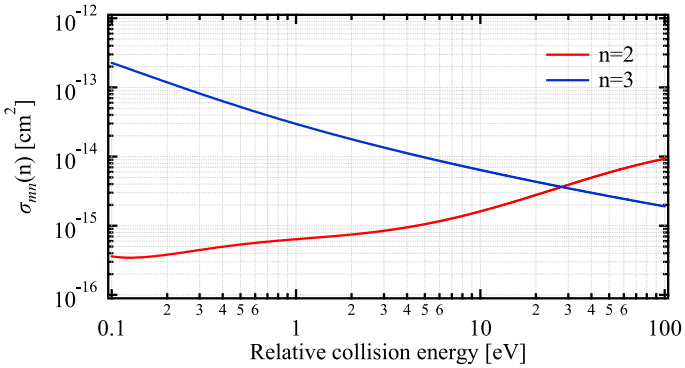

Fig. 6.5. Cross sections for electron capture into n=2 and 3 levels in $H^- + H^+ \rightarrow H^0 + H^0$ mutual neutralization reaction [5].

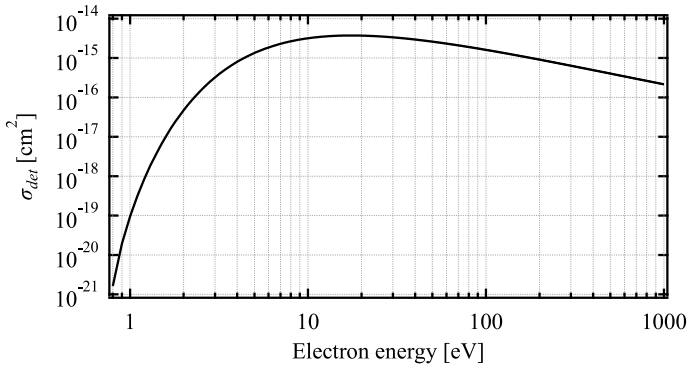

Fig. 6.6. Cross section for electron detachment: $H^- + e^- \rightarrow H^0 + 2e^-$ [5].

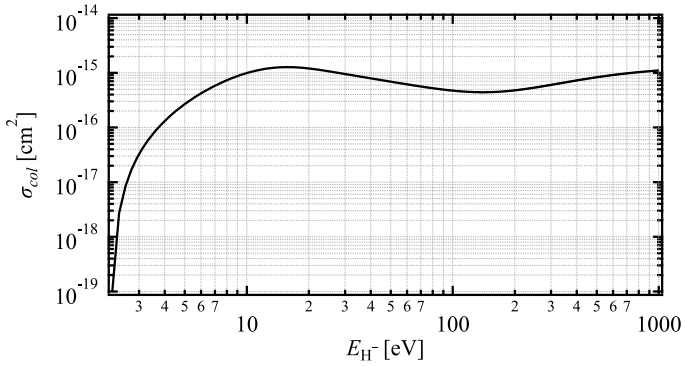

Fig. 6.7. Cross section for collisional electron detachment process in $H^- + H_2 \rightarrow H^0 + H_2 + e^-$ [5].

6.3 Atomic hydrogen injection toward a plasma grid in a negative hydrogen ion source

6.3.1 Prior researches

Figure 6.8 shows a conceptual diagram of this study. As mentioned in the previous section, the principle mechanism of the H^- ion production can be due to reflections of positive hydrogen ions [10] and those of hydrogen atoms [11, 12, 13, 14, 15, 16]. However, this mechanism of H^- ion production by hydrogen atom reflection has not been directly confirmed in the actual ion source operating condition yet. The contributions of H^0 for H^- surface production at low work function surfaces outside of the ion source has been being investigated for a long time by using thermal cracker [11, 12, 13, 14], 26.5 MHz RF [15], 2.45 GHz ECR [16] atomic sources. A behavior of additional atomic hydrogen injection from several types of atomic sources mentioned in the previous chapters in the cesiated/uncesiated H^- ion source operating condition has been surveyed. The H^- surface production mechanism does not work on uncesiated ion source because electrons in the conduction level of a high work function metal surface do not accomplish transition to the affinity level of atomic hydrogen. Instead, the H^- ion production processes under a cesium-free condition include dissociative attachment to vibrationally excited hydrogen molecules that are produced through recombinative desorption at metal surface due to an atomic hydrogen incidence. Thus, additional atomic hydrogen injection will destroy or create the volume produced H^- ions under the uncesiated condition. In this section, the effect due to additional injection of atomic hydrogen in the cesiated/uncesiated H^- ion source using three types of atom sources which produce hydrogen atoms of different velocity distributions is discussed.

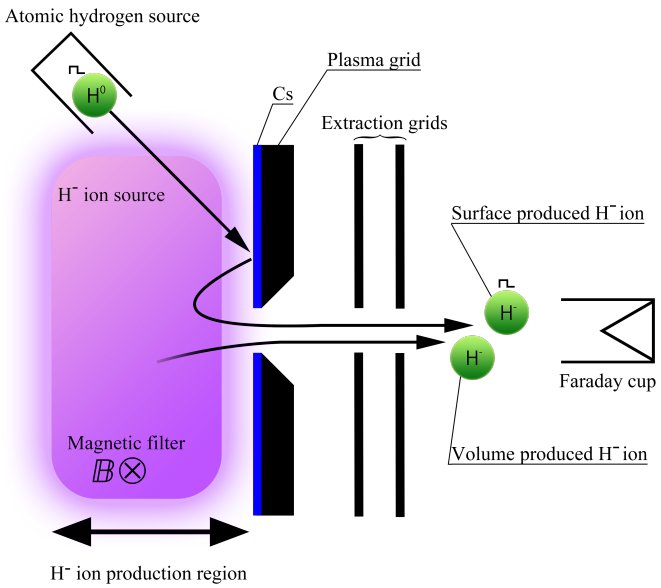

Fig. 6.8. A conceptual diagram of the experiment.

6.3.2 Experimental system

The main component of the experimental system shown in Fig. 6.9 is a small multicusp type H^- ion source equipped with an atomic hydrogen source, cesium oven, and the extraction system. Two tungsten filaments (diameter 0.3 mm, length 40 mm) arranged at the center of the chamber to ignite and sustain a plasma. According to the total cross section for ionization of H_2 by electron impact shown in Fig. 6.10, the electrons with 60 to 80 eV energy are capable to sustain a plasma efficiently [17, 18]. In this experiment, the 80 V negatively biased filaments emit the thermionic electrons with around 80 eV toward the surrounded chamber wall. This source chamber (96 mm inner diameter × 169 mm length) has twelve rows of Nd-Fe cusp magnets (5 mm × 5 mm × 127 mm, $B_{max} \approx 1030$ G) at the outside wall to enhance the plasma confinement. A hydrogen gas pressure of the ion source is maintained by monitoring pressure inside the chamber by an ionization gauge. The ion source has two ports to direct atomic beams to the surface of the plasma grid. One of these ports mounts an atomic hydrogen source among a thermal cracking source, a microwave driven CCP source and a LICP source. The distance from the source tip to the center of the plasma grid is 80 mm for the thermal cracking source, 120 mm for the CCP source, and 10 mm for the LICP source, respectively. The thermal cracking and microwave CCP and LICP sources emit positive ions and electrons as well as hydrogen atom. However, these charged particles are deflected by strong Nd-Fe magnets before coming into the ion source chamber. Another port located at the position symmetric to the atom source with respect to the H^- ion source center axis contains an oven system that evaporates cesium vapor to enhance the H^- ion production.

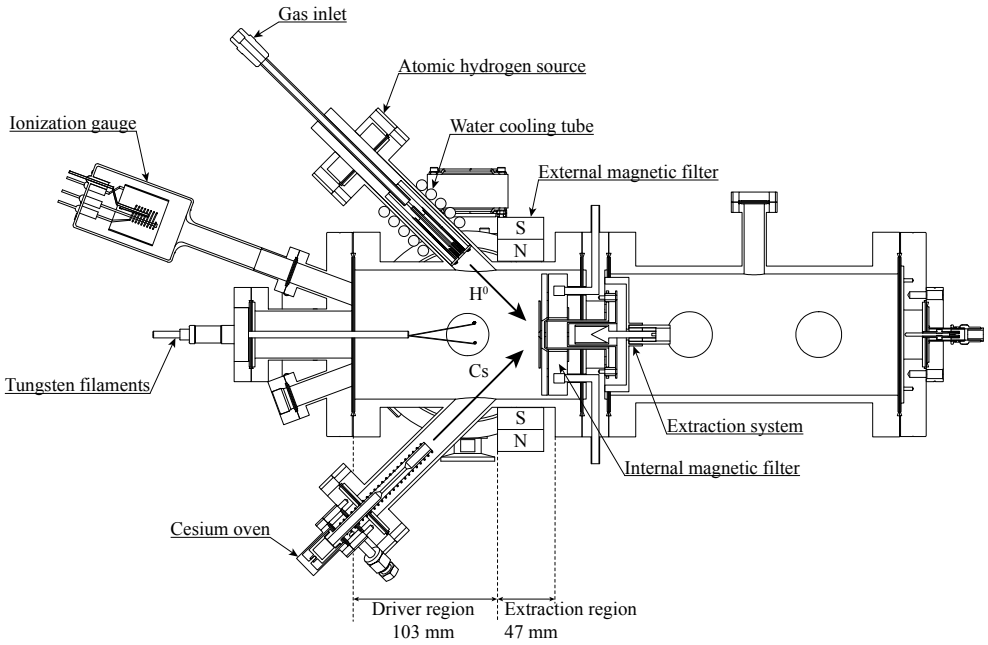

Fig. 6.9. Cross-sectional view of the multicusp type ion source with the hot discharge cathode, negative ion extraction system, magnetic filters, cesium oven, and an atomic hydrogen source.

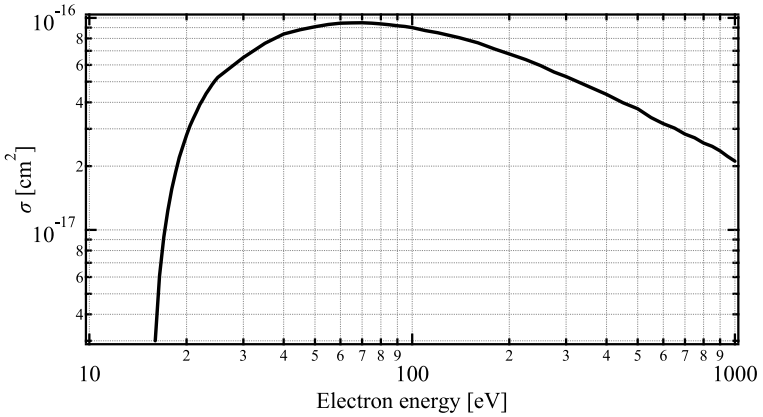

Fig. 6.10. Total cross section for ionization of H_2 by electron impact [17, 18].

The H^- volume production process through a dissociative attachment for the vibrationally excited molecules requires low electron temperature ($\approx$ 1 eV) region in the vicinity of the plasma grid. Two pairs of Nd-Fe magnets arranged around the chamber outer wall produce a magnetic field with the intensity high enough to prevent primary electrons from penetrating into the extraction region. The field with the orientation perpendicular to the beam extraction axis extends a region of low electron temperature plasma occupying 47 mm from the end part of the ion source. This high intensity magnetic field around the extraction region serves as magnetic filter field contributing to the enhancement of the H^- ion extraction while further reducing the co-extracted electron current coupled to the biased plasma grid [19].

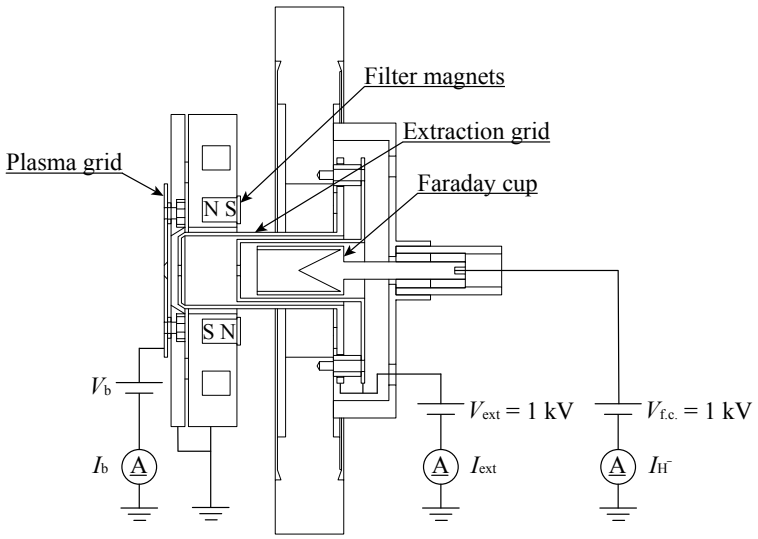

Fig. 6.11. Schematic drawing of the H^- (I_{H^-}) and co-extracted electron current (I_{ext}) measurement circuit.

Figure 6.11 shows the schematic diagram of the H^- ion extraction system assembled on a ICF 152 standard flange. In addition to external magnetic filter shown in Fig. 6.9, a

pair of water-cooled Nd-Fe magnets (30 × 12 × 7 mm) behind the plasma grid enhances the magnetic filter field near the extraction region. The magnets form the field of the 330 G intensity at the center of the plasma grid to enhance H^- ion current and reduce co-extracted electron current [19]. The 50 mm diameter plasma grid with 3 mm diameter extraction hole is made of molybdenum. Electrons and H^- ions are extracted through 3 mm apertures of plasma grid and extraction electrode with 1 kV extraction voltage. The extracted electrons are deflected by the filter magnetic field to strike the inner wall of the extraction electrode. The current that runs through the power supply to bias the extraction electrode, I_{ext}, is assumed mainly composed of these co-extracted electrons. Meanwhile, H^- ion current, I_{H^-} is monitored by a Faraday cup installed downstream of a beam collimation aperture. In this series of experiments, the discharge current was limited below 1.5 A to avoid over-heating of the system. The gas pressure was maintained at 1.3 Pa pressure for microwave driven CCP source to stably supply atomic hydrogen as will be discussed in the following subsection.

6.3.3 Hydrogen atom injection in uncesiated condition

Leung *et al* found that a small positive bias for the source plasma grid does not only enhance the extracted H^- ion current but also reduce the co-extracted electron current [19]. A proper positive bias with respect to wall potential is an effective way for an efficient H^- ion current extraction with a small amount of electron current. In this experiment, the co-extracted electron current and extracted H^- ion current were measured simultaneously by sweeping the plasma grid bias voltage (V_b) from 0 to 5 V. The H^- ion extraction was attempted with atomic hydrogen injection before/after the cesium introduction. All the thermal cracking source, the CCP source, or the LICP source produced the excited species including atomic hydrogen toward the plasma grid. Figures 6.12 (a) and (b) show the two examples of H^- ion and electron current dependences upon the plasma grid bias with atomic hydrogen injection from the thermal cracking cell and microwave CCP to the plasma grid of the uncesiated ion source. As shown in Fig. 6.12 (a), the injection of the atomic hydrogen produced by the thermal cracking cell decreased the H^- ion current by 10% and increased the extraction electron current by 6.1%. Meanwhile, as shown in Fig. 6.12 (b), the atomic hydrogen injection produced by the microwave CCP decreased H^- ion current by 3.5% and increased the extraction electron current by 9.8%. The input power for thermal cracking source and microwave CCP source were fixed to 170 W and 70 W, respectively.

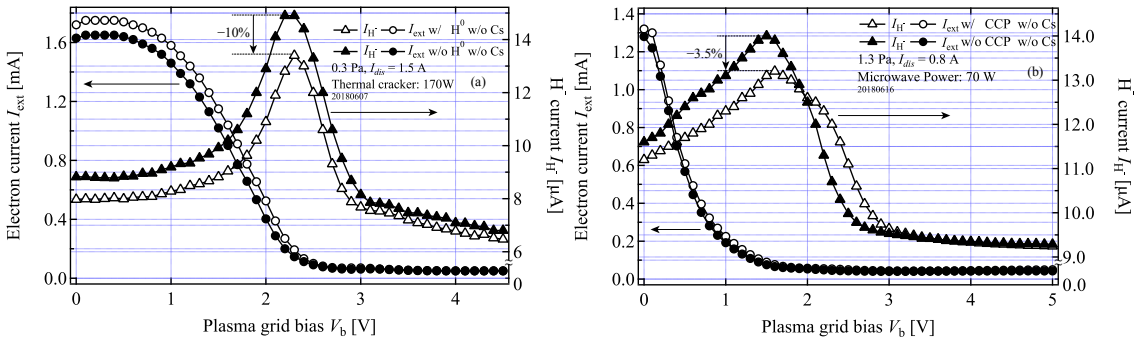

Fig. 6.12. The influence on extracted H^- current for atomic hydrogen injection from the thermal cracking cell and microwave CCP. (a) H^0 injection from the thermal cracker source to the uncesiated source: 0.3 Pa, 1.5A. (b) H^0 injection from the microwave CCP source to the unesiated source: 1.3 Pa, 0.8 A.

6.3.4 Hydrogen atom injection in cesiated condition

In the condition similar to the uncesiated one, H^- ions and electrons were extracted from the cesiated ion source. Cesium is introduced by the cesium oven shown in Fig. 6.13. The 128 mm long cesium oven is composed of a cesium reservoir, support of the reservoir, sheathed heater, and nozzle. The sheathed heater wound around the nozzle heats the cesium poured into the reservoir. The oven attached to the lower port of the ion source shown in Fig. 6.9 evaporated cesium toward the plasma grid 118 mm away by sheathed heater coil with 20 W (> 120 °C) continuous power input. An optical emission from the source plasma produces a wavelength spectrum that gives ion/neutral excited species which are present in the volume. The flange mounting the atomic source was replaced with a glass viewport to observe the plasma grid surface looking into the cesium oven from the port located at the symmetric position with respect to ion source axis. The typical OES (optical emission spectrum) of the hydrogen plasma sustained in cesiated ion source is shown in Fig. 6.14.

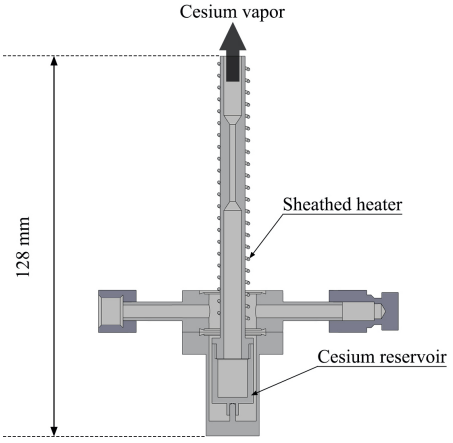

Fig. 6.13. A sectional view of the cesium oven.

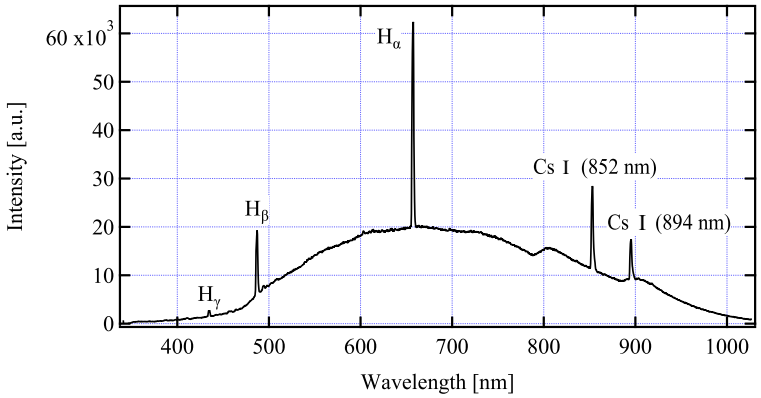

Fig. 6.14. A typical optical emission spectrum in the cesiated H^- ion source. The spectrum was taken at 1.0 Pa hydrogen discharge condition.

The measured spectrum exhibits existence of atomic hydrogen corresponding to Balmer series, atomic cesium line spectra: 852 and 894 nm, and continuum background emission from the tungsten filaments. Figures 6.15 (a) and (b) show the influence on extracted H^- ion current for atomic hydrogen injection to the cesiated ion source. Atomic hydrogen injection by the thermal cracking source to the cesiated ion source increased the H^- ion current by 15%. Meanwhile, CCP hydrogen atom injection increased the H^- ion current slightly by 1.0%. Atomic hydrogen injections also contributed a little to the H^- ion enhancement when the plasma grid bias exceeded the voltage corresponding to the H^- ion current peak.

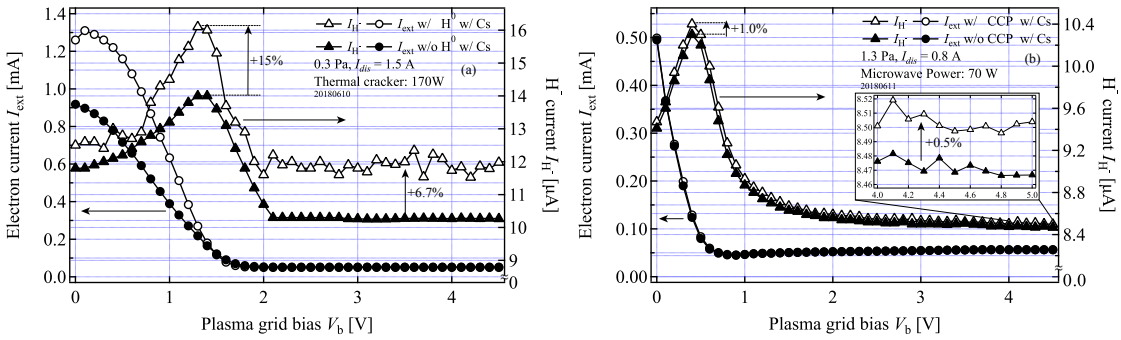

Fig. 6.15. The influence on extracted H^- current for atomic hydrogen injection from the thermal cracking cell and microwave CCP. (a) H^0 injection from the thermal cracker source to the cesiated source: 0.3 Pa, 1.5A. (b) H^0 injection from the microwave CCP source to the cesiated source: 1.3 Pa, 0.8 A.

The LICP source can ignite and sustain a plasma discharge at a lower pressure and lower input power (~ 20 W)compared with CCP source as shown in Chapter 3. With or without adding cesium, any influence on H^- ion extraction due to H^0 injection from the LICP source have never been observed.

6.3.5 Discussion

As shown in Fig. 6.12, increase in the extracted electron current were observed with atomic hydrogen injection under an uncesiated condition. The increment was derived from H^- destruction process due to H^0 injection in the vicinity of plasma grid surface. Meanwhile, changes in the gas pressure inside the ion source and discharge current had not been observed when the atomic hydrogen source was turned on. This implies that the H^0 incident from the atomic source disturbs only the region near the extraction hole of the ion source. Therefore, the present discussion deals with only the H^- destruction processes by additionally injected neutral atomic hydrogen.

Atomic hydrogen produced by a thermal cracking source and that by a microwave CCP source destroys the volume produced H^- ions on uncesiated ion source through the associative detachment process as shown in Fig. 6.12 except the case of LICP injection. The 10% H^- reduction due to H^0 injection from the thermal cracking source was observed, while the H^- reduction by the CCP atom injection was lower than that of thermal cracking source. One of the reasons for this reduced effect is the lower velocity of H^0 from the CCP and LICP source as shown in the previous chapter. However, another factor volume production of vibrationally excited molecules may be present. As indicated in the OES result for CCP source of Chapter 3, a hydrogen microwave discharge in a CCP accompanies sizable amount of vibrationally excited molecules. The injection of undeflected electrically neutral H_2^* transported to the extraction region of the uncesiated ion source should enhance the H^- volume production. Thus, the H^- detachment process by H^0 injection from the CCP source may not appear so much due to the enhancement of H^- volume production by additional H_2^* even though the hydrogen atoms from the CCP source destroy the H^- ions.

Figures 6.15 (a) and (b) show different characteristics upon H^- extraction but they cannot be directly compared as the operating pressure was different. In order to compare the influence of atomic hydrogen injection from the thermal cracker source at the same pressure, the characteristics were measured by thermal cracker source with the same experimental condition as Fig. 6.15 (b) at the CCP source. The result is shown in Fig. 6.16: 1.3 Pa operation pressure, 0.8 A discharge current. In order to compare the influence of H^0 injection with the corresponding change in plasma potential, the curves of the graph for the H^0 injection shifted by 0.3 V to a lower potential and expanded in the 2.0 V range as shown in Fig. 6.16 (b).

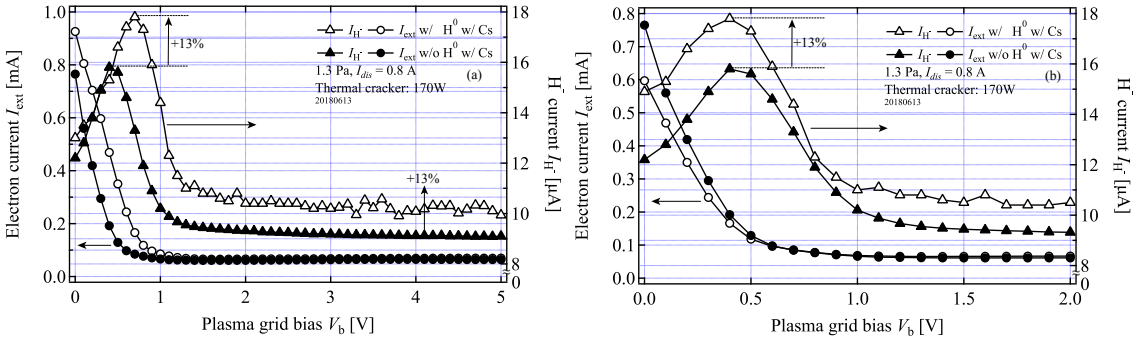

Fig. 6.16. The influence on extracted H^- current for atomic hydrogen injection from the thermal cracking source to cesiated ion source. (a) characteristics taken under the 1.3 Pa pressure, 0.8 A discharge current condition. (b) Same graph with the peak shift and abscissa expansion.

Comparing the peaks with and without H^0 injection using thermal cracker source is 13% enhancement of H^- ion current observed in Fig. 6.16. In the range of $V_b > 2$ V seems to indicate the H^- surface production due to atomic hydrogen incidence from thermal cracking source to cesiated ion source. Meanwhile, that of CCP injection caused 1.0% minute contribution to the H^- ion enhancement as shown in Fig. 6.15 (b). According to the result of the previous chapter, the number of produced atomic hydrogen from those two types of atomic sources are comparable from the experimental result of H^0 attachment to the fullerene ion. However, the effective temperature of atomic hydrogen generated in the thermal cracking cell is higher than that of the CCP source. While the LICP source has shown to have good hydrogen cracking efficiency, the effective temperature of atomic hydrogen is relatively low ($\approx$ 600 K). Seidl *et al* also showed poor contribution of atomic hydrogen injection from hydrogen discharge to low work function surface, while a clear enhancement was observed with thermal cracking source heated up to 2700 K [13]. This implies the number of atomic hydrogen that satisfies the required energy to transfer electrons to the H^0 affinity level is smaller for the CCP source. The hydrogen atom injection from CCP and LICP to cesiated surface with the faint contribution to H^- ion enhancement can be attributable to the smaller fraction of high energy atoms in the high energy tail part of the energy distribution functions.

6.4 Conclusion

Figure 6.17 shows the energy level diagram for negative hydrogen ion production. Although the surface produced H^- ions must have sufficient kinetic energy to escape from the metal surface, the threshold energy of the H^- ion production is believed to be $(\phi_W - E_a)$ as shown in the figure. The minimum work function, ϕ_W , for the Cs/H/Mo surface can be about 1.6 eV [20]. Thus, atomic hydrogen must have kinetic energy above 0.85 eV. The atomic hydrogen injection produced in the 2nd gen LICP never produced H^- ions in this

experiment because the population of atomic hydrogen which has kinetic energy above 0.85 eV in the energy distribution for 600 K is only 32.1 ppm. The kinetic energy distributions of atomic hydrogen produced in the thermal cracking source were also calculated for the case of 180 W and 260 W power input as shown in Fig. 6.18. In contrast, the populations of atomic hydrogen which have kinetic energy above 0.85 eV are 0.05% and 0.50% for 180 W and 260 W, respectively. The observed surface produced H^- ions in this experiment of thermal cracker source are attributable to the small amount of hydrogen atoms with kinetic energy higher than the threshold. The population of atomic hydrogen which has the energy above 0.85 eV emitted from the 3rd gen CCP source can be smaller than that of thermal cracking source. The energy distribution of the 70 W hydrogen CCP exhibited only 0.019% component above the threshold energy. Thus, the relationship between the surface produced H^- current and implied atomic energy corresponds to the atomic temperatures obtained by the velocity distribution measurement in Chapter 4 as the case of the peptide analysis.

A series of experiments demonstrated the general understanding of the H^- surface production mechanism in the actual ion source operating condition by using three types of developed atomic hydrogen sources. The difference in energy distribution of the produced atoms experimentally revealed that the both H^- surface production and destruction processes require some threshold energies. The 2nd gen LICP source could not achieve the atomic hydrogen energy to satisfy the escaping energy for surface produced H^- ions leaving the cesiated surface. Meanwhile, the tail of the thermal distributions of produced hydrogen atoms from the 3rd gen CCP and thermal cracking sources meet the requirement for H^- surface production and associative detachment of the H^- ions. Experiments with stable higher energy hydrogen atom flux, and monitoring the ion source parameters will contribute to the further understanding of the H^0 behavior under the ion source operating conditions.

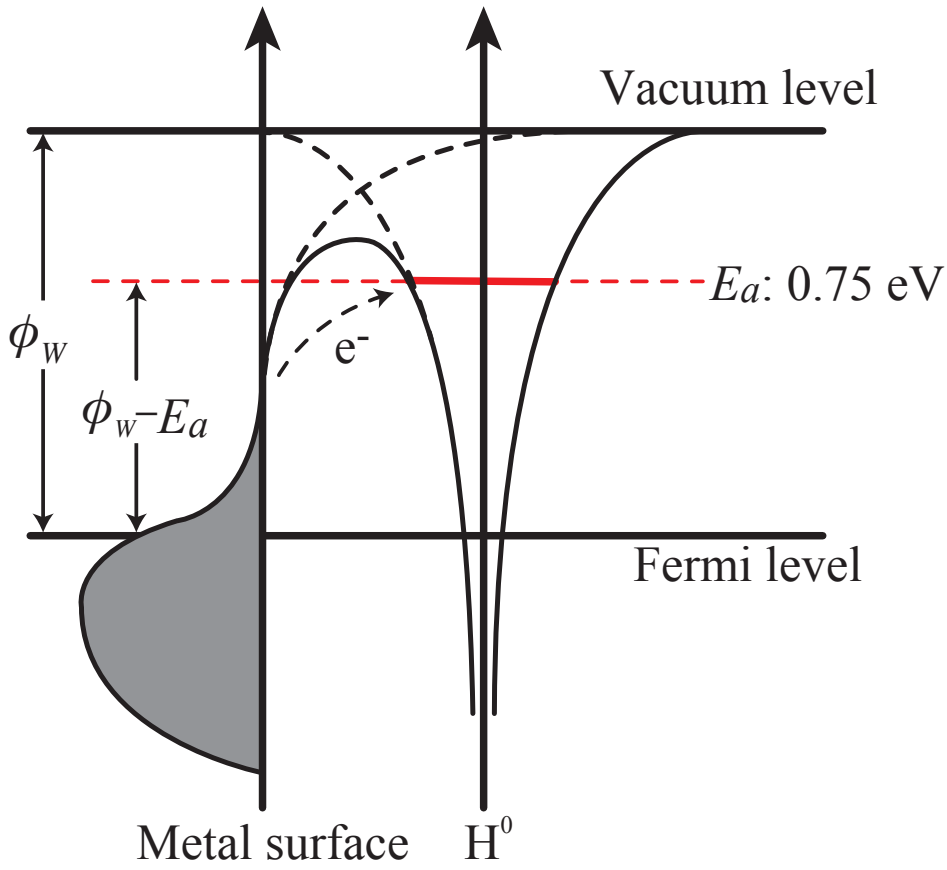

Fig. 6.17. Energy level diagram for negative hydrogen ion production, where ϕ_W is the work function of metal and E_a is the electron affinity.

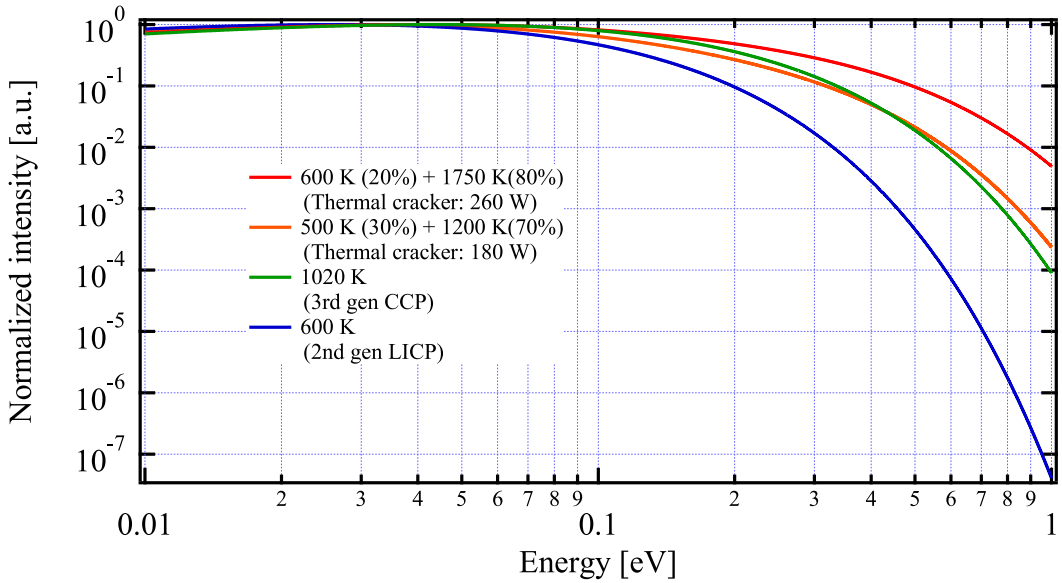

Fig. 6.18. Kinetic energy distributions for thermal cracking cell, 3rd gen CCP source and 2nd gen LICP source.

References

[1] J. D. Lawson, "Some Criteria for a Power Producing Thermonuclear Reactor", *Proc. Phys. Soc. B* **70(1)**, 6 1957.

[2] K. W. Ehlers, "Negative ion sources for neutral beam systems", *J. Vac. Sci. Technol. A* **1(2)**, 974 1983.

[3] M. Bacal, A. M. Bruneteau, W. G. Graham, G. W. Hamilton, and M. Nachman, "Pressure and electron temperature dependence of H^- density in a hydrogen plasma", *J. Appl. Phys.* **52(3)**, 1247 1981.

[4] J. R. Hiskes and A. M. Karo, "Generation of negative ions in tandem high-density hydrogen discharges", *J. Appl. Phys.* **56(7)**, 1927 1984.

[5] R. K. Janev, D. Reiter, and U. Samm, *Collision Processes in Low-Temperature Hydrogen Plasmas* (Forschungszentrum Zentralbibliothek, Julich, 2003).

[6] J. M. Wadehra, "Dissociative attachment to rovibrationally excited H_2", *Phys. Rev. A* **29**, 106 1984.

[7] K. Prelec and Th. Sluyters, "Formation of Negative Hydrogen Ions in Direct Extraction Sources", *Rev. Sci. Instrum.* **44(10)**, 1451 1973.

[8] D. Faircloth and S. Lawrie, "An overview of negative hydrogen ion sources for accelerators", *New J. Phys.* **20**, 025007 2018.

[9] A. L. Schmeltekopf, F. C. Fehsenfeld, and E. P. Ferguson, "Laboratory Measurement of the Rate Constant for $H^- + H \rightarrow H_2 + e$", *Astrophys. J.* **148**, L155 1967.

[10] M. Seidl, H. L. Cui, J. D. Isenberg, H. J. Kwon, B. S. Lee, and S. T. Melnychuk, "Negative surface ionization of hydrogen atoms and molecules", *J. Appl. Phys.* **79(6)**, 2896 1996.

[11] W. G. Graham, "Negative hydrogen ion production by low energy hydrogen atom bombardment of surfaces", *Phys. Lett. A* **73(3)**, 186 1979.

[12] A. Pargellis and M. Seidl, "Formation of H^- ions by backscattering thermal hydrogen atoms from a cesium surface", *Phys. Rev. B* **25**, 4356 1982.

[13] M. Seidl, S. T. Melnychuk, S. W. Lee, and W. E. Carr, "Surface production of negative hydrogen ions by reflection of hydrogen atoms from cesium oxide surfaces", *AIP Conf. Proc.* **210(1)**, 30 1990.

[14] S. T. Melnychuk and M. Seidl, "Reflection of hydrogen atoms from alkali and alkaline earth oxide surfaces", *J. Vac. Sci. Technol. A* **9(3)**, 1650 1991.

[15] T. Okuyama and Y. Mori, "Cesium catalysis effect of H^- ion production in volume production type of H^- ion source", *Rev. Sci. Instrum.* **63(4)**, 2711 1992.

[16] B. S. Lee and M. Seidl, "Surface production of H^- ions by hyperthermal hydrogen atoms", *Appl. Phys. Lett.* **61(24)**, 2857 1992.

[17] Y. Kim and M. E. Rudd, "Binary-encounter-dipole model for electron-impact ionization", *Phys. Rev. A* **50(5)**, 3954 1994.

[18] J. Yoon, M. Song, J. Han, S. H. Hwang, W. Chang, B. Lee, and Y. Itikawa, "Cross Sections for Electron Collisions with Hydrogen Molecules", *J. Phys. Chem. Ref. Data* **37(2)**, 913 2008.

[19] K. N. Leung, K. W. Ehlers, and M. Bacal, "Extraction of volume-produced H^- ions from a multicusp source", *Rev. Sci. Instrum.* **54(1)**, 56 1983.

[20] G. D. Alton, "Semi-empirical mathematical relationships for electropositive adsorbate induced work function changes", *Surf. Sci.* **175**, 226 1986.

Chapter 7

Further Applications of Versatile Sources

7.1 Atomic nitrogen production

As discussed in the section 2.1, atomic nitrogen plays an important role in the MBE (Molecular Beam Epitaxy) process. The triple bond between nitrogen molecules is the strongest bond among the covalent bonds as shown in Table 7.1. Unlike the thermal cracking source, microwave driven radical beam sources can dissociate nitrogen molecules by electron impact excitations.

Table 7.1. Bond-dissociation energies of molecules.

Gas species	Energy [eV]
H-H	4.519
H-O	4.436
H-OH	5.169
N-N	9.798
N≡N	9.805
O=O	5.165

Figure 7.1 shows the typical OES (Optical emission spectrum) of the nitrogen plasma produced in the 3rd gen CCP source of the plume mode. In the nitrogen plasma, the energy levels of the molecular nitrogen are lower than that of the hydrogen molecules [1]. Moreover, metastable nitrogen molecules ($A^3\Sigma_g^+$) are abundant in the low-energy nitrogen plasma because the transition from $A^3\Sigma_g^+$ to $X^1\Sigma_g^+$ are the spin-forbidden transition from the triplet to singlet states as shown in Fig. 7.2. The OES of 3rd gen CCP showed the

abundant first positive band ($B^3\Pi_g - A^3\Sigma_g^+$), second positive band ($C^3\Pi_u - B^3\Pi_g$), and a small amount of first negative band ($B^2\Sigma_u^+ - X^2\Sigma_g^+$). This suggested that the electron energy taking part in the electron impact excitation in the plasma is insufficient to dissociate the nitrogen molecules.

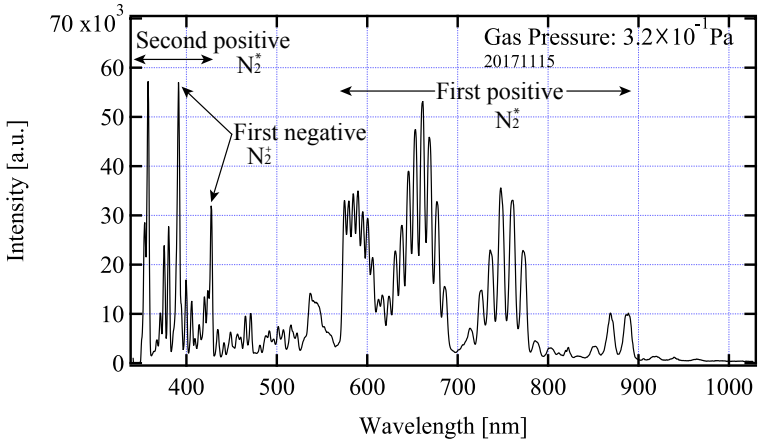

Fig. 7.1. A tyical optical emission spectrum of 3rd gen nitrogen CCP at 3.2×10^{-1} Pa with 75 W power input.

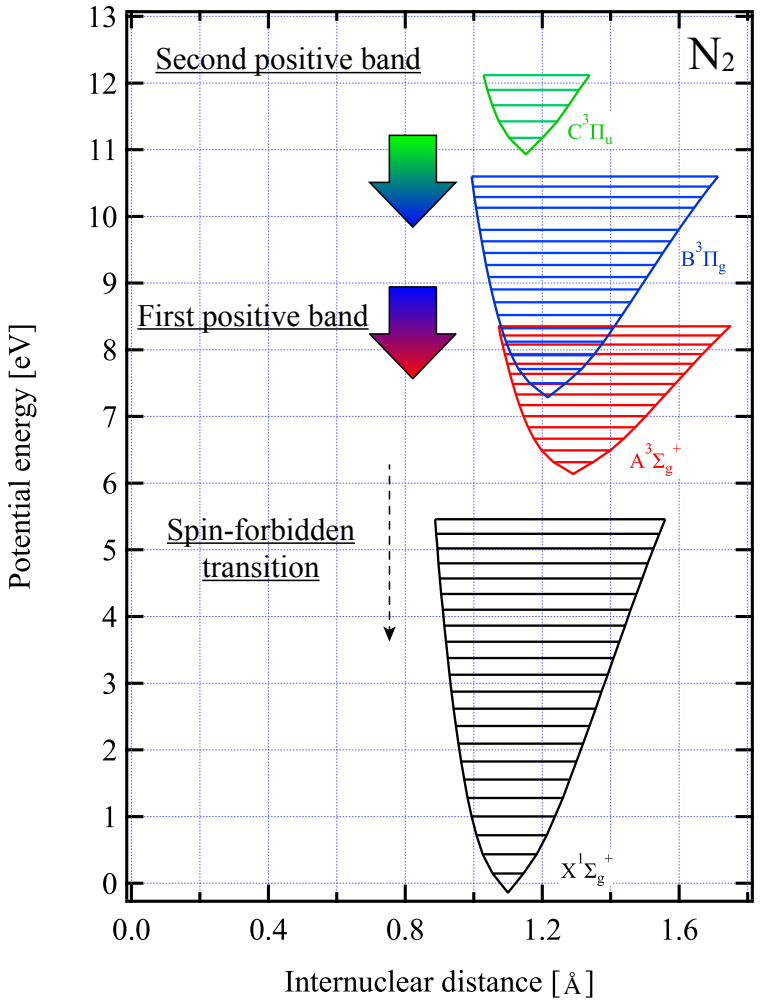

Fig. 7.2. Energy potential diagram of the nitrogen molecule [1].

Figure 7.3 (a) shows the typical OES of the nitrogen plasma taken by the 2nd gen LICP source. Most of the spectra were identical with that of the 3rd gen CCP, however, the spectrum of the 2nd gen LICP source exhibited lower peaks of the second positive band spectra. This suggests the electron energy in the nitrogen LICP is lower than that of the 3rd gen CCP. Figure 7.3 (b) shows the result of OES at the minimum gas pressure to sustain the plasma with 60 W maximum power input. Though the OES result has a substantial amount of first and second positive series spectra that belong to lower energy states, low operation pressure and higher input power contributes to enhance intensities of the three atomic nitrogen lines, 747 nm, 822 nm, and 869 nm in addition to the first negative series. This implies that low operation pressure and high power input are the important factor to produce the atomic nitrogen in the microwave excited LICP source.

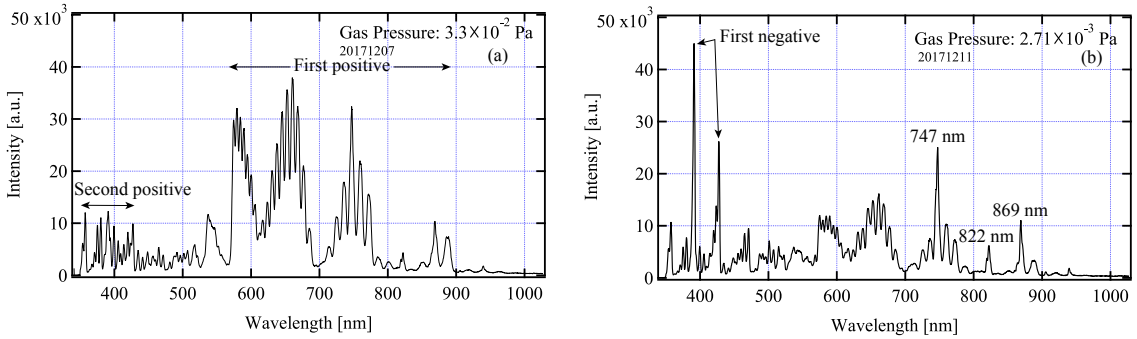

Fig. 7.3. A typical OES of 2nd gen nitrogen LICP. (a) 3.3×10^{-2} Pa with 50 W power input (b) 2.7×10^{-3} Pa with 60 W power input.

In order to apply additional power into the LICP source, the 1.5th gen LICP source ignited nitrogen plasma to see the atomic nitrogen production performance. Figure 7.4 shows the OES result of nitrogen plasma sustained in the 1.5th gen LICP source at 1.5×10^{-2} Pa with 100 W power input. The spectrum clearly showed three atomic nitrogen spectra including triplet fine structure of atomic nitrogen. Although the OES of 1.5th gen nitrogen LICP at the 5.0×10^{-2} Pa exhibited the similar tendency with Fig. 7.3 (b), the minimum operation pressure contributed to a higher degree of dissociation without meta-stable nitrogen molecules. An RF atomic nitrogen source for RF-MBE has an optimum discharge pressure at the 10^2 Pa. The intense atomic lines with poor molecular series in the OES of the 1.5th gen LICP is comparable with the result of the RF source in the Ref. [2] at the 500 W power input. Thus, the 1.5th gen LICP source under a low operation pressure and high power input conditions are appropriate for use of atomic nitrogen source to open a new chemical analysis of nitrogen atom based techniques.

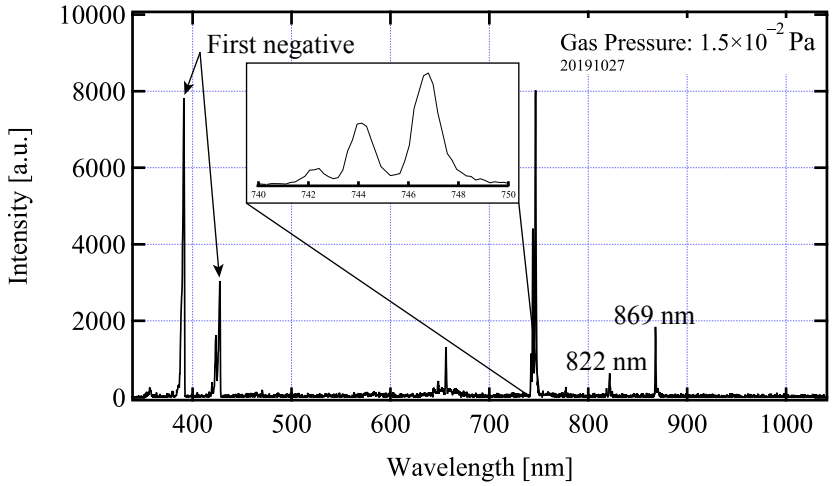

Fig. 7.4. An OES result of nitrogen plasma produced in 1.5th gen LICP source at 1.5×10^{-2} Pa with 100 W power input.

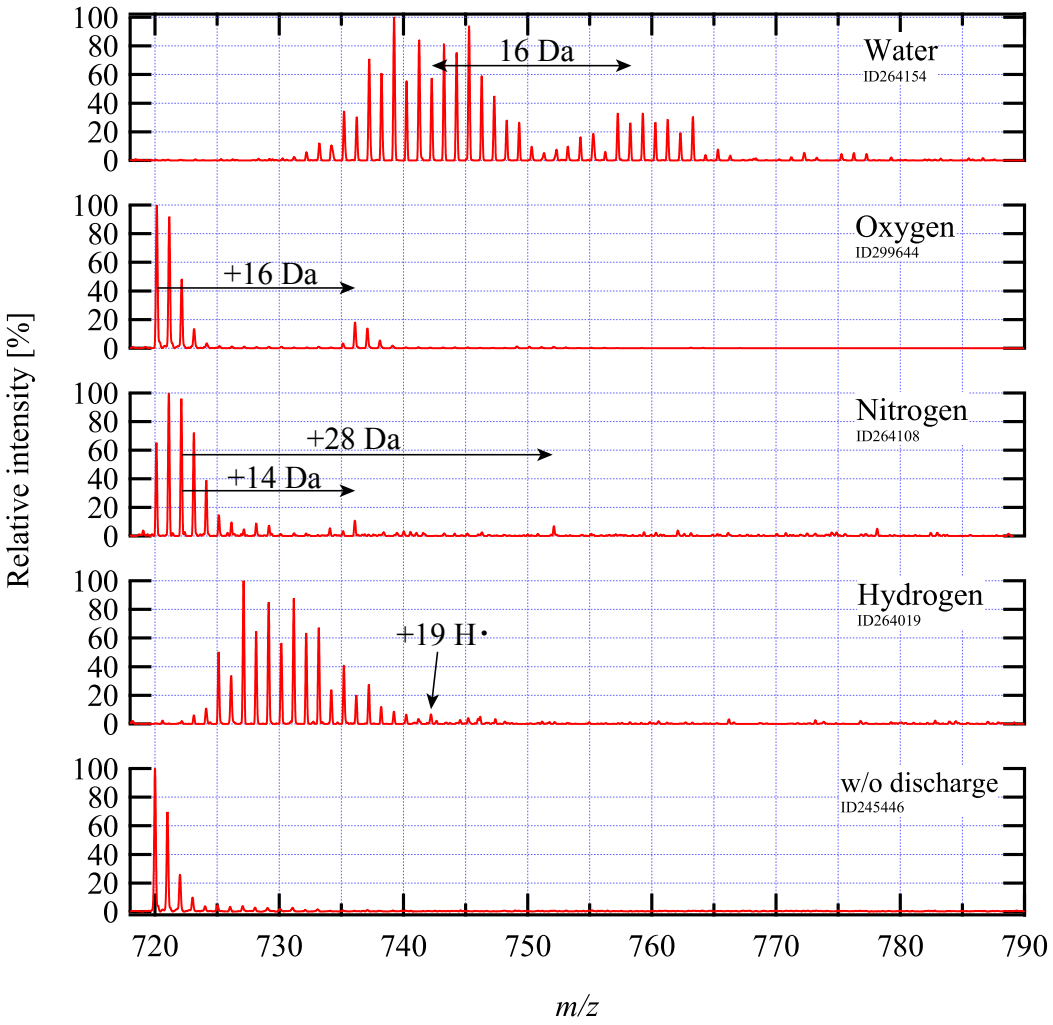

Fig. 7.5. Product ion spectra of several kinds of radical attachment to fullerene ion radical $C_{60}^{+\bullet}$ for 1.0 s reaction time using 2nd gen LICP source.

7.2 Double bond analyses with atomic oxygen

A principal difference between the thermal cracking source and a microwave excitation source is the variety in which microwave source produce radical species. In order to make full use of the microwave driven radical source versatility, the role of an atomic oxygen as a trigger of the biomolecular fragmentation was investigated. Before the atomic oxygen injection to the biomolecules, radical attachment reaction to the fullerene ion radical $C_{60}^{+\bullet}$ for several radical species was examined. Figure 7.5 shows the product ion spectra of radical attachment reaction to the $C_{60}^{+\bullet}$ with nitrogen, oxygen, and water vapor plasmas sustained in the 2nd gen LICP source for 1 s reaction time. Though the fundamental mechanism for the attachment reaction of radicals except for the hydrogen has not been investigated, the result showed clearly radical attachment attributable to radical species characterized in each discharge. Especially in the spectrum of the water vapor discharge, radical attachments at higher masses are observed compared with pure hydrogen discharge shown in Chapter 5. Unlike the case of pure hydrogen discharge, the time evolution spectra show two groups. Since the mass difference between the first and the second peak groups to compare in Fig. 7.5 show separation of 16 Da, O or OH• in the water vapor plasma seems to cause these characteristic mass spectra with two peak-groups. However, the reactive species which is/are responsible for these unique spectra cannot be specified at this moment apart from that a water plasma can produce at least two kinds of reactive species. Asakawa calculated the production energy of $C_{60}O^{+\bullet}$ from the trapped $C_{60}^{+\bullet}$ by injecting triplet atomic oxygen as shown in Fig. 7.6 [3, 4]. As the case of atomic hydrogen, ^{3}O easily attaches to the fullerene ion through the exothermic reaction regardless of incident atomic energy. The existence of ^{3}O has already confirmed by the OES of pure O_2 as 844.6 nm ($3p^3P \rightarrow 3s^3S^0$) in Fig. 5.15.

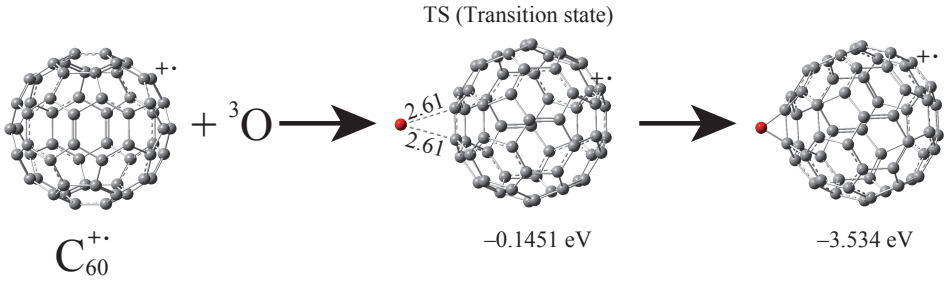

Fig. 7.6. A scheme of the oxygen atom attachment to fullerene ion radical $C_{60}^{+\bullet}$.

In this section, atomic oxygen irradiation to a phospholipid is discussed to apply for a double bond analysis. This study used phosphatidylcholine (PC 18:1(9Z)), which contains a single fatty acid chain, as the model compound. Conventional LE-CID (low-energy collision induced dissociation) spectrum shown in Fig. 7.7 does not have fragment

ions from carbon chains but only have the head-group fragment ions [5].

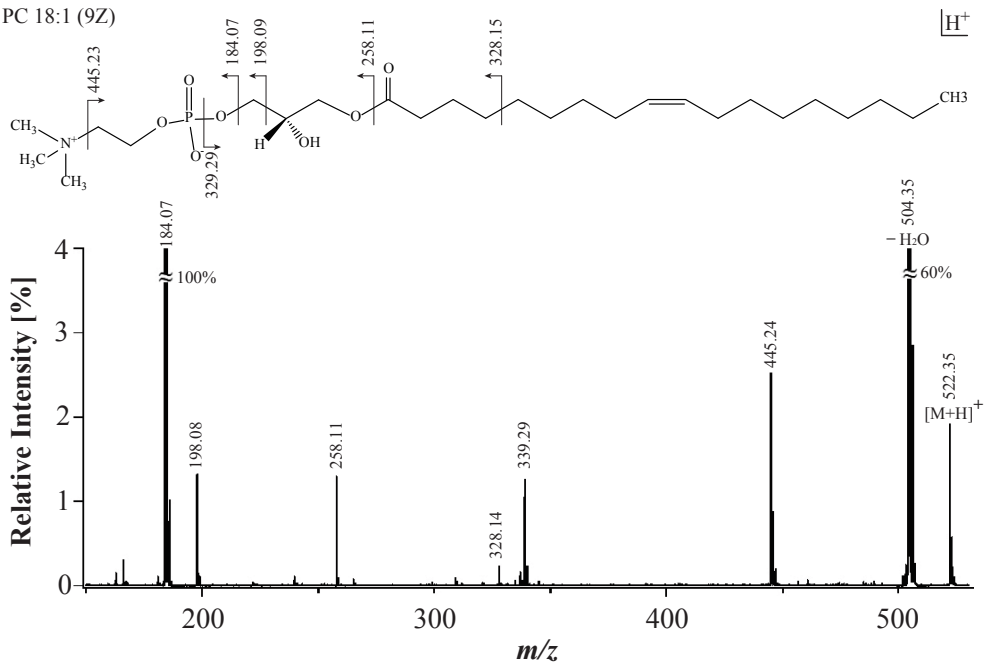

Fig. 7.7. A CID-MS/MS mass spectrum of phosphatidylcholine.

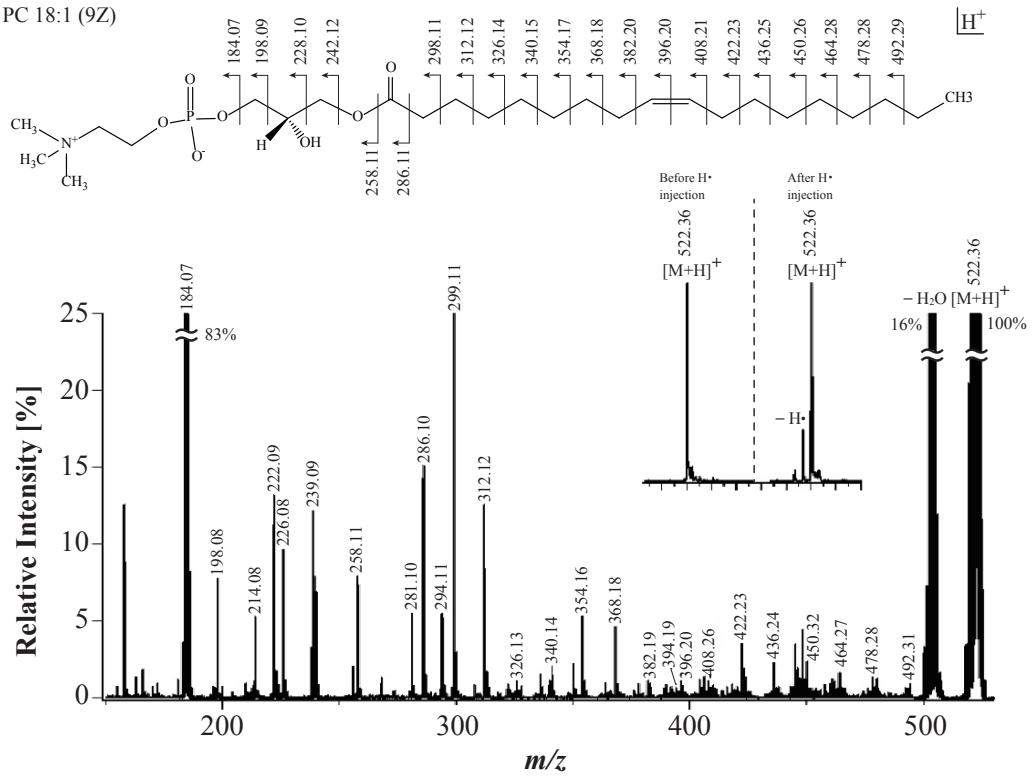

Fig. 7.8. A HAD-MS/MS spectrum of singly protonated phosphatidylcholine (Lyso-PC 18:1(9Z)). Inset shows isotopic distributions of precursor ion before and after atomic hydrogen injection.

In contrast, HAD spectrum of singly protonated phosphatidylcholine (Lyso-PC 18:1(9Z), 526.36 Da, 10 pmol) formed through the interaction of hydrogen radical with the isolated precursor ions inside the ion trap as shown in Fig. 7.8. Supplementary collisional activation was applied to the precursor ions after H irradiation to enhance the product ion intensity [6]. The result exhibited cleaving of both carbon single bond and double bond. Figure 7.9 shows the mechanism of that fragmentation due to the H• abstraction obtained by DFT calculation [4]. The corresponding transition state barrier for the hydrogen abstraction (TS1-1) has the energy of 0.35 eV; the products of R1 and H_2 are more stable than the reactants by 0.43 eV. The transition state barrier for homolytic C-C bond cleavage (TS1-2) from the viewpoint of the R1 is 1.44 eV. Therefore, approximately 0.025% of H• in the kinetic energy distribution of 260 W thermal cracking cell can contribute to the C-C bond cleavage by HAD as an endoergic reaction.

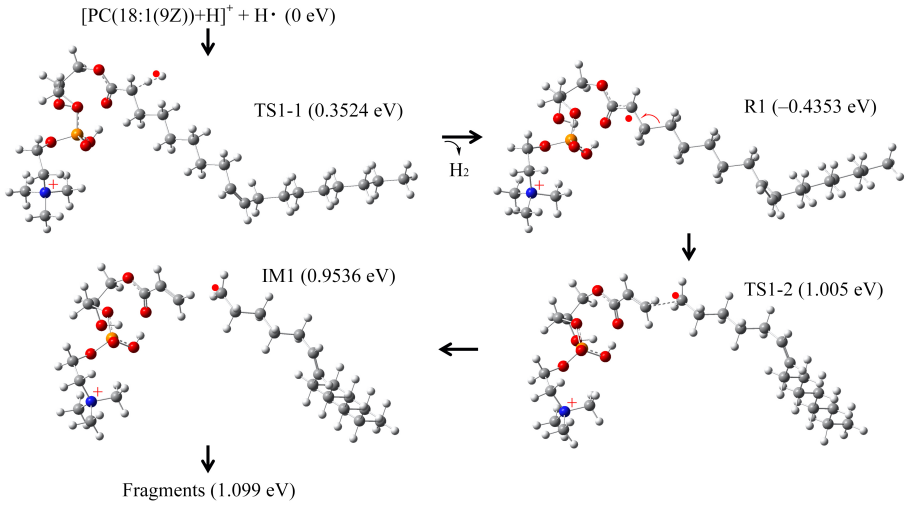

Fig. 7.9. Fragmentation pathway of PC 18:1 (9Z) by H· abstraction.

Figure 7.10 shows the mass spectrum of saturated and unsaturated phospholipid with dissociation induced by water vapor LICP injection. The unsaturated phospholipid has an oxidized product ions unlike saturated phospholipid. The experimental result implies that the atomic oxygen irradiation to the phospholipid can induce the cleavage of the carbon double bond, because there are no hydrogen radicals in the energy distribution of 600 K for 2nd gen hydrogen LICP (0.49 ppb). Figure 7.11 shows the fragmentation pathway of the fragmentation by ^{3}O attachment obtained by DFT calculation. According to the result, the fragment ion produced by water vapor LICP irradiation is attributable to the interactions between R2 and the abundant background O_2 gas in Fig. 7.11. The generated radical immediately reacts with O_2 and a fragment ion was generated by subsequent radical-induced dissociation induced by triplet atomic oxygen (OAD: Oxygen Attachment Dissociation) when O_2 was present in the ion trap. The reaction between the analyte radical and O_2 hampers the identification of the double bond position in the fatty acyl

chain. Because the OAD process is exothermic reaction, the 2nd gen LICP source that cannot produce energetic atomic hydrogen to induce the C-C cleavage is appropriate for double bond analysis.

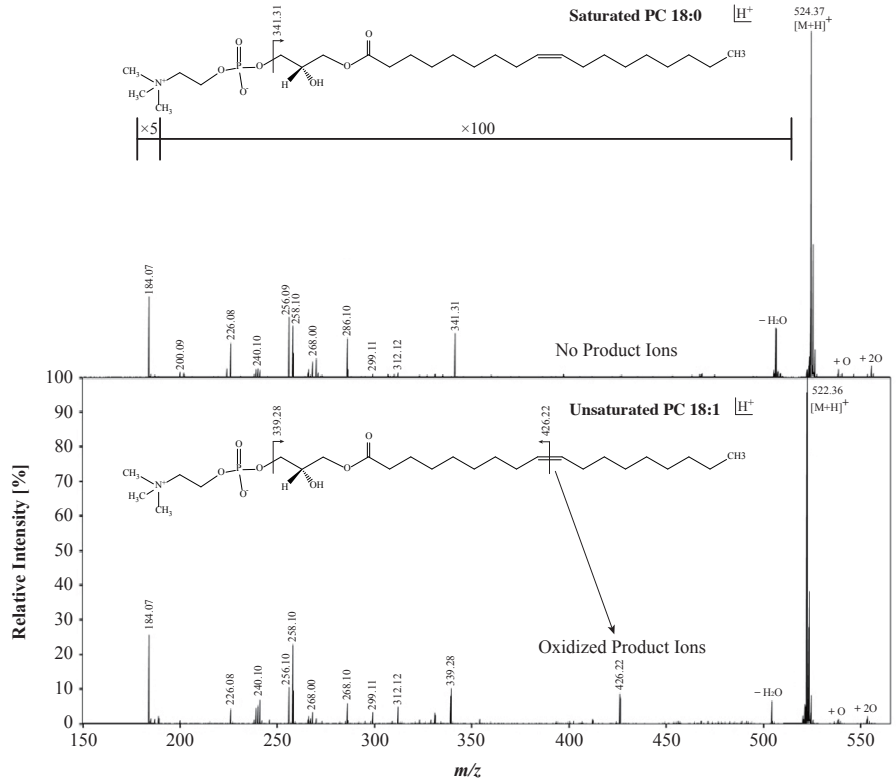

Fig. 7.10. OAD-MS/MS spectrum of saturated and that of unsaturated phospholipid with dissociation induced by water vapor LICP.

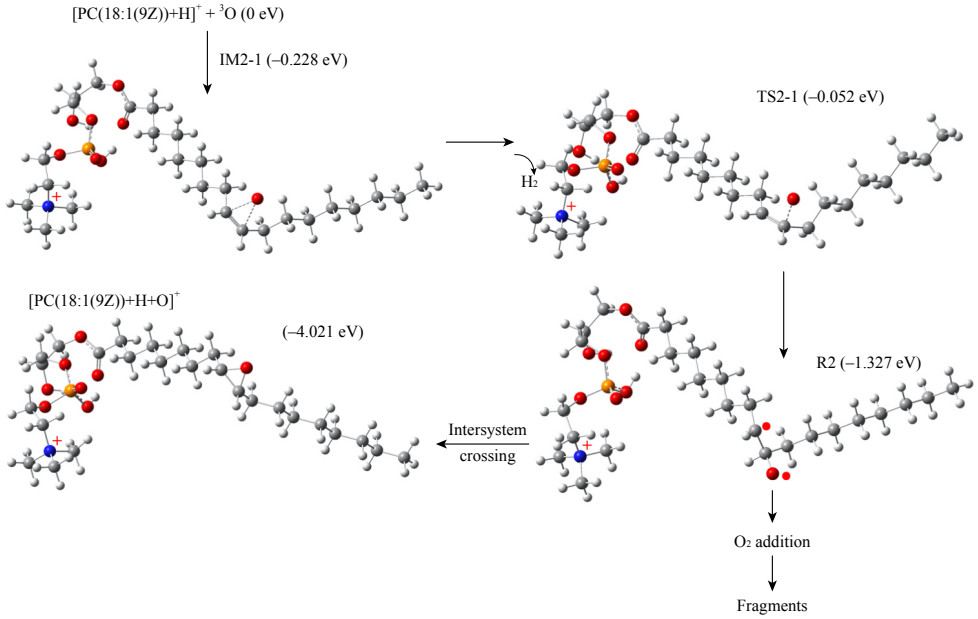

Fig. 7.11. Fragmentation pathway of PC 18:1 (9Z) by ^{3}O attachment.

7.3 Atomic hydrogen temperature of 1.5th gen LICP source

As described in the section 5.2, atomic hydrogen produced in the 2nd gen LICP source did not show any cleavages through a HAD reaction for both hydrogen and water vapor plasmas. Meanwhile, atomic hydrogen formed in the water plasma of the 1st gen LICP source achieved HAD reaction only once at the 120 W power input. These results suggest that the 1st gen LICP source may have been worked as a 1.5th gen LICP source with a high efficiency power transmission to the source plasma at a higher power input than the limit of 2nd gen LICP source. Thus, the atomic hydrogen produced in the high power LICP source has a possibility to realize HAD reaction. In order to investigate the effect of the input power on the atomic temperature formed in the LICP source, the velocity distribution function of the hydrogen atoms emitted from the 1.5th gen LICP source were measured. The 1.5th gen LICP source requires hydrogen gas flow above 5 sccm, input power above 100 W, and well impedance matched condition to sustain the LICP with high brightness mode. Figure 7.12 shows the measured and theoretical curves of velocity distribution functions for atomic hydrogen produced in the 1.5th gen LICP source with 100 W power input and 5 sccm hydrogen gas flow. The red line indicates the measured curve, while black lines correspond to the theoretical curves from 700 K to 2000 K with 100 K step temperature. According to the graph, a rising slope of the measured curve is steeper than the theoretical curves on the assumption of Maxwellian. This implies that the velocity distribution function of the atomic hydrogen produced in the 1.5th gen LICP source does not obey Maxwellian but has a single velocity component distribution function. Although determination of the atomic temperature from the experimental system may be impossible, a series of experiments suggests that the steep rising slope attributable to the fast velocity component may realize peptide cleavages through the HAD reaction.

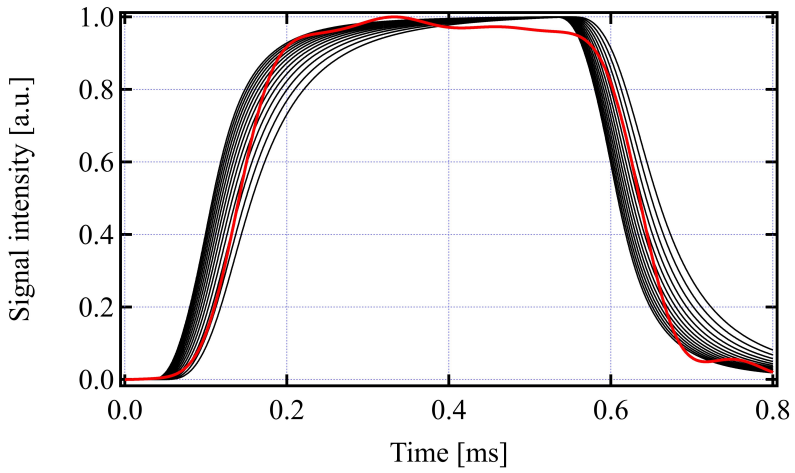

Fig. 7.12. The measured and thoretical curves of velocity distribution functions for atomic hydrogen produced in the 100 W 1.5th gen LICP source. The red curve indicates the measured curve, while black lines are corresponding to the thoretical curves from 700 K to 2000 K with 100 K step temperature.

7.4 Radical heating by RF field induction

As discussed in the previous section, development of a radical heating method to realize HAD reaction with a single LICP source is a promising scheme. For a plasma produced with 2.45 GHz ECR, an ion plasma frequency ω_{pi} is higher than 13.56 MHz RF frequency, while the ions in the ECR plasma can not follow the oscillating microwave electric field. The ion species produced in the ECR plasma have a possibility to be accelerated by additional RF electric field. In this section, preliminary results for dual frequency LICP source is described.

Figure 7.13 shows the scematic diagram of the dual frequency LICP source. The source possesses an additional 20 turns spiral antenna for 13.56 MHz RF power input at the vaccum pressure side. The RF power is delivered through an impedance matching network (Tokyo HY-POWER, MB-300) as shown in Fig. 7.14 from an RF power supply (Tokyo HY-POWER, RF-300).

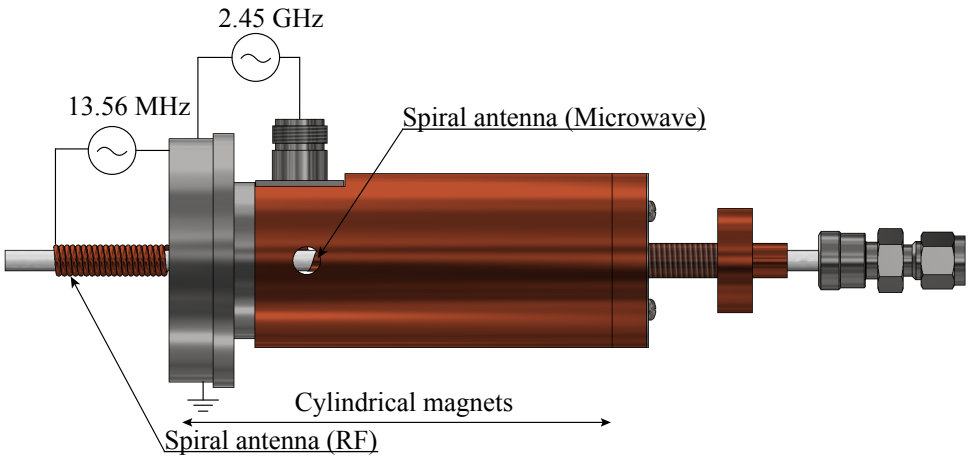

Fig. 7.13. A schematic diagram of the dual frequency LICP source.

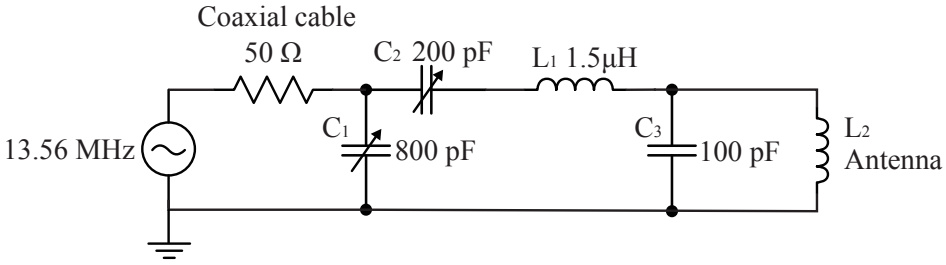

Fig. 7.14. An original matching network of MB-300(Tokyo HY-POWER).

The original matching network could not reduce the reflection power due to the off resonance of the circuit due to narrow range of tuning coverage to the small spiral antenna. In order to explore the appropriate matching circuit, eight types of impedance matching

circuits were tested as shown in Figs. 7.15. Eventually, Fig. 7.15 (h) showed a wide matching coverage for the 20 turns spiral antenna made of a 1.5 mm diameter copper wire at 13.56 MHz.

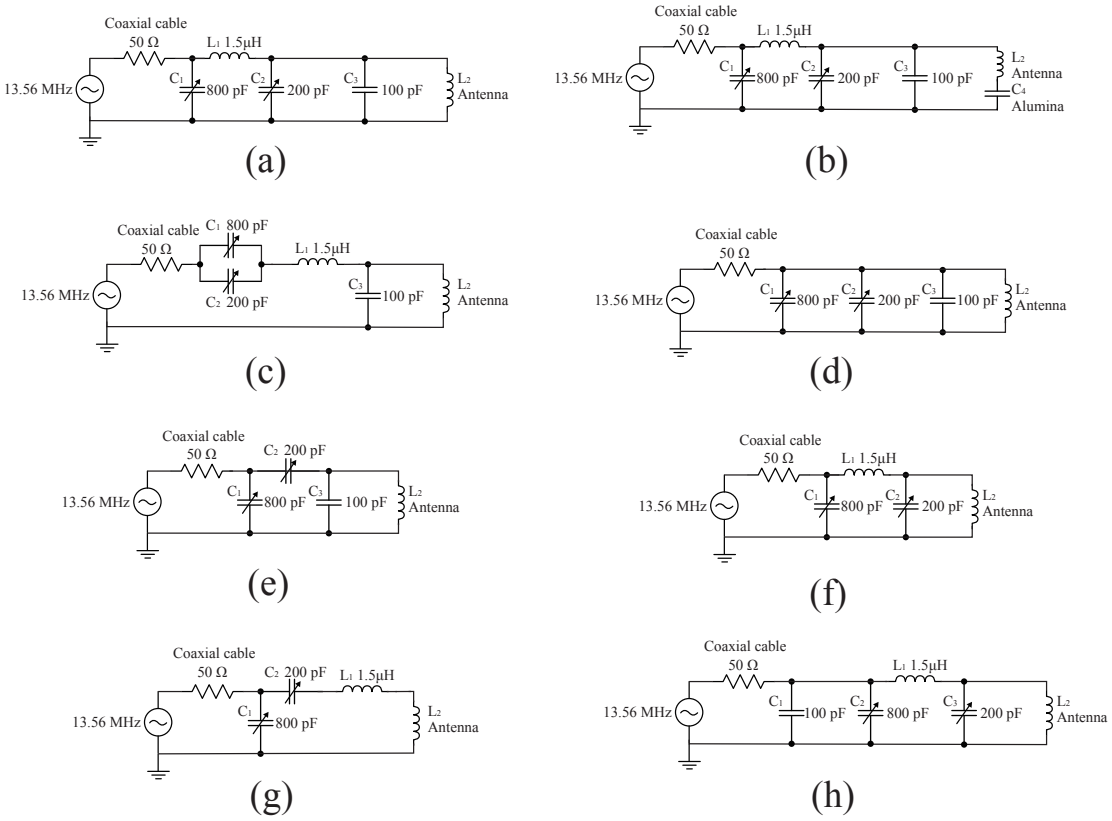

Fig. 7.15. Eight types of matching networks for 13.56 MHz RF.

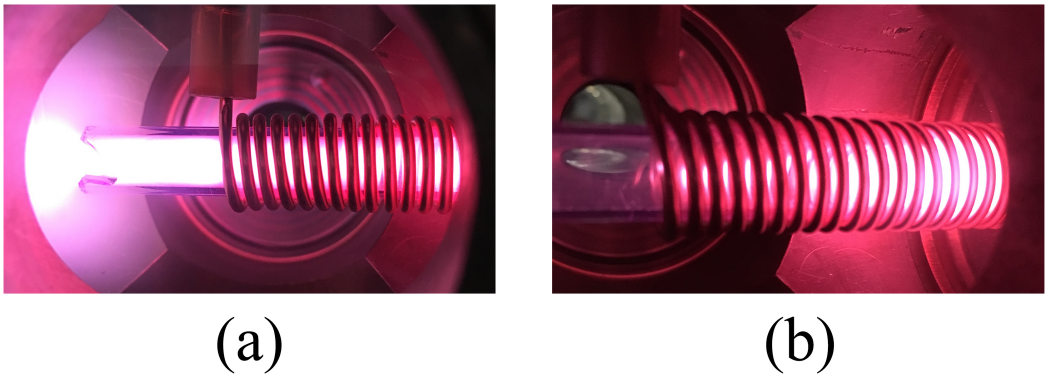

Fig. 7.16. Two types of discharge modes of the dual frequency LICP source. (a) High pressure above 2.0 Pa. (b) Below 2.0 Pa.

Figures 7.16 show the two plasma modes realized in dual frequency discharge. The extended plasma shown in Fig. 7.16 (a) was sustanined only above 2.0 Pa hydrogen atmosphere, the optical emission characteristic is similar to CCP which exhibit the low

degree of dissociation. In contrast, Fig. 7.16 (b) exhibited the high degree of dissociation with LICP like optical characteristic below 2.0 Pa hydrogen pressure. Figure 7.17 shows the example of the optical emission spectrum of the dual frequency discharge at 1.0 Pa hydrogen pressure. According to the result, the dual frequency mode exhibited the intense emission more than the simple addition of single discharges. High power input to the spiral antenna installed at the atmospheric pressure side shortens the lifetime due to the oxidization of the antenna surface. Therefore, if the RF power input is possible to compensate the microwave power consumption, the realization of both higher radical temperature and longer antenna lifetime is expected. A miniaturized adaptor to feed the RF power to the small space at the source tip is necessary because the large current setup can not be installed to the velocity distribution function measurement system. This scheme, however, requires substantial amount of work to realize efficient RF matching with small size circuit components.

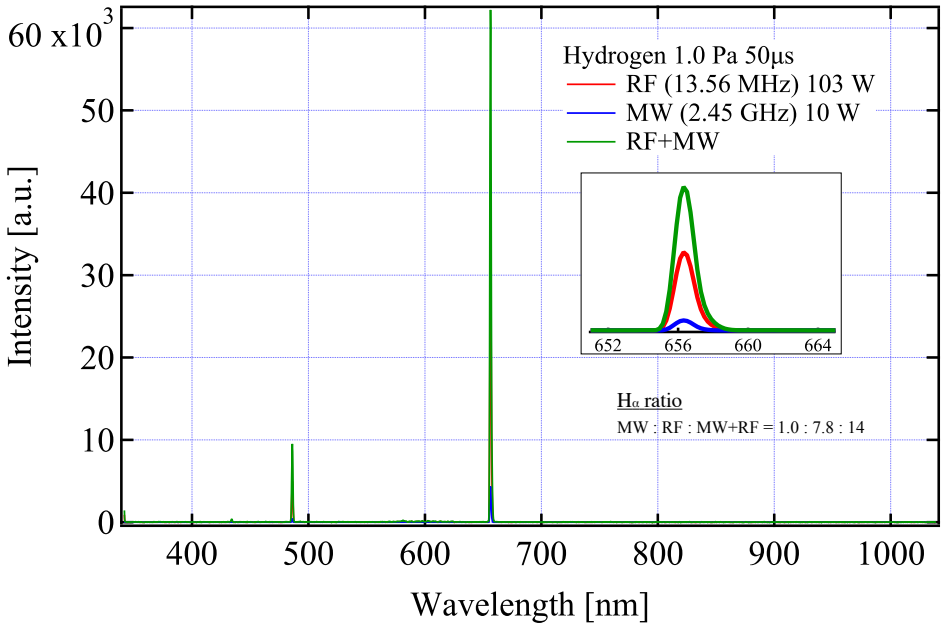

Fig. 7.17. An example spectrum of dual frequency discharge.

7.5 Conclusion

In this chapter, the alternative usages and future challenges of 2nd gen radical sources have explored.

1. Although the attachment reaction to the fullerene ion has not been confirmed except for hydrogen radicals, other kinds of radical irradiation to the trapped fullerene ion, for example oxygen and nitrogen radicals, can attach to the $C_{60}^{+\bullet}$. This finding is an

effective way to confirm the existence of neutral H, N, and O atoms because the $C_{60}^{+\bullet}$ is considered insensitive to neutral molecules.

2. Most of the RF driven atomic nitrogen sources desiged for MBE applications require high operating pressure and high power input, however, the ECR based nitrogen LICP can operate the source below the 10^{-2} Pa. In order to enhance the dissociation of strong nitrogen bonds, more stable operation with higher input power and lower gas pressure is desirable to realize intense atomic nitrogen beam production without molecules.

3. A new double-bond analytic method, OAD, has been invented. A triplet atomic oxygen attachment to the phospholipid ions within the oxygen atmosphere induces cleavage at the carbon double-bonds. Meanwhile, energetic atomic hydrogen induces the cleavage at the both single and double bonds of the phospholipid ions. Therefore, the LICP sources that can produce low-energy atomic oxygen without energetic radicals are suitable to double-bond analyses rather than the CCP and thermal cracker sources. Conventional method utilizes the ozone gas to induce the double bond cleaving of lipids under the high gas pressure condition [7]. Whereas the OAD method resolved these defects of the conventional way at the both points on safety and operating pressure ($\approx 10^{-3}$ Pa).

4. The velocity distribution function of 1.5th gen LICP source suggested the existence of the higher energy component than typical Maxwellian distribution. Experimental result of the HAD reaction with water vapor plasma discussed in Chapter 5 may have been originated from the high energy component of high input power LICP. Thus, increase in the input microwave capacity to 2nd gen LICP source will contribute to realization of HAD cleaving with LICP source.

5. Combination discharge of 2.45 GHz microwave and 13.56 MHz RF was performed on the 2nd gen LICP source to increase the radical temperature in the ECR plasma. A small inductance RF antenna was matched by the modified matching network configured as a pi-type low pass filter. The optical emission spectrum showed the higer Balmer-alpha intensity compared to each single RF and microwave discharge, however, the discharge system have not been optimized. In the current setup, the incomplete connection to the ground of the RF spiral antenna that just touches the LICP flange at one point of the antenna induces discharge fluctuation and unstable power reflection. Although the preliminary result showed the possibility to realize the higher radical temperature by combination of RF and microwave powers, engineering developments are remained toward the stable operation.

References

[1] A. Lofthus, "The Spectrum of Molecular Nitrogen", *J. Phys. Chem. Ref. Data* **6(1)**, 113 1977.

[2] T. Ohachi, N. Yamabe, H. Shimomura, T. Shimamura, O. Ariyada, and M. Wada, "Measurement of nitrogen atomic fulx for RF-MBE growth of GaN and AIN on Si substrates", *J. Crystal Growth* **311**, 2987 2009.

[3] D. Asakawa (private communication).

[4] M. J. Frisch, G. W. Trucks, H. B. Schlegel, G. E. Scuseria, M. A. Robb, J. R. Cheeseman, G. Scalmani, V. Barone, G. A. Petersson, H. Nakatsuji, X. Li, M. Caricato, A. V. Marenich, J. Bloino, B. G. Janesko, R. Gomperts, B. Mennucci, H. P. Hratchina, J. V. Oritz, A. F. Izmaylov, J. L. Sonnenberg, D. Williams-Young, F. Ding, F. Lipparini, F. Egidi, J. Goings, B. Peng, A. Petrone, T. Henderson, D. Ranasinghe, V. G. Zakrzewski, J. Gao, N. Rega, G. Zheng, W. Liang, M. Hada, M. Ehara, K. Toyota, R. Fukuda, J. Hasegawa, M. Ishida, T. Nakajima, Y. honda, O. Kitao, H. Nakai, T. Vreven, K. Throssell, J. J. A. Montgomery, J. E. Peralta, F. Ogliaro, M. J. Bearpark, J. J. Heyd, E. N. Brothers, K. N. Kudin, V. N. Staroverov, T. A. Keith, R. Kobayashi, J. Normand, K. Raghavachari, A. P. Rendell, J. C. Burant, S. S. Iyengar, J. Tomasi, M. Cossi, J. M. Millam, C. Adamo, R. Cammi, J. W. Ochterski, R. L. Martin, K. Morokuma, O. Farkas, J. B. Foresman, and D. J. Fox, *Gaussian 16*, revision A.03; Gaussian, Inc., Wallingford, CT, 2016.

[5] H. Takahashi, Y. Shimabukuro, D. Asakawa, S. Yamauchi, S. Sekiya, S. Iwamoto, M. Wada, and K. Tanaka, "Structural Analysis of Phospholipid Using Hydrogen Abstraction Dissociation and Oxygen Attachment Dissociation in Tandem Mass Spectrometry", *Anal. Chem.* **90(12)**, 7230 2018.

[6] D. L. Swaney, G. C. McAlister, M. Wirtala, J. C. Schwartz, J. E. Syka, and J. J. Coon, "Supplemental Activation Method for High-Efficiency Electron-Transfer Dissociation of Doubly Protonated Peptide Precursors", *Anal. Chem.* **79(2)**, 477 2007.

[7] M. C. Thomas, T. W. Mitchell, D. G. Harman, J. M. Deeley, R. C. Murphy, and S. J. Blanksby, “Elucidation of Double Bond Position in Unsaturated Lipids by Ozone Electrospray Ionization Mass Spectrometry”, *Anal. Chem.* **79(13)**, 5013 2007.

Chapter 8

Conclusions

This study discussed production mechanisms, velocity distribution determination, and applications of low-energy atomic hydrogen sources. Developed microwave driven atomic hydrogen sources are classified into two groups by the geometry of antennas: CCP (capacitively coupled plasma) and LICP (localized inductively coupled plasma) types. Figure 8.1 summarizes the progress of the radical source development. Several generations of radical sources were developed with some improvements in hardware structure as shown in Fig. 8.1. In order to compare the performance of developed sources, the thermal cracking type atomic hydrogen source that is the most typical hydrogen atom production method was also developed in this study. An optical spectrometer and developed velocity distribution measurement system determined the characteristics of three types of radical sources. The low-energy atomic hydrogen and oxygen produced by the developed radical sources open new possibilities for biomolecular analyses.

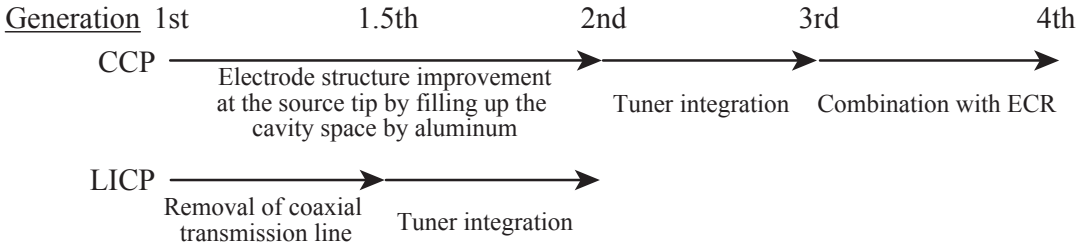

Fig. 8.1. A progress of the microwave driven radical source development.

Chapter 1 provided the information on the demand emerging from the life science study for stable low-energy atomic hydrogen production to accelerate the structural analyses of biomolecules. Conventional electron based techniques revealed some complex structure of fragile biomolecules, however, these methods were possible to apply for limited analyzable targets. Contrary to the conventional ways, neutral hydrogen based HAD (Hydrogen Attachment/Abstraction Dissociation) method has a possibility to drastically

expand the analyzable target species. In this chapter, problems of existing techniques, research methodology, and scope of this study were stated.

Chapter 2 illustrated the first phase of the radical source development. In order to produce several kinds of reactive radical species, microwave excitation type radical sources have been developed. An RF (radio frequency) based plasma generator does not produce abundant high temperature atomic components and can easily realize proper antenna structure to produced radical species. This study adopted the effusion from the RF plasma as a low-energy radical beam production to satisfy the HAD's criterion without excessive energetic species, while there are several other neutral beam production methods. Examination for electrode structures of the CCP type radical sources revealed that the electric field concentration at the source tip is an important factor to ignite and sustain the CCP under the low pressure condition. Several improvements in the stray capacitance/inductance components of the spiral antenna excited LICP source based on the ECR (electron cyclotron resonance) were made. The 1.5th gen LICP source exhibited the high degree of dissociation from the OES (optical emission spectroscopy) result without any observable molecular band spectra. Although typical MHz-RF driven magnetized ICP (inductively coupled plasma) shows the E (electrostatic) - H (electromagnetic) - W (propagating wave) mode transitions due to the change in the field configuration within the plasma, that phenomena for the GHz-RF driven ECR plasma excited by multi-turns spiral antenna have not been investigated. A jump on the Balmer-alpha line intensity corresponding to the mode transition in the developed 1.5th gen LICP source was observed.

Tuner-integrated type radical beam sources are discussed in Chapter 3. The developed CCP and LICP radical sources in Chapter 2 requires fine impedance matching to the load by a troublesome adjustment of the externally equipped triple stub tuner. For long-time operation, microwave leakage and heat loss from the stub tuner were not negligible. In order to resolve these problems, tuner-integration to the radical sources were carried out. A plunger structure realized an operation without the power loss at the triple stub tuner and easier tuning procedure by tuner integration for the CCP radical source. The 3rd gen CCP source can produce the plasma plume which is the extracted ions by positive self bias voltage under the high gas pressure, high power input, and efficient impedance matching condition. Meanwhile, the ECR assisted 4th gen CCP source required more difficult matching operation than the 3rd gen CCP radical source due to unpredictable capacitance component in the source cavity. The built-in type CCP source can be further improved by expanding the tunable region on the Smith chart because the single plunger/stub circuit is highly restricted in the matching condition.

Whereas, the LICP source had achieved low operating pressure ($\sim 10^{-3}$ Pa), high degree of dissociation, and simple matching system by the tuner-integration. When the antenna and the permanent magnets were properly arranged, the assembled source has exhibited the possible mode jumps. This characteristic plasma coupling to microwave

power of the newly developed multi-loop locally excited microwave ICP is considered to realize the high efficiency in atom production. The LICP source can produce a wide variety of electrically neutral species from selections of gas/liquid samples without exposing the produced plasmas to any metallic component that recombines atoms on the surface.

In Chapter 4, in order to clarify the velocity distribution functions of the developed radical sources, MSTOF (mass separated time of flight) based velocity distribution function measurement system was developed. The adoption of the pulse counting measurement for poor atomic hydrogen signal achieved the data acquisition with sufficient S/N ratio by maintaining the high vacuum condition below 6×10^{-5} Pa during the operation and the suppression of the background noises by beam skimmers and cooling shroud. Temperature of the atomic hydrogen was determined by employing the χ^2 test to the theoretical curve. As a result, atomic hydrogen temperature produced in the 2nd gen LICP source is about 600 K. In contrast, hydrogen atoms formed in the thermal cracking source have two representative temperatures attributable to the tungsten filament and capillary temperatures. The 3rd gen CCP source requires very high gas flow rate ($\geqq$ 60 sccm) to ignite and sustain the plasma plume. In order to measure the atomic temperature of the CCP, the pumping speed at the flight tube was increased to satisfy the sufficient S/N ratio. As a result, the atomic temperatures from 872 K to 1027 K were acquired for the 3rd gen CCP source.

Chapter 5 demonstrated the peptide analysis by using developed radical sources. Before the biomolecular analysis, radical transportation from the source to the reaction chamber was confirmed by hydrogen attachment reaction to fullerene ion. The experimental results concluded that the 3rd gen CCP and 2nd gen LICP source have sufficient radical production rate comparable to the thermal cracking source, while the 2nd gen CCP source did not achieve enough amount of radical flux to the ion trap. Hydrogen radical irradiation from the 2nd gen hydrogen and water LICP to a peptide ion could not cleave the peptide at all due to its low radical temperature ($\sim$ 600 K). In contrast, hydrogen radicals produced in the 3rd gen hydrogen and water CCP ($\approx$ 930 K) and 1.5th gen water LICP achieved cleavage of the peptide backbone through the HAD processes. Although the atomic temperature of the 1.5th LICP source could not be measured by the velocity distribution measurement system, as they can operate at a higher operating pressure, these experimental results imply that their temperature are higher than that of 2nd gen LICP and lower than that of the thermal cracking cell. A series of experimental results has shown a good agreement to the theoretical results calculated by density functional theory.

In Chapter 6, the developed three types of radical sources are utilized as a probe for the negative hydrogen ion (H^-) surface production at the cesiated low work function surface. The difference in energy distribution functions of the produced hydrogen atoms experimentally revealed that the both H^- ion surface production and destruction processes require some threshold energies. The 2nd gen LICP source could not achieve the atomic hydrogen energy to satisfy the escaping energy for produced H^- ions to leave the cesiated

surface. Meanwhile, the tail of the thermal distributions of produced hydrogen atoms from the 3rd gen CCP and thermal cracking sources meet the requirement for H^- surface production and associative detachment of the H^- ions. Experiments with a stable higher energy hydrogen atom flux, and monitoring the ion source parameters will contribute to the further understanding of the H^0 behavior under the ion source operating conditions. These empirical results regarding to the atomic hydrogen energy in each radical source are qualitatively identical with the results from the HAD experiments.

Chapter 7 discussed the further applications of the developed sources for usages of not only as atomic hydrogen sources but also versatile beam sources for wide variety of radicals. A several kinds of radical irradiation to the fullerene ion was investigated. The result empirically showed that the H, N, and O atoms can attach to fullerene ion as an exothermic reaction. This radical attachment reaction to the fullerene ion is an effective way to confirm the existence of neutral H, N, and O atoms. Nitrogen gas introduction to the ECR-LICP source exhibited the intense atomic nitrogen spectra with less molecular signal under the low gas pressure and high input power (60-100 W) condition. A new technique to elucidate the double-bond position of lipid ions was realized by triplet atomic oxygen (^3O) injection. The ^3O irradiation to the lipid ions induces the cleaving molecules at the double-bond position selectively, while the energetic atomic hydrogen injection induces the sequential cleavages.

The 1st gen LICP source showed the HAD reaction with its water plasma only once as a 1.5th gen driving mode. The more stable 1.5th gen LICP source exhibited the velocity distribution function steeper than Maxwell distributions. Thus, the high energy component in the energy distribution may have been contributed to the realization of HAD reaction by this source. In order to realize both HAD and OAD by a single LICP source, energy control and increase in input power capacity to next generation LICP source are expected.

Lastly, the future perspectives for further applications and developments in biomolecular analyses based upon the radical induced dissociation are enumerated below.

1. The high operating pressure of the 3rd and 4th gen CCP source is a problem for both HAD system and velocity distribution function measurement system. Further understanding of the microwave plasma plume may contribute to a better CCP operating condition. This may contribute to the elucidation of the HAD mechanism by the precise atomic temperature/energy control by the CCP.

2. Latest 2nd gen LICP source can not apply high power to the antenna due to the external antenna configuration, while the well impedance matched condition is obtained easily. According to the experimental results of 1.5th gen water HAD, realization of the high power LICP will greatly contribute to the mass spectrometric research. Thus, better electric insulation at the atmospheric pressure side, improved

microwave transmission to the antenna installed at the vacuum side, or double antenna installation for both vacuum and atmospheric pressure sides may increase the power capacity to the LICP source to realize both HAD and OAD reactions by a single radical source.

Acknowledgement

First and foremost, the author should like to express my sincere gratitude to my advisor Prof. Motoi Wada for his excellent support and guidance for four years since the author entered Plasma Physics Laboratory in 2016. The author should also like to thank Prof. Mamiko Sasao of Tohoku University, Dr. Hitoshi Yamaoka of RIKEN SPring-8 center, Dr. Nozomi Tanaka of Osaka University, and Dr. Daiki Asakawa of National Institute of Advanced Industrial Science and Technology for the valuable discussions. The author would like to give my thank to Dr. Kenta Doi, Shingo Masaki, Kentaro Yoshioka, Ippei Yamada, James Hernandez II, and all the members of Plasma Physics Laboratory for worthwhile casual discussions.

The author must appreciate the technical and financial supports of Dr. Koichi Tanaka, Dr. Shinichi Iwamoto, and Dr. Hidenori Takahashi of Koichi Tanaka Mass Spectrometry Research Laboratory, Shimadzu corporation throughout the collaboration research. This research project would not have been possible without their support and the great research environment of the Shimadzu corporation.

A special thank goes to Dr. Morgan Dehnel, Anand George, Nicolas Savard, and Stephane Melanson of D-PACE, Paul Williams and the all the members of Buckley Systems and Dr. Neil Broderick of the University of Auckland for their support during my stay in Auckland for one month. The collaboration research in Auckland about RF driven negative hydogen ion source was extremely worthwhile and enjoyable experience.

The author thank all research members of my study, expecially Daisuke Kuwahara, Tatsuya Masuda, Tatsuya Kuzumi, Tatsuhiro Tokai, and Keita Bito, for their hard works on the research project.

Lastly my deppest gratitude goes to my mother and father for the support and encouragement for 25 years.

Publications

Journal papers

1. Y. Shimabukuro, H. Takahashi, and M. Wada, "Electrode structure of a compact microwave driven capacitively coupled atomic beam source", *Jpn. J. Appl. Phys.* **57(1S)**, 01AA02 (2018).

2. H. Takahashi, Y. Shimabukuro, D. Asakawa, S. Yamauchi, S. Sekiya, S. Iwamoto, M. Wada, and K. Tanaka, "Structural Analysis of Phospholipid using Hydrogen Abstraction Dissociation and Oxygen Attachment Dissociation in Tandem Mass Spectrometry", *Anal. Chem.* **90**, 7230 (2018).

3. Y. Shimabukuro, H. Takahashi, S. Iwamoto, K. Tanaka, and M. Wada, "Tandem Mass Spectrometry of Peptide Ions by Microwave Excited Hydrogen and Water Plasmas", *Anal. Chem.* **90**, 7239 (2018).

4. H. Takahashi, Y. Shimabukuro, D. Asakawa, A. Korenaga, M. Yamada, S. Iwamoto, M. Wada, and K. Tanaka, "Identifying Double Bond Positions in Phospholipds Using Liquid Chromatography-Triple Quadrupole Tandem Mass Spectrometry Based on Oxygen Attachment Dissociation", *Mass Spectrom.*, **8(2)**, S0080 (2019).

5. Y. Shimabukuro, H. Takahashi, S. Iwamoto, K. Tanaka, and M. Wada, "Microwave Excitation of a Low-energy Atomic Hydrogen", *Plasma Sources Sci. Technol.*, **29**, 015005 (2020).

6. T. Eguchi, M. Sasao, Y. Shimabukuro, F. Ikemoto, M. Kisaki, H. Nakano, K. Tsumori, and M. Wada, "A compact electron cyclotron resonance negative hydrogen ion source for evaluation of plasma electrode materials", *Rev. Sci. Instrum.* **91**, 013508 (2020).

7. N. Tanaka, F. Ikemoto, I. Yamada, Y. Shimabukuro, M. Kisaki, W. A. Dino, M. Sasao, M. Wada, and H. Yamaoka, "Positive and negative hydrogen ion reflections of low-energy atomic and molecular hydrogen ion beam from HOPG and Mo surfaces", *Rev. Sci. Instrum.* **91**, 013313 (2020).

Conference papers

1. Y. Shimabukuro, D. Kuwahara, and M. Wada, "Contribution of Atomic Hydrogen Flux on H^- Ion Beam Extracted from a Negative Hydrogen Ion Source", *AIP Conf. Proc.* **2011**, 050008 (2018).

2. Y. Shimabukuro, T. Kuzumi, and M. Wada, "Injection of atomic hydrogen from a thermal cracker cell to plasma grid surface of a H^- ion source", *AIP Conf. Proc.* **2052**, 020004 (2018).

3. A. George, S. Melanson, D. Potkins, T. Stewart, M. Dehnel, Y. Shimabukuro, and N. Broderick, "Improvements in RF Multicusp Negative Ion Source", *10th Int. Particle Accelerator Conf.*, **TUPTS001**, Melbourne, Australia, May, 1928 (2019).

International conferences

1. Y. Shimabukuro, H. Takahashi, and M. Wada, "Development of Compact Microwave Driven Atomic Beam Sources", ISPlasma 2017/IC-PLANTS2017, 03P73, Chubu University, Aichi, 2017 03/03.

2. Y. Shimabukuro, H. Takahashi, S. Iwamoto, K. Tanaka, and M. Wada, "Development of a Compact Microwave Driven ICP Atom Source for Hydrogen Attachment/Abstraction Dissociation (HAD) for Tandem Mass Spectrometry", 65th ASMS Conference on Mass Spectrometry, WP352, Indianapolis, USA, 2017 06/07.

3. Y. Shimabukuro, D. Kuwahara, and M. Wada, "Contribution of Atomic Hydrogen Flux on H^- Ion Beam Extracted from a Negative Hydrogen Ion Source", 17th International Conference on Ion Source (ICIS 2017), Mo81, Geneva, Switzerland, 2017 10/16.

4. Y. Shimabukuro, H. Takahashi, S. Iwamoto, K. Tanaka, and M. Wada, "A Compact Microwave Driven Tuner-Free Capacitively Coupled Plasma Atom/Ion Source", The 10th EU-Japan Joint Symposium on Plasma Processing, P-24, Okinawa, 2017 12/04.

5. Y. Shimabukuro, H. Takahashi, S. Iwamoto, K. Tanaka, and M. Wada, "A Tuner Integrated Microwave Driven Atomic Source for Radical Induced Dissociation Mass Analysis", ISPlasma2018/IC-PLANTS2018, 07aB08O, Meijo University, Aichi, 2018 03/07.

6. H. Takahashi, Y. Shimabukuro, D. Asakawa, S. Iwamoto, M. Wada, and K. Tanaka, "Radical-Induced Dissociation of Isomeric Compounds Using Gas-phase Radical

Species (H•, OH•, N•, O•)", 66th ASMS Conference on Mass Spectrometry, WOH pm 02:30, San Diego, USA, 2018 06/06.

7. Y. Shimabukuro, H. Takahashi, S. Iwamoto, K. Tanaka, and M. Wada, "Development of Tuner Integrated Microwave Driven Radical Beam Sources for Radical Induced Dissociation Molecular Structural Analysis", XXII International Mass Spectrometry Conference, WP-175, Florence, Italy, 2018 08/29.

8. Y. Shimabukuro, T. Kuzumi, and M. Wada, "Injection of Atomic Hydrogen from a Thermal Cracker Cell to Plasma Grid Surface of H^- Ion Source", The 6th International Symposium on Negative Ions, Beams, and Sources, 40, Novosibirsk, Russia, 2018 09/04.

9. Y. Shimabukuro, F. Ikemoto, I. Yamada, and M. Wada, "Alumina Capillary Compact Microwave Ion Source", 10th International Particle Accelerator Conference, TUPTS031, Melbourne, Australia, 2019 05/21.

10. A. George, S. Melanson, D. Potkins, T. Steward, M. Dehnel, Y. Shimabukuro, and N. Broderick, "Improvements in RF Multicusp Negative Ion Source", 10th International Particle Accelerator Conference, TUPTS031, Melbourne, Australia, 2019 05/21.

11. H. Takahashi, Y. Shimabukuro, D. Asakawa, S. Yamauchi, S. Iwamoto, M. Wada, and K. Tanaka, "Oxygen Attachment Dissociation MS/MS for Differentiation between Cis and Trans Fatty Acids", 67th ASMS Conference on Mass Spectrometry, ThP 400, Atlanta, USA, 2019 06/06.

12. N. Tanaka, F. Ikemoto, I. Yamada, Y. Shimabukuro, M. Kisaki, W. A. Dino, M. Sasao, M. Wada, and H, Yamaoka, "Positive and Negative Ion Reflections of Low-Energy Ion Beam from Materials Surface", 18th International Conference on Ion Sources, MonP37, Lanzhou, China, 2019 09/02.

13. T. Eguchi, M. Sasao, Y. Shimabukuro, J. Hernandez, M. Kisaki, H. Nakano, M. Wada, and K. Tsumori, "A Compact ECR Negative Hydrogen Ion Source for Evaluation of Plasma Grid Materials", 18th International Conference on Ion Sources, TueP29, Lanzhou, China, 2019 09/03.

14. M. Sasao, T. Eguchi, Y. Shimabukuro, J. Hernandez, M. Kisaki, H. Nakano, K. Tsumori, M. Wada, and G. Cartry, "Prospect of Cs-free Hydrogen Negative Ion Sources Using C12A7 Plasma Electrodes", 18th International Conference on Ion Sources, ThuM05, Lanzhou, China, 2019 09/05.

15. Y. Shimabukuro, T. Tokai, K. Bito, and M. Wada, "Comprehensive Study on the Low-energy Atomic Hydrogen Beam: From Production to Velocity Distribution Measurement", The 3rd International Symposium of the Vacuum Society of the Philippines, O-10, Cebu City, Philippines, 2020 01/08.

16. T. Tokai, Y. Shimabukuro, K. Bito, F. Ikemoto, and M. Wada, "Investigation on proton ratios when a small amount of inert gases in hydrogen plasma" The 3rd International Symposium of the Vacuum Society of the Philippines, P-04, Cebu City, Philippines, 2020 01/08.

17. Y. Shimabukuro, H. Takahashi, S. Iwamoto, K. Tanaka, and M. Wada, "The Forefront Development of Novel Radical Induced Dissociation Techniques toward Realization of Next-generation Medical Diagnostics", The 3rd International Symposium of the Vacuum Society of the Philippines, O-28, Cebu City, Philippines, 2020 01/10.

Domestic conferences

1. Y. Shimabukuro, H. Takahashi, and M. Wada, "Development of a Compact Atom Beam Source by Capacitively Coupled Plasma at 2.45 GHz", The 77th Japanese Society of Applied Physics Autumn Meeting 2016, 16p-P2-1, Niigata, 2016 09/16.

2. Y. Shimabukuro, H. Takahashi, M. Wada, "Development of a Compact Microwave Driven Atomic Beam Sources", The 33rd Japan Society of Plasma Science and Nuclear Fusion Research Annual Meeting, 30pP04, Miyagi, 2016 11/30.

3. H. Takahashi, Y. Shimabukuro, S. Yamauchi, S. Sekiya, S. Iwamoto, M. Wada, and K. Tanaka, "Novel fragmentation mass spectrometry employing hydrogen attachment/abstraction dissciation (HAD) and several gas-phase neutral radicals (H•, O, OH•)", The 65th Annual Conference on Mass Spectrometry Japan 2017, 2D-O1-0950, Ibaraki, 2017 05/18.

4. Y. Shimabukuro, H. Takahashi, and M. Wada, "Atomic Temperature of H• Produced by Microwave Driven Inductively Coupled Atomic Source", The 78th Japanese Society of Applied Physics Autumn Meeting 2017, 5p-S22-14, Fukuoka, 2017 09/05.

5. Y. Shimabukuro, T. Okumura, H. Takahashi, S. Iwamoto, K. Tanaka, and M. Wada, "Production and evaluation of radical beams generated in tuner integrated compact microwave plasma sources", The 35th Japan Society of Plasma Science and Nuclear Fusion Research Annual Meeting, 3P32, Osaka, 2018 12/03.

6. Y. Shimabukuro, H. Takahashi, S. Iwamoto, K. Tanaka, and M. Wada, "The forefront of a development of low energy radical beam sources for new radical induced dissociation in tandem mass spectrometry", The 67th Annual Conference on Mass Spectrometry Japan 2019, 3D-O2-1505, Ibaraki, 2019 05/15.

7. Y. Shimabukuro, T. Tokai, K. Bito, and M. Wada, "Velocity distribution measurement of low-energy atomic hydrogen with pulse counting detection", The 36th Japan Society of Plasma Science and Nuclear Fusion Research Annual Meeting, 30P12, Osaka, 2019 11/30.